Imperial College London

HEAD LAB

# BRAIN INJURY MITIGATION EFFECTS OF NOVEL HELMET TECHNOLOGIES IN OBLIQUE IMPACTS

Fady F. Abayazid

This thesis is submitted in partial fulfilment of the requirements for the degree of Doctor of Philosophy

FEBRUARY 28, 2022

DYSON SCHOOL OF DESIGN ENGINEERING
Imperial College London, South Kensington, London, SW7 2AZ

# Statement of Originality

I hereby declare that the work presented in this thesis is my own. Where information is derived from other studies, the sources are indicated in the text and appropriately referenced.

Fady F. Abayazid

# Copyright Statement

# Acknowledgements

First and foremost, I would like to offer a sincere and deep appreciation to my supervisor, Dr Mazdak Ghajari, for generously providing his time, advice, commitment, and mentorship throughout my PhD for topics related to this PhD and beyond. His open-mindedness, generosity and empathy meant that his leadership was invaluable to me. I would also like to offer great thanks to my father, mother, and sister for encouraging me to take the leap and pursue a PhD in the first place. Last, but certainly not least, I would like to thank the woman who became my wife during my PhD for playing a part in shaping the man I am today.

There are many other friends and academics who many thanks is owed to, such as Professor Maria Charalambides, Dr Ruth Brooker, Dr Helena Stigson, and many others for supporting my journey and sharing data with me that has formed the foundation of much of the work presented here. A special thanks goes to Professor Michael Gilchrist and Dr Andrew Phillips for their invaluable feedback and focused attention during the thesis examination and the viva.

# Publications

## Journal Papers

Abayazid, F. F., & Ghajari, M. (2020). Material characterisation of additively manufactured elastomers at different strain rates and build orientations. *Additive Manufacturing*, *33*(December 2019), 101160. https://doi.org/10.1016/j.addma.2020.101160

Abayazid, F., Ding, K., Zimmerman, K., Stigson, H., & Ghajari, M. (2021). A New Assessment of Bicycle Helmets: The Brain Injury Mitigation Effects of New Technologies in Oblique Impacts. Annals of Biomedical Engineering. https://doi.org/10.1007/s10439-021-02785-0

Fahlstedt, M., Abayazid, F., Panzer, M. B., Trotta, A., Zhao, W., Ghajari, M., Gilchrist, M. D., Ji, S., Kleiven, S., Li, X., Annaidh, A. N., & Halldin, P. (2021). Ranking and Rating Bicycle Helmet Safety Performance in Oblique Impacts Using Eight Different Brain Injury Models. *Annals of Biomedical Engineering*, *49*(3), 1097–1109. https://doi.org/10.1007/s10439-020-02703-w

## Conference Presentations and Proceedings

Abayazid, F. F. (2020). Material characterisation of AM elastomers at various strain rates and print orientations. *International Conference on Rheology*.

Abayazid, F. F. (2021). The brain injury mitigation effects of new helmet technologies in oblique impacts. *26th Congress of the European Society of Biomechanics*.

## Pending Publications

Abayazid, F. F., Carpanen, D., & Ghajari, M. (n.d.). *A new class of recoverable circular cell honeycombs for controlling shear and compressive responses during oblique impacts*. (under review)

Abayazid, F. F., & Ghajari, M. (n.d.). *Evaluation of novel recoverable circular cell honeycombs for reducing brain strain in oblique impacts*. (in preparation)

# Abstract

Cyclists are a rapidly growing group of the world population, particularly after the COVID-19 pandemic which made cycling an attractive form of active mobility for commuters. Yet, cyclists are among the most vulnerable road users. Their severe injury and fatality rate per passenger mile are several folds larger than car occupants and bus passengers. Analysis of accident data shows that impacts to a cyclist's head occur at an angle in vast majority of real-world head collisions. This produces large rotational head motion. There is significant body of research that shows rotational head motion is the key determinant of brain deformation and subsequent damage to the brain tissue. Hence, novel helmet designs adopt shear-compliant layers within a helmet with the aim of reducing the rotational head acceleration and velocity during an impact, hence reducing risk of brain injury.

Cellular materials can be engineered to have interesting mechanical properties such as negative Poisson ratio or anisotropy. Their cellular structure gives rise to a unique combination of properties which are exploited in engineering design: their low density makes them ideal for light-weight design, and their ability to undergo large deformations at relatively low stresses make them ideal for dissipating kinetic energy with near-optimal deceleration. As revealed in this thesis, it also is possible to engineer cellular structures to have high or low shear stiffness with minimal change to their axial stiffness, and vice versa. This has the potential to be very beneficial for cases that require oblique impact management where both axial and shear stiffnesses play a role. However, this domain has seldom been explored, let alone applied to a use case which may result in improved performance that saves lives such as helmets.

The main question this thesis aims to address is: Can helmets be improved to reduce the risk of cyclist brain injury in oblique impacts? To answer this question, it was necessary to first assess conventional helmets and emerging technologies aiming to improve helmets in oblique impacts. Hence, 27 bicycle helmets with various technologies were assessed in three different oblique impact conditions. The outcome of studying this proved that helmets may be improved with shear compliant mechanisms between the head and helmet. However, the improvements were marginal and highly dependent on impact site. This is hypothesised to be due to the presence of expanded polystyrene (EPS) foam alongside these shear-compliant mechanisms which hinders their performance. We found that one of the best performing helmets in oblique impacts was one that utilises air and entirely replaces EPS foam yet had some drawbacks such as lack of reusability and shell structure. This encouraged the work that followed which aimed to replace the EPS foam layer in helmets with an air-filled rate-sensitive cellular structure. This work leveraged finite element modelling which employed visco-hyperelastic material models which were validated with axial and oblique impact tests of the bulk material and

cellular array samples different speeds. The novelty is that the axial and shear stiffness of the cells could be tailored independently with simple changes to the geometry of the cells. This led to an exciting investigation to determine whether shear-compliant cells outperformed their shear-noncompliant counterparts, which exhibit similar axial stiffness, with respect to brain injury metrics in a helmet. The results showed that, although this may be the case, often the shear-compliant cells dissipated less energy during impact and bottomed-out as a result, leading to adverse effects. Hence, introduction of shear-complaint structures in helmets should be done with care as the energy is dissipated in shear with such cellular structures during oblique impacts which needs to be properly managed. In future, the performance improvements may be implemented for different impact speeds utilising the viscoelastic nature of the cells and inflation of the cells to change their shape.

# Contents

Statement of Originality ..... 1

Copyright Statement ..... 2

Acknowledgements ..... 3

Publications ..... 4

Journal Papers ..... 4

Conference Presentations and Proceedings ..... 4

Pending Publications ..... 4

Abstract ..... 5

1 Chapter One: Introduction ..... 21

1.1 Hypotheses ..... 22

1.2 Thesis Outline ..... 22

2 Chapter Two: Literature Review ..... 25

2.1 Head Injury Mechanisms ..... 25

2.1.1 Traumatic Brain Injury (TBI) ..... 27

2.1.2 Imperial College Traumatic Brain Injury Model ..... 28

2.2 Helmets ..... 31

2.2.1 Shell ..... 32

2.2.2 Foam Liner ..... 33

2.2.3 Comfort Foam & Retention System ..... 37

2.3 Advancements in Helmet Technology ..... 38

2.4 Helmet Test Standards ..... 42

2.5 Helmet Impact Mechanics ..... 46

2.5.1 Axial Impacts ..... 46

2.5.2 Oblique Impacts ..... 47

3 Chapter Three: A New Brain Injury Mitigation Assessment of Bicycle Helmets in Oblique Impacts 51

3.1 Introduction ..... 52

3.2 Methods ..... 53
3.2.1 Bicycle Helmets ..... 53
3.2.2 Oblique Impact Tests ..... 55
3.2.3 Kinematics-based Measures of TBI ..... 57
3.2.4 Finite Element Modelling of TBI ..... 57
3.2.5 Statistical Analysis ..... 58
3.3 Results ..... 58
3.3.1 Head Motion ..... 58
3.3.2 Kinematics-based Measures ..... 58
3.3.3 Strain Across the Whole Brain ..... 61
3.3.4 Strain in the Corpus Callosum ..... 63
3.3.5 Strain in Sulci ..... 63
3.4 Discussion ..... 64
3.5 Conclusion ..... 67
3.6 Appendix ..... 68
3.6.1 Kinematic-based Metrics ..... 68
3.6.2 Brain Strain-based Metrics ..... 72
4 Chapter Four: Material Characterisation of Additively Manufactured Elastomers at Different Strain Rates and Build Orientations ..... 76
4.1 Introduction ..... 77
4.2 Methods ..... 79
4.2.1 Experimental Methods ..... 79
4.2.2 Numerical Methods ..... 82
4.3 Results ..... 84
4.3.1 Experimental Results ..... 84
4.3.2 Model Predictions of Stress Relaxation Responses ..... 92
4.3.3 Model Predictions of Tension and Compression Responses at Different Strain Rates 93
4.4 Discussion ..... 95

4.5 Conclusion ..... 98
4.6 Appendix ..... 99
4.6.1 Images ..... 99
4.6.2 Tension ..... 100
4.6.3 Compression ..... 101
4.6.4 Stress Relaxation and DMA ..... 102
4.6.5 Determining Prony Series Constants from DMA Results ..... 103
5 Chapter Five: A New Class of Recoverable Circular Cell Arrays for Controlling Shear and Compressive Responses During Oblique Impacts ..... 105
5.1 Introduction ..... 105
5.2 Materials and Methods ..... 107
5.2.1 Experimental Methods ..... 107
5.2.2 Visco-hyperelastic Material Model and Properties ..... 109
5.2.3 Computational Methods ..... 111
5.3 Results ..... 114
5.3.1 Finite Element Model Validation ..... 114
5.3.2 Curvature Amplitude Effect in Axial Loading ..... 117
5.3.3 Curvature Direction Effect in Oblique Impacts ..... 117
5.3.4 Shape Selection Strategy for Oblique Impact Performance ..... 120
5.3.5 The Effect of Curvature with Strain Rate ..... 121
5.4 Discussion ..... 122
5.5 Conclusion ..... 126
5.6 Appendix ..... 127
5.6.1 Bespoke Oblique Impact Drop Tower ..... 127
5.6.2 Bulk Material and Single Cell Validation ..... 129
5.6.3 Parameter Calculation ..... 133
5.6.4 Edge Effects and Boundary Condition ..... 134
5.6.5 Deformation Modes ..... 135

5.6.6 Derivation of Axial Performance of Benchmark Materials ..... 135
6 Chapter Six: Influence of Compressive-Shear Properties of Novel Helmet Liners on Brain Injury Metrics During Oblique Impacts ..... 138
6.1 Introduction ..... 138
6.2 Materials and Methods ..... 140
6.2.1 Experimental Methods ..... 140
6.2.2 Helmet Modelling ..... 141
6.2.3 Brain Injury Modelling ..... 147
6.3 Results ..... 148
6.3.1 Validation ..... 148
6.3.2 Performance Comparison ..... 149
6.4 Discussion ..... 154
6.4.1 Influence of Shear Stiffness ..... 155
6.4.2 Influence of Axial Stiffness ..... 156
6.4.3 Comparison to the Conventional Helmet ..... 157
6.4.4 Reversal of Rotational Acceleration Direction in Retrofitted Helmets ..... 157
6.4.5 Limitations and Future Work ..... 159
6.5 Conclusion ..... 160
7 Conclusions and Future Work ..... 162
8 References ..... 165

# List of Figures

Figure 1 – Left: Different types of hematomas as a result of brain injury.Right: Schematic of cerebral contusion as a result of abrupt head motion. [30] ..... 26
Figure 2 – ICL TBI model of the human brain (right) with details of the corpus callosum and sulci. ... 29
Figure 3 – Cutouts showing fundemental common components between a bicycle (right) and motorcycle helmet (left) [64]. ..... 32
Figure 4 – PC stress-strain curves at various strain rates adapted from [70]. ..... 33
Figure 5 – Microstructure of cellular materials: (a) open-cell polyurethane, (b) closed-cell polyethylene, (c) nickel, (d) copper, (e) zirconia, (f) mullite, (g) glass, (h) a polyether foam with both open and closed cells. [74] ..... 34
Figure 6 – Representative nominal (engineering) stress-strain curve of EPS and similar foams under compressive loading [68]. ..... 35
Figure 7 – A) Comparison of the dissipated work of foam and a fully dense elastic solid at a given stress threshold. Both axes are normalised by the elastic modulus of the parent solid. B) A representation of the compressive stress-strain response of EPS foam of different densities [80]. ..... 36
Figure 8 – Hövding airbag in the undeployed (left) and deployed (right) positions [89]. ..... 38
Figure 9 – Multi-directional Impact Protection Systems (MIPS) which is essentially a low friction slip layer (yellow) placed between the rider's head and the outer shell [91]. ..... 39
Figure 10 – Conical liner helmet (Blanco et al.) [69] ..... 40
Figure 11 – A viscoelastic add-on liner comrpised of two mechanically-connected rubber parts. Their implementation in a motorcycle helmet is shown on the left, and their deformed state in compression and shear is shown on the right (Ghajari et al.) [93] ..... 41
Figure 12 – Hierarchial lattice liner (Khosroshahi et al.) [95] ..... 41
Figure 13 – Schematic of apparatus used for the shock absroption test of BS EN 1078 [13]. ..... 43
Figure 14 - Geometry of a helmeted head contact area with a flat rigid anvil. [115] ..... 46
Figure 15 – Analytical representation of a helmeted head impacting a flat rigid anvil during oblique impact. [119] ..... 48
Figure 16 – Analytical representation of a helmeted head impacting a flat rigid anvil during oblique impact. [119] ..... 49
Figure 17 – Mid-sagittal cross-sectional views of some of the helmets used in this study (from left to right): A conventional helmet, a 'multi-directional impact protection system' (MIPS) helmet, a corrugated 'wavy' cellular liner (WaveCel) helmet, a shear pad (SPIN) helmet and an airbag helmet (Hövding 3.0). ..... 55

Figure 18 – Setup of the three experimental impact conditions carried out for each helmet (A). For each of the impacts, three translational and three rotational acceleration time-history pulses are recorded about the CoG of the HIII headform (B). These are then applied to the detailed finite element model of TBI (C) which is then further analysed to extract brain strain as an injury metric in regions-of-interest such as the corpus callosum and sulci (D). The three impacts were selected to produce different head rotations (A, B). Impact 1, with the initial position of the headform X-, Y- and Z-axis 0°, produces predominant rotation about the X-axis. For impact 2, the initial position of the headform was X-, Y-axis 0° and Z-axis -90°, which produces predominant rotation about the Y axis. For impact 3, the Initial position of the headform was X- and Z-axis 0° and 65° around Y-axis. This impact produces large rotation about the Z-axis compared to the other impacts. All impacts were vertical against a 45-degree anvil with 40-grit sandpaper at 6.3m/s (A). ..... 56
Figure 19 – (A) Snapshots from the high-speed videos of a helmet from each technology category captured 10 ms apart, 10 and 20 ms after the start of impact 1. (B) Mean resultant translational and rotational time-history pulses colour-coded by technology. A filled region bounds the minimum and maximum recorded traces across all helmets where more than one helmet was assessed for a given technology. The results show that acceleration pulses peaked between 8 – 10 ms with an impact duration under 20 ms except for the Hövding 3.0 airbag helmet (white). Due to the larger size of the inflated airbag helmet, the impact duration was significantly increased and hence the peak was dramatically reduced. In all cases, translational accelerations did not exceed 150 g and rotational accelerations rarely exceeded 8 krads $ms^{-1}$. ..... 59
Figure 20 – The performance of all the helmets in impact condition 1 (left), 2 (middle) and 3 (right) grouped by technology (marker fill colour) with respect to the four kinematic metrics assessed (PTA, PRA, PRV and BrIC). Solid white horizontal lines represent the mean metric value of each technology. The dotted white horizontal lines represent the mean for conventional helmets (red). The red and green margins represent regions where the performance would be significantly worse or better than conventional helmets for that metric ($p<0.05$). The right-hand side axis of each plot represents the percentage difference of the metric value of each helmet with respect to the mean of the conventional helmets. The results show that, in most cases, helmets perform either significantly better than (green marker edge) or insignificantly different to conventional helmets, with rare occasions where helmets perform significantly worse (red marker edge). Note: Each marker represents the average value of the repeat tests for that particular helmet. ..... 61
Figure 21 – Voxel-wise representation of the maximum Green Lagrange strain in the brain in the transverse plane as a result of each impact condition for each helmet. The coloured marker to the left

of each helmet name represents the technology. The results show a large variation in brain strain patterns across helmets and across impact conditions for each helmet. ..... 62
Figure 22 – The performance of all the helmets in impact condition 1 (left), 2 (middle) and 3 (right) grouped by technology (marker fill colour) with respect to the Green-Lagrange strain across the entire brain (global) as well as in brain regions-of-interest (corpus callosum and sulci). For the global and corpus callosum, the 90$^{th}$ percentile strain value was used. For the sulci, the mean strain value was used. Solid white horizontal lines represent the mean metric value of each technology. The dotted white horizontal lines represent the mean for conventional helmets (red). The red and green margins represent regions where the performance would be significantly worse or better than conventional helmets for that metric ($p>0.05$). The right-hand side axis of each plot represents the percentage difference of the metric value of each helmet with respect to the mean of the conventional helmets. The results show that, in most cases, helmets perform either significantly better than (green marker edge) or insignificantly different to conventional helmets, with rare occasions where helmets perform significantly worse (red marker edge). Note: Each marker represents the average value of the repeat tests for that particular helmet..... 64
Figure 23 - Stratasys Connex3 Objet500 printer bed with printed X- Y- and Z- tension (A, B and C respectively), compression (D, E and F) and DMA (G, H and I) samples. Streaks left by the PolyJet printing process can be seen lengthwise along the X-tensile sample (A) and along the width of the Y-sample (B). ..... 79
Figure 24 - TA Q800 DMA tester setup with x-direction A30 specimen on the dual-cantilever clamp. ..... 82
Figure 25 - Tensile stress-strain results showing the effects of strain rate on A30 (A) and T+ (B) and the effects of build orientation on A30 (C) and T+ (D)..... 85
Figure 26 – Ultimate tensile stress and strain of A30 (left) and Tango+ (right) at various strain rates 87
Figure 27 - Compressive loading and unloading stress-strain results for A30 (A) and Tango+ (B) Y-samples at varying strain rates. Comparison between compressive stress-strain responses of A30 (C) and Tango+ (D) X-, Y- and Z- samples at the lowest and highest strain rates. ..... 89
Figure 28 - Cyclic loading of A30 and Tango+ X- samples at strain rates 0.05 /s (blue) and 0.5 /s (red). ..... 90
Figure 29 – Normalised relaxation profiles for A30 and T+ samples at different strain levels (A). Stress relaxation results for X-, Y- and Z- A30 samples at 20% strain with a 0.3 s ramp time (B)..... 90
Figure 30 - DMA loss tangent and storage modulus (E') results temperatures relevant to glass transition of A30 (left) and Tango+ (right) samples printed in different orientations. ..... 91

Figure 31 - DMA TTS frequency-domain storage (E') and loss (E'') moduli (left) and loss tangent (right) master curves for A30 shifted using Williams-Landel-Ferry shift constants $C_1$=10.5, $C_2$=100. ..... 91
Figure 32 – Relaxation modulus of our Prony series prediction overlaid on the experimental results of A30 and T+ from a 100s relaxation test. ..... 92
Figure 33 - The visco-hyperelastic material model prediction vs. experiment for A30 and T+ tensile (A,B) and compressive (C,D) loading responses at various strain rates. ..... 94
Figure 34 – Comparison between the relaxation test results and our Prony series prediction and that reported in [164]. ..... 97
Figure 35 - comparison between pristine and failed A30 tensile specimen showing no residual plastic strain (left). Scanning electron microscope image along the Y-Z plane showing 16 micrometre layer thickness (right). ..... 99
Figure 36 - A30 X- sample during tensile testing at 0.03 /s at the start of testing (left) and at 56% strain (right). ..... 100
Figure 37 – (A) Comparison between A30 and Tango+ tensile responses at the lowest and highest tested strain rates and (B) exemplar set of results (A30, 0.05 /s strain rate) showing the repeatability achieved in tests. ..... 101
Figure 38 - Cyclic loading stress-strain curves of A30 (A) and Tango+ (B) Z- samples at a strain rate of 0.5 /s with no idling between cycles (blue) and a 20 second idle (red). ..... 101
Figure 39 - Repeats of A30 relaxation tests (A) and DMA TTS results (B). Stress relaxation of A30 (C) and T+ (D) at different strain levels. ..... 102
Figure 40 - Experimental vs. numerical approximation of E' and E'' master curves. The Prony series parameters obtained from this approximation were normalised by the instantaneous modulus obtained using Equation (28)-(29). ..... 103
Figure 41 – Schematic of the custom-built drop tower for experimental impact testing under axial and oblique impact conditions. ..... 108
Figure 42 – Computational pipeline. **A.** Parameterised unit cell with height $h$ and radius $R$, wall thickness $t$ and arc radii $r1$ and $r2$ and arc angle $\theta$. **B.** Hexagonal packing arrangement of unit cell to make the honeycomb. **C.** Axial and oblique load testing of cellular array. **D.** Postprocessing and pre-buckling (region I), post-buckling (region II) and densification (region III) parameter identification. **E**. The geometry of all shape amplitudes ranging from -1 (concave) to 1 (convex) with the intermediate shape amplitudes in increments of 0.25. ..... 112
Figure 43 – FE model validation of concave (left) and convex (right) cell arrays during axial impact via deformation and force-history responses. The test was set up such that a 5 kg aluminium impactor block was released from a height into guided free-fall such that the final velocity prior to impact was

5.6 m/s. CORA scores of the FEA axial force-history response (red) is 'Good' for concave cell arrays and 'Fair' for convex cell arrays in comparison to experimental (black). Shaded grey areas show the performance window of the combined experimental repeat impact tests. ..... 114
Figure 44 – FE model validation of concave (left) and convex (right) cell arrays during oblique impact via deformation and force-history responses. The test was set up such that a 5 kg aluminium impactor block was released at 45° from a height into guided free-fall onto the specimens fixed to a swivel table inclined to 45° such that the final resultant velocity prior to impact was 5.6 m/s. CORA scores of the FEA axial (Z-axis) force-history response (solid red) is 'Marginal' for concave cell arrays and 'Good' for convex cell arrays in comparison to experimental (black). The scores were 'Good' and 'Fair' for the shear (Y-axis) forces (dashed), respectively. Shaded grey areas show the performance window of the combined experimental repeat impact tests..... 115
Figure 45 – **A.** Axial stress-strain curves of 1.5 mm wall concave (red) and convex (blue) cell arrays at the extremities of the shape amplitudes investigated, i.e. -1 and 1 respectively, in axial compression at 7.5 m/s. The black vertical lines lead to FEA model deformation sequence at axial compressive strains of 0.1, 0.3 and 0.5 with contours of von-mises stress ($\sigma vm$). **B.** The effect of different shape amplitudes, ranging from concave (-1) to convex (1), on $\sigma z(ave)$ and $U$ in axial loading at 5 m/s. Cell arrays with the same unit cell wall thickness are connected by non-orthogonal dotted lines, whose relative densities is represented by their marker size. ..... 116
Figure 46 - Axial (**A.**) and shear (**B.**) stress-strain curves of 2.0 mm wall concave (red) and convex (blue) cell arrays at the extremities of the shape amplitudes investigated, i.e. -1 and 1 respectively, in 45° compression at 7.5 m/s. The FEA model deformation sequence at axial compressive strains of 0.1, 0.3 and 0.6 are presented above the plot (connected with black dotted lines) with contours of von-mises stress ($\sigma vm$). ..... 118
Figure 47 - **A.** Axial stress contours of axial loading (top row) and oblique loading (middle row) as well as shear stress contours in oblique loading (bottom row) at an axial loading velocity of 5 m/s. The figure shows how the stress-strain relationship changes with shape. Each of the columns represents a different cell wall thickness. The effect of different shape amplitude on $\sigma z(ave)$ (**B.**) and $\tau zy(ave)$ (**C.**) in in 45° compression at 7.5 m/s. $U$ of each data point is represented by the marker colour. Cell arrays with unit cells with the same wall thickness are connected by non-orthogonal dotted lines, whose relative densities is represented by their marker size. ..... 119
Figure 48 - **A.** The influence of shape amplitude on the average shear to axial stress ratio during 7.5 m/s oblique loading with different wall thicknesses. Larger ratios are achieved with concave shapes in the region left of the dotted black vertical line which marks a straight-wall cell. **B.** Variation of the individual axial and shear stress components with different shapes, indicated by the maker colour. The

relative densities are represented by the marker size. Solid lines represent lines of best fit. Dotted lines connect equivalent shapes of different relative densities. ..... 121
Figure 49 - **A.** Stress-strain curves of 2.0 mm wall concave cell arrays (shape = -1) during 45$^{o}$ impact at 2.5, 5.0 and 7.5 m/s, with the shaded areas representing the internal energy at each impact velocity. The results show that increasing the impact speed increases the stresses at all strains until densification. **B.** and **C.** show the average axial and shear stresses respectively with overlaid internal energy results (marker colour) of all shape amplitudes with 1.5 mm cell walls during 45$^{o}$ impact at 2.5, 5.0 and 7.5 m/s. The results show that increasing the impact velocity increases both axial and shear stress components across all shapes whilst maintaining the underlying trend in the stresses observed due to shape changes. ..... 122
Figure 50 - **A.** Normalised comparison of peak axial stress ($\sigma z$) vs. internal energy ($U$) between the concave, straight and convex cell arrays and other cellular materials, including Polyethylene (PE), Polyurethane (PU) foams and regular honeycombs (HC) in out-of-plane (Ax.) and in-plane (Tr.) loading, at different relative densities represented by their marker size. **B.** Relationship between densification strain ($\varepsilon D$) and relative density ($\rho$) of all shapes in axial and oblique impacts, with the lines of best fit marked with solid and dotted lines respectively for each impact condition. The grey line represents the relationship for foams and honeycombs following Ashby et al. [80]. ..... 124
Figure 51 – Left: Colour-coded drop tower subassemblies: Green: Main frame, Purple: Carriage, Yellow: Magnet assembly, Red: Base. The cross-sectional profile of the aluminium extrudes is outlined in black. A rendering of the drop tower is shown on the right. ..... 127
Figure 52 – The dial mechanism: The plate bolted to the carriage (purple) is held to the slotted plate (orange) mounting the impacting block via a center bolt. This angle is adjusted by removing the impacting block, loosening the center bolt, pivoting the orange plate and retightening. The orange plate has open slots that allow the impacting block to detach and slide off during impact, whilst the carriage and dial continue to fall post impact till they are caught by a mat on the floor. ..... 128
Figure 53 – The trigger signal and data aquisition components and routes of the drop tower. 1 - An Aruindo (a) is used to energise the magnet (b) that lifts the carriage with the impactor. Once the hoist raises the carriage assembly to the desired drop height, the Arduino is once again triggered to de-energise the magnet and release the carraige. The carriage then falls with the impactor block it supports. As it falls, it interrupts an optical switch (c) placed on the main frame track. This sends a signal to the Arduino to send a trigger signal to the data aquisition module (National Istruments CDAQ) chassis (f) and the high-speed camera (g). The NI CDAQ is at this point already collecting data sent from the loadcell (d) through the Kistler LabAmp charge amplifier (e). The trigger signal only acts as a timestamp for time = 0ms. ..... 129

Figure 51 – The experimental impact test setup showing a solid Agilus30 cylindrical specimen rested on the steel plate attached to the loadcell of which the impact response at different impact speeds is used for the subsequent finite element model validation. The upper left section of the figure shows the convex cell 3D printed in Agilus30 after the removal of the support material and adhesion to the hard plastic (VeroBlack) back plate.....130
Figure 52 – High-speed video of experimental test with the overlaid finite element model prediction of drop-tower impacts at 4 m/s (**A.**) and 2 m/s (**B.**) on bulk Agilus30 material samples and 2.2 m/s impact on convex cellular structure with entrapped air and 2mm wall thickness (**C.**). Experimental load-cell force-history of the repeat impacts on the bulk material sample (**D.**) and the cellular structure (**E.**) are compared to the finite element model prediction with different mesh densities and element formulations.....131
Figure 53 – **A.** Finite element model of the honeycomb array with different centrally-packed layers with their regions marked by different colours. **B.** The finite element model with the periodic boundary condition which ties nodes of the outer null faces to the corresponding node of the central cell, with an exemplar constrained node set in red. **C.** The stress-strain and corresponding internal energy curves during axial loading of 2 mm concave and convex cells with different number of layers. .....134
Figure 54 – Deformation modes of concave (top) and convex (bottom) cells at small shape amplitudes. The figure shows that convex cell walls experience higher order buckling modes in comparison to concave cells of the same amplitude at all thicknesses above $t$ = 0.5 mm. .....135
Figure 55 – Experimental impact setup for all three oblique impact tests carried out for following validations and comparison. Prior to each impact, a halo ring attached to a monorail simply supports the helmeted headform during free fall. During the impact, the halo ring drops past the anvil leaving the helmeted headform free during impact during which headform translational and rotational accelerations are recorded for further analyses.....141
Figure 56 – The process of reverse engineering the bicycle helmet. .....142
Figure 57 – Experimental setup for obtaining the material properties of the polycarbonate that forms the helmet shell in study.....143
Figure 58 – Left: compressive stress-strain curve of EPS foam with a density of 120 g/l as used in the finite element model of the conventional helmet. Right: Tensile stress-strain curves of the PC helmet shell material.....144
Figure 59 – Top left shows a unit cell of the retrofitted helmet liner with a section cut showing the height $h$ and radius $R$, wall thickness $t$ and arc radii $r1$ and $r2$ and arc angle $\theta$. In this study, three variations were chosen, where the following base values were used: $h$ = 25mm, $R$ = 12.5mm and $t$ = 2mm. The arc radii $r1$ and $r2$ and arc angle $\theta$ were reversed to obtain the concave and convex cell

variants assessed in this study. The helmeted head models fitted with concave, straight and convex cells are shown in the bottom left, middle, and right respectively. ..... 146
Figure 60 – Validation of the helmet finite element model in three oblique impact conditions. The top half of the figure shows the figure shows animation frames at 0 ms, 10 ms and 20 ms of the FEA and experimental predictions. The bottom half shows the resultant translational and rotational time-histories of each impact showing the correlation between the experimental results and finite element model predictions. ..... 148
Figure 61 – Animation frames at 10 and 20 ms after impact, and translational and rotational time-histories of each helmet in impact 1..... 149
Figure 62 – Animation frames at 10 and 20 ms after impact, and translational and rotational time-histories of each helmet in impact 2..... 150
Figure 63 – Animation frames at 10 and 20 ms after impact, and translational and rotational time-histories of each helmet in impact 3. The bar chart shows a summary of the kinematic injury metrics (PTA, PRA, PRV and BrIC) of each of the helmets in each of the impact conditions. ..... 151
Figure 64 – Horizonal (z-normal) plane sections of the brain showing strain contour predictions for each helmet in all impact conditions. The bar chart below summarises the 90$^{th}$ percentile GL strain and the mean strain across the sulci for each helmet in each impact condition. ..... 153
Figure 65 – Section cut view of the helmeted head with concave (left) and convex (right) cell liners with close-up views showing the shearing of the cells at and around the impact zone. As concave cells have a higher shear stiffness than convex cells, helmets with concave cells had a lower shear strain as seen in the close-ups. Helmets with the shear-stiffened cells had a larger accelerations and energy dissipation at the start which meant the crush distance was reduced. ..... 155
Figure 66 – Enveloped pressure distribution on the head across time in impact 1 resulting from contact with the conventional (left) and straight cell-fitted (right) helmet liners. The conventional helmet displays a much more asymmetric pressure distribution leading to a large bending moment about the head, whereas the straight cells resulted in a more symmetric distribution later in the impact due to the flexibility of the shell, resulting in an eventual reversal of the rotational acceleration..... 158

# List of Tables

Table 1 - Scoring system for the GCS. ..... 27
Table 2 - Details of the Imperial College Traumatic Brain Injury finite element model ..... 29
Table 3 - Material properties of the brain tissue used in Imerial College Traumatic Brain Injury model. ..... 30
Table 4 - Material properties of the head tissue used in Imerial College Traumatic Brain Injury model. ..... 30
Table 5 - Comparative summary of different cycling helmet testing standards. ..... 42
Table 6 - Comparative summary of different motorcycle helmet testing standards. ..... 44
Table 7 - Summary of all the bicycle helmets included in the study with their respective technologies dedicated for managing rotational motion of the head in impact and advertised helmet type i.e. Urban/Skate, Road, or Mountain Bike (MTB). ..... 54
Table 8 - The PTA percentage difference, z-score and p-value of each helmet (referenced by the HID) in comparison to the conventional helmets for each impact condition. The HID cell colours represent the different technologies (see Figure 17). ..... 68
Table 9 - The PRA percentage difference, z-score and p-value of each helmet (referenced by the HID) in comparison to the conventional helmets for each impact condition. The HID cell colours represent the different technologies (see Figure 17). ..... 69
Table 10 - The PRV percentage difference, z-score and p-value of each helmet (referenced by the HID) in comparison to the conventional helmets for each impact condition. The HID cell colours represent the different technologies (see Figure 17). ..... 70
Table 11 - The BrIC percentage difference, z-score and p-value of each helmet (referenced by the HID) in comparison to the conventional helmets for each impact condition. The HID cell colours represent the different technologies (see Figure 17). ..... 71
Table 12 - The global 90$^{th}$ percentile brain strain percentage difference, z-score and p-value of each helmet (referenced by the HID) in comparison to the conventional helmets for each impact condition. The HID cell colours represent the different technologies (see Figure 17). ..... 72
Table 13 - The CC 90$^{th}$ percentile brain strain percentage difference, z-score and p-value of each helmet (referenced by the HID) in comparison to the conventional helmets for each impact condition. The HID cell colours represent the different technologies (see Figure 17). ..... 73
Table 14 - The mean brain sulci strain percentage difference, z-score and p-value of each helmet (referenced by the HID) in comparison to the conventional helmets for each impact condition. The HID cell colours represent the different technologies (see Figure 17). ..... 74
Table 15 - Nominal stress values at 50% tensile strain of A30 and T+ at various strain rates ..... 86

Table 16 - Dissipated work density (DWD) of A30 and T+ in compression at various strain rates..... 88
Table 17 - Ogden quasi-static hyperelastic material parameters for A30 and T+. ..... 93
Table 18 - Prony parameters for visco-hyperelastic material model for A30 and T+. ..... 93
Table 19 - Root Mean Square Percentage Error (RMSPE) of the visco-hyperelastic model prediction for all tests on A30 and T+. ..... 94
Table 20 - Stress values of A30 and T+ X- samples at 50% strain in compression and comparative decrease between max. and min. strain rates relative to tension. *Tension values have been reported in Table 15. ..... 100
Table 21 - Prony pairs for A30 and T+ obtained from DMA time-temperature superposition tests. 104
Table 22 – Visco-hyperelastic material model constants for Agilus30 ..... 113
Table 23 – Thermodynamic properties of air ..... 114
Table 24 - Buckling stress, average shear stress, and internal energy of concave and convex cell shapes with 2.0 mm wall thickness during 7.5 m/s oblique loading. ..... 120
Table 25 - Experimental and simulated results of drop tower impacts on the bulk material specimens. ..... 132
Table 26 - Experimental and simulated results of drop tower impacts on convex cells. ..... 133

# 1 Chapter One: Introduction

Cycling is the most popular mode of active mobility, with many environmental and health benefits [1–3]. The number of cyclists are steadily increasing in Europe, United States and worldwide since 2009 [4,5], particularly after the COVID-19 pandemic which has led to doubling of weekday cycling rates in the UK, and tripling on weekends [6].

Unfortunately, cyclists are among the most vulnerable road users. Their severe injury and fatality rate per passenger miles are several folds larger than car occupants and bus passengers [7]. More cyclists were fatally injured in 2018 than in any year since 1990 in the U.S. according to the U.S. Department of Transportation [5]. Notably, the head is the most common body part to be severely injured during an accident [8]. For instance, an analysis of the Swedish Traffic Accident Data Acquisition (STRADA) database showed that 42% of injuries leading to severe impairment were blows to the head [8]. Impacts to the head can lead to traumatic brain injury (TBI) with fatal and lifelong consequences and large economic costs [9]. Hence, cyclists are often advised to wear helmets as helmets can play a key role in protecting their head and brain against impacts [10–12]. Previous work has shown that 19% of helmeted cyclists suffered severe TBI compared to 48% of non-helmeted cyclists [12]. This study, amongst others, shows that there are still opportunities to reduce TBI in helmeted cyclists through improving helmet design.

Today, helmets must pass standard tests such as EN1078. In such tests, helmets are assessed under vertical impacts and the translational rigid body motion of the headform is used to evaluate their protection effects [13]. However, analysis of accident data shows that in vast majority of real-world head collisions, impacts to the head occur at an angle which produces large rotational head motion [14–17]. Additionally, a significant amount of research has concluded that rotational head motion, not translational, is the major contributor to straining of brain tissue which is a key contributor to TBI [14–17].

The research confirming the importance of rotational kinematics on brain injury has prompted several helmet liner technologies to come to market with the aim of replacing or working with expanded polystyrene (EPS) given the limitations it has in addressing head rotation resulting from oblique head-to-surface impacts albeit its widespread use. Such technologies typically introduce a regular cellular structure such as WaveCel, Koroyd and HEXR, or they add a slip layer such as MIPS and SPIN. WaveCel is a cellular structure formed of interconnected ‘wavy’ walls that crumple upon impact whilst allowing shearing to reduce rotational stiffness. Similarly, HEXR and Koroyd employ hexagonal and circular honeycomb structures respectively.

However, the performance improvement, or lack of improvement of current bicycle helmets, particularly those that incorporate new rotational damping technologies, are still unclear. The limited research available to the public tackling this topic present limited assessments such as single helmets or single impact location with little or no brain injury assessments and often with conflict of interest. Hence, more research is required for a comprehensive understanding of how these new and emerging helmet technologies are performing in comparison to conventional helmets.

Additionally, compressive-shear behaviour of these engineered cellular structures used in helmet liners at coupon level isolated from the entire helmet system in oblique impacts prior to their integration into a full helmet liner. Hence, little guidance exists on how to reduce rotational head motion via design changes to a unit cell prior to the helmet build stage – a stage at which design changes can be expensive and often too late to incorporate.

## 1.1 Hypotheses

As mentioned, whether existing helmets with rotational management technologies reduce brain injury likelihood is still largely unclear. Moreover, how engineered cellular structures can reduce rotational head motion is also unclear. Hence, in this thesis, we start tackling these knowledge gaps by addressing the high-level hypothesis: *Brain injury likelihood resulting from rotational head motion during oblique impacts can be reduced using novel helmet technologies*. This high-level hypothesis is broken down into several sub-hypotheses addressed across the chapters:

1. Helmet technologies that include shear-management layers will reduce the rotational head motion and hence reduce brain tissue strain.
2. Cell arrays can be engineered to shear-compliance which would lead to lower kinematic and brain injury metrics than those engineered to shear-stiffness during oblique impacts.

The hypotheses above are tackled in several stages throughout the thesis as outlined below.

## 1.2 Thesis Outline

The aim of Chapter 2 is to review the current literature to gain a broad understanding of the different types of head injury, with more specificity into brain injury and TBI in particular, being the leading cause of fatality in road traffic accidents (RTAs) and is one that may be prevented or reduced in rate with helmets [18]. We also take a deeper look into the different components and materials of conventional helmets, particularly those engineered to reduce the risk of head injury, as well as advancements in the field of helmets and the challenges we currently face with existing helmet testing standards and analyses.

Chapter 3 aimed to address the first sub-hypothesis: *Helmet technologies that include shear-compliant layers will reduce the rotational head motion and hence reduce brain tissue strain*. As detailed in the Chapter 2, the discrepancy between the real-world impact mechanics leading to brain injury and current helmet standards led to difficulty in understanding the potential of helmets in reducing rotational motion and brain injury likelihood, particularly those that incorporate new rotational damping technologies. Hence, Chapter 3 of this thesis bridges this knowledge gap by presenting the outcome of an assessment investigating the performance of conventional bicycle helmets as well as those with rotational damping systems, and even airbag helmet, in oblique impacts. Brain injury simulations are carried out where the brain tissue strain in regions of interest associated with TBI such as the corpus collosum and sulci are assessed. The outcome of this chapter was published in the Annals of Biomedical Engineering journal [19].

From Chapter 4 onwards, we started tackling the second sub-hypothesis: *Cell arrays with engineered shear-compliance will lead to lower kinematic and brain injury metrics than those with shear-stiffness*.

The first phase of this is an assessment of an array of hexagonally-packed circular cells in isolation during both axial and oblique impacts whilst varying several design parameters of the cells and monitoring their axial and shear stiffness. The second phase is an assessment of a subset of these structures fitted into a full helmet model in oblique impacts where rotational head motion is monitored. The aim of this is to provide some insight on whether a relationship exists between the axial and shear stiffness of cell arrays and their ultimate capacity to reduce the rotational head motion which is well linked with brain injury. The hypothesis is that a shear-compliant array of cells would ultimately lead to lower rotational head acceleration, and hence brain tissue strain and likelihood of injury.

Hence, Chapter 4 is where the characterisation of two additively manufactured rate-sensitive materials made available to prototype the cell arrays is presented, one of which would be carried forward to the prototyping of the cell arrays given the results which showed that it has superior mechanical properties. In this chapter, a comprehensive visco-hyperelastic material model of both these materials was developed and validated from extensive experimental data which is imperative for the proceeding simulations carried out on both coupon level and full helmet level with this material. The work of this chapter was published in the journal Additive Manufacturing [20].*

In Chapter 5, a bespoke impact test rig is purpose-built and used to test the cell arrays under both axial and oblique impacts. The results of this activity are then used to validate a finite element model of the cell arrays in both axial and shear deformation at strain rates relevant to bicycle helmet impacts. Following this, a large design of experiments looking at the axial and oblique impact performance of

the cell arrays is presented whereby the sensitivity of both axial and shear stress-strain performance of the cell arrays to design changes such as cell wall curvature and thickness is addressed. This chapter concludes that adding curvature to cell walls dramatically altered their shear stiffness, as well as axial. However, the direction of curvature had a significant influence on whether the shear stiffness was increased or decreased – whereas axial stiffness reduced with curvature regardless of direction as expected. This provided an exciting opportunity to tailor axial and shear stiffnesses independently simply by changing the direction of the cell wall curvature, from concave to convex.

Chapter 6 starts with a reverse-engineering process of a conventional helmet whereby the helmet is scanned for the creation of a finite element model which is then validated against oblique experimental impacts in various locations. The helmet is then retrofitted with the cell arrays developed and validated in the previous chapter to assess whether the cell arrays offer any improvement in these impact locations via kinematic injury metrics and brain injury simulations.

Finally, Chapter 7 houses the conclusions, limitations and future work of the chapters presented in this thesis.

*It should be noted that the choice of an elastomeric parent material for the cell arrays and the studies that followed Chapter 4 was decided very early on in the project with far-reaching targets in mind which is now being considered for future work. This included benefits of elastomeric materials over conventional plastic materials such as being recoverable and reusable, highly rate-sensitive which meant potential for being optimal for several impact speeds and energies rather than one, as well as inflatable which enables collapsible helmets and those with adjustable stiffness, topology and crushing distance.

# 2 Chapter Two: Literature Review

In this chapter, existing personal protective equipment (PPE) technologies will be covered with an emphasis on helmets of several types and categories, particularly the bicycle helmet category for its current importance for cyclist safety and the uptake of cycling due to the COVID-19 pandemic.

The fundamental principles on which several PPE equipment for impact protection and other crashworthiness equipment and structures are designed are not too different to that of helmets as covered later in this chapter. In such cases, the objective is typically to reduce the peak force or acceleration experienced by a given structure, whether that be a human body or otherwise, during an impact to ensure it is below a given threshold. The peak force or acceleration threshold is usually defined by injury or damage tolerances for that structure. The constraints for this objective are usually driven by the need for a lightweight structure or one that occupies minimal space, or both as is the case with a helmet. A helmet needs to be both small for favourable aerodynamics and appearance, as well as light to minimize strain on the user's neck. Hence, the peak force and mass or crushing distance thresholds are usually defined first and drive design decisions down the line. At this point, the material selection becomes critical as it is one of the few design variables that can dramatically change the response whilst satisfying several design constraints. Hence, we will take a deeper look into the materials that are often employed in such equipment to fulfil the task of dissipating the impact energy. This involves an overview of the basic analytical methods and material models used to describe their behaviour.

The majority, if not all, standard PPE equipment usually must meet certain performance criteria in standard tests set by international institutions or authorities before they can be employed commercially. There are several such standard tests for helmet set by different institutions which are covered in this chapter. These standards are in many cases the driving force behind helmet design decisions and hence the limitations in these standards often translate into limitations in the protective capacity of helmets as we will see later.

As such, the limitations of current helmet materials and design, as well as recent technological advancements, are outlined with regards to their obvious objective: mitigate head injury. Hence, common head injury mechanisms such as TBI are briefly reviewed first.

## 2.1 Head Injury Mechanisms

As the human head can be classified broadly into skin, skull and brain, injuries to any of these structures can be named head injury. Scalp damage is usually the lease severe, although severe bleeding would need to be attended to immediately. More serious injuries are skull fractures and brain

injuries. A skull fracture can be a linear fracture, a depressed fracture or a penetrating fracture [21–23]. A linear fracture is least severe as usually there is no bone displacement and is local however may grow. Depressed and penetrating skull fractures are usually more serious and may lead to brain injury [21,23]. Brain injury can be focal or diffuse, where focal injuries refer to cerebral contusion (local bruising of the brain) or hematomas (local swelling from blood collection outside the brain vessels) [22,24–26]. Hematomas can be epidural, subdural or intracerebral as shown in Figure 1 [18,27]. Although hematomas and brain contusions are usually a result of insult to the brain, they can be classed as closed-head injuries as they can occur whilst the skull and dura mater remain intact [26,28,29].

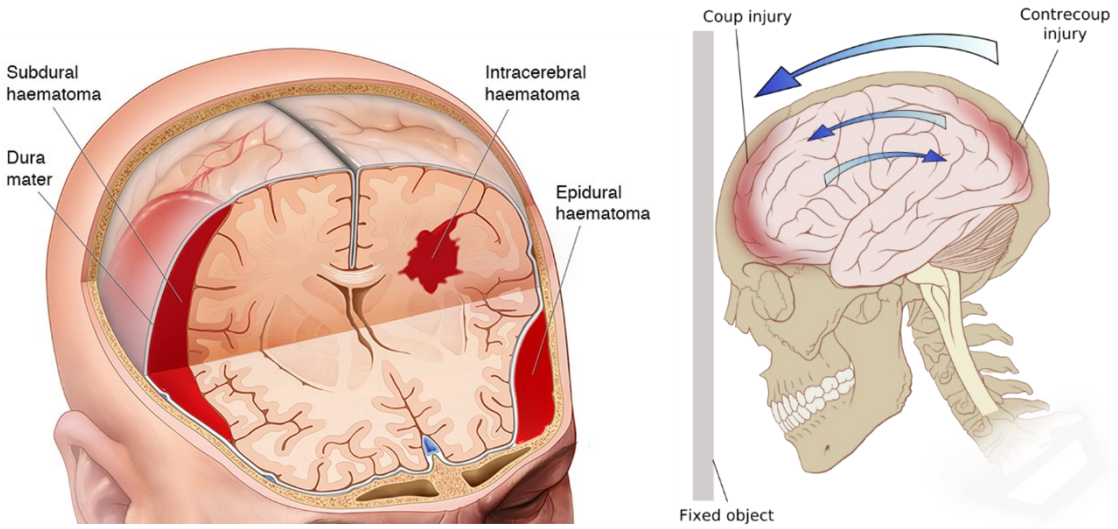


*Figure 1 – Left: Different types of hematomas as a result of brain injury.Right: Schematic of cerebral contusion as a result of abrupt head motion. [30]*

Brain (or cerebral) contusions can be thought of as bruising of the brain tissue and are usually the result of abrupt movement of the head which results in the brain impacting the skull within the head causing tissue damage or bruising usually at the impact location and directly opposite. These locations are often referred to as coup and counter-coup sites respectively (Figure 1) [31,32]. Brain contusions are often accompanied by another form of closed head injury such as hematomas or local microhemorrhages [28,31,33].

Both brain contusions and hematomas may lead to symptoms which include dizziness, problems with memory, speech, managing emotions and thinking and are often classified as traumatic brain injuries (TBIs) [26,34]. The consequences of TBI can be short-lived or life-long depending on the severity, however studies have shown that even mild head injuries can be serious particularly if preceded by previous head injuries, suggesting that the consequences are cumulative [31,35].

Diffuse brain injuries usually fall under diffuse axonal injury (DAI) or concussion which is commonly classed as a mild traumatic brain injury (mTBI) [36,37]. DAI is the term used to describe the disturbance or damage of neural axons. However, both terms broadly describe a family of symptoms which include temporary unconsciousness and impairment of muscle control and other functions. In any case, a concussion or TBI is usually the result of an external force such as a blunt blow to the head from a fall or road traffic accident [36].

### 2.1.1 Traumatic Brain Injury (TBI)

Traumatic Brain Injury (TBI) is the leading cause of fatality in road traffic accidents (RTAs) and is one of the most common but least understood injuries to the body [18]. The consequences of TBI on an individual can be fatal if not lifelong and incurable [23,26,28,33,34,36,38,39]. The definition of TBI across literature is often inconsistent as there is much controversy regarding the exact pathology and diagnosis of TBI. To add complexity, TBI can be mild (mTBI), moderate or severe [31,37]. The classification is usually dictated by an assessment of a patients verbal and motor responses. The most common system for TBI classification is the Glasgow Coma Scale (GCS) which scores a patient 3 - 15 points depending on assessment of severity (Table 1) [21,37]. The test commonly includes eye response, verbal response, and motor response scores. It is generally agreed that a score of 13 and above is mild, 8 or below is severe and in between is moderate [37,40]. However, these thresholds are only generally agreed upon, and are very subjective to the case and the assessor as reviewers have criticised [40–42].

*Table 1 - Scoring system for the GCS.*

| Score | Eye | Verbal | Motor |
|---|---|---|---|
| **1** | Closed | None | None |
| **2** | Opens with pain | Moans | Extension to painful stimuli |
| **3** | Opens with voice | Nonsensical words | Abnormal flexion to painful stimuli |
| **4** | Opens spontaneously | Words expressing confusion | Withdrawal from painful stimuli |
| **5** | N/A | Orientated, converses normally | Localizes to painful stimuli |

It is estimated that 1.7 million TBIs occur annually costing $60 billion in the United States alone, of which 17.6% were recorded as a result of RTAs [29,43]. For this reason, research on TBI has been

extensively focused on two domains: diagnosis and prevention. Diagnosis focuses on detecting TBI symptoms and pathologies as early as possible. Currently, advanced imagining technologies such as magnetic resonance imaging (MRI) and functional MRI (fMRI) are used extensively to monitor changes to brain structure and function. For example, diffusion tensor imaging (DTI) is an MRI technique that utilises the diffusivity of water to map out axonal bundles known as white matter tracts. Water diffusion in white matter tracts is anisotropic due to the structure of axonal membranes and their myelin sheaths. This anisotropy is picked up by DTI technology and allows for visualisation of white matter tracts. If abnormal diffusivity is observed, it could indicate damage in the tracts [36,44,45]. Biomarkers are also a popular method for identifying TBI severity acting as consequential "footprints". Protein biomarkers in cerebral spinal fluid (CSF) surrounding the brain can indicate the molecular processes resulting from brain damage or repair allowing for disease progression and severity to be monitored [35]. On-field and operational helmet sensing technology is also a potential domain for early diagnosis as it provides insight into the accelerations endured by the head during an impact, indicating potential for TBI [46].

Prevention focuses on utilising technological means such as helmets to avoid TBI occurring in the first place which is the main focal area of this research. Studies have shown that the use of protective head gear in sports such as American football and cycling reduces the stresses and strains within the brain [47–50], which has been shown to be related to TBI pathologies [34,39]. Hence, the use of personal protective equipment (PPE) such as helmets particularly for road users is highly advised and is enforced by law in the US, UK, EU. states and other countries throughout Asia [51–53] as discussed in the next section.

### 2.1.2 Imperial College Traumatic Brain Injury Model

In attempts to better understand the causes and best prevention methods for TBI, researchers have combined existing knowledge of imaging technology and FEA to develop detailed FE models of human and rat brains for assessment of the biomechanics of TBI through reconstruction of impacts with known outcomes. Detailed FE models of the brain facilitate easier and deeper assessments of the effectiveness of different helmets. Brain FE models currently vary in level of fidelity and detail [54]. One reason for this is that material properties of the brain and human tissue in general are not easy to obtain, particularly for strain-rates relevant to impact. Ghajari et al. [39] have developed an FEA model of the human brain via segmentation of MRI images into 1.5 mm voxels, namely the Imperial College Traumatic Brain Injury (IC TBI) model. This makes it one of the highest resolutions of a FE brain model in scientific literature, consisting of over half a million FE nodes (Table 2). The model has important anatomical details for predicting TBI with respective visco-hyperelastic material properties (Table 3 and Table 4). Specifically, the definitions leveraged the Ogden hyperelastic material model

with Prony series viscoelasticity which is described in more detail in Section 4.2.2. This material model in general and this brain injury model in particular are used extensively in this thesis.

*Table 2 - Details of the Imperial College Traumatic Brain Injury finite element model*

| Number of Brain Elements | Number of Brain Nodes | Intracranial Volume [dm$^3$] | Brain Material Properties |
|---|---|---|---|
| 386.0 k (continuous mesh) | 576.8 k | 1.4 | Visco-hyperelastic (Ogden model with Prony series viscoelasticity) |

Previous computational studies have shown that head impacts can produce large mechanical strains in key brain regions; corpus callosum and sulci (Figure 2) [39,55]. The corpus callosum is the largest white matter tract, which connects two hemispheres and is a location typically associated with diffuse axonal injury after head impacts [56]. Sulci is where the pathology of the neurodegenerative disease, chronic traumatic encephalopathy, in sporting collisions and white matter damage in survivors of single head impacts have been seen [39,57]. Hence, in addition to using measures of brain injury based on head kinematics, we used this detailed finite element model of TBI to predict strain in the sulci and corpus callosum during oblique impacts in Chapters 3 and 6.

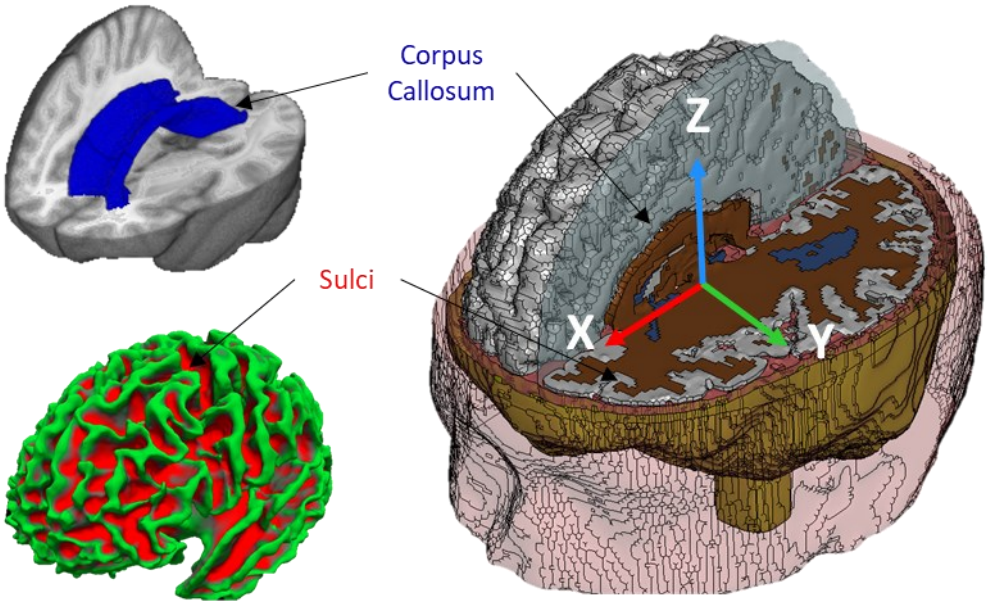


*Figure 2 – ICL TBI model of the human brain (right) with details of the corpus callosum and sulci.*

The model was used to simulate the brain response during impacts. This is done by prescribing accelerations recorded from real world accident data or through dummy reconstructions to the model's skull. The accelerations recorded from the impacts that need brain injury assessment are transformed to the local co-ordinate system located at the centre of gravity of the skull where they would be applied to the model to match the kinematics experienced by the head in the model and the test of interest. More details of this procedure can be found in in Chapters 3 and 6.

A recent study employing this model showed that maximum brain tissue strain occurred in locations near the depths of the sulci where an abnormal amount of Tau protein accumulation is usually found with TBI patients suffering from chronic traumatic encephalopathy (CTE), a neurodegenerative disease linked to repeated blows to the head. [39]. Hence, reducing the strain endured by brain tissue during an accident is likely the most effective way to protecting the brain from TBI.

*Table 3 - Material properties of the brain tissue used in Imerial College Traumatic Brain Injury model.*

| **Tissue** | **ρ [kg/m³]** | **$\mu_1$ [Pa]** | **$\alpha_1$** | **$\mu_2$ [Pa]** | **$\alpha_2$** | **K [MPa]** |
|---|---|---|---|---|---|---|
| **Brain** | 1040 | 53.8 | 10.1 | -120.4 | -12.9 | 50 |
| **Brain stem** | 1040 | 15.8 | 28.1 | -106.8 | -29.5 | 50 |
| **$T_i$ [ms]** | $T_1$ = 0.001 | $T_2$ = 0.01 | $T_3$ = 0.1 | $T_4$ = 1 | $T_5$ = 10 | $T_6$ = 100 |
| **$G_i$ [kPa]** | $G_1$ = 320 | $G_2$ = 78 | $G_3$ = 6.2 | $G_4$ = 8.0 | $G_5$ = 0.1 | $G_6$ = 3.01 |

*Table 4 - Material properties of the head tissue used in Imerial College Traumatic Brain Injury model.*

| **Tissue** | **ρ [kg/m³]** | **$\mu_1$ [kPa]** | **$a_1$** | **Poisson's ratio** |
|---|---|---|---|---|
| **SAS and ventricles** | 1040 | 20 | 2 | 0.4998 |
| **Falx and tentorium** | 1130 | 25.5 | 32.9 | 0.45 |
| | $T_i$ [ms] | $T_1$ = 5 | $T_2$ = 44 | $T_3$ = 474 |
| | $G_i$ [kPa] | $G_1$ = 328 | $G_2$ = 291 | $G_3$ = 161 |
| **Pia mater** | 1130 | 2.6 | 32.9 | 0.45 |
| | Ti [ms] | $T_1$ = 5 | $T_2$ = 44 | $T_3$ = 474 |
| | Gi [kPa] | $G_1$ = 32 | $G_2$ = 29 | $G_3$ = 16 |

There is significant body of research that shows rotational motion of the head is the key determinant of brain deformation and subsequent damage to the brain tissue [14–17]. These studies have led to new proposals from Fédération Internationale de Motocyclisme (FIM) and European Committee for Standardization Working Group 11 (CEN/TC158/WG11) for helmet testing under oblique impacts and using injury criteria based on head rotation [58–61]. These proposals and potential solutions, such as helmets, are discussed in the next section.

## 2.2 Helmets

The importance of helmets cannot be understated. Helmets are the primary protective wearable for the head of a vulnerable road user [51–53,62]. A comprehensive evaluation by Kraus et al. [53] showed that of the motorcycle riders wearing a helmet, only 26.2% sustained head injury as compared to 48.8% of those not wearing a helmet. Moreover, motorcycle helmet users sustained fewer skull fractures and intracranial head injuries, and sustained less severe head injuries overall [51]. A later study by Yu et al. published in 2011 found that in Taiwan, helmeted-head riders were four times less likely to sustain head injury and ten times less likely to sustain brain injuries. It also reported that half-coverage helmet users were more than twice as likely to sustain head injury compared to full-face helmet users [52].

This thesis takes a particular interest in bicycle helmets for several reasons. Cycling is the most popular mode of active mobility, with many environmental and health benefits [1–3]. The number of cyclists are steadily increasing in Europe, United States and worldwide since 2009 [4,5]. For instance, the pedal cyclist traffic increased by 16% in Great Britain between 2009 and 2019 [63]. The recent COVID-19 pandemic has led to a large increase in cyclist traffic, which is likely to be permanent. The UK's Secretary of State for Transport has reported "*We've seen around a 100% increase in weekday cycling. At weekends, that increase has been up to around 200% compared to pre-COVID-19 levels. We want to use this recovery to permanently change the way we travel with huge levels of investment.*" [6].

However, cyclists are among the vulnerable road users. Their severe injury and fatality rate per passenger miles are several folds larger than car occupants and bus passengers [7]. More cyclists were fatally injured in 2018 than in any year since 1990 in the U.S. according to the U.S. Department of Transportation [5]. Notably, the head is the most common body part to be severely injured during an accident [8]. For instance, an analysis of the STRADA (Swedish Traffic Accident Data Acquisition) database showed that 42% of injuries leading to severe impairment were blows to the head [8]. Impacts to the head can lead to traumatic brain injury (TBI) with fatal and lifelong consequences and large economic costs [9]. Hence, cyclists are often advised to wear helmets as helmets can play a key role in protecting their head and brain against impacts [10–12]. Previous work has shown that 19% of helmeted cyclists suffered severe TBI compared to 48% of non-helmeted cyclists [12].

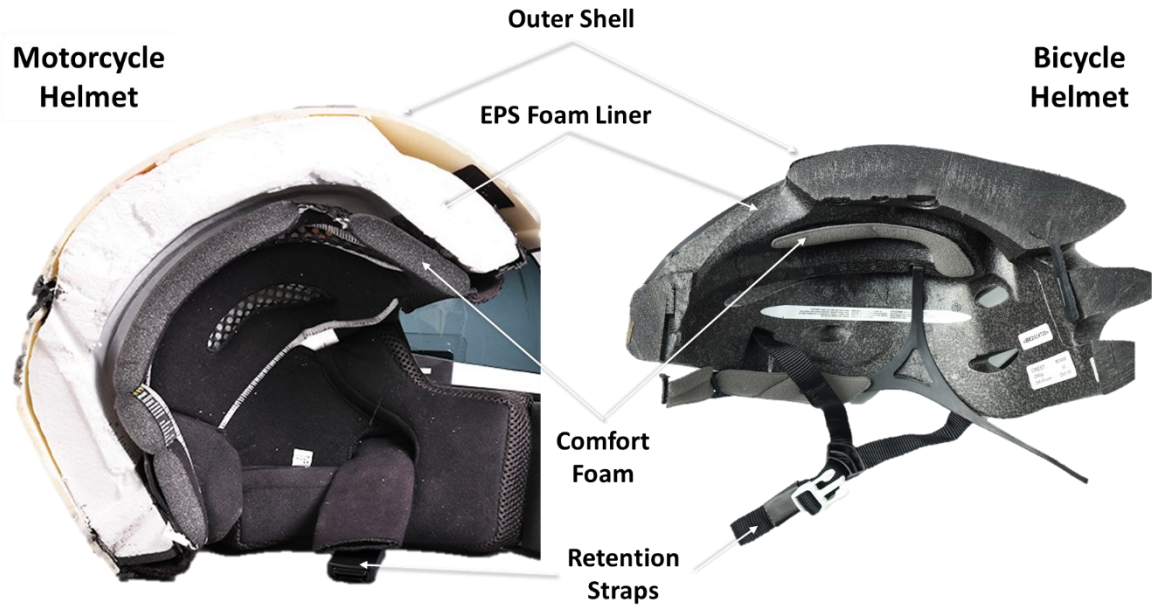


*Figure 3 – Cutouts showing fundemental common components between a bicycle (right) and motorcycle helmet (left)* [64].

Helmets are generally divided by their use category such as motorcycle helmets, bicycle helmets (in which are subcategories such as road helmets, mountain bike helmets and urban helmets), equestrian helmets and ski helmets. Despite use case and design differences, most of these helmets share common fundamental components, shown in Figure 3, which are crucial for their protective capacity and performance under dynamic loading conditions that result from an impact. These are: 1 - An outer shell. 2 - An inner foam liner. 3 – Comfort foam. 4 - A retention system.

### 2.2.1 Shell

The outer shell is usually made from a thin and hard layer of a thermoplastic i.e. polycarbonate (PC), acrylonitrile-butadiene-styrene (ABS), or composite material in higher-end models i.e. carbon fibre reinforced resins and plastics (CF, CRP), fibre glass reinforced plastics (FRP) or even Kevlar® [65–68]. The purpose of the outer shell is to protect the user from localised impacts from sharp objects such as kerbstones. Hence it also serves the purpose of distributing a localised load onto a larger area of energy absorbing material, such as foam, which lies beneath. The shell itself absorbs some of the impact energy through plastic deformation - however reports have shown this is a minor contribution compared to the inner liner which has been reported to absorb as much as 45% [66,69]. However, these results should be interpreted with caution as they rely on the material used and the impact scenario.

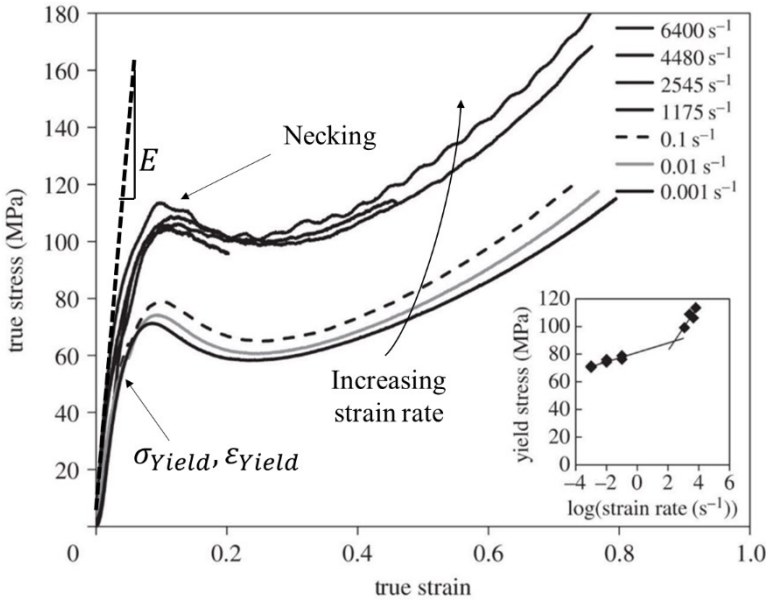


*Figure 4 – PC stress-strain curves at various strain rates adapted from* [70].

Both PC and ABS are affordable and durable thermoplastics with good impact resistance, and hence are the most used materials for helmet shells – particularly bicycle helmets. Both plastics exhibit elastic-plastic material behaviour with strain-hardening and have similar mechanical properties. However, polycarbonate is typically preferred due to its transparency and marginally superior mechanical properties such as Young's modulus, yield stress, impact and thermal resistance albeit being slightly more costly. As per the CAMPUS® database (ISO 527-1/-2), the Young's Modulus ($E$) of PC typically ranges between 1800 - 5300 MPa and the yield stress ($\sigma_{Yield}$) ranges between 36 – 90 MPa depending on the grade and fillers [71]. On the other hand, $E$ for ABS ranges between 1310 – 3620 MPa and $\sigma_{Yield}$ ranges between 25 – 69 MPa. The yield strain ($\varepsilon_{Yield}$) for both plastics ranges between 1-6%, after which strain-hardening behaviour is observed until failure as see in Figure 4.

As typically seen in thermoplastics, both materials have marginal strain-rate sensitivity [70]. However, this strain-rate sensitivity is typically ignored for analytical and computational helmet assessments for impact as strain rates typically do not exceed 10/s [72,73].

### 2.2.2 Foam Liner

The main purpose of the inner liner is to absorb as much of the kinetic energy of a helmeted head during impact as possible while minimising deceleration magnitude and time duration. The latter two parameters are of course connected by basic equations of motion - such that the larger the kinetic energy per unit mass, the larger the velocity magnitude, and thus the larger deceleration magnitude required to bring the head to a full stop - or the longer the deceleration duration would need to be. A longer deceleration duration would mean a larger helmet which is an unattractive option for buyers and is uncomfortable for users as moments of inertia increase with a larger helmet radius. Thus, the

design optimisation problem involving a helmet inner liner is one where the objective functions and design constraints are in conflict, non-linearly related and time dependent. The objective functions in this case are minimising deceleration magnitude and period, and constraints are on maximum mass and volume. Of course, cost and manufacturability need to also be considered.

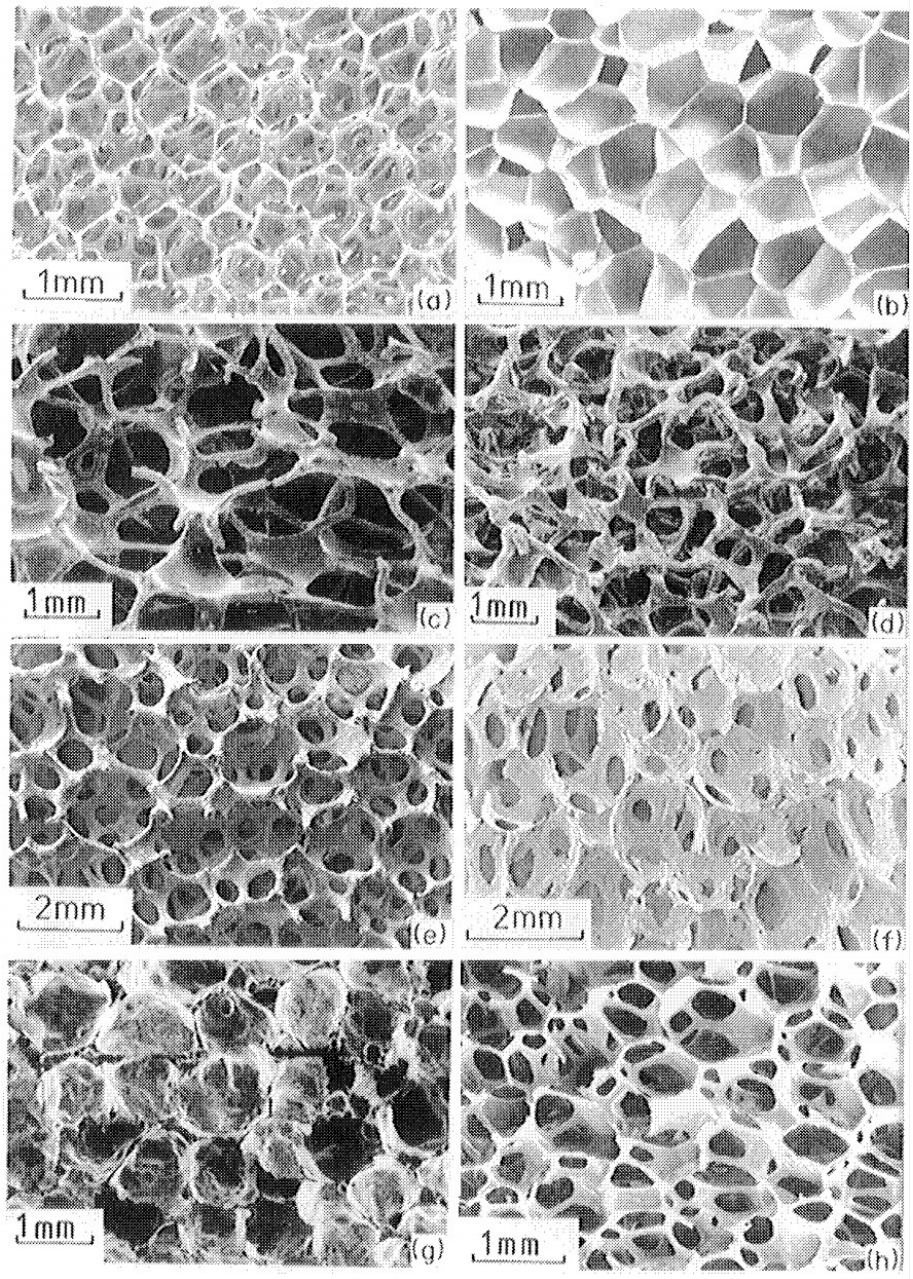


*Figure 5 – Microstructure of cellular materials: (a) open-cell polyurethane, (b) closed-cell polyethylene, (c) nickel, (d) copper, (e) zirconia, (f) mullite, (g) glass, (h) a polyether foam with both open and closed cells.* [74]

For this reason, the inner liner is usually made from an expanded foam such as expanded polystyrene (EPS), polypropylene (EPP), or polyurea (PU) foam [75–78]. Foams generally have similar microstructures characterised by stochastically shaped air cells defined by trusses or thin walls of the parent material (i.e. polystyrene in the case of EPS). These cells are formed as a result of the

manufacturing process where polystyrene beads mixed with a low-boiling point expander are heated and fused together [79]. Example microstructures are seen in Figure 5. This makes them good candidates for light-weight energy absorbing materials. Reasons for this are discussed in more detail in the forthcoming paragraphs.

Generally, there are two classes of foams, whereby each could be recoverable (elastomeric), such as PU, or irrecoverable (plastic), such as EPS: One type is open-cell foams whereby the air is free to flow between cells as the cell walls have orifices (small holes, Figure 5 (f)). In some cases, the 'orifices' are so large that the cell walls become effectively trusses where the cell walls connect Figure 5 (a, c, d, e). The other type is closed-cell foams whereby the cells completely enclose the air trapped within them during the manufacturing process (Figure 5 (b)). This makes them slightly stiffer in comparison to their open cell counterparts, particularly at large compressive strains (60-80%). Although there are subtle differences in their mechanical properties and general parent materials, their crushing behaviour is similar and can be defined using the same empirical models with minor corrections applied to closed-cell foams to account for the entrapped air.

One of the reason foams such as EPS are chosen materials for these objectives is that they exhibit a unique compressive stress-strain behaviour during crushing whereby the crushing force is constant with increasing crushing distance. Their compressive stress-strain behaviour can be characterised by three regions as shown in Figure 6: I – Elastic Compression, II – Plastic Crushing and III - Densification.

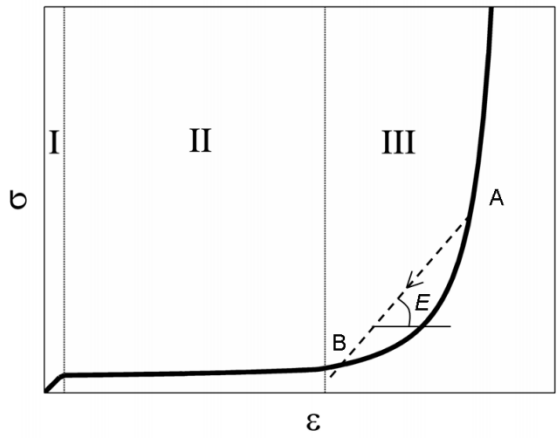


*Figure 6 – Representative nominal (engineering) stress-strain curve of EPS and similar foams under compressive loading* [68].

In region I, the cell walls or trusses elastically bend or buckle under compressive strain, typically below 5%, whereby the foam returns to its original shape when the load is removed. Note that this characterises the elastic modulus of the foam, which is usually different, and smaller, than the elastic modulus of the parent material which makes up the foam cell walls themselves. If the compressive strain is increased beyond the limits of region I, the cell wall or truss buckling deformation transitions

into the plastic regime, whereby cells begin to successively collapse at the characteristic yield stress of this foam. This successive collapse of cell layers occurs up until the majority of the cells have collapsed and densification occurs, characterised by a steep rise in the stress-strain response as seen in region III.

This characteristic stress-strain response means that, given a required peak stress threshold on a structure during impact defined by some design constraints or tolerances, foams can dissipate several folds more energy than their parent solid material as depicted in Figure 7A. However, as one can also see from the figure, this increase in dissipated energy is largest when the stress threshold is only marginally larger than the yield stress of the foam. Hence, the yield stress of a foam is an important mechanical property which determines how appropriate it is for a given impact-attenuating system.

Considering this, it is important to be able to tailor the yield stress of a foam to enable optimal energy dissipation at different impact energies. A solution is to vary the density of the foam, which in turn leads to thicker or thinner cell walls and trusses with higher or lower buckling stresses respectively. In doing so, the dissipated work during crushing is increased or decreased respectively as shown in Figure 7B.

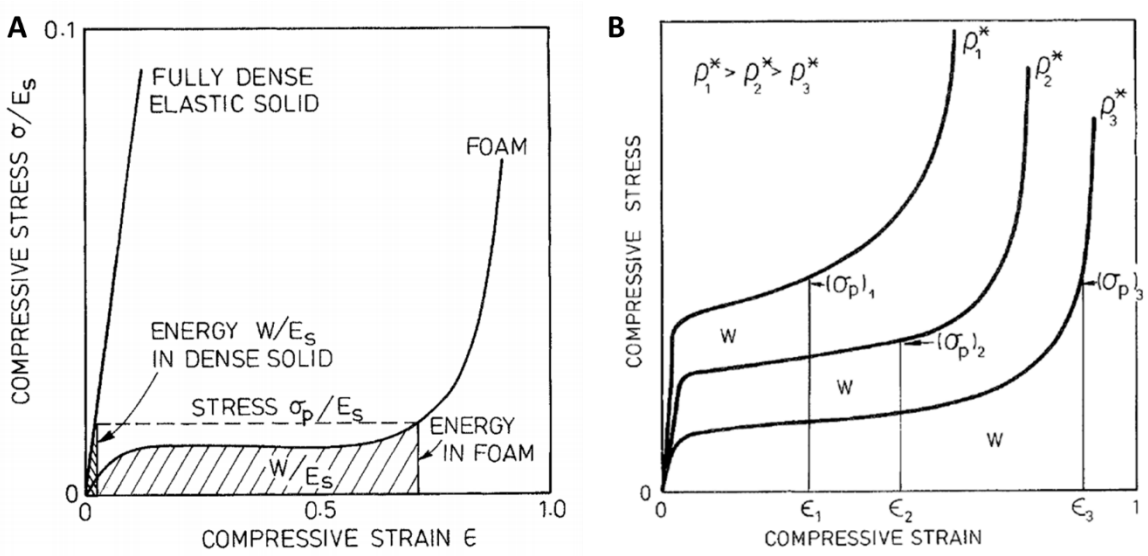


*Figure 7 – A) Comparison of the dissipated work of foam and a fully dense elastic solid at a given stress threshold. Both axes are normalised by the elastic modulus of the parent solid. B) A representation of the compressive stress-strain response of EPS foam of different densities* [80].

The phenomenon observed in region II, whereby increasing compressive strain is achieved at a near-constant stress, is why foams are superior to many materials in achieving the goal required by several PPE mentioned earlier: dissipating the impact energy at the lowest possible force. Hence, in the design of a helmet with a fixed crushing distance and impact speed as an example, where a given allowable peak force is defined by skull fracture tolerances, the corresponding peak stress can be derived from

the contact area between the helmet and anvil and hence an appropriate foam density can be chosen to dissipate the required impact energy.

However, an issue remains which is central leading to the work carried out later in this thesis: *how may one tailor the shear stiffness of foams without interrupting the designated normal compressive stiffness to best cater for oblique impacts?*

Limited studies have investigated the compressive-shear performance of helmet foams. Ling et al. investigated the compressive-shear response of EPS foam under oblique impact loading with various impact speeds and angles. The results from the study consistently showed that both axial and shear stresses at yield of EPS increased with foam density [81]. Similarly, a study by Khosroshahi et al. [78] investigating the biaxial loading response of EPS foam showed that the both axial and shear stiffness of EPS foams increased with foam density at various levels of normal compression. This implies that there is no clear way of decoupling the normal and shear stiffnesses of conventional EPS foams.

As a result of this, several helmet technologies have come to market to try addressing this gap by promoting add-ons to a helmet in the form of slip-layers. In this way, they sought to reduce the shear stiffness of the helmet system by allowing sliding between various interfaces of the helmet, such as between the helmet and head, or the shell and foam, or shell and ground or impacting surface. The hypothesis here is that this newly introduced shear compliance to the helmet can reduce the rotational acceleration of the head during an oblique impact, and hence reduce the risk of brain tissue strain and injury. Such technologies are reviewed in section 2.3 and studied in detail in Chapter 3.

### 2.2.3 Comfort Foam & Retention System

As each human head has a unique shape, a helmet plastic liner foam such as EPS may not fit perfectly on a user's head, and hence may lead to some uncomfortable contact points given its apparent rigidity. Hence, the purpose of the comfort foam is to take shape in the gaps between both surfaces increasing the static contact area and leading to a more comfortable fit. This means it is usually substantially softer than the liner foam itself, generally made of soft and flexible foams with low density as open-cell PU or polyvinyl chloride (PVC), and hence has negligible contribution to the energy dissipation during head impact [65,82].

The retention system of a helmet is an important one often tested for certification and is particularly important for cyclists where a helmet may easily slide off. It is usually a belt strap made of polyethylene terephthalate (PET) or nylon bolted to either side of the helmet shell or liner and serves the purpose of securing the helmet to the user's head [65]. Nonetheless, there are records of a considerable number of helmet roll-offs leaving the head unprotected even with the strap secured

[83]. In many cases, this is unavoidable given the severity and angle of some head impacts leading to high tangential forces, particularly for high-speed motorcyclists.

## 2.3 Advancements in Helmet Technology

Advancements in helmet liner technology in fields such as sports and military have been major due to the financial support of both industries. The NFL has launched an ongoing initiative in 2016 named 'The Engineering Roadmap' that has pledged to invest £60 million into football biomechanics research and the development of novel protective equipment. So far, over £1.6 million has been invested into 13 new liner technologies including air-filled chambers called 'Crash Clouds' to the development of new viscoelastic materials and auxetic foams [84]. FE models of the headform and neck used in helmet testing standards have been developed and made open-source to accelerate development of helmet innovation via crowd-sourcing [85]. Xenith, one of the largest NFL helmet producers utilises air-filled thermoplastic polyurethane (TPU) chambers for liner impact attenuation. A study investigated the effects of orifice size and chamber material by conducting uniaxial rail impacts of a 5kg mass on chambers with TPU 45D and TPU 90A. Results showed that the reducing vent diameter led to higher energy absorption due to longer air retention periods and that softer variant (TPU 90A) reduced transmitted force at lower impact speeds (1.3 - 2.3 m/s) however bottomed out at higher impact speeds (3 m/s) [86]. Other NFL helmet technologies include viscoelastic foams, collapsible columns and buckling rods [87,88].

*Figure 8 – Hövding airbag in the undeployed (left) and deployed (right) positions* [89].

Bicycle helmets have also seen one innovation which utilised air-chamber technology. Hövding, the Swedish company behind the innovation, have released a bicycle helmet that actively inflates in the incidences of abrupt motion or fall using sensors such as accelerometers [49]. A study on the use of such an airbag as a cycling helmet has shown potential to reduce forces to the head by 3-6 fold [49], however the helmet lacks necessary protective features such as a hard shell to pass helmet test

standards that require kerbstone impacts and thus is limited to cyclists with restrictions from certain markets. The most concerning aspect of the helmet is the potential for false-negative triggering i.e. not deploying during an impact. Of course, this would leave the victim with effectively no helmet. Additionally, the airbag folding means it cannot be reused, even after a false-positive deployment. The airbag also uses a high-stiffness fabric with no orifices to maximise energy absorption via pressure relief leading to low frequency oscillations which could be dangerous for the brain [49].

However, perhaps the most popular advancement in bicycle helmet technology is MIPS, mentioned previously, which includes a thin low-friction layer between the helmet outer shell and inner liner (Figure 9) [75,90]. The Phillips Head Protection System (PHPS) similarly introduces a low friction slip layer that lays on top of the outer shell [65]. Both technologies aim to reduce the friction between the head, helmet, and impact surface as a means of managing rotational acceleration. Bliven et al. [75] evaluated the performance of a new 'WAVECEL' bicycle helmet comprising of wave-shaped plates that crease under compression and fold under shear loading, leading to organised elastic buckling. The paper reports a 73% reduction in rotational acceleration of a 6.2 m/s 45° impact using their helmet technology as opposed to using traditional EPS [75]. However, these results were not replicated anywhere else. Additionally, due to the nature of the wave-shaped plates, the liner is inherently anisotropic, and therefore this performance and is not guaranteed for all other impact directions as we will see in the next chapter. Given the unpredictable nature of road traffic accidents, this is a major drawback.

*Figure 9 – Multi-directional Impact Protection Systems (MIPS) which is essentially a low friction slip layer (yellow) placed between the rider's head and the outer shell* [91].

Advancements in motorcycle helmet liners have included composite structures utilising a hybrid of PU foam expanded in an open cell lattice [92], viscoelastic add-ons [93], bilayer cones [94], varying density

recovering foams [92] and functionally graded structures such as hierarchical lattices [95]. Blanco et al. Investigated the effectiveness of using ABS cones that would plastically deform upon impact and found improvement in head acceleration and HIC in seven of the eight cases considered (Figure 10). The upside of this technology is that the performance can be tailored to different areas of the helmet simply by changing the geometrical dimensions of the cone, on which a parametric analysis and design of experiments (DoE) was carried out (Figure 10) [69]. Similar liner concepts including conical structures was evaluated by Teng et al. [96]. Their study concluded that single-cone configurations dominated over double-cones. However, such conical liners presents manufacturing complexities absent with traditional uniform EPS liners and do not present any advantage with regards to repeat impacts. Ramirez et al. [92] evaluated the performance of a viscoelastic PU foam filling a viscoelastic thiol-ene polymer lattice and reported energy absorption results comparable to traditional EPS, with the advantage that their foam-filled lattice fully recovers after impact, whereas traditional EPS permanently deforms after impact.

However, none of the aforementioned studies have investigated or optimised their designs for rotational acceleration, one of the main contributors to brain injury [34,39]. Ghajari et al. [93] investigated the effectiveness of a viscoelastic add-on liner on reducing strain and strain-rate of brain tissue during impact (Figure 11), however found the add-on to show marginal improvements only in low speed frontal impacts. Khosroshahi et al. [95] investigated the impact attenuation capacity of a hierarchical lattice (Figure 12) - one that has varying stiffness through the thickness - and found that such a structure could reduce the peak linear acceleration by as much as 60% in linear impacts and rotational acceleration by as much as 70% in oblique impacts with a speed of 7.5 m/s.

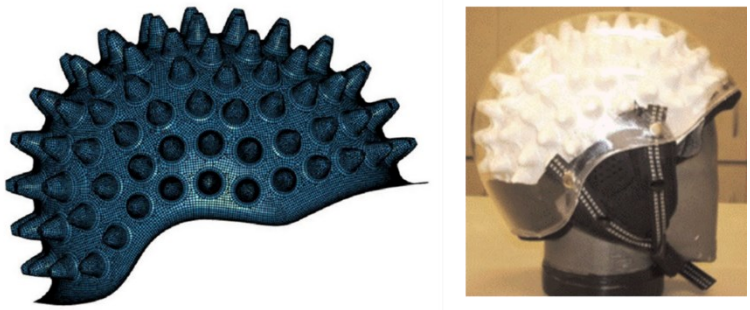

*Figure 10 – Conical liner helmet (Blanco et al.)* [69]

The study found correlating benefits in stress and strain measures of the THUMBS FE brain model. However, currently, the proposed helmet is heavy and difficult to manufacture, and would not provide the same benefits after multiple impacts and has not reported the same benefits at different speeds. Moreover, no topological optimisation on such a graded lattice has been done, leaving room for future work.

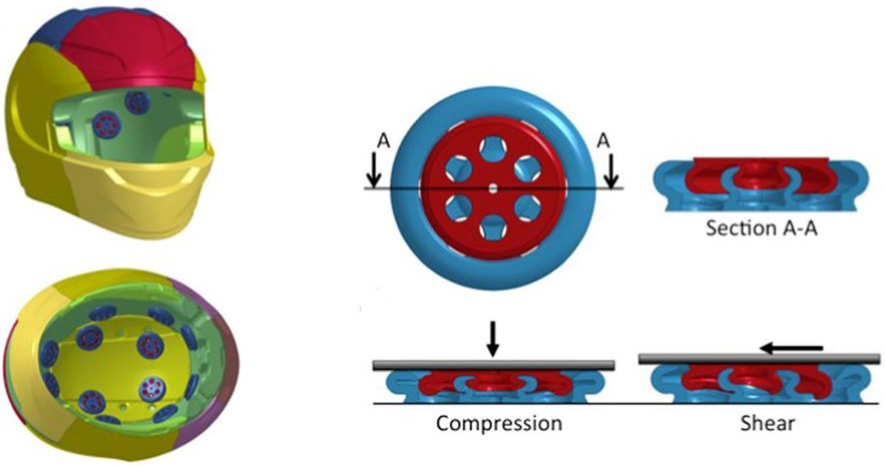


*Figure 11 – A viscoelastic add-on liner comrpised of two mechanically-connected rubber parts. Their implementation in a motorcycle helmet is shown on the left, and their deformed state in compression and shear is shown on the right (Ghajari et al.)* [93]

Viscoelastic materials have also shown promise in snow sport PPE technologies such as back protectors. Back protectors were traditionally made of hard shells prior to new back protectors using viscoelastic soft-shells being introduced [97]. Viscoelastic soft-shells allowed increased mobility which is particularly important for snow sports as well as protection against repeat impacts [98]. However, the stiffness of the viscoelastic materials, and consequently the protector, is quite sensitive to temperature as is the case with the majority of viscoelastic materials [97–100]. This poses an issue for

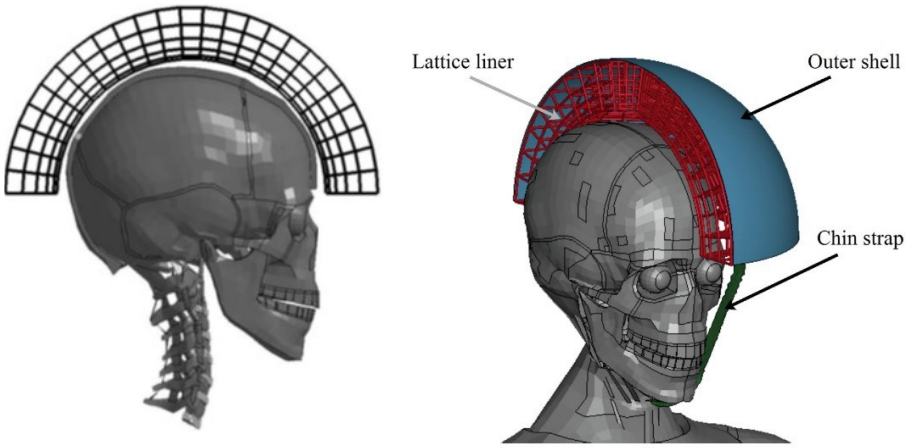


*Figure 12 – Hierarchial lattice liner (Khosroshahi et al.)* [95]

PPE equipment utilising such materials for applications in extreme weather conditions such as skiing and snowboarding. Hence, viscoelastic materials with good impact attenuation properties yet lower glass-transition temperatures than a user would ever experience, such as -30°C, are highly desirable [87].

## 2.4 Helmet Test Standards

As each category of helmets serves the user in different end conditions, each have different components and designs as per application, and hence abide by different standards. For example, American football and lacrosse helmets abide by National Operating Committee on Standards for Athletic Equipment (NOSCAE) certification [48,101], whereas motorcycle helmets either British Standard (BS) 6658 or United Nations Economic Commission for Europe (UNECE) regulation 22.05 [65,68,102].Bicycle helmets abide by the Consumer Product Safety Commission (CPSC), Snell or American Society for Testing and Materials (ASTM) and American National Standards Institute (ANSI) standards [25,47,65,103]. See Table 5 and Table 6 for a summary on bicycle and motorcycle helmet standards respectively.

The British Standard (BS) EN 1078 is the most common test standard for bicycle helmets in the UK [13]. The test requires testing of the construction of the helmet including shock absorbing properties at various temperatures, retention system, field of vision as well as marking and information that must be on the helmet as sold. One of the main aspects of the test is the impact shock absorption, which stipulates that the peak headform *translational* acceleration of each impact shall not exceed 250 g during an impact velocity of 5.42 m/s on a flat anvil or 4.57 m/s on a kerbstone anvil. Three helmets for each headform size that fits within the manufacturers' claimed head size range must be tested. The helmet must be first fitted, and the test area marked using datum lines following a procedure outlined in the standard document. Notably, no rotational kinematics of the headform are measured albeit the headform being allowed to rotate. As per the test setup in the standard document (Figure 13), the headform is supported using a mobile system that guides the helmet during free fall, such as a halo, to a perfectly vertical drop perpendicular to the anvil.

*Table 5 - Comparative summary of different cycling helmet testing standards.*

| | **BS EN 1078/1080** | **Snell B-90/95** | **ASTM F1952-15** |
|---|---|---|---|
| **Impact** | x | x | x |
| **Anvil** | F, K | F, H, K | F, H, K |
| **Repeat Impact** | x | x | x |
| **Speed** | F: 5.42 m/s, K: 4.57 m/s | *F: 6.57 m/s, H, K: 5.05 m/s | *F: 6.2 m/s, H, K: 5.6 m/s |
| **Impact Threshold** | 250 g | 300 g | 300 g |
| **Retention** | x | x | x |

| | | | |
|---|---|---|---|
| **Roll-off** | x | x | x |
| **Field of Vision** | x | x | |
| F, H, K and E stand for flat, hemispherical, kerbstone and edge anvils respectively. *Reported testing speeds vary depending on test conditions and therefore the nominal of testing speeds has been reported for each standard. | | | |

Other bicycle helmet tests include Snell B-90/95 which is similar to EN 1078 with an additional hemispherical anvil and higher impact speeds yet a more forgiving peak acceleration threshold [104]. An even more severe test is the ASTM F1952-15 which covers performance requirements for helmets used by downhill mountain bicycle riders. “Studies have shown higher risk to the head and face for this sport as compared to recreational street riding; hence, this specification requires greater impact protection and provides performance criteria for chin bars on full-face helmets but does not require full-face helmets.” [105]

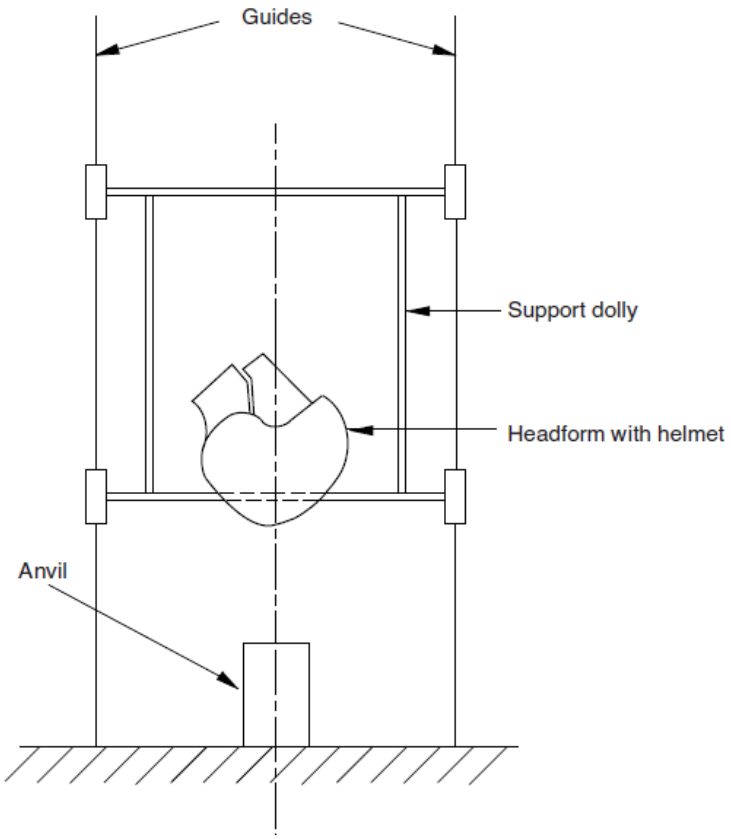


*Figure 13 – Schematic of apparatus used for the shock absroption test of BS EN 1078 [13].*

Motorcycle helmets must undergo region-specific certification tests which are often more rigorous and well-defined than for bicycle helmets (Table 6). This is not only driven by the fact that

motorcyclists travel at higher speeds than cyclists, but that wearing a helmet is mandated by law in the UK, EU, Australia, Canada and several states in the US, unlike bicycle helmets which are mandatory in only a handful of countries around the world.

*Table 6 - Comparative summary of different motorcycle helmet testing standards.*

| | **UNECE R22.05** | **Snell M2010** | **FMVSS 218** | **BSI 6658** |
|---|---|---|---|---|
| **Impact** | x | x | x | x |
| **Penetration** | | x | x | |
| **Retention** | x | x | x | x |
| **Roll-off** | x | x | | x |
| **Rigidity test** | x | | | |
| **Friction test** | x | | | x |
| **Anvil** | F, K | F, H, E | F, H | F, H |
| **Repeat Impact** | | x | x | x |
| **Speed** | 7.5 m/s | *7.75 m/s | *6 m/s | *6.5 m/s |

F, H, K and E stand for flat, hemispherical, kerbstone and edge anvils respectively. *Reported testing speeds vary depending on test conditions and therefore the highest of testing speeds has been reported for each standard.

Informed by clinical research into head injury and skull fracture tolerances, the Head Injury Criterion (HIC) was developed as an attempt to relate measures of linear impact deceleration magnitudes ($|a(t)|$) and durations ($t_2 - t_1$) to the onset of skull fracture and concussion [25,65,66].HIC is used today as an injury metric in many safety standards governing the automotive industry and has been employed by several researchers investigating the effectiveness of helmets [103,106].

$$HIC = \max\left\{(t_2 - t_1)\left(\frac{1}{t_2 - t_1}\int_{t_1}^{t_2}|a(t)|dt\right)^{2.5}\right\} \quad (1)$$

However, as expressed in Equation (1), the HIC does not account for rotational acceleration which is hypothesised to be a major contributor to brain injury resulting from high stresses and strains in brain tissue [34,39] (See section 2.1). Helmet testing standards today still fail to accommodate for the effects of rotational acceleration on brain injury albeit significant research suggesting otherwise. Henceforth,

new head injury criteria and helmet testing standards have been proposed that account for rotational acceleration [25,65,90,107] and a movement towards helmet liners that can manage rotational head acceleration in oblique impacts has been initiated [69,75,95] as discussed in the previous section.

One of the main bottlenecks limiting the adoption of new helmet testing standards which consider rotational acceleration measures is the lack of reliable criterion and thresholds that can be used to determine whether a helmet passes or fails, or sufficiently protects from brain injury. There have been several attempts to come up with such criteria, one of which is the Brain Injury Criterion (BrIC) developed by Takhounts et al. [16,108]. The criterion considers the peak rotational velocity about each anatomical axis of the headform separately, irrespective of the time each occurs. The peak rotational velocity about each axis is then normalised by a corresponding 'critical maximum' rotational velocity which is different for each axis as expressed in Equation (2).

$$BrIC = \sqrt{(\max\{\omega_x(t)\}/\omega_{xC})^2 + (\max\{\omega_y(t)\}/\omega_{yC})^2 + (\max\{\omega_z(t)\}/\omega_{zC})^2}. \quad (2)$$

The anatomical axis of the head in this case are X, Y and Z which correspond to the normal of the coronal (frontal), midsagittal and transverse planes respectively. $\omega_{xC}$, $\omega_{yC}$ and $\omega_{zC}$ are the components of the critical rotational velocity with values 66.25, 56.45 and 42.87 rads/s respectively as recommended by Takhounts et al. [16]. A BrIC value provides a probability of injury for different abbreviated injury scales (AIS) based on animal data and varies between different headforms. I.e. a 30% risk of AIS 3+ TBI corresponds to a BrIC value of 0.92 if measured with a Hybrid III headform, or 0.89 if measured with ES-2re or WorldSID headforms [108]. Such complexity and the need for further validation of the injury risk curves beyond scaled animal data is partly why thresholds for such injury assessment metrics have not yet been adopted in legally recognised helmet testing standards.

It is noteworthy to mention that the listed standards drop the tested helmet mounted onto a 5kg detached headform onto a rigid anvil, whereas the human neck and body can play a significant role in the dynamics of the impact response, particularly for impacts exceeding 20-30 ms duration [68,109,110]. Ghajari et al. have shown that the presence of the body can increase the resultant linear acceleration by 28% and the head-helmet contact force by 93% in 7.5 m/s impacts using the Hybrid III d compared to detached headform impacts. Adding to the problem is the fact that the Hybrid III neck form is the most widely used dummy neck form in crash tests [111], yet it does not represent key features of the human neck particularly important in such head-first impacts [110,112,113]. This includes the natural curvature that assists buckling-induced energy absorption [109,114].

## 2.5 Helmet Impact Mechanics

### 2.5.1 Axial Impacts

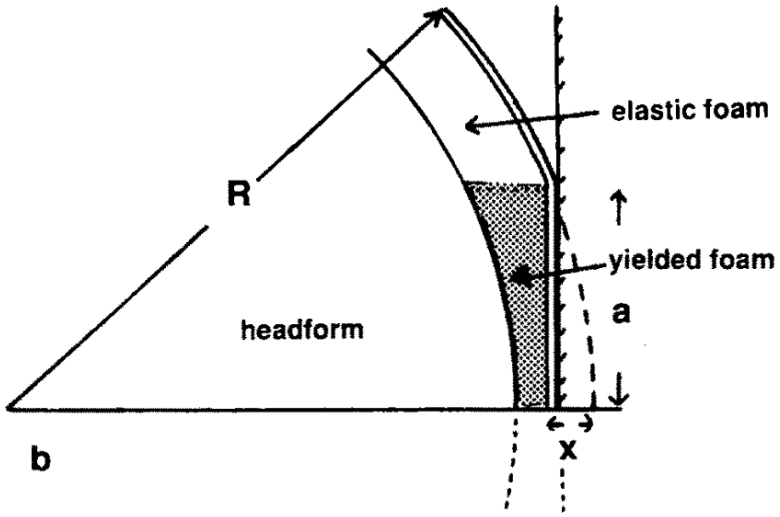


*Figure 14 - Geometry of a helmeted head contact area with a flat rigid anvil.* [115]

Mills et al. [115] derived an analytical model for the force a helmet exerts on a headform during an axial impact. The assumptions here are that the headform and helmet are perfectly coupled, and that the headform is rigid. This assumption is conservative however plausible as rigid headform are employed in helmet tests today as previously discussed. In reality, the scalp and skull deform slightly during impact to absorb some energy. Moreover, the stiffness of the shell is neglected for simplicity, leaving only the only the stiffness of the liner to be considered. This again is slightly conservative approach given that the helmet shell has been reported to dissipate 10-30% of the impact energy [XX].

In the case of a flat, rigid surface and a locally spherical liner with a perfectly fitted headform, the liner will deform a distance ($x$) from the outer surface in contact with the anvil [115]. This births a circular contact area between that increases as the liner further deforms onto the anvil as shown in Figure 14. Using Pythagoras' theorem of right-angled triangles, this area has a diameter ($a$) that can be expressed as:

$$a^2 = R^2 - (R - x)^2 = 2Rx - x^2 \approx 2Rx \tag{3}$$

Where the distance ($R$) is the total radius of the headform and liner. Given that the deformed distance ($x$) is much smaller than the radius ($R$), and that all the force acts on a circular contact area ($A$) in the opposite to the direction of travel, the force exerted on the headform can be expressed as:

$$F = AP = \pi a^2 P \approx \pi(2Rx)P \tag{4}$$

Where P is the force per unit area of contact i.e. contact pressure or stress. It is commonly assumed that polymeric foams such as EPS widely used in helmets exert a constant stress per unit strain beyond the yield stress [68,116–118]. As EPS yields at very small strains as compared to the deflections in impact, it is assumed that the foam beneath the contact area has yielded (Figure 14). Therefore, the stress ($P$) can be assumed to be the yield stress of foams ($\sigma_Y$) which remains nearly constant for EPS foam during crush [68,116]. Assuming the helmeted head has a constant effective body mass ($m_B$) with negligible gravitational forces as compared to impact forces, we can substitute Equation (4) using Newton's second law of motion to obtain the acceleration ($\ddot{x}$), which can otherwise be thought of as the rate of liner deformation:

$$F = m_B\ddot{x} = -2\pi RxP \tag{5}$$

Therefore, equation (5) can be expressed as a linear homogenous differential equation.

$$\ddot{x} + \left[\frac{2\pi RP}{m_B}\right]x = 0 \;\rightarrow\; \ddot{x} + [k]x = 0 \tag{6}$$

The general solution to the differential Equation (6) can be solved to obtain the position of the headform as a function of time ($x(t)$) and differentiated twice to obtain the acceleration ($\ddot{x}(t)$).

$$x(t) = \frac{\dot{x}(0)}{k}\sin\left(\sqrt{k}x\right) \rightarrow \dot{x}(t) = \dot{x}(0)\cos\left(\sqrt{k}x\right) \rightarrow \ddot{x}(t) = -k\dot{x}(0)\sin\left(\sqrt{k}x\right) \tag{7}$$

Where $\dot{x}(0)$ is the initial impact velocity (hereon referred to as $V_0$) which can be reduced by $\sqrt{\alpha}$ where $\alpha$ is the ratio of the total kinetic energy to that absorbed by the liner as detailed in [68].

$$\frac{1}{2}m_B V_0^2 = IE_{shell} + IE_{liner} = \alpha IE_{liner} \therefore IE_{liner} = \frac{1}{2}m_B\left(\frac{V_0}{\sqrt{\alpha}}\right)^2 \tag{8}$$

It is clear from equation (7) that the force is dependent on $x$ due to the dependency of the contact area. However, if the material stress ($P$) was likewise a function of $x$ where the stress increased linearly with strain i.e. $P(x) = Px$ like in solid linear elastic materials then the $k$ term in equation (5) would be $x^2$, hence such materials that are linear elastic under impact deformations are not used as helmet liners. However, if $P(x) = P/x$ then the force ($F$) and consequential head acceleration ($\ddot{x}$) end up being constant. This is an interesting outcome as a constant acceleration is arguably the best acceleration profile i.e. one that has reduced all the maxima - leading to the average acceleration.

### 2.5.2 Oblique Impacts

Deriving an analytical model for head motion during oblique impacts is slightly more complicated and involves more assumptions than axial impacts. Mills et al. [119] derived an analytical model to predict the response of helmets in oblique impacts by considering slices of width $w$ and headform of radius $R$

(Figure 15), leading to a theoretical contact area between the helmet and impact surface $A$ expressed as:

$$A = w\sqrt{2Rx} \tag{9}$$

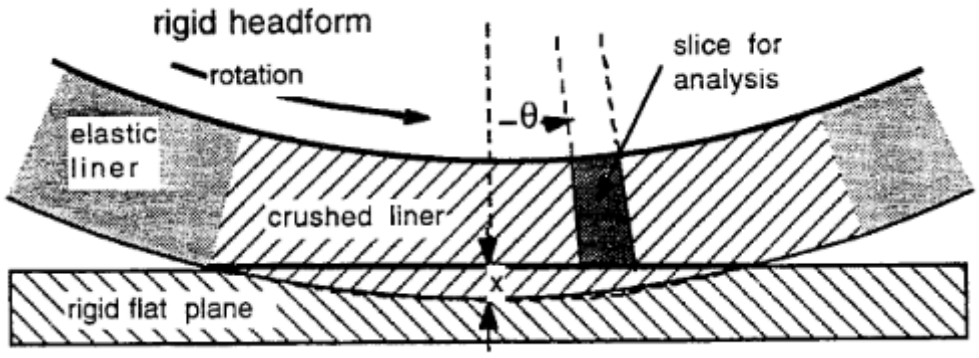


*Figure 15 – Analytical representation of a helmeted head impacting a flat rigid anvil during oblique impact.* [119]

Like the assumptions in the previous section considering axial impacts, the authors also assume that the helmet is perfectly coupled with the headform (Figure 16). This assumption may introduce more errors when considering oblique impacts as the tangential component of the contact force between the helmet and impact surface is now present and would naturally cause the helmet to slide over the head. However, such sliding motion is limited in reality due to the dissimilar elliptical curvatures of the human head and a helmet, as well as the presence of a chin strap [119]. The model also neglects any shear strain of the foam at the sides of the contact area, and hence the force perpendicular to the impact surface is dependent on the compressive yield stress of the foam only. This assumption is not plausible for all helmet liners, especially those with large lattice or cellular structures as we will see later.

Another assumption is that the head is perfectly spherical, or circular when considering a 2D cross-section, and therefore the centre of gravity of the head remains perfectly always aligned with the perpendicular force vector (Figure 15). Hence, any rotation of the headform would be solely accounted for by the tangential force component (Figure 16). Given that shear strains in the foam are neglected, this tangential force component becomes only a function of the contact area and moment of inertia of the helmet and headform.

$$F_T = \tau w L \tag{10}$$

Here, $L$ is the contact length over which the compressive strain in the foam is increasing. Given that the helmet and headform are assumed to be perfectly coupled, the rotational velocity of the headform with no sliding can be expressed simply as:

$$\dot{\omega} = V_T/R \tag{11}$$

When sliding, the rotational acceleration of the headform may be calculated from the moment $M$ applied to the headform by the tangential force $F_T$. I.e.

$$M = RF_T = I\ddot{\omega} \tag{12}$$

Hence, it is necessary to determine the coefficient of friction to evaluate whether the helmet is rolling or sliding using a time-stepping scheme that checks the tangential force required to induce rolling with no sliding, and hence calculating the required shear stress from the contact area, after which the feasibility of the required shear stress is determined using the coefficient of friction and axial crushing stress. If the required shear stress is not feasible, then sliding is assumed.

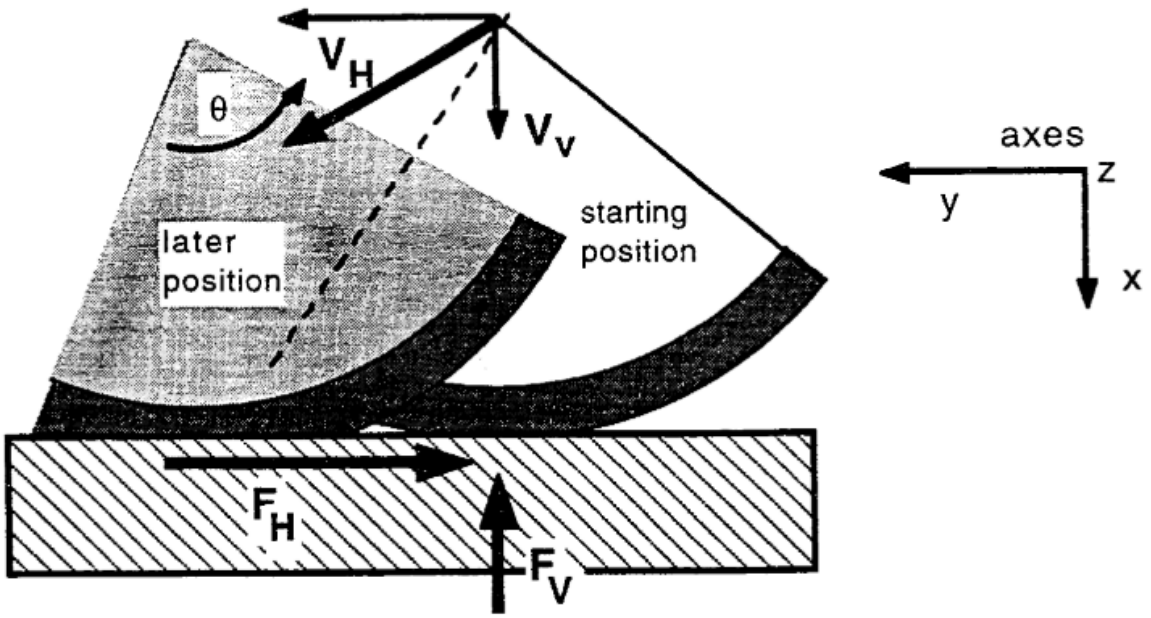


*Figure 16 – Analytical representation of a helmeted head impacting a flat rigid anvil during oblique impact.* [119]

As discussed, several assumptions were made to allow for simple computation which may lead to large errors and approximations that would not be acceptable for helmets with different helmet liners such as those investigated later. For this reason, finite element analysis (FEA) has been employed and utilised extensively in this work for more accurate assessments.

In closing, the points discussed in this section clarify that a helmet design that enhances crash performance involves three dimensions: 1 - Material properties, 2 - Liner geometry, 3 - Biomechanical brain response - hence each of them constitutes a chapter of the following thesis.

We start with an assessment of current helmet technologies which aim to reduce rotational head motion and hence brain tissue strain and injury likelihood in the next chapter. This provides a benchmark to assess the proposed improvements against.

# 3 Chapter Three: A New Brain Injury Mitigation Assessment of Bicycle Helmets in Oblique Impacts

New helmet technologies have been developed to improve the mitigation of traumatic brain injury (TBI) in bicycle accidents. However, their effectiveness under oblique impacts, which produce more strains in the brain in comparison with vertical impacts adopted by helmet standards, is still unclear. Here we used a new method to assess the brain injury prevention effects of 27 bicycle helmets in oblique impacts, including helmets fitted with a friction-reducing layer (MIPS), a shearing pad (SPIN), a wavy cellular liner (WaveCel), an airbag helmet (Hövding) and several conventional helmets. We tested whether helmets fitted with the new technologies can provide better brain protection than conventional helmets. Each helmeted headform was dropped onto a 45° inclined anvil at 6.3 m/s at three locations, with each impact location producing a dominant head rotation about one anatomical axes of the head. A detailed computational model of TBI was used to determine strain distribution across the brain and in key anatomical regions, the corpus callosum and sulci. Our results show that, in comparison with conventional helmets, most helmets incorporating new technologies significantly reduced peak rotational acceleration and velocity and maximal strain in corpus callosum and sulci. Only one helmet with MIPS significantly increased strain in the corpus collosum. The helmets fitted with MIPS and WaveCel were more effective in reducing strain in impacts producing sagittal rotations and a helmet fitted with SPIN in coronal rotations. The airbag helmet was effective in reducing brain strain in all impacts, however, peak rotational velocity and brain strain heavily depended on the duration of the impact period considered for analysis. These results suggest that incorporating different impact locations in future oblique impact test methods and designing helmet technologies for the mitigation of head rotation in different planes are key to reducing brain injuries in bicycle accidents.

*Keywords*: traumatic brain injury; helmets; rotational motion; oblique impacts; standards;

It is noteworthy to mention that much of the work in this chapter has formed the basis of the publication cited below, whereby the majority of the data analysis, figures and writing of the publication was done by the publication's first author and the author of this thesis.

Abayazid, F., Ding, K., Zimmerman, K., Stigson, H., & Ghajari, M. (2021). A New Assessment of Bicycle Helmets: The Brain Injury Mitigation Effects of New Technologies in Oblique Impacts. Annals of Biomedical Engineering. https://doi.org/10.1007/s10439-021-02785-0

## 3.1 Introduction

Cycling is the most popular mode of active mobility, with many environmental and health benefits [1–3]. The number of cyclists are steadily increasing in Europe, United States and worldwide since 2009 [4,5]. For instance, the pedal cyclist traffic increased by 16% in Great Britain between 2009 and 2019 [63]. The recent COVID-19 pandemic has led to a large increase in cyclist traffic, which is likely to be permanent. The UK's Secretary of State for Transport has reported "*We've seen around a 100% increase in weekday cycling. At weekends, that increase has been up to around 200% compared to pre-COVID-19 levels. We want to use this recovery to permanently change the way we travel with huge levels of investment.*" [6].

However, cyclists are among the most vulnerable road users. Their severe injury and fatality rate per passenger miles are several folds larger than car occupants and bus passengers [7]. More cyclists were fatally injured in 2018 than in any year since 1990 in the U.S. according to the U.S. Department of Transportation [5]. Notably, the head is the most common body part to be severely injured during an accident [8]. For instance, an analysis of the STRADA (Swedish Traffic Accident Data Acquisition) database showed that 42% of injuries leading to severe impairment were blows to the head [8]. Impacts to the head can lead to traumatic brain injury (TBI) with fatal and lifelong consequences and large economic costs [9]. Hence, cyclists are often advised to wear helmets as helmets can play a key role in protecting their head and brain against impacts [10–12]. Previous work has shown that 19% of helmeted cyclists suffered severe TBI compared to 48% of non-helmeted cyclists [12]. This study, amongst others, shows that there are still opportunities to reduce TBI in helmeted cyclists through improving helmet design.

The functional design of bicycle helmets has been driven by standard test methods (e.g. EN1078), where helmets are assessed under vertical impacts and the linear motion of the headform is used to evaluate their protection effects [13]. However, analysis of accident data shows that in most real-world head collisions, impacts to the head occur at an angle which produces large rotational motions. There is a significant body of research that shows rotational motion of the head is the key determinant of brain deformation and subsequent damage to the brain tissue [14–17]. These studies have led to new proposals from Fédération Internationale de Motocyclisme (FIM) and European Committee for Standardization Working Group 11 (CEN/TC158/WG11) for helmet testing under oblique impacts and using injury criteria based on head rotation [58–61]. However, the effects of current bicycle helmets, particularly those that incorporate new technologies to reduce head rotation, on mitigating brain injuries under oblique impacts are still unclear.

Limited studies have assessed the performance of bicycle helmets with new technologies dedicated to mitigating rotational head motion [75,120]. These previous studies assessed the performance of helmets in a single impact location. In contrast, a significant body of research has shown that the location and direction of impact has a large effect on rotational kinematics of head and brain deformation [16,58,121,122]. In addition, helmets are likely to provide different levels of protection against impacts at different locations [123]. Hence, it is important to assess the performance of helmets under oblique impacts with different directions and locations.

In this study, we evaluated brain protection effects of a range of commercially available helmets under different oblique impacts. We studied helmets with EPS liners (conventional), helmets fitted with the friction-reducing 'multi-directional impact protection system' (MIPS) [75], helmets with a corrugated 'wavy' cellular liner (WaveCel) [75], helmets fitted with shearing pads (SPIN) and the airbag helmet Hövding 3.0 [49]. We tested whether helmets fitted with these new technologies provide better or worse brain protection in oblique impacts than conventional helmets.

Previous computational studies have shown that head impacts can produce large mechanical strains in key brain regions; corpus callosum and sulci [39,55]. The corpus callosum is the largest white matter tract, which connects two hemispheres and is a location typically associated with diffuse axonal injury after head impacts [56]. Sulci is where the pathology of the neurodegenerative disease, chronic traumatic encephalopathy, in sporting collisions and white matter damage in survivors of single head impacts have been seen [39,57]. Hence, in addition to using measures of brain injury based on head kinematics, we used a detailed finite element model of TBI to predict strain in the sulci and corpus callosum during oblique impacts (Figure 18).

## 3.2 Methods

### 3.2.1 Bicycle Helmets

27 commercially available bicycle helmets were selected from the European market (both online and in-store), representing a large number of commonly used helmets. The price ranged from £10 to £275, reflecting a wide range of designs. Since we used a Hybrid III 50$^{th}$ percentile male dummy headform with a 58 cm circumference, we selected helmets with a size range that included 58cm. Table 7 lists all the helmets and their rotational technology, if any. Helmets without a dedicated rotational technology are referred to as 'conventional' and serve as the controls for evaluating the effectiveness of the helmets incorporating rotational technologies. Four new technologies were investigated. 15 helmets were fitted with the 'multi-directional impact protection system' (MIPS) – a low-friction slip-layer that lies between the helmet liner and the head (Figure 17) which enhances the decoupling between the helmet and head rotations [90]. We also included a helmet with the corrugated 'wavy'

cellular liner called WaveCel (Figure 17). This liner technology is claimed to increase shear-compliance during collapse and mitigate head rotation [75]. Another technology that we evaluated was the add-on shear pads, called SPIN (Figure 17). This technology is also claimed to increase the relative motion between the helmet and head, thus mitigating head rotation. Finally, we included a radical technology, the airbag helmet Hövding 3.0 (Figure 17) [49]. This helmet has been shown to reduce the head linear acceleration by several folds [49] and has been shown to reduce peak head rotational acceleration in oblique impacts [61].

*Table 7 - Summary of all the bicycle helmets included in the study with their respective technologies dedicated for managing rotational motion of the head in impact and advertised helmet type i.e. Urban/Skate, Road, or Mountain Bike (MTB).*

| Helmet Name | Helmet ID (HID) | Rotational Technologies | Type |
|---|---|---|---|
| **Abus Hyban 2** | 1 | - | Urban/Skate |
| **Bell Crest Universal** | 7 | - | Urban/Skate |
| **Biltema Bicycle Helmet** | 2 | - | Road |
| **Closa Design Fuga** | 24 | - | Urban/Skate |
| **Giro Caden** | 26 | - | Urban/Skate |
| **Halford Commuter Helmet** | 12 | - | Urban/Skate |
| **Rockrider MTB ST 500** | 20 | - | MTB |
| **Van Rysel RoadR 900** | 19 | - | Road |
| **Bell Super Air R** | 8 | MIPS | MTB |
| **Bell Trace** | 10 | MIPS | Road |
| **Biltema Bicycle Helmet** | 15 | MIPS | Road |
| **Bontrager Solstice** | 6 | MIPS | Road |
| **Giro Agilis** | 17 | MIPS | Road |
| **Giro Caden** | 29 | MIPS | Urban/Skate |
| **Giro Quarter FS** | 27 | MIPS | Urban/Skate |
| **Lazer Blade** | 3 | MIPS | Road |
| **Occano** | 28 | MIPS | Road |
| **Scott Vivo Plus** | 22 | MIPS | MTB |
| **Smith Convoy** | 13 | MIPS | Road |
| **Specialized Ambush ANGi MIPS** | 25 | MIPS | MTB |
| **Specialized S-Works Prevail II w/ ANGi MIPS** | 23 | MIPS | Road |
| **Sweet Protection Outrider** | 21 | MIPS | Road |

| | | | |
|---|---|---|---|
| **Tec Quadriga** | 18 | MIPS | Road |
| **Bontrager Specter WaveCel** | 4 | WaveCel | Road |
| **POC Axion SPIN** | 14 | SPIN | MTB |
| **POC Tectal SPIN** | 16 | SPIN | MTB |
| **Hövding 3.0** | 5 | Airbag | Road |

* Helmets 9 & 11 do not exist in the analysis albeit these helmet IDs were reserved for them prior to this study.

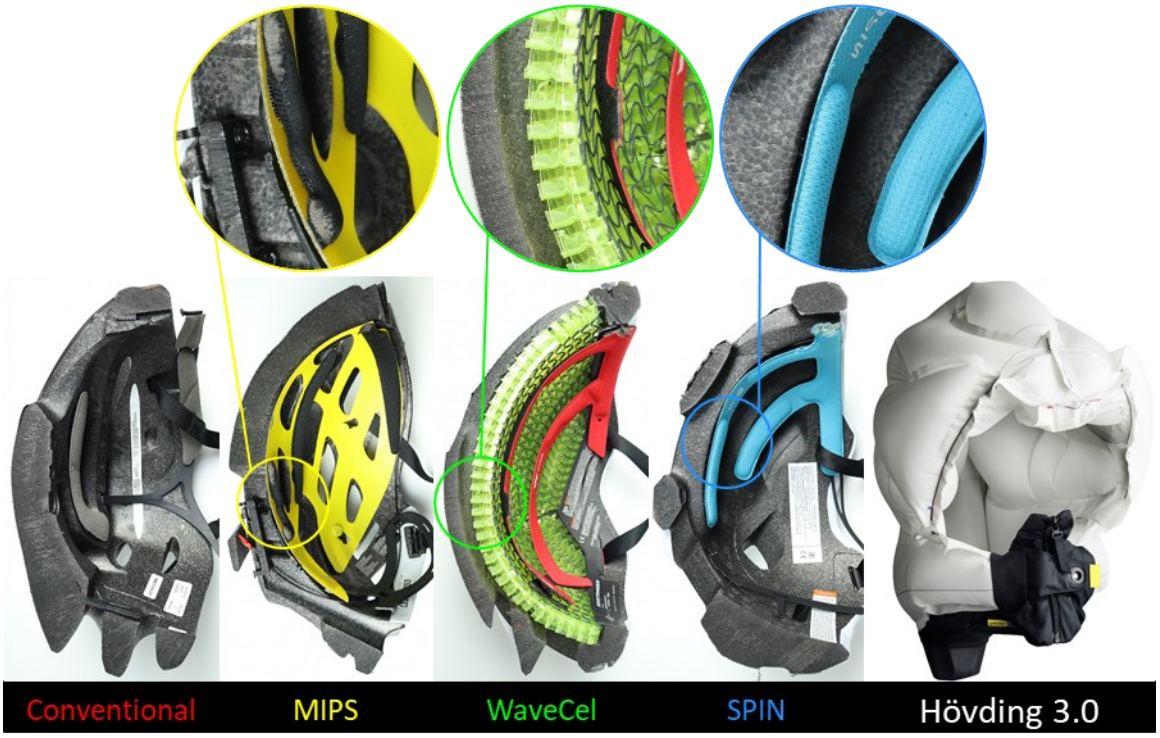


*Figure 17 – Mid-sagittal cross-sectional views of some of the helmets used in this study (from left to right): A conventional helmet, a 'multi-directional impact protection system' (MIPS) helmet, a corrugated 'wavy' cellular liner (WaveCel) helmet, a shear pad (SPIN) helmet and an airbag helmet (Hövding 3.0).*

### 3.2.2 Oblique Impact Tests

In order to test helmets under oblique impacts at different locations, we used the method proposed by the CEN Working Group 11 "Rotational test methods" [124]. This method requires testing helmets under three different oblique impacts, shown in Figure 18A. These impacts are representative of impacts in bicycle accidents and are based on the simulation of 1024 bicycle accidents [124,125].

The helmet was mounted onto the 50$^{th}$ male Hybrid III headform, the chin strap was fastened and the helmeted headform was dropped onto a 45° anvil covered with a 40-grit sandpaper representing asphalt. The impact speed was 6.3m/s. A digital inclinometer was used to position the helmeted headform, and a camera system was used to ensure precision in positioning. An array of nine

accelerometers in the 3-2-2-2 arrangement was mounted inside the headform [126]. This method allowed us to determine the linear and rotational accelerations of the centre of gravity (CoG) of the headform with respect to the head-fixed axes (Figure 18B,C). The accelerations were acquired at a frequency of 20kHz and filtered using an IOtechDBK4 12-pole Butterworth low-pass filter [127].

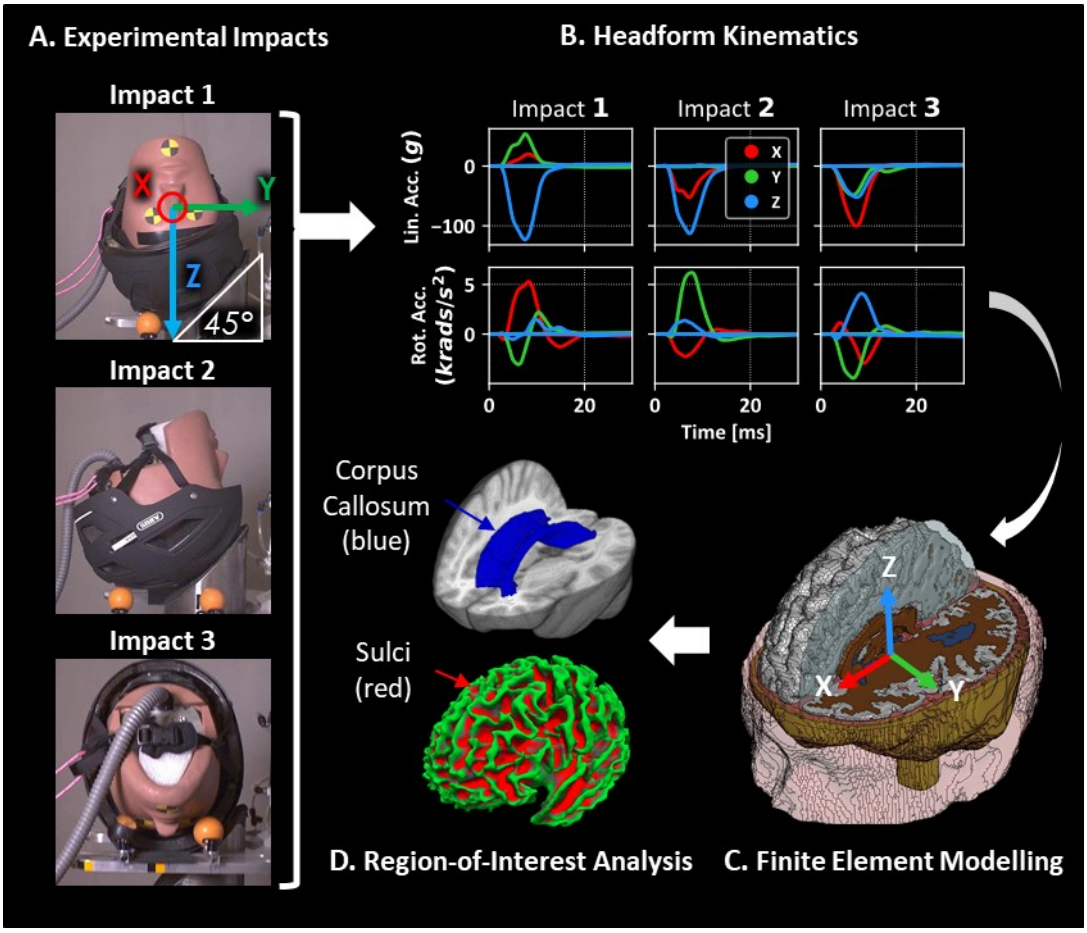


*Figure 18 – Setup of the three experimental impact conditions carried out for each helmet (A). For each of the impacts, three translational and three rotational acceleration time-history pulses are recorded about the CoG of the HIII headform (B). These are then applied to the detailed finite element model of TBI (C) which is then further analysed to extract brain strain as an injury metric in regions-of-interest such as the corpus callosum and sulci (D). The three impacts were selected to produce different head rotations (A, B). Impact 1, with the initial position of the headform X-, Y- and Z-axis 0°, produces predominant rotation about the X-axis. For impact 2, the initial position of the headform was X-, Y-axis 0° and Z-axis -90°, which produces predominant rotation about the Y axis. For impact 3, the Initial position of the headform was X- and Z-axis 0° and 65° around Y-axis. This impact produces large rotation about the Z-axis compared to the other impacts. All impacts were vertical against a 45-degree anvil with 40-grit sandpaper at 6.3m/s (A).*

Each helmet was tested at least twice for each impact location using two separate helmets to analyse the variability. The mean responses for all six accelerations were calculated and used for further analysis. All tests were performed by a test lab accredited for testing and certification in accordance with the European standard via Folksam Insurance Group. They were using the same test set-up as for the regulatory tests. Thereby, each helmet was inspected, and the impact locations were chosen to be far separated from prior impact location to minimize influence of prior damage in subsequent tests.

### 3.2.3 Kinematics-based Measures of TBI

The linear and rotational accelerations of the headform's CoG were processed to extract the kinematic injury metrics that are commonly used to predict brain injury, including peak translational acceleration (PTA), peak rotational acceleration (PRA), peak rotational velocity (PRV) and brain injury criterion (BrIC) [16]. The peak values are the maximum of the magnitude of each vector:

$$PTA = \max\left\{\sqrt{a_x(t)^2 + a_y(t)^2 + a_z(t)^2}\right\} \quad (13)$$

$$PRA = \max\left\{\sqrt{\dot{\omega}_x(t)^2 + \dot{\omega}_y(t)^2 + \dot{\omega}_z(t)^2}\right\} \quad (14)$$

$$PRV = \max\left\{\sqrt{\omega_x(t)^2 + \omega_y(t)^2 + \omega_z(t)^2}\right\} \quad (15)$$

$$BrIC = \sqrt{(\max\{\omega_x(t)\}/\omega_{xC})^2 + (\max\{\omega_y(t)\}/\omega_{yC})^2 + (\max\{\omega_z(t)\}/\omega_{zC})^2}. \quad (16)$$

In these equations, $\vec{a} = (a_x, a_y, a_z)$ is the translational acceleration, $\vec{\omega}$ is the rotational velocity and $\dot{\vec{\omega}}$ is the rotational acceleration. For the calculation of BrIC, the peak angular velocities about each axis were employed regardless of the time at which each peak occurs, and $\omega_{xC}$, $\omega_{yC}$ and $\omega_{zC}$ are the components of the critical rotational velocity with values 66.25, 56.45 and 42.87 rads/s respectively as recommended by Takhounts et al. [16].

### 3.2.4 Finite Element Modelling of TBI

We used an anatomically detailed finite element model of TBI to predict the distribution of strain across the brain during oblique impacts [39,93,128]. The model incorporates fine details of brain anatomy such as sulci and gyri. The prediction of the model for brain displacement has been validated against recent cadaver experiments where the post-mortem human subject heads were subjected to well-controlled rotations [54].

To simulate the impacts, the skull was assumed rigid due to its negligible deformation in helmeted impacts and the headform CoG accelerations from the experimental impacts were applied to the skull at the CoG of the head model (Figure 18B,C). Simulations were carried out using the non-linear explicit dynamics solver LS-DYNA (R10.0, LSTC, US). Each simulation spanned 30 ms from the start of impact except for the Hövding impact which spanned 75 ms due to the extended time it remained in contact with the anvil. These durations ensured full capture of the peak brain deformation and strains resulting from the impact. The simulation outputs were postprocessed to determine the maximum principal Green-Lagrange strain, i.e. principal tensile strain, at each element of the brain (called strain hereafter) and results were written into a NIFTI (Neuroimaging Informatics Technology Initiative) file for further analysis.

We determined the 90$^{th}$ percentile value of strain across the whole brain as a measure of overall brain response to the impact. We also determined strain in two regions of interest, corpus callosum and sulci (Figure 18D). For the corpus callosum, the 90$^{th}$ percentile strain was determined. To determine strain in sulci, first Freesurfer was used to segment the structural MRI used to generate the FE model. This process resulted in an accurate spatial map of the grey/white matter boundary, which was then subdivided into regions of interest based on the Destrieux Atlas, including labelling of 30 gyri and 33 sulci in each hemisphere. The NIFTI image of strain was registered to the Freesurfer space using a standard affine transformation. This allowed for the calculation of mean strain within the anatomically correct sulcal maps.

### 3.2.5 Statistical Analysis

The performance of each helmet fitted with a new technology was compared with the performance of conventional helmets serving as controls. The mean and standard deviation of the injury metrics of conventional helmets were used to calculate helmet-specific Z-scores. A Z score of -1 indicates that the performance measure of the helmet is one standard deviation smaller than the mean of the controls. We used a significance level of 0.05, which for a two-sided test is equivalent to a Z-score outside the -1.96 to +1.96 range [129]. Hence, a helmet that is significantly different to conventional helmets would have a Z-score outside these bounds. We also determined the percentage change of each outcome measure of a helmet with respect to the mean of the conventional helmets.

## 3.3 Results

### 3.3.1 Head Motion

Snapshots of the high-speed videos for impact 1 are shown in Figure 19A for some helmets along with the mean and bounds of the linear and rotational acceleration time histories for all impacts in Figure 19B. Between 8 – 10ms, when both linear and rotational accelerations have reached their peak, the helmets have rotated noticeably on the headform except the Hövding airbag helmet. At time 20ms, headform accelerations have reached near zero for all helmets, except for Hövding, causing noticeable headform rotation (Figure 19A).

The performance of the Hövding helmet is very different to the other helmets. It remains in contact with the anvil for 2-3 folds longer than the other helmets and as a result the acceleration of the headform is 2-3 folds smaller than that with other helmets across all impacts (Figure 19B).

### 3.3.2 Kinematics-based Measures

Some of the helmets fitted with the new technologies had significantly different PTA, PRA, PRV and BrIC compared to conventional helmets (Figure 20). The helmets fitted with MIPS had significantly

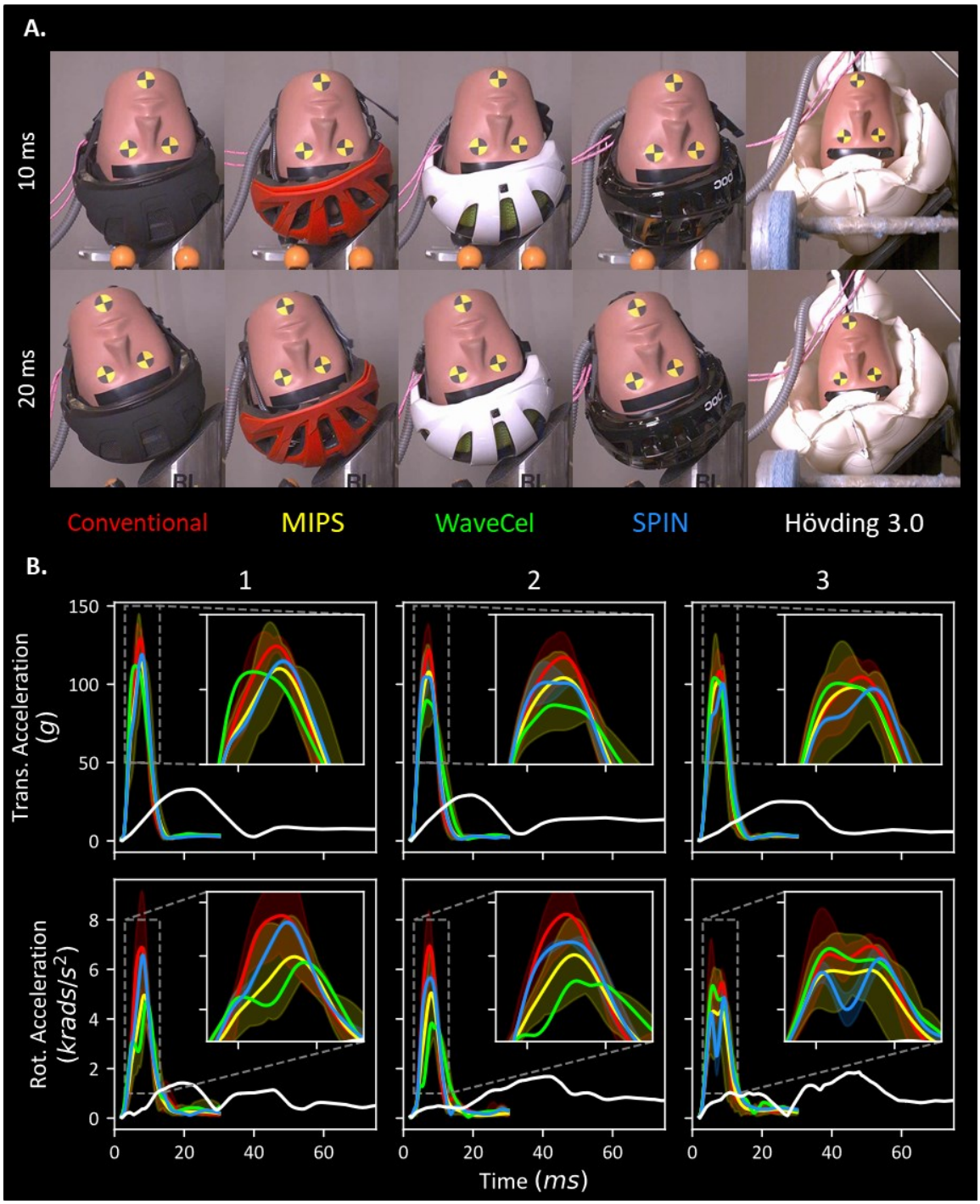


*Figure 19 – (A) Snapshots from the high-speed videos of a helmet from each technology category captured 10 ms apart, 10 and 20 ms after the start of impact 1. (B) Mean resultant translational and rotational time-history pulses colour-coded by technology. A filled region bounds the minimum and maximum recorded traces across all helmets where more than one helmet was assessed for a given technology. The results show that acceleration pulses peaked between 8 – 10 ms with an impact duration under 20 ms except for the Hövding 3.0 airbag helmet (white). Due to the larger size of the inflated airbag helmet, the impact duration was significantly increased and hence the peak was dramatically reduced. In all cases, translational accelerations did not exceed 150 g and rotational accelerations rarely exceeded 8 krads ms$^{-1}$.*

lower PTA compared to conventional helmets for all impacts (impact 1: 7 – 21%, 2: 19 – 36%, 3: 18 – 28% - for z-scores and p-values please see Tables 2-5). However, one of the helmets with MIPS had a significantly higher PTA for impact 1 (11%) and another MIPS helmet had a significantly higher PTA for

impact 3 (17%). 33% of the helmets fitted with MIPS had significantly lower PRA in impact 1 (38 – 46%), 53% in impact 2 (30 – 52%) and 40% in impact 3 (22 – 35%). Similarly, 40% of the helmets fitted with MIPS had significantly lower PRV in impact 1 (33 – 50%), 60% in impact 2 (16 – 47%) and 47% in impact 3 (16 – 35%). Finally, 47% of the helmets fitted with MIPS had significantly lower BrIC in impact 1 (25 – 45%), 60% in impact 2 (16 – 46%) and 40% in impact 3 (15 – 41%). When comparing the Giro Caden helmet versions with and without MIPS, we find that all kinematic-based injury metrics are reduced with the MIPS version (Tables 1-5). When comparing the Biltema helmet versions with and without MIPS, we find that all kinematic-based injury metrics are reduced with the MIPS version except for PTA, which was increased. None of the helmets fitted with MIPS had significantly higher rotational measures of brain injury compared to the conventional helmets.

In comparison to conventional helmets, the WaveCel helmet had significantly lower PTA in impacts 1 and 2 (1: 15% and 2: 27%). This helmet also had significantly reduced PRV in impact 1, and PRA and PRV in impact 2 (1: 33% reduction in PRV, 2: 46% reduction in PRA and 20% reduction in PRV). The WaveCel helmet had a significantly lower BrIC in impact 1 and 2 (1: 29%, 2: 19%).

The helmets fitted with SPIN (Axion and Tectal), hereon referred to as SPIN 1 and SPIN 2 respectively, presented different responses. Only SPIN 1 had a significantly lower PTA in impact 1 and 3 compared to conventional helmets (1: 10%, 3: 13%). However, only SPIN 2 had a significantly lower PTA in impact 2 (16%). Neither SPIN helmets had significantly lower PRA, PRV or BrIC in impact 1 and 2. Only SPIN 1 had a significantly lower PRA, PRV and BrIC in impact 3 (PRA: 24%, PRV: 20%, BrIC: 19%).

Finally, the airbag helmet had significantly reduced PTA and PRA in comparison to all helmets in all impacts considering both 30 and 75 ms analysis durations. PTA was significantly reduced in all three impacts with this helmet in comparison to conventional helmets irrespective of duration (1: 75%, 2: 76% and 3: 76%). PRA was also significantly reduced almost identically across all three impacts. However, the reduction in PRA slightly depended on analysis duration particularly for impact 3 (1: 80%, 2: 76% and 3: 66% @ 30ms; 1: 80%, 2: 79% and 3: 74% @ 75ms). PRV and BrIC were more dramatically affected by analysis duration. We found both PRV and BrIC to be significantly larger with this helmet in impact 2 (PRV: 69%, BrIC: 70%) and 3 (PRV: 20%, BrIC: 16%) and within normal ranges in impact 1 considering a 75ms analysis duration. Considering a 30ms duration, PRV and BrIC were significantly reduced in both impact 2 (PRV: 60%, BrIC: 62%) and 3 (PRV: 47%, BrIC: 55%) and within nominal ranges in impact 1.

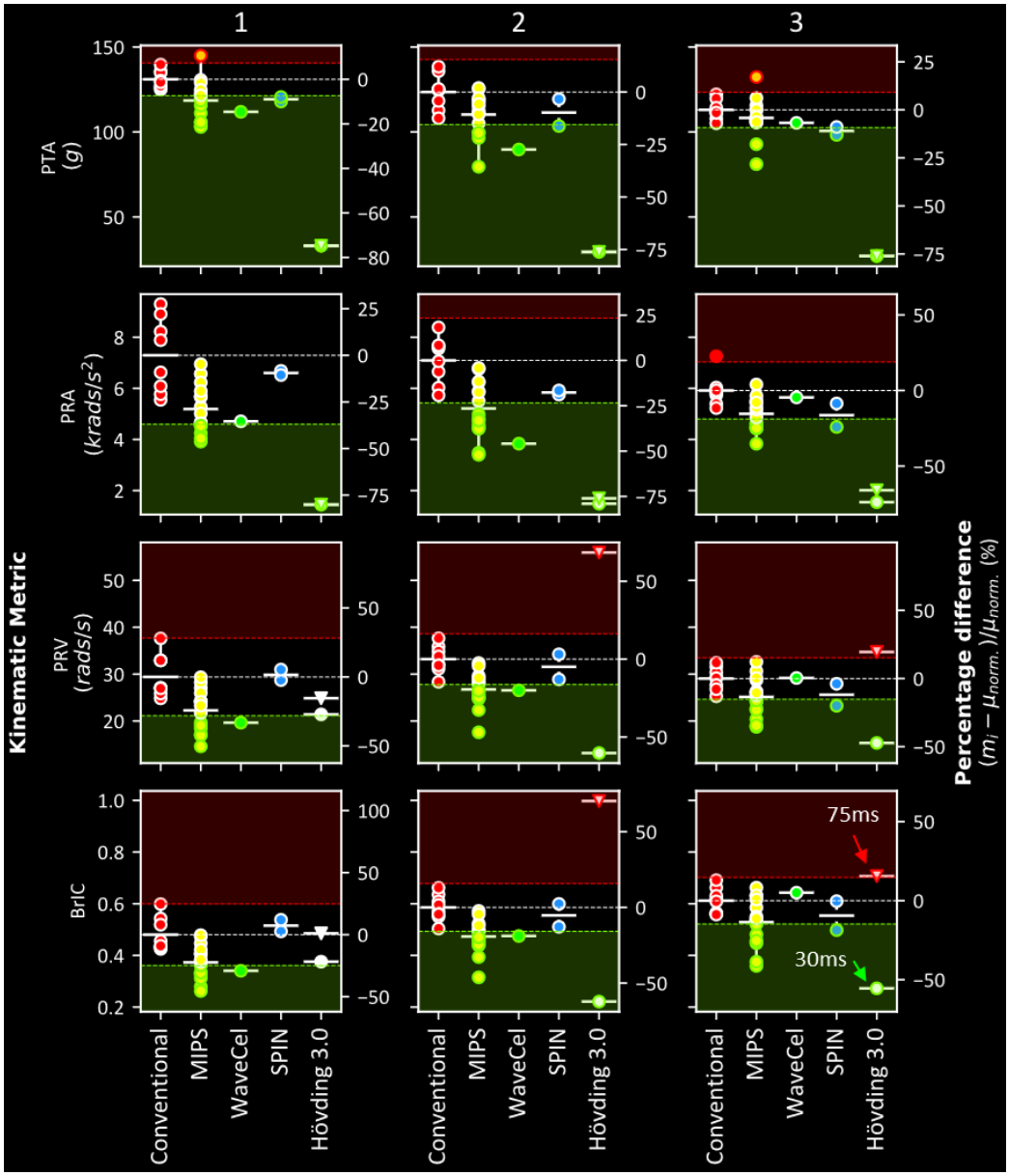


*Figure 20 – The performance of all the helmets in impact condition 1 (left), 2 (middle) and 3 (right) grouped by technology (marker fill colour) with respect to the four kinematic metrics assessed (PTA, PRA, PRV and BrIC). Solid white horizontal lines represent the mean metric value of each technology. The dotted white horizontal lines represent the mean for conventional helmets (red). The red and green margins represent regions where the performance would be significantly worse or better than conventional helmets for that metric ($p<0.05$). The right-hand side axis of each plot represents the percentage difference of the metric value of each helmet with respect to the mean of the conventional helmets. The results show that, in most cases, helmets perform either significantly better than (green marker edge) or insignificantly different to conventional helmets, with rare occasions where helmets perform significantly worse (red marker edge). Note: Each marker represents the average value of the repeat tests for that particular helmet.*

### 3.3.3 Strain Across the Whole Brain

We observed a large variation in strain distribution across the brain when using different helmets in impacts 1, 2 and 3 (Figure 21). The axial sections of the brain show that the three impact conditions led to noticeably different strain patterns for each helmet. Generally, larger strains where more focused in the cortical regions and the corpus callosum.

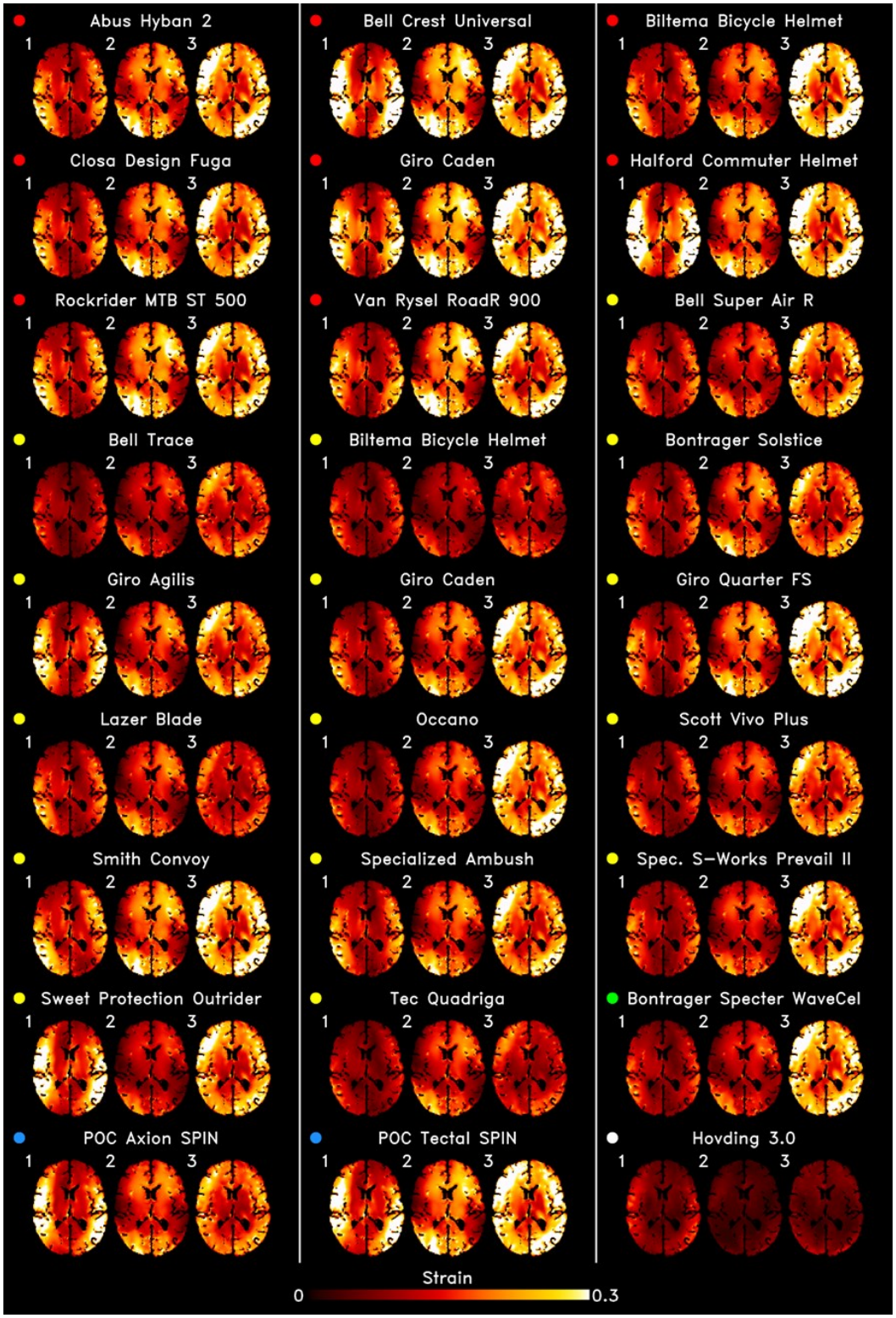


*Figure 21 – Voxel-wise representation of the maximum Green Lagrange strain in the brain in the transverse plane as a result of each impact condition for each helmet. The coloured marker to the left of each helmet name represents the technology. The results show a large variation in brain strain patterns across helmets and across impact conditions for each helmet.*

To better show the effects of the technology on brain strain, we plotted the 90$^{th}$ percentile strain across the whole brain in Figure 22. A large variation in the strain can be seen across the helmets, from

0.01 with the airbag helmet to 0.19 with a conventional helmet. Compared to the performance of conventional helmets, strain was within normal ranges in all MIPS helmets for impact 1. In impacts 2 and 3, strain was significantly lower in 60% of MIPS helmets (2: 35 – 66%, 3: 23 – 51% - for z-scores and p-values please see Tables 6). When comparing the Giro Caden and Biltema helmet versions with and without MIPS, we find that strain measures in all brain regions are reduced with the MIPS versions.

Likewise, strain was lower in the WaveCel helmet in impact 2 (59%), but not in impact 1 or 3. Strain was also significantly reduced in impact 3 in the SPIN 1 helmet. However, no significant reductions were observed for the other impacts nor in the SPIN 2 helmet. The airbag helmet significantly reduced the strain in all three impacts irrespective of analysis duration (1: 86, 2: 90% and 3: 82% @ 30ms and 1: 81, 2: 89% and 3: 82% @ 75ms). None of the helmets fitted with the new technologies showed increased global strain compared to the conventional helmets.

### 3.3.4 Strain in the Corpus Callosum

The 90$^{th}$ percentile strain in corpus callosum (CC) was generally larger than that across the whole brain, ranging from 0.08 – 0.28. Most helmets with new technologies had significantly lower CC strains. On one occasion, a helmet showed a significantly higher CC strain. Significantly lower strain in the CC was found with 47% of MIPS fitted helmets in impact 1 (33 – 52%), 73% in impact 2 (19 – 54%) and 40% in impact 3 (17 – 31% - for z-scores and p-values please see Tables 7). A significantly increased CC strain was found with one of the helmets fitted with MIPS in impact 3 (18%). Significantly lower CC strain was found with the WaveCel helmet in impact 1 and 2 (1: 32%, 2: 34%), but not 3. Of the SPIN helmets, a significant reduction in CC strain was found only with SPIN 1 in impact 3 (24%). A significant reduction in the CC strain was found in all impacts with the Hövding 3.0 helmet considering both analysis durations (1: 60%, 2: 66% and 3: 67% @ 30ms and 1: 48%, 2: 51% and 3: 48% @ 75ms,).

### 3.3.5 Strain in Sulci

Finally, we determined the mean strain across all sulcal regions for all helmeted headform impacts. Strain in sulci was ranging from 0.06 – 0.27 and it was generally larger than the 90$^{th}$ percentile strain across the whole brain. Significant reduction in sulci strain was found with 40% of MIPS fitted helmets in impact 1 (33 – 50%), 67% in impact 2 (20 – 53%) and 53% in impact 3 (16 – 45% - for z-scores and p-values please see Tables 8). Significantly lower sulci strain was found with the WaveCel helmet in impacts 1 and 2 (1: 33%, 2: 34%) but not 3. Of the SPIN helmets, the sulci strain was significantly lower only with SPIN 1 in impact 3 (25%). A significant reduction in the sulci strain was found with the airbag helmet in all impacts irrespective of analysis duration (1: 57%, 2: 74% and 3: 75% @ 30ms; 1: 47%, 2:

61% and 3: 51% @ 75ms). None of the helmets fitted with new technologies showed significantly increased sulcal strain compared to the conventional helmets.

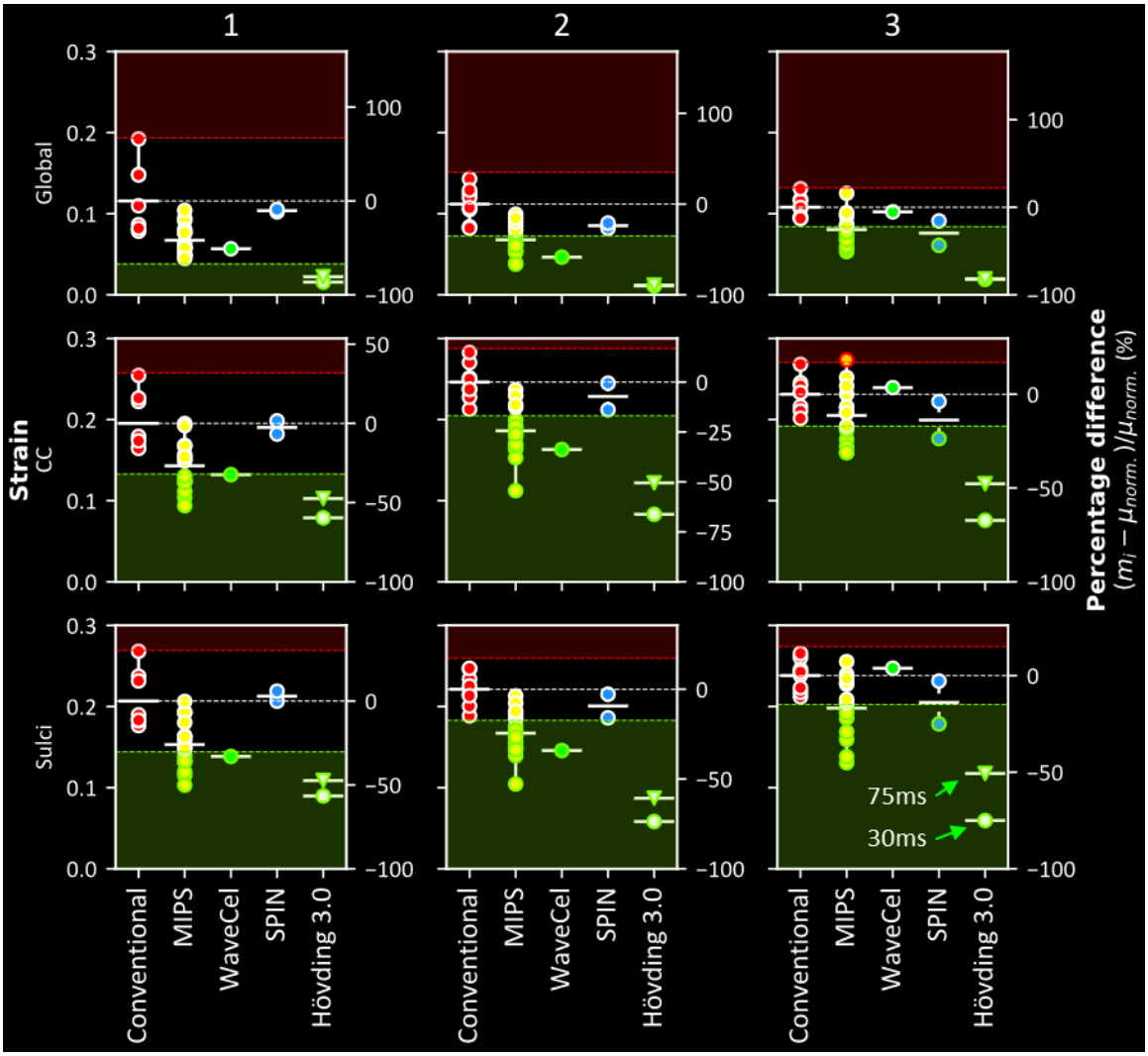


*Figure 22 – The performance of all the helmets in impact condition 1 (left), 2 (middle) and 3 (right) grouped by technology (marker fill colour) with respect to the Green-Lagrange strain across the entire brain (global) as well as in brain regions-of-interest (corpus callosum and sulci). For the global and corpus callosum, the 90$^{th}$ percentile strain value was used. For the sulci, the mean strain value was used. Solid white horizontal lines represent the mean metric value of each technology. The dotted white horizontal lines represent the mean for conventional helmets (red). The red and green margins represent regions where the performance would be significantly worse or better than conventional helmets for that metric (p>0.05). The right-hand side axis of each plot represents the percentage difference of the metric value of each helmet with respect to the mean of the conventional helmets. The results show that, in most cases, helmets perform either significantly better than (green marker edge) or insignificantly different to conventional helmets, with rare occasions where helmets perform significantly worse (red marker edge). Note: Each marker represents the average value of the repeat tests for that particular helmet.*

## 3.4 Discussion

We showed that the new helmet technologies can provide better protection under oblique impacts than conventional helmets. For this assessment, we used a new test method proposed by CEN/TC158/WG11, designed to represent real-world oblique impacts and recorded translational and

rotational motions of the headform. This enabled a unique brain strain analysis which considers key anatomical regions such as corpus collosum and sulci using a highly detailed TBI model. The results of this study show that in comparison with the conventional helmets, the helmets fitted with MIPS, WaveCel, SPIN and Hövding can reduce peak rotational acceleration and velocity, BrIC, overall brain strain and strain in corpus callosum and sulci. None of these helmets showed a significant increase across all measures of injury compared to the conventional helmets, except for two helmets fitted with MIPS and the Hövding when considering a 75ms analysis duration.

Our results show that the effectiveness of helmets in comparison with the conventional helmets depends on their technology, impact location and injury metric. For example, the number of MIPS helmets that were more effective than conventional helmets depends on the impact location. The discrepancy in performance of the helmets across impact locations could be due to the various thicknesses of the helmets in the different impact locations which may affect the resultant force vector and subsequent head motion [119]. Another potential reason for the discrepancy between impact conditions is the geometric shape of the headform which is not symmetric about all anatomical planes. A helmet may rotate easier with less constraints imposed by the head in the coronal plane (impact 1) than the transverse plane (impact 3). A similar case may be found when comparing the coronal to the mid-sagittal rotations (impact 1 vs. impact 2). This may explain why helmets with MIPS and WaveCel were less effective in impacts 2 and 3 than 1 with respect to rotational kinematic and brain injury metrics. For the WaveCel helmet, its anisotropic liner design may also contribute to the different performances. Although cadaveric studies assessing the effect of the direction of rotational acceleration on TBI is limited, a few computational studies have shown that the brain tissue strain and TBI likelihood resulting from rotational acceleration in the transverse plane (axial rotation) can be larger than strain resulting from rotation in other anatomical planes [16,130,131]. Hence, considering the poorer performance of some of the helmets with dedicated rotational damping systems in impact 3 than impacts 1 and 2, the performance of the helmets in future should better address rotations in the transverse plane.

These findings support the use of three different impact locations such as in this study, in contrast to previous work that has considered one impact location to compare injury mitigation of helmets [120]. The choice of these locations is also an important one. We employed three oblique impact locations based on the method proposed by the CEN/TC158/WG11, which was derived from a head impact location probability map of 1024 simulated cyclist falls [124,125]. Our results provide further evidence as to why future standard methods designed to assess the mitigation effects of helmets on rotational motion of the head should include several impact locations.

A recent study introducing a novel comparable method for assessing helmets, named Summation of Tests for the Assessment of Risk (STAR), reinforces the finding of this study [132]. The STAR method summarises the performance of a helmet into a single value based on head kinematics and concussion risk curves derived from American football players. Although the study used a National Operating Committee on Standards for Athletic Equipment (NOCSAE) headform, the study also emphasises the importance of evaluating several impact locations. However, the STAR assessment was limited to MIPS and conventional helmets. Here, we expanded on these results with a wider range of helmet technologies, including WaveCel, SPIN and an airbag helmet. Moreover, we determined the influence of these technologies on the brain using our computational model of TBI.

The airbag helmet, Hövding, outperformed all helmets by far in most metrics except PRV and BrIC when considering a 75ms duration. When considering only the first 30ms of impact, the airbag helmet outperforms all helmets across all injury metrics considered in this study. Reasons for this are likely due to the impact kinematics which result from the large size and low stiffness of the helmet. These features result in a prolonged impact period (~3 times longer than conventional) with a significantly lower peak acceleration as seen in Figure 19B and shown in previous work [49]. Analysis of the high-speed videos reinforces this, revealing that the headform has rotated noticeably less than conventional helmets during the same period. Our brain model shows that this is favourable with respect to brain tissue strain. However, the prolonged duration of impacts with this helmet means that the effect of the neck is likely to be considerable in a real-life impact. Furthermore, due to the size of the airbag, interaction with the shoulder and neck during the impact is likely. It is also noteworthy that BrIC was developed on the basis of 30 ms impacts [16], and hence may not be suitable for longer duration impacts such as with the Hövding or similar future technologies.

We determined strain in the corpus callosum and sulci during impacts. Corpus callosum is the largest white matter tract in the human brain and a common location of axonal injury after severe TBI [56]. Previous work has shown clear relationship between mechanical strain and pathology, including axonal damage and neuroinflammation [133,134]. These pathologies can persist several years after an injury and have been shown to contribute to accumulation of tau proteins in depths of sulci in cases of chronic traumatic encephalopathy [135]. In an in-vivo experiment on guinea pig's optic nerve, Bain et al. determined a 0.21 strain threshold for producing structural damage [44]. A recent study using an in-vivo controlled cortical impact model in rats has shown that increasing strain from below 0.1 to around 0.4 increases axonal damage and neuroinflammatory responses in white matter [45]. This suggests that decreasing strain is an effective way of reducing pathology. Hence, we predicted strain in corpus callosum and sulci to, for the first time, determine the effects of the new helmet technologies on reducing strains in these key regions of the brain. The predicted strains were in the

range reported in this recent animal work, though due to differences in biology and computational models, we cannot directly compare the results. However, this previous work again confirms that the new technologies, which reduce the strain in the brain and key anatomical regions are effective methods for reducing axonal damage and neuroinflammation post-injury.

This study has some limitations. We used a Hybrid III headform in this study, which is one of the most biofidelic headforms with regards to the head shape and size, mass and moments of inertia [136]. However, it has a vinyl rubber skin which has a larger coefficient of friction in contact with fabric than the human scalp [137]. The coefficient of friction of the surrogate skin should be improved in future to produce more biofidelic test conditions. Similar to previous studies [138], we used an isolated headform, thus ignored the potential effects of the neck during impacts. Several studies have shown that primary peak loads from head-first impacts are less affected by the presence of a neck [114,139]. Some studies on helmets have used a HIII neck, but this neck has limitations, such as stiffness in axial loading [75], which can have adverse effects on the results [110,113]. Future work should address the development of a surrogate neck that is biofidelic in head-first impacts. This should enable current and future helmets, particularly those that produce head accelerations with longer durations than conventional helmets, such as the airbag helmet, to be evaluated with improved fidelity. We have attempted to assess similar helmets with and without the technologies where possible (i.e. Giro Caden MIPS vs no MIPS, Biltema MIPS vs no MIPS). However, we were limited with the availability of helmets with and without the same technologies in the current market.

The impact locations targeted in this study are proposed by CEN/TC158/WG11. It is noteworthy that these are simulations of cyclist falls in two scenarios, namely hitting a curb or skidding. A true real-world database would include all physical accident scenarios, including common impacts against motorised vehicles.

A final notable limitation is regarding the statistical evaluation method employed. We used a z-scoring approach to test whether an individual helmet performed better or worse than ‘conventional helmets’. This method enables future comparisons of new helmets to be tested against an established control or benchmark group of helmets. However, we are limited in this study by a small control sample size, which can lead to potential biases. This method can be optimised in future by testing the ‘diagnostic accuracy’ in the context of a different control sample sizes.

## 3.5 Conclusion

In summary, our assessment of 27 commercially available bicycle helmets shows that most helmets with new technologies have the potential to reduce peak rotational acceleration and velocity and maximal strain in corpus callosum and sulci in oblique impacts. However, the outcome is highly

sensitive to impact location. Hence, incorporating different impact locations in future oblique impact test methods and designing helmet technologies for the mitigation of head rotation in different planes are key to reducing brain injuries in bicycle accidents, where helmets are worn. Moreover, it is apparent that helmets that entirely replace EPS foam liners, such as the Hövding, stand a better chance at significantly reducing the brain injury metrics than add-on technologies such as MIPS, WaveCel and SPIN in these impacts if deployed correctly. Hence, a future proposal entirely replacing EPS foam liners with a novel system able to react to the impact occurrence, speed, or energy, rather than a passive add-on technology, could increase the potential for safety improvement. This liner, as discussed earlier, would benefit from the physical properties of elastomers which are recoverable and rate sensitive to react to the impact speed or energy. Hence, in the next chapter, we focus on characterising a few candidate materials that fulfil these requirements to leverage finite element analyses to support the design, optimisation, manufacturing, and testing stages of the proposal.

## 3.6 Appendix

### 3.6.1 Kinematic-based Metrics

*Table 8 - The PTA percentage difference, z-score and p-value of each helmet (referenced by the HID) in comparison to the conventional helmets for each impact condition. The HID cell colours represent the different technologies (see Figure 17).*

| *PTA* | Impact 1 | | | Impact 2 | | | Impact 3 | | |
|---|---|---|---|---|---|---|---|---|---|
| HID | **% diff.** | **z-score** | **p-value** | **% diff.** | **z-score** | **p-value** | **% diff.** | **z-score** | **p-value** |
| 3 | -9 | -2.416 | 0.016 | 1.4 | 0.18 | 0.857 | 2.3 | 0.482 | 0.63 |
| 6 | -7.4 | -1.985 | 0.047 | -9.8 | -1.242 | 0.214 | 0.2 | 0.035 | 0.972 |
| 8 | -20.9 | -5.591 | 0 | -3.8 | -0.475 | 0.635 | -0.1 | -0.012 | 0.99 |
| 10 | -6.1 | -1.632 | 0.103 | 1.9 | 0.239 | 0.811 | -4.5 | -0.948 | 0.343 |
| 13 | 10.7 | 2.85 | 0.004 | -6.8 | -0.862 | 0.389 | -5.8 | -1.228 | 0.219 |
| 15 | -0.3 | -0.077 | 0.939 | -4.3 | -0.539 | 0.59 | 17.1 | 3.641 | 0 |
| 17 | -15.2 | -4.061 | 0 | -2.9 | -0.368 | 0.713 | -4.8 | -1.02 | 0.308 |
| 18 | -19.3 | -5.16 | 0 | -19.4 | -2.447 | 0.014 | 6.1 | 1.307 | 0.191 |
| 21 | -21.4 | -5.72 | 0 | -21.9 | -2.767 | 0.006 | -17.9 | -3.807 | 0 |
| 22 | -11.8 | -3.15 | 0.002 | -14.9 | -1.888 | 0.059 | -6 | -1.273 | 0.203 |
| 23 | -19.2 | -5.14 | 0 | -35.6 | -4.501 | 0 | -28.3 | -6.017 | 0 |

| | | | | | | | | | |
|---|---|---|---|---|---|---|---|---|---|
| 25 | -9.6 | -2.571 | 0.01 | -9.1 | -1.145 | 0.252 | -6.7 | -1.415 | 0.157 |
| 27 | -1.5 | -0.408 | 0.683 | -10.7 | -1.348 | 0.178 | -4.7 | -1.003 | 0.316 |
| 28 | -4.7 | -1.266 | 0.206 | -19.5 | -2.463 | 0.014 | -3.6 | -0.763 | 0.445 |
| 29 | -7.2 | -1.93 | 0.054 | -5.7 | -0.727 | 0.467 | -6.3 | -1.351 | 0.177 |
| 4 | -14.6 | -3.905 | 0 | -27.4 | -3.463 | 0.001 | -6.8 | -1.441 | 0.15 |
| 14 | -10 | -2.669 | 0.008 | -3.4 | -0.428 | 0.669 | -13 | -2.774 | 0.006 |
| 16 | -7.9 | -2.125 | 0.034 | -16.2 | -2.047 | 0.041 | -8.9 | -1.899 | 0.058 |
| $5_{30ms}$ | -74.8 | -19.984 | 0 | -76.2 | -9.632 | 0 | -76.1 | -16.205 | 0 |
| $5_{75ms}$ | -74.8 | -19.984 | 0 | -76.2 | -9.632 | 0 | -76.1 | -16.205 | 0 |

*Table 9 - The PRA percentage difference, z-score and p-value of each helmet (referenced by the HID) in comparison to the conventional helmets for each impact condition. The HID cell colours represent the different technologies (see Figure 17).*

| *PRA* | Impact 1 | | | Impact 2 | | | Impact 3 | | |
|---|---|---|---|---|---|---|---|---|---|
| HID | **% diff.** | **z-score** | **p-value** | **% diff.** | **z-score** | **p-value** | **% diff.** | **z-score** | **p-value** |
| 3 | -27.6 | -1.466 | 0.143 | -17 | -1.423 | 0.155 | -35.2 | -3.658 | 0 |
| 6 | -35.9 | -1.906 | 0.057 | -22.4 | -1.877 | 0.061 | -14.9 | -1.545 | 0.122 |
| 8 | -46.3 | -2.458 | 0.014 | -37 | -3.101 | 0.002 | -25.2 | -2.617 | 0.009 |
| 10 | -41.8 | -2.216 | 0.027 | -35.4 | -2.966 | 0.003 | -21.7 | -2.257 | 0.024 |
| 13 | -9.9 | -0.526 | 0.599 | -4.7 | -0.395 | 0.693 | -6.5 | -0.676 | 0.499 |
| 15 | -31.2 | -1.655 | 0.098 | -50.9 | -4.265 | 0 | -22.3 | -2.312 | 0.021 |
| 17 | -14.6 | -0.773 | 0.44 | -12.1 | -1.016 | 0.31 | -7.9 | -0.824 | 0.41 |
| 18 | -37.8 | -2.007 | 0.045 | -29.7 | -2.49 | 0.013 | -24.2 | -2.517 | 0.012 |
| 21 | -4.8 | -0.253 | 0.8 | -37.7 | -3.156 | 0.002 | -24.8 | -2.574 | 0.01 |
| 22 | -36.5 | -1.936 | 0.053 | -32 | -2.682 | 0.007 | -17.9 | -1.856 | 0.063 |
| 23 | -37.8 | -2.006 | 0.045 | -52.1 | -4.361 | 0 | -12.6 | -1.309 | 0.191 |

| | | | | | | | | | |
|---|---|---|---|---|---|---|---|---|---|
| 25 | -22.4 | -1.19 | 0.234 | -17.6 | -1.47 | 0.142 | -11.1 | -1.149 | 0.251 |
| 27 | -21.9 | -1.163 | 0.245 | -11.6 | -0.974 | 0.33 | 4 | 0.412 | 0.68 |
| 28 | -44.5 | -2.363 | 0.018 | -33.2 | -2.777 | 0.005 | -3.5 | -0.365 | 0.715 |
| 29 | -19.2 | -1.02 | 0.308 | -4.2 | -0.35 | 0.726 | -7.9 | -0.82 | 0.412 |
| 4 | -35.4 | -1.88 | 0.06 | -45.9 | -3.845 | 0 | -4.6 | -0.475 | 0.635 |
| 14 | -8.4 | -0.443 | 0.658 | -18.8 | -1.576 | 0.115 | -24.1 | -2.506 | 0.012 |
| 16 | -10.6 | -0.563 | 0.573 | -16.6 | -1.387 | 0.165 | -8.6 | -0.89 | 0.373 |
| $5_{30ms}$ | -74.8 | -19.984 | 0 | -76.2 | -9.632 | 0 | -76.1 | -16.205 | 0 |
| $5_{75ms}$ | -74.8 | -19.984 | 0 | -76.2 | -9.632 | 0 | -76.1 | -16.205 | 0 |

*Table 10 - The PRV percentage difference, z-score and p-value of each helmet (referenced by the HID) in comparison to the conventional helmets for each impact condition. The HID cell colours represent the different technologies (see Figure 17).*

| *PRV* | Impact 1 | | | Impact 2 | | | Impact 3 | | |
|---|---|---|---|---|---|---|---|---|---|
| HID | **% diff.** | **z-score** | **p-value** | **% diff.** | **z-score** | **p-value** | **% diff.** | **z-score** | **p-value** |
| 3 | -17.6 | -1.226 | 0.22 | -22.5 | -2.705 | 0.007 | -29.8 | -3.845 | 0 |
| 6 | -33.1 | -2.304 | 0.021 | -16.3 | -1.964 | 0.05 | -22 | -2.836 | 0.005 |
| 8 | -17.8 | -1.238 | 0.216 | -24.5 | -2.954 | 0.003 | -17 | -2.194 | 0.028 |
| 10 | -41.6 | -2.897 | 0.004 | -32.7 | -3.938 | 0 | -23 | -2.968 | 0.003 |
| 13 | -8 | -0.56 | 0.575 | -2.5 | -0.304 | 0.761 | -9.5 | -1.222 | 0.222 |
| 15 | -37.3 | -2.597 | 0.009 | -47 | -5.662 | 0 | -35.5 | -4.58 | 0 |
| 17 | -4 | -0.276 | 0.783 | -13.8 | -1.667 | 0.096 | -10 | -1.29 | 0.197 |
| 18 | -42.4 | -2.955 | 0.003 | -15.3 | -1.842 | 0.065 | -34.3 | -4.429 | 0 |
| 21 | -0.2 | -0.017 | 0.986 | -25.5 | -3.065 | 0.002 | -16 | -2.067 | 0.039 |
| 22 | -35.2 | -2.451 | 0.014 | -24.5 | -2.95 | 0.003 | -12.3 | -1.593 | 0.111 |
| 23 | -26.2 | -1.823 | 0.068 | -19.7 | -2.376 | 0.018 | 5.4 | 0.695 | 0.487 |

| | | | | | | | | | |
|---|---|---|---|---|---|---|---|---|---|
| 25 | -11.7 | -0.814 | 0.416 | -10.8 | -1.303 | 0.193 | -10.5 | -1.358 | 0.174 |
| 27 | -18.1 | -1.26 | 0.208 | -4.4 | -0.532 | 0.595 | 12.3 | 1.583 | 0.113 |
| 28 | -50.4 | -3.508 | 0 | -20.3 | -2.449 | 0.014 | -1.2 | -0.16 | 0.873 |
| 29 | -20.8 | -1.45 | 0.147 | -12.2 | -1.464 | 0.143 | 0.4 | 0.051 | 0.959 |
| 4 | -33.2 | -2.312 | 0.021 | -20 | -2.414 | 0.016 | 0.4 | 0.052 | 0.959 |
| 14 | -2.3 | -0.161 | 0.872 | -13 | -1.57 | 0.116 | -20 | -2.578 | 0.01 |
| 16 | 5.3 | 0.37 | 0.711 | 3.1 | 0.376 | 0.707 | -3.8 | -0.496 | 0.62 |
| $5_{30ms}$ | -27.2 | -1.894 | 0.058 | -60.4 | -7.271 | 0 | -47.3 | -6.102 | 0 |
| $5_{75ms}$ | -15.5 | -1.077 | 0.281 | 68.5 | 8.248 | 0 | 19.5 | 2.517 | 0.012 |

*Table 11 - The BrIC percentage difference, z-score and p-value of each helmet (referenced by the HID) in comparison to the conventional helmets for each impact condition. The HID cell colours represent the different technologies (see Figure 17).*

| *BrIC* | Impact 1 | | | Impact 2 | | | Impact 3 | | |
|---|---|---|---|---|---|---|---|---|---|
| HID | **% diff.** | **z-score** | **p-value** | **% diff.** | **z-score** | **p-value** | **% diff.** | **z-score** | **p-value** |
| 3 | -15.5 | -1.224 | 0.221 | -22.8 | -2.837 | 0.005 | -26.9 | -3.575 | 0 |
| 6 | -30.8 | -2.431 | 0.015 | -16.1 | -2.005 | 0.045 | -21.4 | -2.847 | 0.004 |
| 8 | -15.2 | -1.204 | 0.229 | -21.6 | -2.691 | 0.007 | -12.8 | -1.707 | 0.088 |
| 10 | -41.8 | -3.304 | 0.001 | -32.8 | -4.076 | 0 | -25.4 | -3.37 | 0.001 |
| 13 | -1.4 | -0.11 | 0.912 | -2.3 | -0.287 | 0.774 | -4.3 | -0.578 | 0.563 |
| 15 | -32.5 | -2.57 | 0.01 | -46.2 | -5.744 | 0 | -41.3 | -5.486 | 0 |
| 17 | -7 | -0.554 | 0.58 | -14.6 | -1.812 | 0.07 | -12.4 | -1.644 | 0.1 |
| 18 | -35.2 | -2.776 | 0.006 | -15.6 | -1.935 | 0.053 | -38.6 | -5.136 | 0 |
| 21 | -0.4 | -0.031 | 0.975 | -25.2 | -3.131 | 0.002 | -14.9 | -1.974 | 0.048 |
| 22 | -30.6 | -2.42 | 0.016 | -24.4 | -3.039 | 0.002 | -10.1 | -1.34 | 0.18 |
| 23 | -24.9 | -1.965 | 0.049 | -19.5 | -2.422 | 0.015 | 2.9 | 0.392 | 0.695 |

| | | | | | | | | | |
|---|---|---|---|---|---|---|---|---|---|
| 25 | -12.2 | -0.961 | 0.337 | -10.7 | -1.328 | 0.184 | -11.3 | -1.507 | 0.132 |
| 27 | -21.9 | -1.73 | 0.084 | -4.6 | -0.572 | 0.567 | 8.2 | 1.094 | 0.274 |
| 28 | -45.4 | -3.586 | 0 | -19.7 | -2.452 | 0.014 | 3.3 | 0.437 | 0.662 |
| 29 | -20.2 | -1.593 | 0.111 | -12 | -1.49 | 0.136 | 0.7 | 0.096 | 0.924 |
| 4 | -29.1 | -2.298 | 0.022 | -18.9 | -2.347 | 0.019 | 5 | 0.669 | 0.503 |
| 14 | 2.6 | 0.208 | 0.835 | -12.8 | -1.595 | 0.111 | -18.6 | -2.476 | 0.013 |
| 16 | -7.9 | -2.125 | 0.034 | -16.2 | -2.047 | 0.041 | -8.9 | -1.899 | 0.058 |
| $5_{30ms}$ | -74.8 | -19.984 | 0 | -76.2 | -9.632 | 0 | -76.1 | -16.205 | 0 |
| $5_{75ms}$ | -74.8 | -19.984 | 0 | -76.2 | -9.632 | 0 | -76.1 | -16.205 | 0 |

### 3.6.2 Brain Strain-based Metrics

*Table 12 - The global 90$^{th}$ percentile brain strain percentage difference, z-score and p-value of each helmet (referenced by the HID) in comparison to the conventional helmets for each impact condition. The HID cell colours represent the different technologies (see Figure 17).*

| *Global* | Impact 1 | | | Impact 2 | | | Impact 3 | | |
|---|---|---|---|---|---|---|---|---|---|
| HID | **% diff.** | **z-score** | **p-value** | **% diff.** | **z-score** | **p-value** | **% diff.** | **z-score** | **p-value** |
| 3 | -45 | -1.313 | 0.189 | -34.7 | -1.938 | 0.053 | -50.7 | -4.491 | 0 |
| 6 | -49.7 | -1.45 | 0.147 | -35.3 | -1.973 | 0.048 | -31.2 | -2.768 | 0.006 |
| 8 | -58.7 | -1.713 | 0.087 | -51.8 | -2.892 | 0.004 | -37.8 | -3.348 | 0.001 |
| 10 | -57.3 | -1.673 | 0.094 | -50.5 | -2.82 | 0.005 | -34.1 | -3.022 | 0.003 |
| 13 | -18.3 | -0.534 | 0.593 | -11.1 | -0.622 | 0.534 | -10.1 | -0.898 | 0.369 |
| 15 | -49.2 | -1.436 | 0.151 | -65.1 | -3.633 | 0 | -47 | -4.164 | 0 |
| 17 | -20.9 | -0.609 | 0.543 | -24.1 | -1.347 | 0.178 | -22.8 | -2.018 | 0.044 |
| 18 | -57.4 | -1.676 | 0.094 | -43.6 | -2.437 | 0.015 | -44.3 | -3.926 | 0 |
| 21 | -10 | -0.292 | 0.77 | -53.2 | -2.97 | 0.003 | -37.2 | -3.294 | 0.001 |

| | | | | | | | | | |
|---|---|---|---|---|---|---|---|---|---|
| 22 | -52.1 | -1.52 | 0.129 | -45.3 | -2.531 | 0.011 | -28.8 | -2.547 | 0.011 |
| 23 | -50 | -1.458 | 0.145 | -66.2 | -3.7 | 0 | -19.4 | -1.717 | 0.086 |
| 25 | -30.3 | -0.884 | 0.377 | -28.5 | -1.589 | 0.112 | -20.7 | -1.829 | 0.067 |
| 27 | -33.7 | -0.983 | 0.326 | -19.8 | -1.107 | 0.268 | 16 | 1.417 | 0.156 |
| 28 | -61.3 | -1.788 | 0.074 | -45.9 | -2.565 | 0.01 | -8.5 | -0.754 | 0.451 |
| 29 | -33.9 | -0.989 | 0.323 | -15.6 | -0.873 | 0.383 | -6.3 | -0.557 | 0.578 |
| 4 | -51 | -1.487 | 0.137 | -58.5 | -3.267 | 0.001 | -5.3 | -0.469 | 0.639 |
| 14 | -11.6 | -0.339 | 0.735 | -26.7 | -1.49 | 0.136 | -43.5 | -3.853 | 0 |
| 16 | -9.1 | -0.265 | 0.791 | -20.9 | -1.166 | 0.244 | -15.6 | -1.381 | 0.167 |
| $5_{30ms}$ | -86.4 | -2.522 | 0.012 | -90.2 | -5.035 | 0 | -82.4 | -7.301 | 0 |
| $5_{75ms}$ | -80.7 | -2.355 | 0.019 | -89.4 | -4.992 | 0 | -81.8 | -7.248 | 0 |

*Table 13 - The CC 90th percentile brain strain percentage difference, z-score and p-value of each helmet (referenced by the HID) in comparison to the conventional helmets for each impact condition. The HID cell colours represent the different technologies (see Figure 17).*

| *CC* | Impact 1 | | | Impact 2 | | | Impact 3 | | |
|---|---|---|---|---|---|---|---|---|---|
| HID | **% diff.** | **z-score** | **p-value** | **% diff.** | **z-score** | **p-value** | **% diff.** | **z-score** | **p-value** |
| 3 | -19.9 | -1.218 | 0.223 | -26.2 | -3.047 | 0.002 | -31.1 | -3.59 | 0 |
| 6 | -35.8 | -2.195 | 0.028 | -22.1 | -2.575 | 0.01 | -24.1 | -2.779 | 0.005 |
| 8 | -22.6 | -1.387 | 0.165 | -33.5 | -3.899 | 0 | -17.7 | -2.04 | 0.041 |
| 10 | -46.8 | -2.871 | 0.004 | -37.9 | -4.413 | 0 | -19.2 | -2.212 | 0.027 |
| 13 | -0.1 | -0.008 | 0.994 | -3.9 | -0.453 | 0.651 | -7.2 | -0.826 | 0.409 |
| 15 | -36.9 | -2.263 | 0.024 | -54.4 | -6.339 | 0 | -28 | -3.227 | 0.001 |
| 17 | -13.9 | -0.853 | 0.394 | -18.7 | -2.182 | 0.029 | -6.6 | -0.761 | 0.447 |
| 18 | -43 | -2.639 | 0.008 | -22.2 | -2.581 | 0.01 | -31 | -3.571 | 0 |
| 21 | -1.4 | -0.087 | 0.931 | -31.8 | -3.704 | 0 | -16.9 | -1.953 | 0.051 |

| | | | | | | | | | |
|---|---|---|---|---|---|---|---|---|---|
| 22 | -37.3 | -2.286 | 0.022 | -27.2 | -3.171 | 0.002 | -10 | -1.151 | 0.25 |
| 23 | -33.3 | -2.039 | 0.041 | -31.1 | -3.616 | 0 | 8.9 | 1.03 | 0.303 |
| 25 | -14.3 | -0.878 | 0.38 | -12.6 | -1.472 | 0.141 | -9.8 | -1.129 | 0.259 |
| 27 | -23.7 | -1.452 | 0.147 | -6.8 | -0.795 | 0.427 | 18.3 | 2.107 | 0.035 |
| 28 | -52 | -3.188 | 0.001 | -26 | -3.032 | 0.002 | 0.1 | 0.006 | 0.995 |
| 29 | -21.1 | -1.294 | 0.196 | -11.3 | -1.317 | 0.188 | 4.4 | 0.506 | 0.613 |
| 4 | -32.4 | -1.986 | 0.047 | -33.8 | -3.933 | 0 | 3.5 | 0.405 | 0.685 |
| 14 | -6.7 | -0.413 | 0.68 | -13.9 | -1.614 | 0.107 | -23.6 | -2.725 | 0.006 |
| 16 | 1.6 | 0.097 | 0.923 | -0.6 | -0.065 | 0.948 | -3.9 | -0.447 | 0.655 |
| $5_{30ms}$ | -59.7 | -3.659 | 0 | -66.2 | -7.712 | 0 | -67.2 | -7.751 | 0 |
| $5_{75ms}$ | -47.5 | -2.91 | 0.004 | -50.5 | -5.878 | 0 | -47.7 | -5.502 | 0 |

*Table 14 - The mean brain sulci strain percentage difference, z-score and p-value of each helmet (referenced by the HID) in comparison to the conventional helmets for each impact condition. The HID cell colours represent the different technologies (see Figure 17).*

| *Sulci* | Impact 1 | | | Impact 2 | | | Impact 3 | | |
|---|---|---|---|---|---|---|---|---|---|
| HID | **% diff.** | **z-score** | **p-value** | **% diff.** | **z-score** | **p-value** | **% diff.** | **z-score** | **p-value** |
| 3 | -23.4 | -1.515 | 0.13 | -25.8 | -2.915 | 0.004 | -33.1 | -4.331 | 0 |
| 6 | -32.7 | -2.12 | 0.034 | -20.4 | -2.312 | 0.021 | -22.1 | -2.886 | 0.004 |
| 8 | -27.6 | -1.788 | 0.074 | -33.2 | -3.758 | 0 | -17.8 | -2.322 | 0.02 |
| 10 | -44.2 | -2.865 | 0.004 | -37.1 | -4.191 | 0 | -29.1 | -3.807 | 0 |
| 13 | -6.5 | -0.424 | 0.672 | -3.7 | -0.424 | 0.672 | -4.5 | -0.593 | 0.553 |
| 15 | -36.3 | -2.354 | 0.019 | -52.8 | -5.971 | 0 | -45.1 | -5.892 | 0 |
| 17 | -7 | -0.452 | 0.651 | -16.3 | -1.84 | 0.066 | -16.5 | -2.151 | 0.031 |
| 18 | -42.3 | -2.741 | 0.006 | -22.8 | -2.573 | 0.01 | -42 | -5.481 | 0 |
| 21 | -0.2 | -0.015 | 0.988 | -31.7 | -3.585 | 0 | -19.5 | -2.541 | 0.011 |

| | | | | | | | | | |
|---|---|---|---|---|---|---|---|---|---|
| 22 | -35.6 | -2.311 | 0.021 | -29.5 | -3.338 | 0.001 | -14.1 | -1.848 | 0.065 |
| 23 | -28.6 | -1.852 | 0.064 | -33.7 | -3.808 | 0 | -3.4 | -0.45 | 0.653 |
| 25 | -12.8 | -0.832 | 0.405 | -13.9 | -1.572 | 0.116 | -12.3 | -1.612 | 0.107 |
| 27 | -20.9 | -1.353 | 0.176 | -7.7 | -0.869 | 0.385 | 7.2 | 0.941 | 0.347 |
| 28 | -50.2 | -3.253 | 0.001 | -26.7 | -3.015 | 0.003 | 0.7 | 0.085 | 0.932 |
| 29 | -21.3 | -1.382 | 0.167 | -12.2 | -1.378 | 0.168 | -1.2 | -0.161 | 0.872 |
| 4 | -33 | -2.141 | 0.032 | -34.1 | -3.86 | 0 | 3.8 | 0.496 | 0.62 |
| 14 | -0.1 | -0.007 | 0.994 | -15.9 | -1.803 | 0.071 | -25 | -3.27 | 0.001 |
| 16 | 5.9 | 0.382 | 0.702 | -2.8 | -0.314 | 0.754 | -2.9 | -0.373 | 0.709 |
| $5_{30ms}$ | -56.6 | -3.671 | 0 | -73.7 | -8.334 | 0 | -75.1 | -9.806 | 0 |
| $5_{75ms}$ | -47.4 | -3.074 | 0.002 | -60.7 | -6.865 | 0 | -50.7 | -6.622 | 0 |

# 4 Chapter Four: Material Characterisation of Additively Manufactured Elastomers at Different Strain Rates and Build Orientations

Additive manufacturing (AM) has enabled conceptual designs to be rapidly prototyped to evaluate and validate the feasibility of complex topologies using materials which were once impossible. AM was typically employed prior to heavy investment in costly tooling processes for volume production. However, AM is used today for manufacturing final products such as helmets and shoe soles which employ flexible elastomers. Finite Element Analysis (FEA) is a key tool for the development of such applications, which requires comprehensive material characterisation utilising advanced material models. However, in contrast to conventional rubbers, AM elastomers have been less explored leading to a few material models with various limitations in fidelity. Therefore, one aim of this study was to characterise the mechanical response of the latest PolyJet elastomers, Agilus30 (A30) and Tango+ (T+), under large strain tension-compression and time-dependent high-frequency/relaxation loadings. Another aim was to calibrate a visco-hyperelastic material model to accurately predict these responses. Tensile, compressive, cyclic, dynamic mechanical analysis (DMA) and stress relaxation tests were carried out on pristine A30 and T+ samples. Quasi-static tension-compression tests were used to calibrate a 3-term Ogden hyperelastic model. Stress relaxation and DMA results were combined to determine the constants of a 5-term Prony series across a large window of relaxation time (10 μs - 100 s). A numerical time-stepping scheme was employed to predict the visco-hyperelastic response of the 3D-printed elastomers at large strains and different strain rates. In addition, the anisotropy in the elastomers, which stemmed from build orientation, was explored. Highly nonlinear stress-strain relationships were observed in both elastomers, with a strong dependency on strain rate. Relaxation tests revealed that A30 and T+ elastomers relax to 50% and 70% of their peak stress values respectively in less than 20 seconds. The effect of orientation on the loading response was most pronounced with prints along the Z-direction, particularly at large strains and lower strain rates. Moreover, the visco-hyperelastic material model accurately predicted the large strain and time-dependent behaviour of both elastomers. Our findings will allow for the development of more accurate computational models of 3D-printed elastomers, which can be utilised for computer-aided design in novel applications requiring flexible or rate-sensitive AM materials.

*Keywords*: Material jetting; PolyJet elastomers; visco-hyperelastic rubbers; material characterisation; anisotropy

It is noteworthy to mention that much of the work in this chapter has formed the basis of the publication cited below, whereby the majority of the data analysis, figures and writing of the publication was done by the publication's first author and the author of this thesis.

Abayazid, F. F., & Ghajari, M. (2020). Material characterisation of additively manufactured elastomers at different strain rates and build orientations. *Additive Manufacturing*, *33*(December 2019), 101160. https://doi.org/10.1016/j.addma.2020.101160

## 4.1 Introduction

Additive manufacturing (AM), commonly known as 3D-printing, has rapidly closed the gap between product design, prototyping and final production. Commercial parts with often critical contribution to functionality are now produced via AM such as automotive brake callipers [140], aerospace parts [141], customised medical and prosthetic implants [142–145] and energy absorbing lattice structures [95,128,146–148].

One of the most promising AM methods is photopolymer jetting (PolyJet), also known as material jetting. PolyJet involves the deposition of voxel-based droplets of photopolymer resins onto a print bed, after which the resins are cured using ultraviolet (UV) lamps [149,150]. This method polymerises the deposited layer and allows for another layer to be added. The layer-by-layer nature of PolyJet makes it one of the fastest AM technologies that currently exist in contrast to line-by-line AM processes such as fused deposition modelling (FDM) or powder-bed fusion (PBF) [150]. Moreover, the deposition of the resin prior to curing means that a wide range of resins with different polymerised properties, called 'Digital Materials' (DMs), can be deposited from the same set of nozzles allowing for the production of multi-material parts [151–153]. In recent years, new flexible elastomers, such as Agilus30 (A30) and Tango+ (T+), have become available to PolyJet technology through the development of novel photopolymer resins. The mechanical flexibility of PolyJet elastomers have made them particularly useful for applications including soft robotic active hinges and actuators [151,154,155], shape memory '4D materials' and composites [151,156–161]. Other applications included wearable electronics [162], compliant systems and metamaterials [152,163].

Computational modelling methods, particularly Finite Element Analysis (FEA), have played a key role in accelerating the development of several of such complex structures that are subjected to large strains and a range of strain rates. This has provided engineers with insight into the performance of their designs in ways otherwise unobtainable. However, it is paramount that material models are well calibrated to experimental tests relevant to the strain and strain rates expected for reliable computational predictions. This is particularly important when the materials employed are

viscoelastic, i.e. time-dependent and sensitive to rate of loading, such as industrial rubbers and the growing family of PolyJet elastomers such as those explored here.

The existing material models of PolyJet elastomers in the literature are widely inconsistent as their time-dependency is often oversimplified [164,165] or entirely overlooked [166–170]. A recent study collected the shear modulus of several of the existing material models for T+ and reported a variation from 0.158 - 0.330 MPa [164]. Reasons for this could be that studies regarded Tango (T) and T+ as linear elastic [170,171] or purely hyperelastic using Neo-Hookean [167] or Arruda-Boyce material models [172], disregarding their time-dependent behaviour. The majority of studies which have explored PolyJet elastomers have focused on their time-independent behaviour [151,164,173]. Ryu et al. explored the accuracy of Neo-Hookean and Mooney-Rivlin hyperelastic material models in predicting the uniaxial tensile response of TangoBlack+ (TB+) alongside other DMs using FEA [174]. Salcedo et al. explored the DM composites by assessing their tensile response with TB+ elastomer and rigid VeroWhite (VW+) co-printed within the same sample with various arrangements [175]. However, none of the studies have explored the viscoelastic response of the elastomers, which we have found to significantly alter the response of the PolyJet elastomers. This renders the existing data insufficient for extracting comprehensive material properties that can accurately represent the mechanical response of the elastomers across a range of loading speeds.

To bridge this gap, we present a comprehensive set of experimental results conducted on pristine A30 and T+ samples, including tensile, compressive, cyclic loading tests as well as dynamic mechanical analysis (DMA) and stress relaxation tests. We then present a visco-hyperelastic material model that can accurately predict the time-dependent properties of the elastomers across two decades of strain rates. To our best knowledge, this is the first paper to provide a visco-hyperelastic material model for PolyJet elastomers using stress relaxation and uniaxial test data.

The importance of modelling viscoelasticity of materials can be seen in [154,176]. Therein, the authors reported significant relaxation of their PolyJet-printed bellow actuators which was not modelled due to insufficient data on the time-dependency and viscoelastic modelling of A30.

Here, we use our experimental data to determine the constants of a time-dependent material model for both T+ and A30 to predict the response of these PolyJet elastomers to tension and compression with promising fidelity across strain rates spanning two orders of magnitude.

Another attribute of PolyJet parts, which is common in several AM methods, is the inherent anisotropy in the final part due to the difference between the inter- and intra-layer mechanical properties [177–183]. Previous studies reported that elastic moduli, ultimate tensile strength and fracture stress of

PolyJet plastics all varied with build orientation [177,179–181]. A few studies on the anisotropy of PolyJet elastomers concluded that parts printed along the print bed (X-Y) plane had the highest elastic modulus [173,184–186]. However, no studies to date have reported the effect of build orientation on the nonlinear time-dependent stress response of PolyJet elastomers. Here we also studied the effect of PolyJet build orientation on the mechanical response of T+ and A30 elastomers at various strain rates. As isotropy was assumed for the presented visco-hyperelastic material model, our work also provides insight into the fidelity of the presented material model in predicting A30 and T+ responses along different build orientations.

## 4.2 Methods

### 4.2.1 Experimental Methods

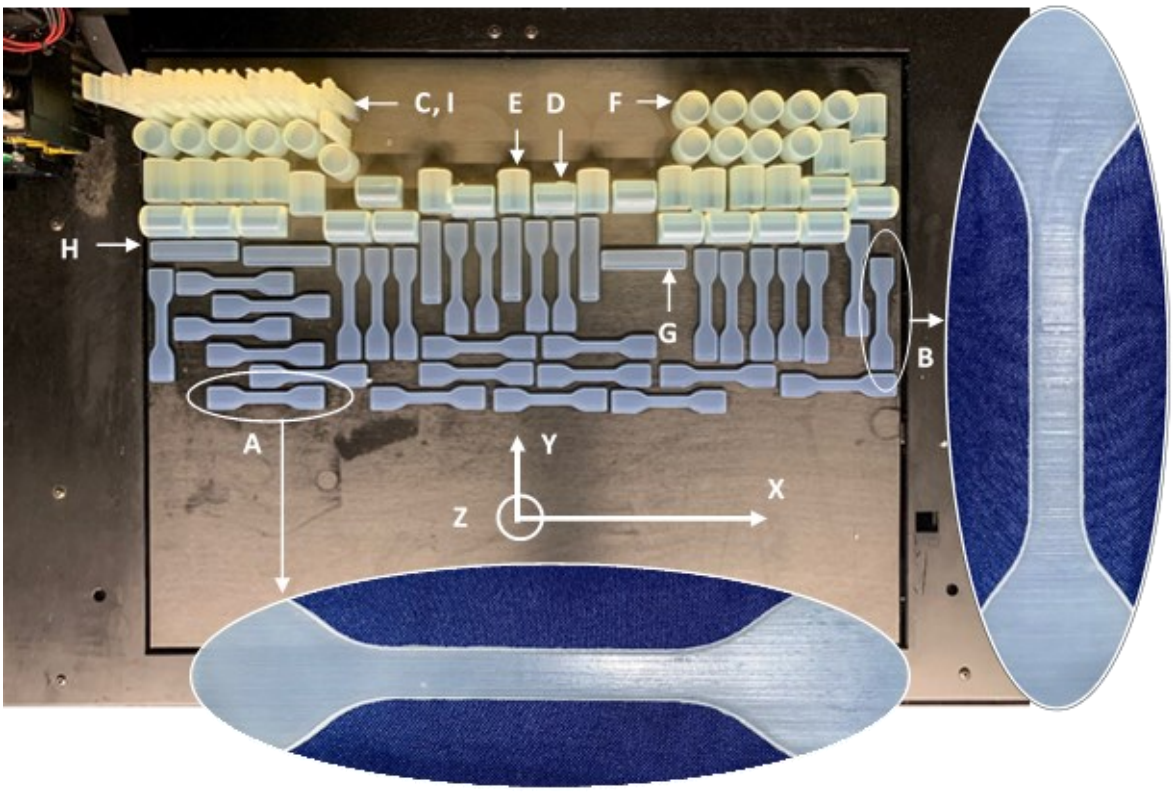


*Figure 23 - Stratasys Connex3 Objet500 printer bed with printed X- Y- and Z- tension (A, B and C respectively), compression (D, E and F) and DMA (G, H and I) samples. Streaks left by the PolyJet printing process can be seen lengthwise along the X-tensile sample (A) and along the width of the Y- sample (B).*

Connex3 Objet500 and Objet260 multi-material 3D-printers were used to print clear A30 and T+ samples respectively (Connex3, Stratasys ltd.). All samples were printed in a single print job as per the arrangement in Figure 23 with one UV lamp in order to minimise the effects of overlapping exposures to multiple UV lamps. Tension, compression and DMA samples printed lengthwise along the X-, Y- and Z-directions will be referred to as X-, Y-, and Z- respectively from hereon (Figure 23). All samples were printed with the matte finish option as the glossy finish could potentially lead to tougher samples due

to over-curing [180]. This meant that each part was coated with support material regardless of overhang criteria and orientation. The support material used was SUP706, a soluble acrylic wax, which was later removed with a water jet. A cleaning tank with a sodium hydroxide solution was not used as it was found to warp thin walls and delicate edges. Layer thickness was confirmed to be 16 microns through scanning electron microscopy measurements of specimen cross sections (see Appendix 4.6.1).

Tension and compression tests were carried out on the elastomers to determine their quasi-static response for hyperelastic modelling and to assess their strain rate sensitivity. Stress relaxation tests and DMA were conducted to assist in understanding and modelling of the time- and temperature-dependent mechanical behaviour of the elastomers.

#### *4.2.1.1 Tension*

Tension samples were dumb-bell pieces (Figure 23) with a narrow section (33 mm length; 6.2 mm width; 2 mm thickness) as per BS ISO 37:2017 Type 1 [187]. At least three specimens were tested for each orthogonal print direction and respective strain rate to ensure results showed good repeatability. Sample gauge sections were then marked for strain measurements for the assistance of image tracking.

An electromechanical Instron Universal Testing System (Instron 5543, Instron) with a 1kN load cell was used for uniaxial tension and compression tests on pristine samples. Pneumatic side-action grips were used for the tension tests to allow for a consistent pressure distribution on the ends of the specimen during testing preventing specimen slippage. This is particularly important for elastomers with a large failure strain as thinning at the ends of the specimen can lead to loss of grip and eventual slipping. All samples were tested within 1 day of printing.

Five discrete strain rates spanning two orders of magnitude were achieved for both tension and compression tests. In tension, strain rates of 0.003, 0.015, 0.30, 0.15 and 0.3 /s were achieved. This provided the three-dimensional material response of stress vs. strain vs. strain rate for each of the orthogonal print directions.

#### *4.2.1.2 Compression*

Compression samples were cylindrical specimens (17.8 mm diameter; 25 mm height) as per BS ISO 7743:2017 Type B [188]. Nut-locking compression platens were used for unconfined compression tests to ensure platen translation or rotation did not occur during tests. Platen surfaces were lubricated with oil to ensure homogenous compression and minimise specimen barrelling effects. Crosshead speeds were set to achieve engineering strain rates of 0.005, 0.025, 0.05, 0.25 and 0.5 /s.

#### 4.2.1.3 Cyclic Loading

Cyclic loading tests on pristine samples with the same dimensions were carried out to assess recoverability of the elastomers and hence whether a visco-hyperelastic material model would be more suitable than a visco-plastic model at this range of strain rates. The samples were compressed to an engineering strain of 0.6, then immediately unloaded to zero extension. Reloading was then either immediately initiated or initiated after 20 seconds of idle time.

#### 4.2.1.4 Stress Relaxation

The stress relaxation tests were initiated by a constant compression rate to 0.05, 0.1 and 0.2 engineering strains, with a ramp time of 1.5 seconds, followed by a 100 second hold period. The relaxation results were later used to calibrate a Prony series used in the material model.

#### 4.2.1.5 Dynamic Mechanical Analysis

DMA samples were bar shaped (10 mm width; 2.5 mm thick; 35 mm effective gauge length; 55 mm total length) for dual-cantilever clamps on a TA Q800 DMA tester (Figure 24) as per the guidelines of TA Instruments [189]. The DMA tester was used in dual-cantilever mode for the storage modulus ($E'$), loss modulus ($E''$) and loss tangent ($\tan(\delta)$) measurements of the elastomers related by:

$$\tan(\delta) = \frac{E''}{E'} \tag{17}$$

Where $\delta$ is the phase lag between the applied strain wave ($\varepsilon(t)$) and measured stress wave ($\sigma(t)$). When the phase lag increases from an elastic state, where both waves are perfectly in phase ($\delta = 0°$), to a viscous fluid state, when both waves are perfectly out of phase ($\delta = 90°$), the loss modulus increases and storage modulus decreases [190]. Hence:

$$E' = \frac{\sigma_{peak}}{\varepsilon_{peak}}\cos(\delta) \; and \; E'' = \frac{\sigma_{peak}}{\varepsilon_{peak}}\sin(\delta) \tag{18}$$

The $\tan(\delta)$ peak determined from DMA results, which occurs when the ratio between the loss modulus and the storage modulus is highest, gave indications of the glass transition temperature ($T_g$) of the elastomers [190].

The first stage of DMA testing was initiated at 80°C wherein each sample was loaded with an oscillatory load frequency of 1Hz in the position shown in Figure 24. During this testing stage, each sample was cooled down to -80°C at a rate of -2°C/minute, thus showing how the moduli $E'$ and $E''$ changed with temperature. The second stage of DMA testing involved a frequency sweep (from 1Hz - 100Hz) at discrete temperature steps 5°C apart starting at 5°C to 20°C. The Williams-Landel-Ferry shift function was used to obtain the time-temperature superposition (TTS) master curves (Eq. (19)).

$$\log(\alpha_T) = -\frac{C_1(T - T_r)}{C_2 + (T - T_r)} \tag{19}$$

The shift factor ($\alpha_T$) is a temperature-dependent multiplier of the oscillatory test frequency at the temperature $T$ that corresponds to a 'new' equivalent frequency at the reference temperature ($T_r = 20°C$) [191]. $C_1$ and $C_2$ are material-dependent constants which we determined through a curve-fitting routine [191,192] and reported in the Results section.

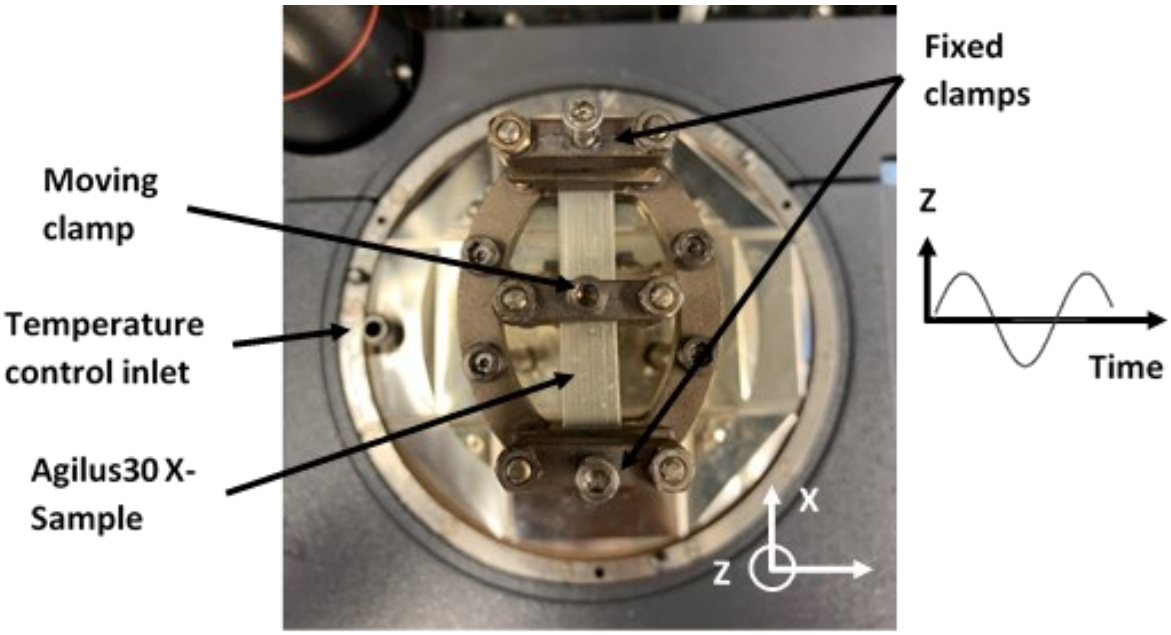


*Figure 24 - TA Q800 DMA tester setup with x-direction A30 specimen on the dual-cantilever clamp.*

### 4.2.2 Numerical Methods

#### *4.2.2.1 Hyperelasticity*

To numerically model the observed visco-hyperelastic material behaviour, isotropy was assumed to allow for characterisation using a well-established strain energy function proposed by Ogden et al. [193] (Eq. (13)). This also allows for relatively easy implementation into FE codes [194,195]. The Ogden strain energy function is given by:

$$W = \sum_{i=1}^{N} \frac{\mu_i}{\alpha_i}\left(\lambda_1^{\alpha_i} + \lambda_2^{\alpha_i} + \lambda_3^{\alpha_i} - 3\right) + \frac{K}{2}(J - 1) \tag{20}$$

where $\lambda_1$, $\lambda_2$, $\lambda_3$ are the deviatoric (volume-preserving) principal stretches, $\mu_i$ are moduli and $\alpha_i$ are non-dimensional material constants. $K$ and $J$ are the material bulk modulus and the elastic volume ratio respectively. Elastomers are often assumed incompressible ($J \cong 1$) and therefore the second term is disregarded [100,164,190,196,197]. This leads to the engineering (nominal) stress expression for uniaxial deformation ($\sigma_{11}$) where $\lambda_2 = \lambda_3 = \lambda_1^{(-1/2)}$:

$$\sigma_{11}^{H} = \frac{\partial \overline{W}}{\partial \lambda_1} = \sum_{i=1}^{N} \mu_i \left( \lambda_1^{\alpha_i - 1} + 2\lambda_1^{\frac{-\alpha_i}{2} - 1} \right) \tag{21}$$

A gradient-based optimisation algorithm in MATLAB was used to determine the constants $\mu_i$ and $\alpha_i$ by calibrating the quasi-static material model in Eq. (21) to the experimental tension-compression stress-strain response at the lowest strain rate. The X-sample mechanical responses were chosen for this characterisation. Errors arising from this choice depend on the print direction and predominant mode and rate of loading of the printed part as explored later in this paper.

#### *4.2.2.2 Visco-hyperelasticity*

A convolution integral was used to model the time-dependent behaviour of the PolyJet elastomers, which is commonly employed to describe the linear viscoelastic stress response of elastomers and biological tissue [190]:

$$\sigma^{VH}(t) = \int_0^t g(t-s) \frac{\partial \sigma_0^H}{\partial s} \partial s \tag{22}$$

Where $\sigma_0$ is the instantaneous hyperelastic stress which fades into the quasi-static stress ($\sigma_\infty$) exponentially with time ($t$) as time tends to infinity i.e. $t \to \infty, \sigma(t) \to \sigma_\infty$. Hence, $g(t-s)$ is a normalised relaxation function ($0 < g(t-s) < 1$) that is modelled here as a generalised Maxwell element expressed in terms of a Prony series of exponentials [194,198,199]:

$$\sigma^{VH} = \int_0^t \left( g_\infty + \sum_{i=1}^{n} g_i e^{-\frac{t-s}{\tau_i}} \right) \frac{\partial \sigma_0^H}{\partial s} \partial s = \underbrace{g_\infty \sigma_0}_{\sigma_\infty^H} + \int_0^t \left( \sum_{i=1}^{n} g_i e^{-\frac{t-s}{\tau_i}} \right) \frac{\partial \sigma_0^H}{\partial s} \partial s \tag{23}$$

$\tau_i$ is the characteristic relaxation time pairing with $g_i$, where $g_i$ is the normalised $i$th elastic moduli ($E_i$).:

$$g_i = \frac{E_i}{E_0} = E_i / (E_\infty + \sum_{i=1}^{n} E_i) \tag{24}$$

Where $E_0$ and $E_\infty$ are the instantaneous and quasi-static elastic moduli respectively.

Three Prony pairs ($g_i$,$\tau_i$) were approximated from the stress relaxation tests using a nonlinear least-squares fit where $1 \leq \tau_i \leq 100$ s. For smaller timescales ($\tau \leq 0.1$ s), the stress relaxation tests become less appropriate to approximate relaxation parameters due to the dynamic effects resulting from crosshead acceleration that confound the results. Therefore, Prony pairs for $\tau \leq 0.1$ s were evaluated from DMA time-temperature superposition master curves using a MATLAB code employing the Levenberg-Marquardt method (see Appendix 4.6.5) [200].

#### 4.2.2.3 Numerical Time-stepping Scheme

A closed-form for the convolution integral solution in Eq. (23) is often difficult to obtain, particularly when advanced strain energy functions with various strain histories are applied. Therefore, a method using finite time increments proposed by Taylor et al. [201] was implemented to solve the integral.

$$\sigma^{VH}(t_{n+1}) = \underbrace{\sigma_\infty^H(t_{n+1})}_{elastic\ comp.} + \underbrace{\sum_{i=1}^{n}\left(\exp\left(-\frac{\Delta t}{\tau_i}\right)h_i(t_n) + \frac{g_i\dfrac{1-\exp\left(-\frac{\Delta t}{\tau_i}\right)}{\frac{\Delta t}{\tau_i}}\left[\sigma_\infty^H(t_{n+1}) - \sigma_\infty^H(t_n)\right]}{g_\infty}\right)}_{viscoelastic\ component}$$

$$\therefore \sigma^{VH}(t_{n+1}) = \sigma_\infty^H(t_{n+1}) + \sum_{i=1}^{n} h_i(t_{n+1}) \tag{25}$$

The first term relates to the hyperelastic (time-independent) stress ($\sigma_\infty^H$) obtained from the 3-term Ogden model parameters fit to the quasi-static tests (Eq. (21)). The second term describes the summation of the viscoelastic (time-dependent) stress contribution ($\sum_{i=1}^{n} h_i$). A detailed derivation can be found in [199,202]. Using this time-stepping scheme, which we implemented in a Python code, we evaluated the stress at each interval of time at discrete strain rates and compared to the monotonic tension and compression test data to determine the accuracy of the material model predictions across a range of strain rates.

## 4.3 Results

### 4.3.1 Experimental Results

We found highly repeatable results across all tests, with small standard deviations (see Appendix 4.6.2 for tension and 4.6.4 for relaxation and DMA repeat results). Standard deviation (SD) values are reported in tables rather than on the graphical results as SD bars were too small to visualise.

#### 4.3.1.1 Tension

The tensile response followed a general S-shaped curve with an initial stiff region up to a strain of 20%, followed by a softer response (Figure 25). This behaviour was more pronounced at higher strain rates (0.3 /s), where the response became increasingly nonlinear. A rise in the stress response prior to failure was observed at higher strain rates due to chain limiting extensibility as failure strain increases.

Z- samples in both materials were softer across all strain rates below 0.3 /s, particularly at strains larger than 50% (Figure 25C,D and Table 15). For A30, Z-sample stress values at 50% strain during the 0.03 /s tests were significantly lower than X- ($t(3)=8.63$, $p<0.001$), whereas Y- samples were not

(t(3)=1.24, p=0.28). A similar observation was made for T+ (p<0.005 and p=0.12 for Z- and Y-samples respectively).

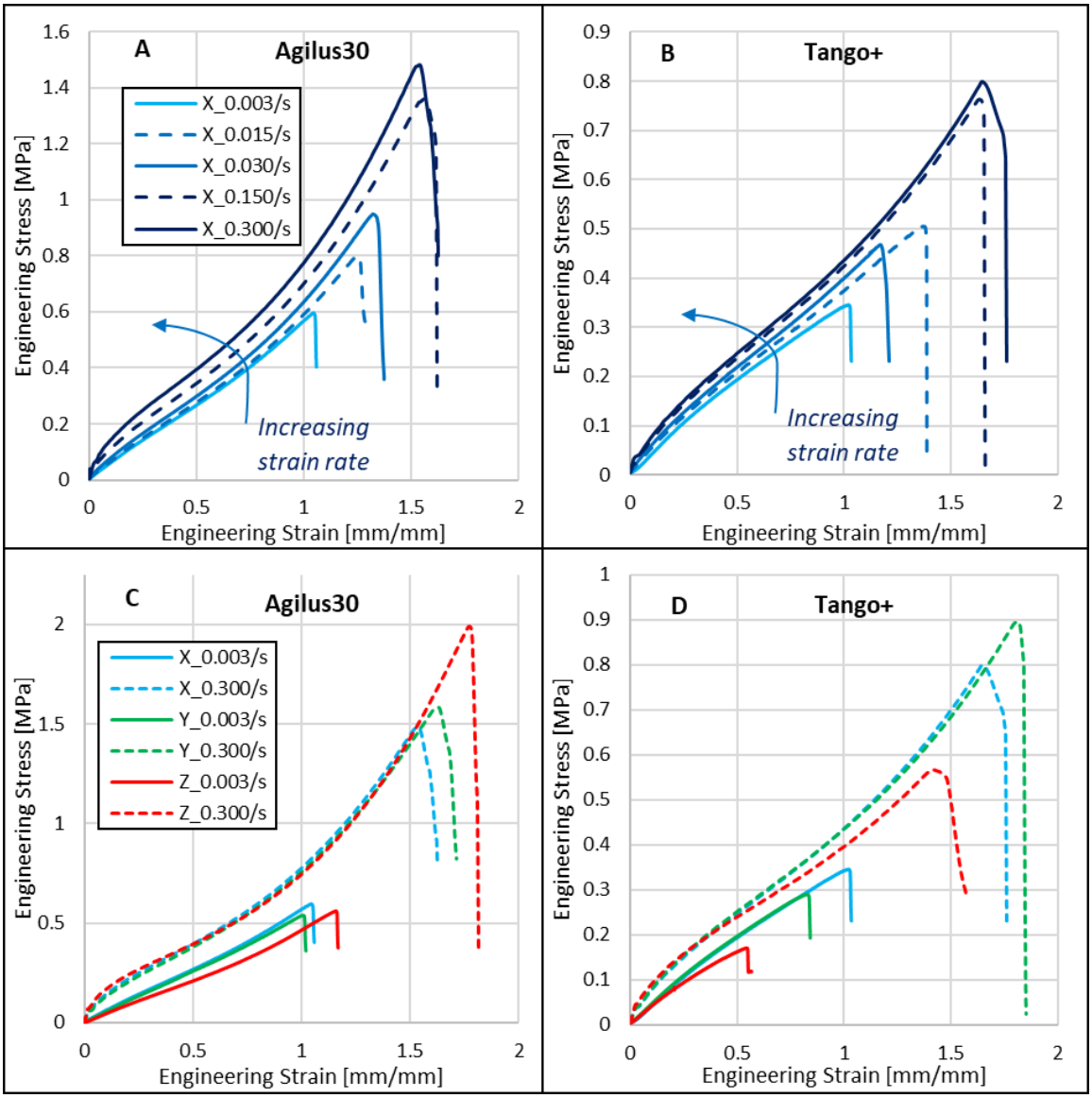


*Figure 25 - Tensile stress-strain results showing the effects of strain rate on A30 (A) and T+ (B) and the effects of build orientation on A30 (C) and T+ (D)*

Interestingly, the offset between Z- stress responses and the other two orthogonal print directions decreases with increasing strain rate, particularly for A30. This trend was observed in both materials. In fact, the response at 20% strain was marginally stiffer in Z- than X- and Y-samples at the highest strain rate (Figure 25C,D).

To better quantify the effects of print direction on stress responses, we determined the stress at 50% strain across all strain rates for both materials and compared them (Table 15). The stress at 50% strain measure was chosen as it is approximately the largest strain value experienced by both elastomers in all strain rates and orientations tested prior to any failure (Figure 26). For A30, increasing the strain

rate from 0.003 to 0.3 /s increased the tensile stress at 50% strain by 67% for X and Y-samples. This increase was almost twice as large for Z-samples, primarily due to their softer response at lower strain rates. In comparison to A30, T+ had lower strain-rate sensitivity across all loading directions.

*Table 15 - Nominal stress values at 50% tensile strain of A30 and T+ at various strain rates*

| **Stress [MPa] v. Strain rate [/s]** | **0.003 /s** | **0.015 /s** | **0.03 /s** | **0.15 /s** | **0.3 /s** | **% increase. 0.003 - 0.3 /s** |
|---|---|---|---|---|---|---|
| **A30** | | | | | | |
| **50% strain: X** | 0.174 | 0.182 | 0.202 | 0.245 | 0.291 | **67%** |
| **(±SD)** | 0.004 | 0.005 | 0.006 | 0.001 | 0.004 | |
| **Y** | 0.163 | 0.193 | 0.187 | 0.242 | 0.273 | **67%** |
| **(±SD)** | 0.011 | 0.003 | 0.016 | 0.006 | 0.002 | |
| **Z** | 0.135 | 0.149 | 0.158 | 0.226 | 0.306 | **127%** |
| **(±SD)** | 0.003 | 0.001 | 0.004 | 0.026 | 0.027 | |
| **T+** | | | | | | |
| **50% strain: X** | 0.194 | 0.208 | 0.220 | 0.241 | 0.248 | **28%** |
| **(±SD)** | 0.004 | 0.002 | 0.001 | 0.002 | 0.003 | |
| **Y** | 0.197 | 0.207 | 0.222 | 0.238 | 0.259 | **31%** |
| **(±SD)** | 0.003 | 0.002 | 0.001 | 0.006 | 0.005 | |
| **Z** | 0.164 | 0.180 | 0.192 | 0.220 | 0.241 | **47%** |
| **(±SD)** | 0.004 | 0.005 | 0.006 | 0.002 | 0.013 | |

In order to better show the effects of strain rate and build orientation on ultimate tensile stress and strain, we plotted them against each other for both A30 and T+ (Figure 26). We found that ultimate tensile stress and strain of both materials increased with strain rate. All samples were re-measured 20 minutes after testing to failure, and no residual strain was observed, indicating the material was fully elastic up to failure.

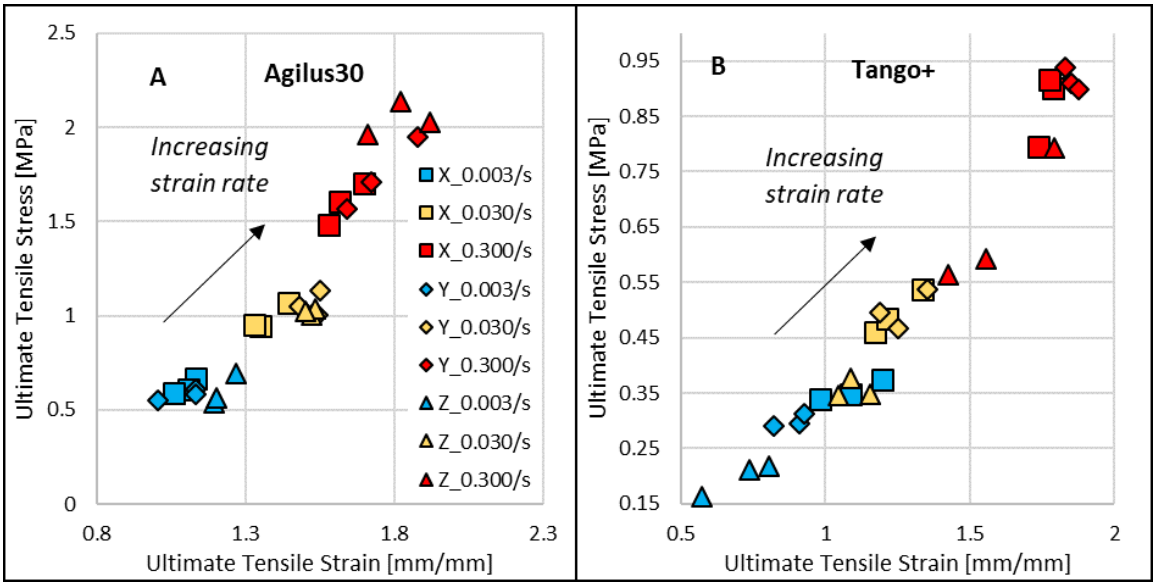


*Figure 26 – Ultimate tensile stress and strain of A30 (left) and Tango+ (right) at various strain rates*

#### 4.3.1.2 Compression

Compressive loading and unloading stress-strain paths were influenced by strain-rate in both materials (Figure 5). An initial stiffness was followed by a yield-like stress-rollover at strains of ~0.05, which was more pronounced at higher strain rates, however less so with T+ than A30 (Figure 27). The dissipated work density (DWD), defined as the area under the stress-strain curve, was larger for A30 than T+, and more influenced by strain rate in A30. We evaluated the DWD as [203,204]:

$$DWD = \int_0^{\varepsilon_{max}} \sigma_{load}\, d\varepsilon - \int_{\varepsilon_{max}}^{\varepsilon_{(0)}} \sigma_{unload}\, d\varepsilon \qquad (26)$$

Our results show that the dissipated work density with T+ increases by almost 10 folds, and nearly 17 folds for A30, when the strain rate is increased by two orders of magnitude (Table 16).

Print direction also had a significant influence on the stiffness in compression. A30 Z- samples were significantly softer than X- at 50% strain during the 0.005 /s tests ($t(3)=4.72$, $p=0.01$), whereas the difference between X- and Y- samples was less significant ($t(3)=2.57$, $p=0.06$). This difference is more pronounced at lower than at higher strain rates, particularly in A30 (Figure 27C,D). A similar observation was made in tension (Figure 25C,D) regarding the difference between Z- samples and other build orientations across strain rates.

*Table 16 - Dissipated work density (DWD) of A30 and T+ in compression at various strain rates.*

| Dissipated work density [MPa] vs. Strain rate | 0.005 /s | 0.025 /s | 0.05 /s | 0.25 /s | 0.5 /s | % increase. 0.005 - 0.5 /s |
|---|---|---|---|---|---|---|
| **A30** | | | | | | |
| **X** | 0.065 | 0.133 | 0.185 | 0.375 | 0.610 | **838%** |
| **(±SD)** | 0.001 | 0.005 | 0.001 | 0.002 | 0.003 | |
| **Y** | 0.054 | 0.114 | 0.161 | 0.359 | 0.583 | **979%** |
| **(±SD)** | 0.002 | 0.002 | 0.004 | 0.001 | 0.002 | |
| **Z** | 0.056 | 0.110 | 0.174 | 0.374 | 0.594 | **960%** |
| **(±SD)** | 0.003 | 0.001 | 0.002 | 0.002 | 0.004 | |
| **T+** | | | | | | |
| **X** | 0.019 | 0.061 | 0.087 | 0.206 | 0.288 | **1416%** |
| **(±SD)** | 0.001 | 0.004 | 0.001 | 0.003 | 0.006 | |
| **Y** | 0.015 | 0.051 | 0.085 | 0.180 | 0.261 | **1640%** |
| **(±SD)** | 0.005 | 0.002 | 0.001 | 0.003 | 0.002 | |
| **Z** | 0.016 | 0.056 | 0.079 | 0.205 | 0.272 | **1700%** |
| **(±SD)** | 0.001 | 0.004 | 0.002 | 0.002 | 0.002 | |

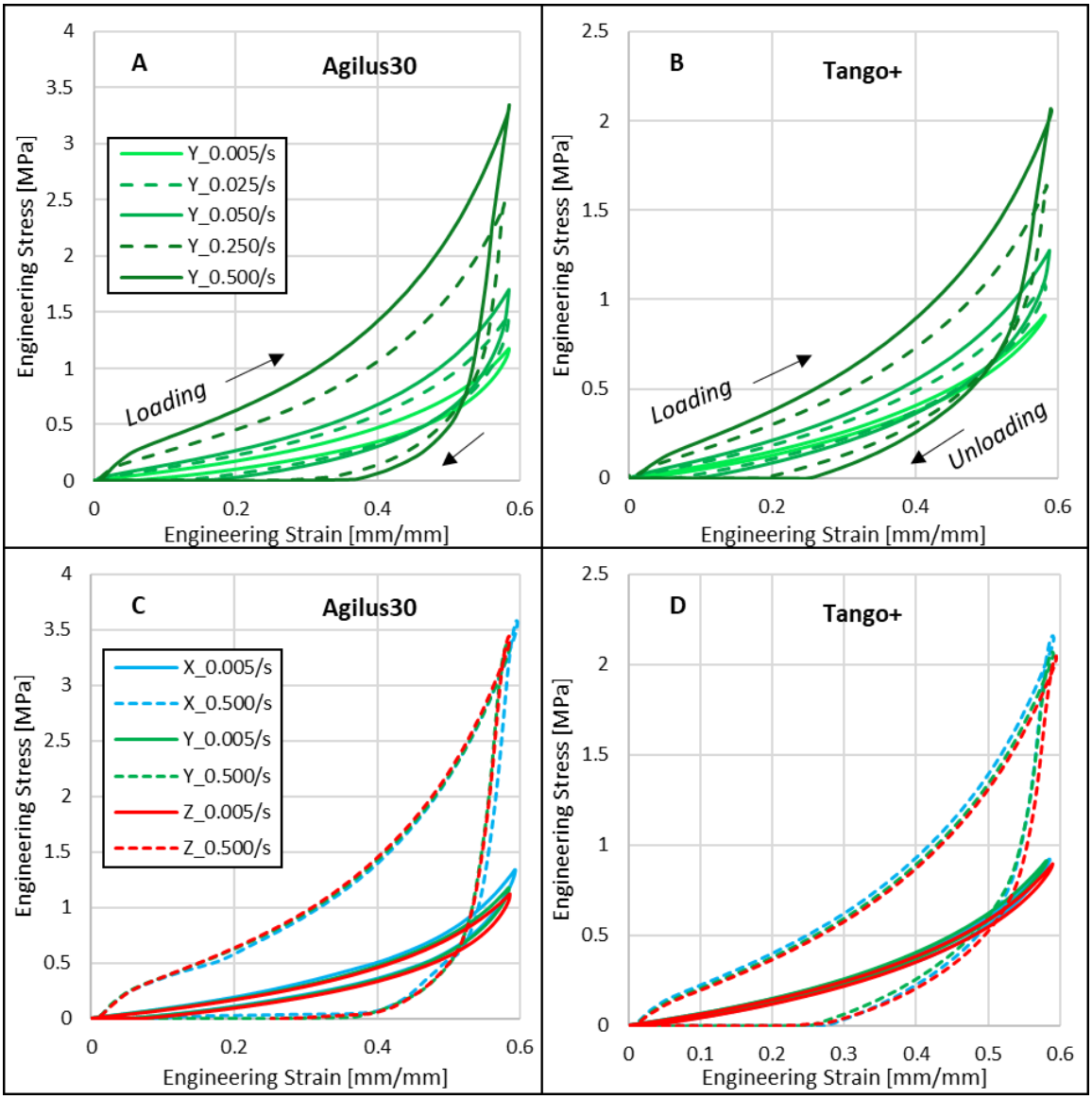


*Figure 27 - Compressive loading and unloading stress-strain results for A30 (A) and Tango+ (B) Y- samples at varying strain rates. Comparison between compressive stress-strain responses of A30 (C) and Tango+ (D) X-, Y- and Z- samples at the lowest and highest strain rates.*

#### *4.3.1.3 Cyclic Loading*

Cyclic test results did not show any permanent plastic deformation, which indicates visco-hyperelastic behaviour rather than visco-plastic (Figure 28). With immediate reloading (blue), A30 had a residual strain of 0.16 in the first cycle and 0.18 in the second cycle. In contrast, T+ samples had a residual strain of 0.09 after the first cycle and 0.1 after the second. When a 20 second idle time lapsed before reloading, both materials fully recovered to their original height, diminishing the residual strain.

Cyclic softening was observed with every subsequent loading cycle with A30, but the softening was less pronounced at lower strain rates (see Appendix 4.6.3). Notably, the unloading path of both materials was less affected by the cyclic loading and idling conditions in contrast to the loading path.

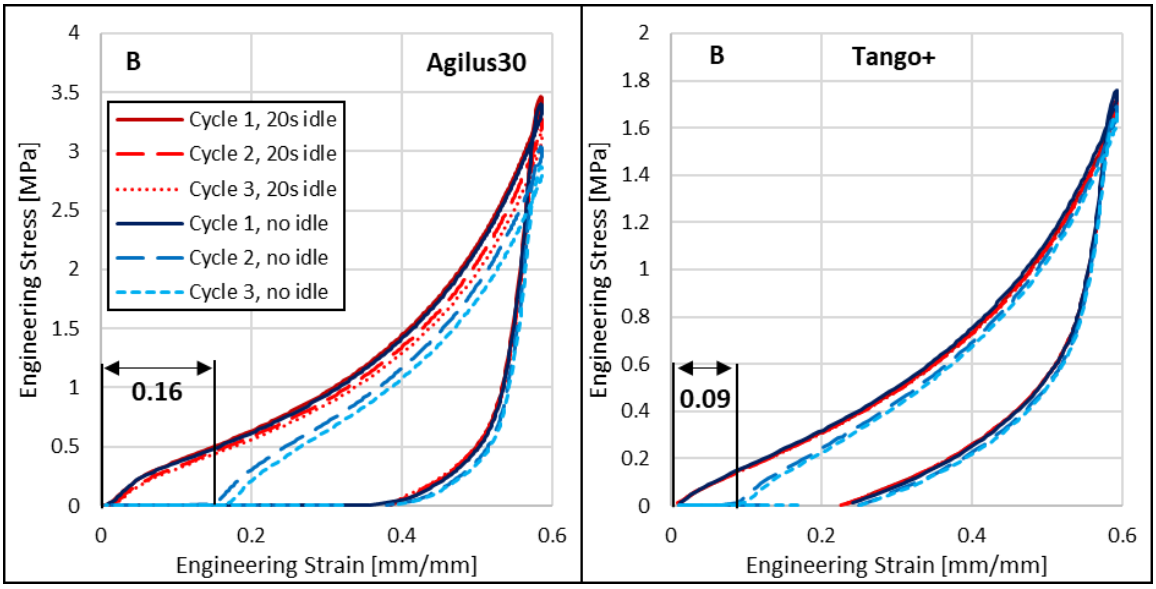


*Figure 28 - Cyclic loading of A30 and Tango+ X- samples at strain rates 0.05 /s (blue) and 0.5 /s (red).*

#### 4.3.1.4 Stress Relaxation

Stress relaxation profiles at 5% - 20% strain normalised by peak stress showed a remarkable overlap for both materials (Figure 29A). Overlapping the normalised profiles of both materials highlights the

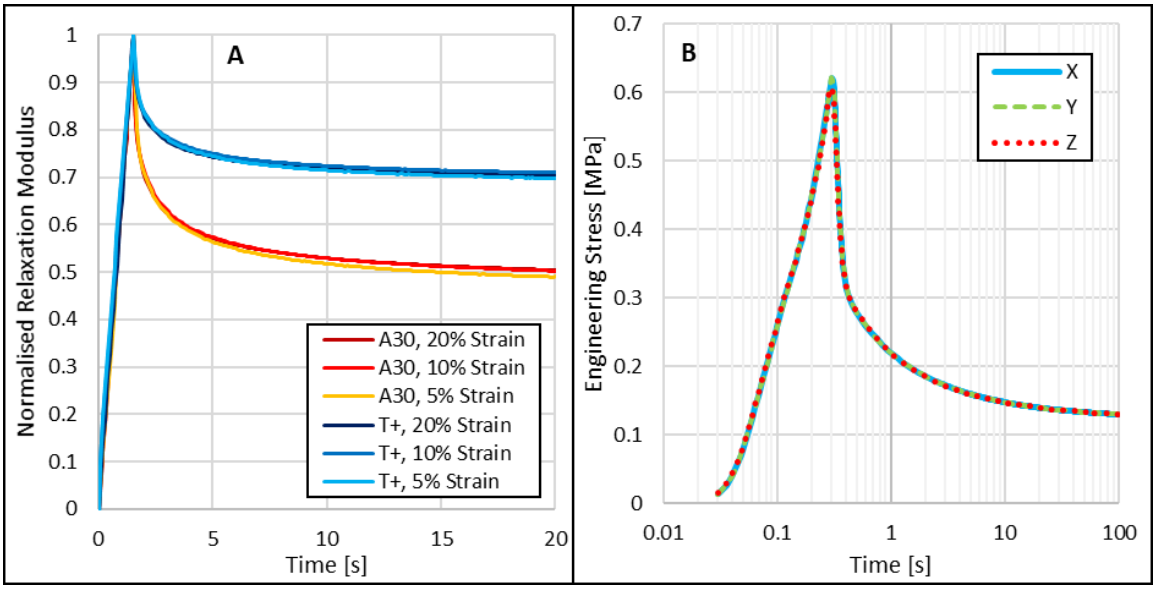


*Figure 29 – Normalised relaxation profiles for A30 and T+ samples at different strain levels (A). Stress relaxation results for X-, Y- and Z- A30 samples at 20% strain with a 0.3 s ramp time (B).*

difference between their characteristic relaxation times. A30 relaxes to more than 50% of the peak stress 20 seconds after the ramp load, whereas T+ relaxes to 70% (Figure 29A). As highlighted by the exemplar results of A30, the relaxation behaviour of both materials showed no significant relationship with build orientation (Figure 29B).

#### 4.3.1.5 Dynamic Mechanical Analysis (DMA)

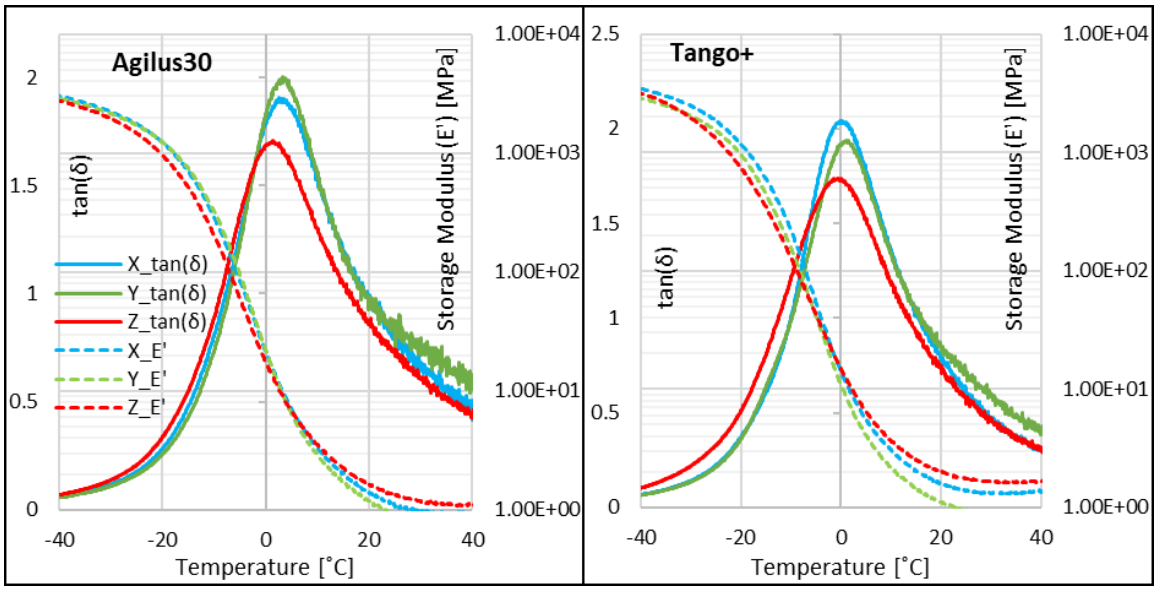


*Figure 30 - DMA loss tangent and storage modulus (E') results temperatures relevant to glass transition of A30 (left) and Tango+ (right) samples printed in different orientations.*

DMA temperature sweep and time-temperature superposition results of both materials showed similar trends in storage modulus and loss tangent (Figure 30), with a continuous decay in storage modulus and one peak in loss tangent near $\sim 0°C$. The peak in loss tangent indicates the glass transition temperature ($T_g$).

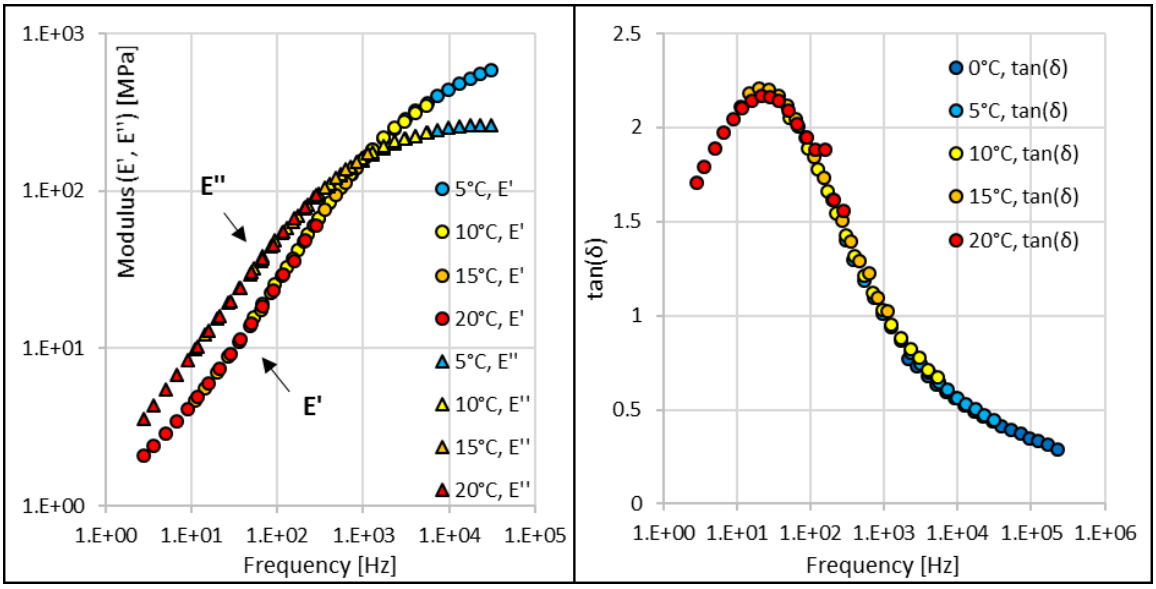


*Figure 31 - DMA TTS frequency-domain storage (E') and loss (E'') moduli (left) and loss tangent (right) master curves for A30 shifted using Williams-Landel-Ferry shift constants $C_1$=10.5, $C_2$=100.*

Z- samples for both materials had a left-shifted average $\tan(\delta)$ and $E'$ curves and lower $\tan(\delta)$ average peak values. Although these findings reinforce the discrepancies found in Z- samples reported

for other tests, the differences in Z- $T_g$ in comparison to X- were not significant (t(3)=1.55, p=0.19 for A30, t(3)=1.5, p=0.20 for T+). Similarly, the difference in $T_g$ of Y- and X- samples were not significant (t(3)=-0.31, p=0.77 for A30, t(3)=-0.5, p=0.64 for T+).

Williams-Landel-Ferry shift constants $C_1 = 10.5, C_2 = 100$ (Eq. (19)) were found to provide a remarkably good fit for $E'$, $E''$ and $\tan(\delta)$ master curves (Figure 31). $E'$ and $E''$ master curves were later used to calibrate the Prony series parameters of the numerical model for time-scales below $\tau \leq 0.1$s (see Appendix 4.6.5).

### 4.3.2 Model Predictions of Stress Relaxation Responses

The Prony series coefficients determined from the stress relaxation tests allowed us to model the relaxation response with remarkable accuracy (Figure 32). The determined Prony series coefficients for A30 and T+ are reported in Table 18. To quantify the accuracy of the numerical model, the root mean squared percentage error (RMSPE) was calculated as:

$$RMSPE = \frac{100}{n}\sum_{i=1}^{n}\sqrt{\frac{\left(y_{i(ref)} - y_{i(pred)}\right)^2}{y_{i(ref)}}} \quad (27)$$

$y_{i(ref)}$ and $y_{i(pred)}$ are the experimental and numerically predicted result points. The RMSPE for 100s stress relaxation tests was 0.5% and 3.5% for A30 and T+ respectively (Table 19).

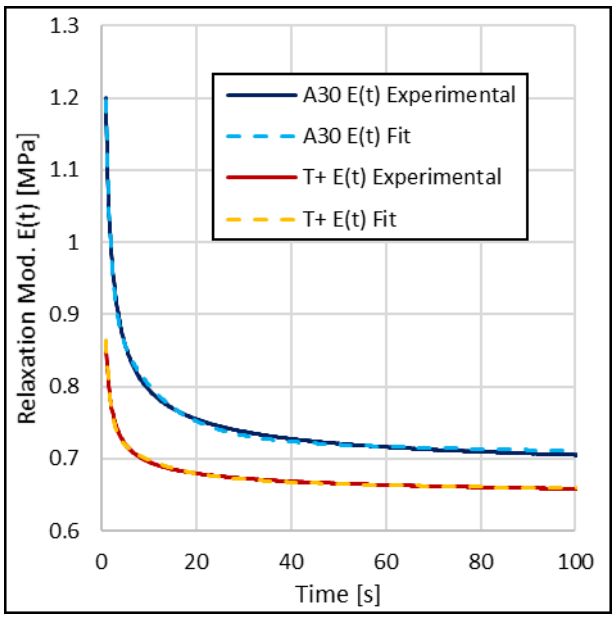


*Figure 32 – Relaxation modulus of our Prony series prediction overlaid on the experimental results of A30 and T+ from a 100s relaxation test.*

### 4.3.3 Model Predictions of Tension and Compression Responses at Different Strain Rates

The Ogden and Prony series parameters of the visco-hyperelastic model for both materials, which were determined using the quasi-static tension-compression and DMA test results, are reported in Table 17 and Table 18 respectively. These parameters were used to predict the stress-strain response of the material in tension and compression at different strain rates. The model generally predicts the response of both elastomers well across 0.003 to 0.5 /s strain rates (Figure 33).

To assess the performance of the model against other build directions, we calculated the RMSPE of the model in comparison to Y- and Z- samples at each compressive and tensile strain rate for both materials (Table 19). The error was largest in compressive loading at the highest strain rate. Our results show that RMSPE varied between 1.3% and 13% for tension and 7.8% and 16.1% for compression of X- samples across both materials (Table 19). The RMSPE is largest with Z- samples at 0.003 /s strain rate (RMSPE=29.9%) as Z- samples were significantly softer than X- and Y- samples at lower strain rates.

*Table 17 - Ogden quasi-static hyperelastic material parameters for A30 and T+.*

| | $\mu_1(\infty)$ [MPa] | $\alpha_1$ | $\mu_2(\infty)$ [MPa] | $\alpha_2$ | $\mu_3(\infty)$ [MPa] | $\alpha_3$ |
|---|---|---|---|---|---|---|
| **A30** | 0.2127 | 1.3212 | 0.0375 | 4.318 | -0.001 | -1.0248 |
| **T+** | 0.1211 | 2.4061 | 0.0209 | 2.408 | -0.001 | -1.0011 |

*Table 18 - Prony parameters for visco-hyperelastic material model for A30 and T+.*

| | | | | | | |
|---|---|---|---|---|---|---|
| **A30** | $g_i$ | 8.38E-01 | 1.26E-01 | 1.03E-02 | 3.00E-03 | 4.39E-04 |
| | $\tau_i$ [s] | 5.08E-03 | 4.97E-02 | 1.00E+00 | 1.00E+01 | 1.00E+02 |
| **T+** | $g_i$ | 7.37E-01 | 1.05E-01 | 4.67E-02 | 1.07E-02 | 3.59E-03 |
| | $\tau_i$ [s] | 9.24E-03 | 1.73E-01 | 1.00E+00 | 1.00E+01 | 1.00E+02 |

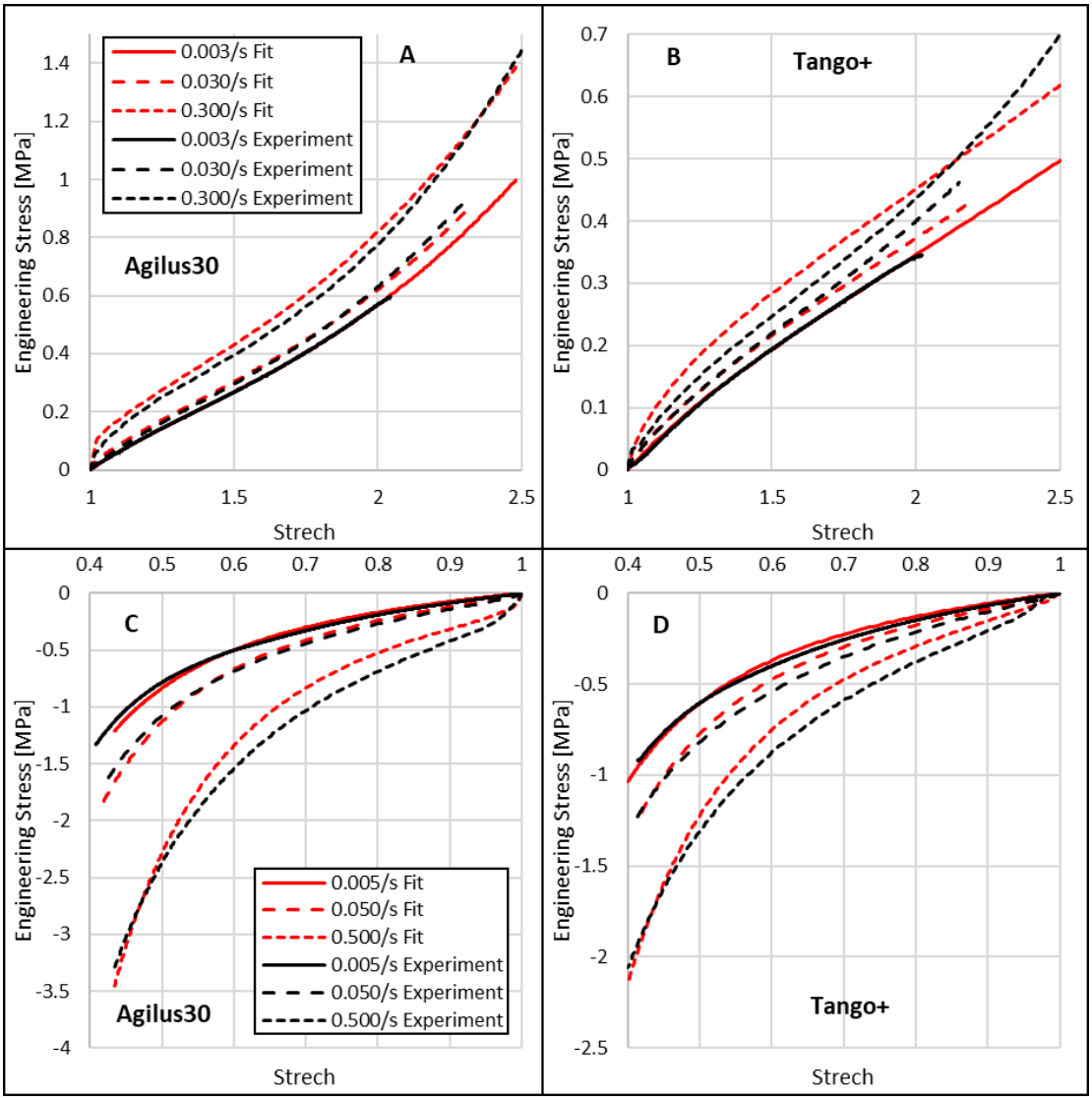


*Figure 33 - The visco-hyperelastic material model prediction vs. experiment for A30 and T+ tensile (A,B) and compressive (C,D) loading responses at various strain rates.*

*Table 19 - Root Mean Square Percentage Error (RMSPE) of the visco-hyperelastic model prediction for all tests on A30 and T+.*

| | **A30** | | | **T+** | | |
|---|---|---|---|---|---|---|
| **Tension** | **0.003 /s** | **0.03 /s** | **0.3 /s** | **0.003 /s** | **0.03 /s** | **0.3 /s** |
| X RMSPE [%] | 1.3 | 10.5 | 7.5 | 3.1 | 4.4 | 13.0 |
| Y RMSPE [%] | 6.1 | 5.6 | 13.9 | 2.7 | 4.2 | 10.3 |
| Z RMSPE [%] | 29.9 | 26.7 | 12.8 | 15.2 | 18.9 | 12.02 |
| **Compression** | **0.005 /s** | **0.05 /s** | **0.5 /s** | **0.005 /s** | **0.05 /s** | **0.5 /s** |
| X RMSPE [%] | 11.3 | 7.8 | 16.8 | 11.6 | 10.8 | 16.1 |
| Y RMSPE [%] | 9.3 | 7.4 | 13.7 | 12.6 | 12.7 | 15.9 |
| Z RMSPE [%] | 7.8 | 6.3 | 13.0 | 9.2 | 4.3 | 16.1 |

## 4.4 Discussion

We determined the mechanical response of two newly developed Polyjet elastomers, A30 and T+, across a wide range of strain and strain rates and along different build orientations. We conducted a comprehensive set of tests including uniaxial tension-compression at discrete strain rates, stress relaxation tests, DMA and cyclic loading, which allowed us to explore the mechanical responses of these digital elastomers. For the first time, we employed a visco-hyperelastic material model to accurately predict the stress-strain response of the elastomers at a range of tensile and compressive strain rates. Our comprehensive experimental data allowed us to determine the constants of this material model. The model utilises a widely used 3-term Ogden hyperelastic strain energy function alongside a 5-term Prony series to model viscoelastic effects in a manner readily compatible with major FEA codes, such as Abaqus and LS-Dyna, allowing for ease of implementation.

We found that the ultimate tensile strength of the elastomers increased with increasing strain rate. This is in agreement with previous studies which reported increased strain at failure and fracture energy at higher strain rates for older PolyJet elastomers; Tango [164,186]. This dependency may be due to entangled dynamics of polymer chains at higher strain rates, which lead to a delayed onset of failure. We noted that many of the tensile failures were near the corners of the gauge section as noted in [173], and thus ultimate tensile strength varied between repeat tests leading to SDs as high as 19.3% (T+ Z- samples, 0.3 /s). This observation is most likely due to the stress concentrations near the region arising from the pixelated approximation of curves in the printing process. Hence, ISO/ASTM sample shapes for determining tensile properties of moulded or cast rubbers may not be appropriate for testing AM rubbers, and development of new tensile sample shapes or testing methods that address the stress concentrations near pixelated edges of PolyJet elastomers may be necessary. It is noteworthy to mention that the manufacturer material data sheet stated a wide range of elongation at break (A30: 220-270%, T+: 170-220%) [205]. The lower end of these ranges are still larger for both elastomers than what we observed here. These differences may be attributed to a different specimen shape, testing strain rate and temperature, printing conditions or other variables.

We determined the loss and storage moduli across a wide range of frequencies using DMA, allowing us to characterise the relaxation modulus for a wide time span (10 µs - 100 s). Our results are in good agreement with previous work that has reported loss and capture modulus for A30 at a limited frequency range [151]. For the first time we broadened the DMA with the time-temperature superpositioning and determined Williams-Landel-Ferry shift function constants ($C_1$, $C_2$) for A30 and T+. These constants characterise the unique time-temperature dependency of the elastomers, and therefore can easily be extended to other methods such as creep tests [100,190], analogous to relaxation tests reported here.

The reported DMA results show a high glass transition temperature ($T_g$) for both materials (nearly $0°C$). The high $T_g$ may limit the suitability of these elastomers in applications where material properties are expected to remain constant with temperature change, a role currently fulfilled by commercial elastomers such as thermoplastic polyurea and polyurethane (TPU) [197,203,206–208]. Nonetheless, PolyJet elastomers have been granted attention in the domain of energy absorption, such as bio-inspired composite armour [166], due to their readiness for multi-material 3D printing. Moreover, the high $T_g$ is also why PolyJet elastomers have dominated applications in 4D printing and active composites utilising thermomechanical programming processes [151,156,160].

The mechanical responses of both A30 and T+ were highly nonlinear and time-dependent across the range of strain rates. The nonlinear and rate dependent behaviour observed in both materials is common of amorphous polymers and may be attributed to molecular chain dynamics [100,209]. Conventional co-polymers such as TPU also show similar trends in stress-strain profiles with increasing strain rate. In addition, we observed an initial high stiffness at higher strain rates, followed by a pronounced yield-like stress-rollover at small strains (~0.05). Similar observations about TPU have been reported previously, which have been attributed to the interplay between 'hard' and 'soft' molecular domains within the polymer network [203,209].

Our relaxation tests assisted in determining the Prony series coefficients, and hence our visco-hyperelastic material model can predict the time-dependent behaviour of both materials with reasonably good fidelity. Previous methods used the stress-strain responses of uniaxial tensile tests at discrete strain rates to calibrate the Prony series coefficients instead of directly calibrating to relaxation tests [164,210]. However, such methods do not guarantee an accurate prediction of the relaxation profiles of the materials as illustrated in Figure 34, regardless of the capability of a model to predict the uniaxial response at discrete strain rates. Hence, we accompany the discrete strain rate tests with stress relaxation tests to determine the material model coefficients, which in turn provides a realistic representation of both uniaxial and relaxation test responses.

The basis of the convolution integral that we used for numerical modelling is the assumption of separable time- and strain-dependent material behaviour. This assumption is widely accepted for many viscoelastic materials including cheese and bread dough [199,211]. We accepted this assumption based on the remarkable overlap of the stress relaxation profiles at varying strain levels (Figure 29). This observation shows that the relaxation response of the PolyJet materials is independent of the applied strain, and hence the assumption of separable time- and strain-dependent behaviour is plausible.

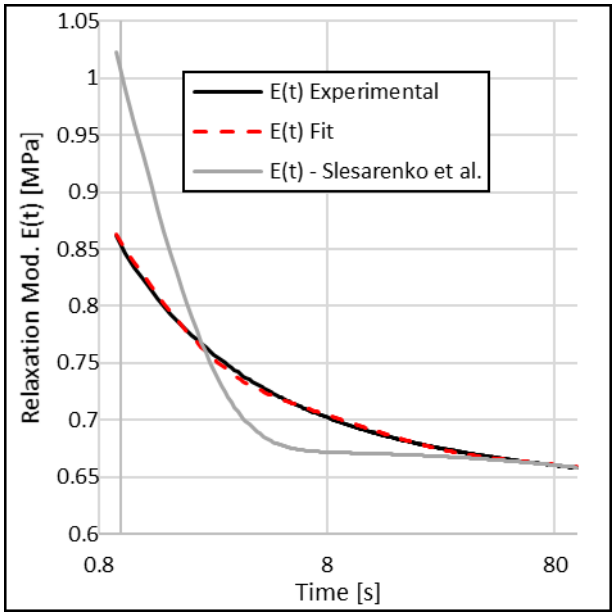


*Figure 34 – Comparison between the relaxation test results and our Prony series prediction and that reported in* [164].

The Ogden hyperelastic model was chosen to characterise the quasi-static response of A30 and T+. This model is well established and utilises a few parameters, and it accurately predicted the hyperelasticity of both elastomers. However, the Ogden hyperelastic function is isotropic. Hence, isotropy was assumed for numerical modelling and therefore was fit to X- sample data as incorporating an anisotropic visco-hyperelastic model would significantly complicate the model and lead to difficulty in application. Nonetheless, the model was still able to predict the response of both materials in Y- and Z- build direction with good accuracy apart from Z- samples at 0.003 /s strain rate where Z- samples were significantly softer. This observation was expected as we previously noted that Z- were significantly softer than X- samples which were used for numerical modelling. Interestingly, the RMSPE of Y- and Z- samples is even lower than X- in compressive loading at 0.3 /s strain rates as anisotropy diminished at higher strain rates. As mentioned, the importance of anisotropy is application specific as it depends on the strain, strain rate and loading mode. Slender load bearing members are typically not recommended to have their primary loading directions along the Z- print axis as printing strength diminishes and build time significantly increases with Z- height and in most AM methods. Nonetheless, the prediction errors were reasonable, indicating that this model will perform reliably when employed e.g. in FEA simulations of large strain problems within the range of strain rates explored here.

Our experimental results on the effect of build orientation on anisotropy of T+ and A30 PolyJet elastomers at large strains with varying strain rates adds to the existing knowledge on anisotropy of PolyJet parts. As anisotropy is often regarded as a limiting factor for the performance and reliability of AM materials and methods, it has attracted much research, however less so for the PolyJet elastomers explored here, in contrast to plastics. Our findings on anisotropy are in line with previous

reports on PolyJet plastics suggesting that Z- specimens had the poorest mechanical properties [177,179–181]. However, we conclude that anisotropy of PolyJet elastomers is sensitive to strain rate as our reported differences in mechanical response due to anisotropy are highest at quasi-static strain rates (below 0.005 /s), and diminished at higher strain rates (above 0.3 /s) as the responses of all three orthogonal print directions converged.

In future, even higher strain rates (10 /s - 1000 /s) relevant to shock absorption and vibrational damping may be explored and may further manifest or diminish the discrepancies due to anisotropy reported here. Moreover, biaxial testing of anisotropic hyperelastic materials such as the explored 3D-printed elastomers is invaluable in providing true and complete characterisation of the mechanical properties, particularly for applications involving pressured walls such as bellow actuators.

Our findings will allow for the development of more accurate computational models of the PolyJet elastomers, which can be utilised in computer-aided designs of novel applications requiring flexible or rate-sensitive 3D-printed materials. Although PolyJet technology is fast and capable of printing multiple materials in a single build, it can also be quite expensive. This is particularly true when parts are iteratively prototyped and printed many times before a final design satisfies requirements. High-fidelity FEA on computational models can reduce printing costs and shorten time to market by reducing the number of physical iterations. One major limitation of this method is the fidelity of available AM material data, particularly of time-dependent elastomers at large strains. The material model and properties presented here can facilitate the development of high-fidelity finite element models of A30 and T+ elastomers and provide a basis for similar developments for current and future AM elastomers.

It is noteworthy to mention that one of the largest and most apparent limitations of this work is the strain rates explored do not span into the dynamic range i.e. 10-100/s which would typically be seen during impacts such as those in helmet foams during an accident.

## 4.5 Conclusion

In this paper, we characterise the latest and most widely employed PolyJet elastomers, A30 and T+, under a range of loading conditions and strain rates (0.003 /s - 0.5 /s) printed in different orientations relative to the print bed plane. Moreover, we present a visco-hyperelastic model that accurately captures the time-dependent response of the PolyJet materials. Our visco-hyperelastic material model was calibrated to relaxation spectra from stress relaxation and DMA tests and was able to capture the time-dependent response of both elastomers. We found the mechanical response of both elastomers to be highly nonlinear and highly dependent on strain rate and build orientation. Both elastomers had a glass transition temperature ($T_g \sim 0°C$). However, the tensile stress at 50% strain of A30 was larger

than T+ and increased by 67% across two orders of magnitude of strain rate for X- and Y- samples, and by more than 127% for Z- samples. These magnitudes were smaller for T+, highlighting a lesser strain rate sensitivity. Nonetheless, a similar trend in tension was observed between build orientation and strain rates. Interestingly, anisotropy due to build orientation diminished at higher strain rates (0.3-0.5 /s). The presented visco-hyperelastic material model accurately predicted the relaxation and monotonic tension-compression responses of both PolyJet elastomers with an error between 1.3% and 16.8% for X- and Y- samples and between 4.3% and 29.9% for Z- samples depending on strain rate. In the next chapter, we aim to validate this material model at higher strain rates more relevant to the impact conditions typically experienced in a helmet crash and utilise it to explore the impact performance of several designs that could potentially replace foam liners via a design of experiments.

## 4.6 Appendix

### 4.6.1 Images

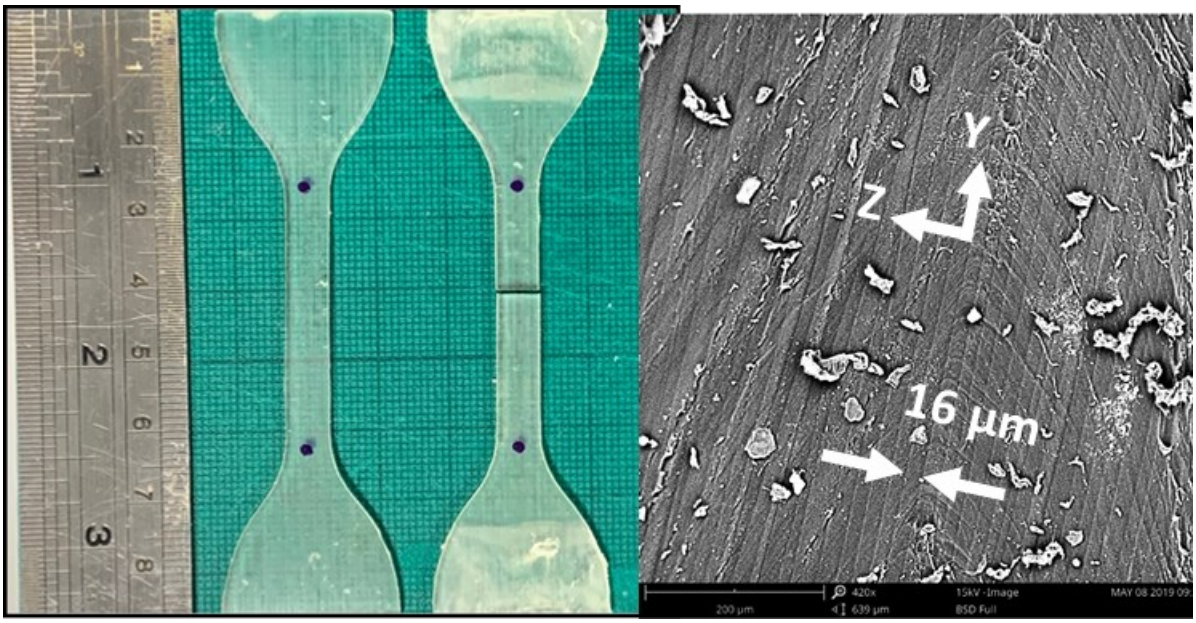


*Figure 35 - comparison between pristine and failed A30 tensile specimen showing no residual plastic strain (left). Scanning electron microscope image along the Y-Z plane showing 16 micrometre layer thickness (right).*

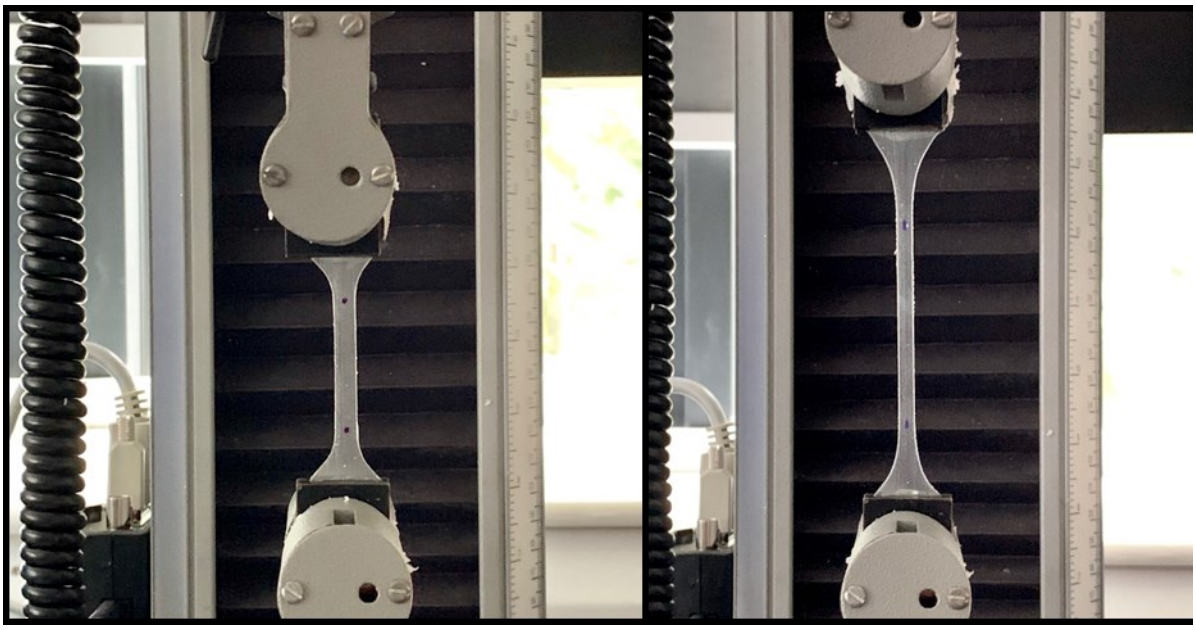

*Figure 36 - A30 X- sample during tensile testing at 0.03 /s at the start of testing (left) and at 56% strain (right).*

### 4.6.2 Tension

*Table 20 - Stress values of A30 and T+ X- samples at 50% strain in compression and comparative decrease between max. and min. strain rates relative to tension. *Tension values have been reported in Table 15.*

| Stress [MPa] v. Strain rate [/s] at 50% Strain | 0.005 /s | 0.05 /s | 0.5 /s | N times larger across the two orders of magnitude of strain rate |
|---|---|---|---|---|
| A30 | | | | |
| Compression | 0.787 | 1.161 | 2.179 | 2.77 |
| (±SD) | 0.020 | 0.002 | 0.003 | |
| Tension | * | * | * | 1.67 |
| T+ | | | | |
| Compression | 0.604 | 0.828 | 1.399 | 2.32 |
| (±SD) | 0.020 | 0.004 | 0.004 | |
| Tension | * | * | * | 1.28 |

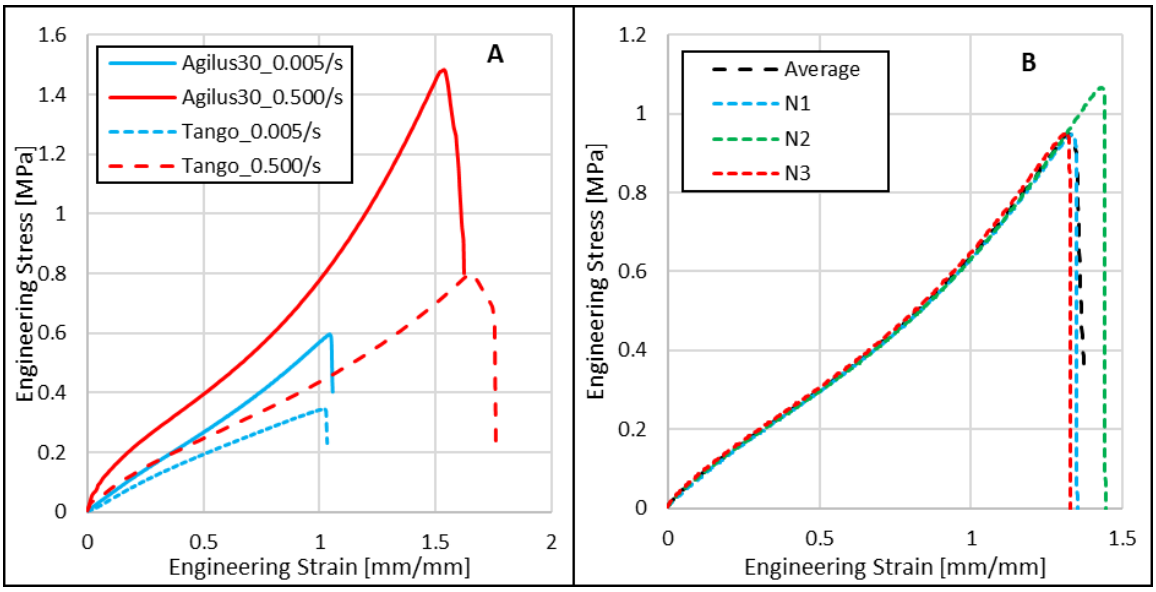


*Figure 37 – (A) Comparison between A30 and Tango+ tensile responses at the lowest and highest tested strain rates and (B) exemplar set of results (A30, 0.05 /s strain rate) showing the repeatability achieved in tests.*

### 4.6.3 Compression

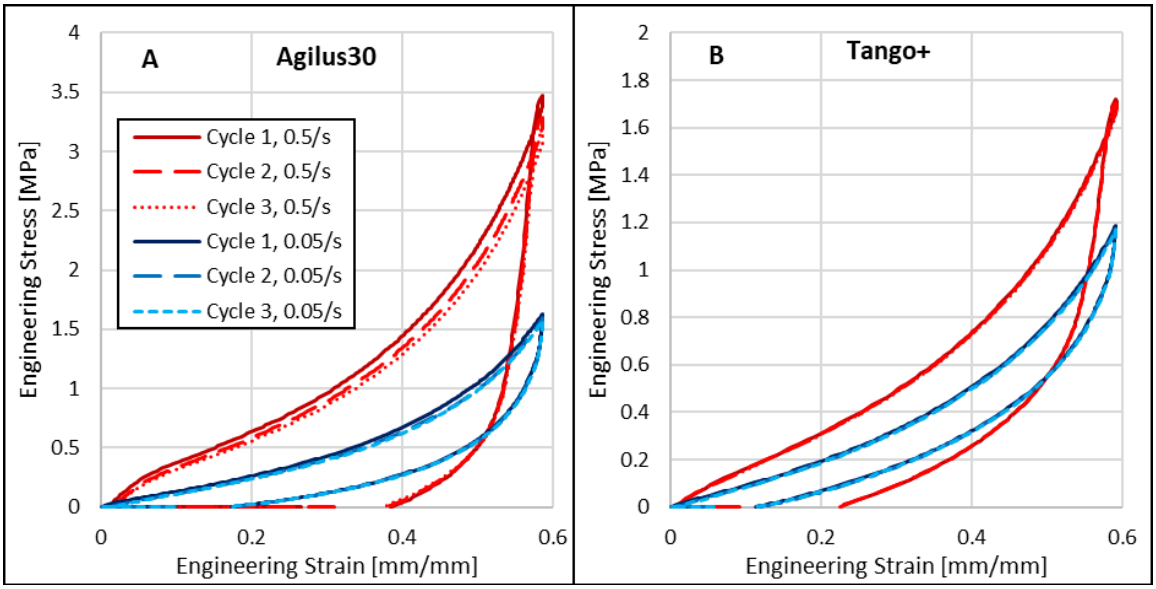


*Figure 38 - Cyclic loading stress-strain curves of A30 (A) and Tango+ (B) Z- samples at a strain rate of 0.5 /s with no idling between cycles (blue) and a 20 second idle (red).*

### 4.6.4 Stress Relaxation and DMA

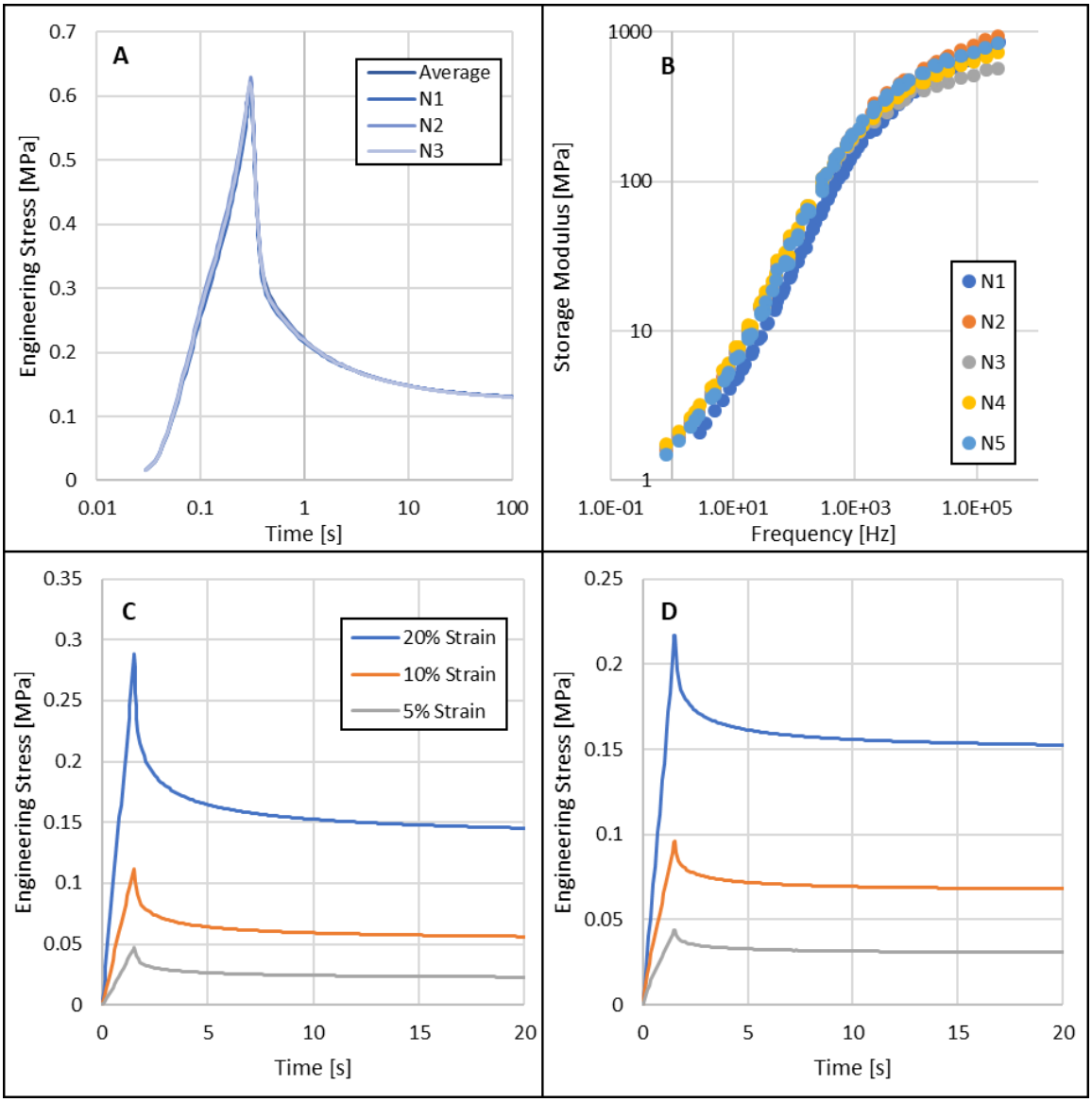


*Figure 39 - Repeats of A30 relaxation tests (A) and DMA TTS results (B). Stress relaxation of A30 (C) and T+ (D) at different strain levels.*

### 4.6.5 Determining Prony Series Constants from DMA Results

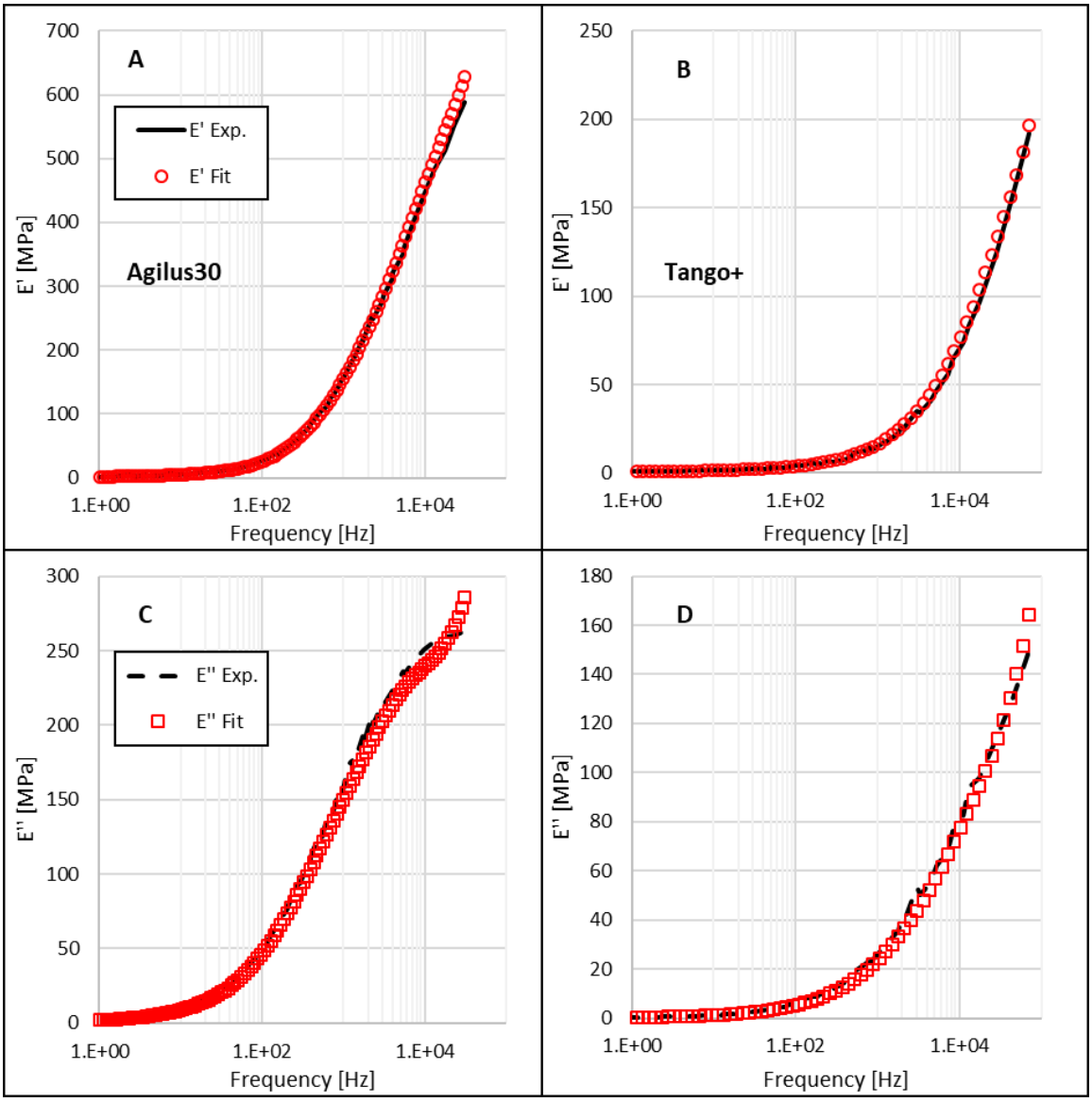


*Figure 40 - Experimental vs. numerical approximation of E' and E'' master curves. The Prony series parameters obtained from this approximation were normalised by the instantaneous modulus obtained using Equation (28)-(29).*

The methods to approximate the Prony series coefficients ($g_i$, $\tau_i$) from relaxation spectra ($E'$, $E''$) have been outlined in detail in several studies [194,200,212]. However, for the sake of completeness, the equations used for the approximation in the MATLAB code are included here.

$$E'(\omega) = E_\infty + \sum_{i=1}^{n} \frac{\tau_i^2 \omega^2 g_i}{\tau_i^2 \omega^2 + 1} \tag{28}$$

$$E''(\omega) = \sum_{i=1}^{n} \frac{\tau_i^2 \omega^2 g_i}{\tau_i^2 \omega^2 + 1} \tag{29}$$

Where:

$E'$, $E''$ are storage and loss moduli respectively.

$\omega$ is the oscillatory frequency of the DMA tester.

$\tau_i$ is the $i$th characteristic relaxation time of the material

$g_i$ is the $i$th normalised modulus of the material

The Levenberg-Marquardt method is used to obtain the fit presented in Figure 40, which resulted in 6 Prony pairs for each material spanning at least 6 orders of magnitude. As there was 1 Prony pair per time decade on average, only two Prony pairs from the DMA tests were used corresponding to 1 μs $\leq \tau \leq$ 0.1 s, as highlighted in Table 21. Pairs with larger characteristic times are more accurately predicted using relaxation tests, and smaller characteristic times were found to have no effect on the response within the window of strain rates explored here and, in any case, would increase computational effort.

*Table 21 - Prony pairs for A30 and T+ obtained from DMA time-temperature superposition tests.*

| **A30** | | **T+** | |
|---|---|---|---|
| **$g_i$** | **$\tau_i$ [s]** | **$g_i$** | **$\tau_i$ [s]** |
| 1.11E+03 | 6.68E-06 | 7.32E+02 | 2.93E-06 |
| 3.29E+02 | 1.51E-04 | 1.18E+02 | 6.87E-05 |
| 1.68E+02 | 1.01E-03 | 2.96E+01 | 6.71E-04 |
| **5.69E+01** | **5.08E-03** | **4.95E+00** | **9.24E-03** |
| **8.57E+00** | **4.97E-02** | **7.09E-01** | **1.73E-01** |
| 1.88E+00 | 6.44E-01 | 8.49E-01 | 5.89E+00 |

# 5 Chapter Five: A New Class of Recoverable Circular Cell Arrays for Controlling Shear and Compressive Responses During Oblique Impacts

Cellular structures such as honeycombs are often required to manage impact loads. Although they have been extensively studied under axial loading, a key question remains largely unaddressed: How may their shear and axial responses be independently tailored for oblique impacts? This question is especially important to answer prior to testing the hypotheses of the next chapter, such as whether lowering helmet liner shear stiffness reduces peak head rotational acceleration. For the first time, we test whether incorporating axisymmetric shape changes in viscoelastic circular honeycomb cells enable independent control over their shear and axial stress-strain responses during oblique impacts. We perform a full-factorial computational design-of-experiments, varying the cell shape from concave to convex and impact velocities from 2.5 to 7.5 m/s. The finite element models demonstrate remarkable agreement with experimental drop tower impacts on additively manufactured viscoelastic specimens. Our results show convex and concave cells demonstrate similar axial stresses. However, concaving straight cylindrical cell walls increases their post-buckling shear stress by over 300% during oblique impacts. In addition, increasing the impact velocity increases both axial and shear stresses by 211%. Our results show that this new class of recoverable honeycombs provides compelling control over its shear response under oblique impacts. Owing to the simplicity of the design intervention, it may be exploited in future to morph the cells during use via various actuation methods for real-time performance adjustment in, e.g., shoes and helmets.

*Keywords*: Cellular structures; honeycomb; oblique impact; energy absorption; viscoelastic

## 5.1 Introduction

There is an ever-growing demand for lightweight, architected structures with tailorable anisotropy and kinetic energy-dissipating properties that satisfy various design constraints. For example, high energy dissipation with low transverse shear stiffness is often desired in the design of helmets for minimal head rotation [128,213], or seismic isolation in earthquake-resistant buildings [214]. In other applications, such as in soles of running shoes, low axial stiffness for cushioning with adequately high shear stiffness is sought to prevent slip [215,216].

Inspired by nature in attempts to fulfil such a variety of design requirements, the ingenuity of engineers has led to a rapidly growing family of engineered cellular solids with a myriad of topologies. Amongst the most popular are hexagonally packed cellular structures, loosely referred to as

honeycombs for resembling bee honeycombs [217], but can also be found in several naturally-occurring materials such as in the microstructure of wood [218].

From a mechanical standpoint, honeycombs have found applications where high energy dissipation per unit mass at a minimal peak force is required, such as in aerospace and automotive. Their applicability is owed to their capacity to sustain large strains at near-constant stresses. The influence of cell wall thickness, size and in-plane cross-sectional shape of honeycombs has been well studied in uniaxial loading conditions, and have shown to significantly alter the response or lead to interesting auxeticity [219,220], negative stiffness [221] and non-affine behaviour [222]. Fractal-like honeycomb cell geometries have also been studied, concluding that the average axial crushing force increases with fractal dimension [223]. More recent studies have shown that introducing folds to the cell walls enables tailoring of the stress-strain response under axial loads [224,225], catering for a large uniaxial out-of-plane performance range with simple changes to the cellular topology.

However, much of this research has focused on tailoring the axial loading performance, whereas most scenarios cellular structures aim to protect against are less idealistic and involve impacts at an angle – i.e. an oblique impact. This in turn induces a complex combination of both shear and axial forces concurrently within the material, which need to be managed differently for impact management. How the topology of a cellular structure such as a circular honeycomb may be simply adjusted for tuneable stiffness in axial and shear responses, which are typical during oblique impacts, is not trivial. We aim to begin addressing this open question in this chapter.

Limited research exists on the combined shear-compressive behaviour of cellular structures typical during oblique impacts. Gilchrist et al. [226,227] have studied the response of expanded polystyrene (EPS) foam under this multiaxial load case, and found that the compressive yield stress decreases in oblique loading in comparison with purely compressive loading. Quasi-static and dynamic responses of metallic hexagonal honeycombs in combined shear-compressive loads have also been studied [228–233], with conclusions that compression occurs via successive folds in the cell wall, and shearing occurs with cell rotation. Fang et al. [234] investigated how the number of cells in multi-cell tubes affects their response in oblique loads, and concluded that increasing the number of cells increases both peak force and energy absorption. However, none of the previous studies have demonstrated a simple design change for tailoring shear and compressive responses of these cellular structures.

In this study, we explore how the shape of hexagonally packed circular cells, hereon referred to as circular honeycombs, affects their performance under both axial and oblique loading. The shapes are realised by applying arc curvatures to the cell walls, forming concave and convex cells simply by

changing the curvature direction. We explore a wide range of curvature amplitudes and investigate, for the first time, the influence of cell shape on the mechanical responses during oblique impact.

While most studies focus on single-use conventional honeycombs made of metals and hard polymers, we employ elastomeric cells which exhibit viscoelasticity (i.e. high rate-dependency and recoverability) where repeated loading is required. Finite element modelling (FE) of viscoelastic materials is not trivial and requires extensive testing. Hence, high fidelity FE models of the additively manufactured viscoelastic cells were developed using new materials properties. Experimental impact tests on the bulk material were used to validate the material model which builds on from previous work [20]. Further experimental impact tests on air-filled concave and convex hexagonally packed cell arrays arranged are used to validate our computational model which we then use for a full-factorial design of experiments (DoE). As elastomeric materials have a high capacity for rate-dependence, we assess how different shapes are affected by the rate of loading at impact speeds ranging from 2.5 – 7.5 m/s.

## 5.2 Materials and Methods

### 5.2.1 Experimental Methods

#### *5.2.1.1 Manufacturing Test Specimens*

A PolyJet multi-material 3D-printer (Connex3, Objet500, Stratasys, USA) was used to print all elastomeric specimens used for the experimentation. The elastomer 'Agilus30' (A30) (Stratasys, USA) was employed as the parent material of the cell arrays in this study as it has demonstrated large tensile strain-to-failure (+150%) and toughness as well as considerable strain rate sensitivity [20]. These characteristics are desirable to protect against a wide range of impact speeds. Solid cylindrical A30 specimens and a single convex cell were printed for an initial validation of the FEA model which showed remarkable agreement with the experimental results (see Appendix 5.6.2). Thereon, arrays of 7 hexagonally packed concave and convex cells with 2mm thick walls were printed for further validation of the FEA model (Figure 41).

#### *5.2.1.2 Oblique Impact Drop Tower Cell Array Impact Tests*

A bespoke drop tower was built which can measure both axial and shear forces experienced by the cellular arrays due to a 5kg block mass impacting the top flat face both axially and at oblique angles at speeds up to 5.6 m/s. For the validations in this paper, both axial ($0^o$) and oblique ($45^o$) impact angles at 5.6 m/s were explored on both concave and convex hexagonally packed cell arrays (Figure 41).

The drop tower, primarily constructed from extruded 45x45 mm aluminium profiles, consisted of a vertical smooth rail which tracks the magnet and carriage assembly (Figure 41). For each test, the

magnet assembly would be lowered via an electrical hoist to the mating plate on the carriage assembly which carries the 5kg mass. Both the magnet and carriage assembly would then be raised to the height that would result in the required final free-fall velocity prior to impact. The magnet would then be energised to release the carriage assembly to fall. As it falls along the rail, it interrupts an optical switch which triggers the data acquisition system and high-speed camera synchronously before the 5kg mass impacts the specimens. Impacts at angle were achievable by varying the angle of the steel swivel table on the base of the tower and the dial mounted to the carriage assembly equally.

Each cell array was printed with a hard plastic base (VeroClear) to which it was fused by the nature of the printing process. This base was designed with countersink holes to fit four M8 screws and T-nuts which fixed the arrays to the swivel table via the T-slot rails running along the swivel tabletop.

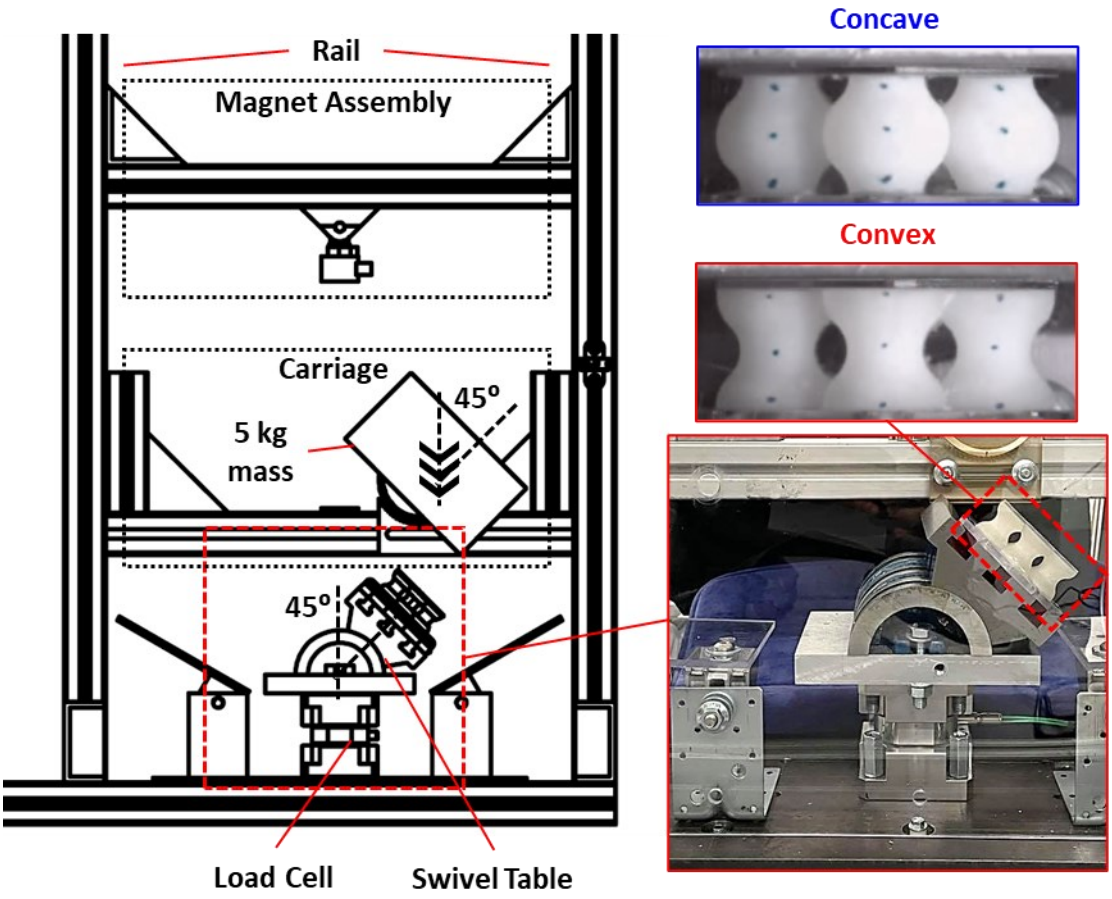


*Figure 41 – Schematic of the custom-built drop tower for experimental impact testing under axial and oblique impact conditions.*

For each test, the axial (Z) and shear (Y) forces were measured by the loadcell which would then be filtered using a low-pass filter at a cut off frequency of 2000 Hz and transformed to the local co-ordinate system of the cell arrays. High speed footage was captured and used for motion analysis and validation of the impact speed. This procedure would then be repeated 5 times to ensure repeatability.

The fidelity of the FEA model was assessed by means of the CORrelation and Analysis (CORA) scoring method. The CORA implementation was based on Gehre et al. [235] and the settings suggested in Giordano and Kleiven [236] commonly used for crash tests were adopted.

### 5.2.2 Visco-hyperelastic Material Model and Properties

Finite element (FE) modelling was used to explore a wide design space. The accuracy of the FE model depends on the fidelity of the material model and accuracy of the material properties to represent the nonlinear rate-dependent behaviour of the elastomeric material. In Chapter 4, we characterised the large-strain visco-hyperelastic response of Agilus30 with good accuracy in both tension and compression for low strain rates (0.003 /s – 0.5 /s). Here, we further develop and validate this material model for strain rates up to 200 /s, which were expected in our experiments due to the high impact speeds. Hence, we briefly outline how the model was extended on for this work. It should be noted that the equations outlined below in Section 5.2.2.1 to 5.2.2.3 largely repeat those in Section 4.2.2, yet are included here for completeness and ease of reference.

#### *5.2.2.1 Hyperelasticity*

The Ogden strain energy function $\bar{W}$ was employed to numerically model the observed visco-hyperelastic material behaviour assuming incompressibility (Eq. (30)) [20,193]. This follows the implementation of MAT_77 in LS-DYNA employed for the forthcoming FEA.

$$\bar{W} = \sum_{i=1}^{N} \frac{\mu_i}{\alpha_i}\left(\lambda_1^{\alpha_i} + \lambda_2^{\alpha_i} + \lambda_3^{\alpha_i} - 3\right), \tag{30}$$

$$2\mu = \sum_{i=0}^{N} \mu_i \alpha_i \tag{31}$$

where $\lambda_1$, $\lambda_2$, $\lambda_3$ are the deviatoric (volume-preserving) principal stretches, $\mu_i$ are shear moduli and $\alpha_i$ are material specific constants. From Eq. (30), the engineering (nominal) stress expression for uniaxial deformation ($\sigma_{11}$) may be derived, where $\lambda_2 = \lambda_3 = \lambda_1^{(-1/2)}$:

$$\sigma_{11}^{H} = \frac{\partial \bar{W}}{\partial \lambda_1} = \sum_{i=1}^{N} \mu_i \left(\lambda_1^{\alpha_i - 1} - \lambda_1^{\frac{-\alpha_i}{2} - 1}\right). \tag{32}$$

The trust-region-reflective algorithm in MATLAB was used to determine the constants $\mu_i$ and $\alpha_i$, summarised in Table 22, as detailed in [20].

#### *5.2.2.2 Visco-hyperelasticity*

The visco-hyperelasticity of A30 was modelled using a convolution integral in the form [190]:

$$\sigma^{VH}(t) = \int_0^t g(t-s)\frac{\partial \sigma_0^H}{\partial s}\partial s, \tag{33}$$

where $\sigma_0$ and $\sigma_\infty$ are the instantaneous and quasi-static hyperelastic stress respectively. Hence, $\sigma(t) \to \sigma_\infty$ as $t \to \infty$. $g(t-s)$ is a normalised relaxation function ($0 < g(t-s) < 1$), which is modelled here as a generalised Maxwell element expressed in terms of a Prony series of exponentials with $n$ Prony terms ($n = 5$) summarised in Table 22 [194,198,199]:

$$\sigma^{VH} = \int_0^t \left( g_\infty + \sum_{i=1}^{n} g_i e^{-\frac{t-s}{\tau_i}} \right) \frac{\partial \sigma_0^H}{\partial s} \partial s = \underbrace{g_\infty \sigma_0}_{\sigma_\infty^H} + \int_0^t \left( \sum_{i=1}^{n} g_i e^{-\frac{t-s}{\tau_i}} \right) \frac{\partial \sigma_0^H}{\partial s} \partial s. \tag{34}$$

$\tau_i$ is the characteristic relaxation time pairing with $g_i$, where $g_i$ is the normalised $i$th shear moduli ($G_i$). I.e.:

$$g_i = \frac{G_i}{G_0} = G_i / (G_\infty + \sum_{i=1}^{n} G_i), \tag{35}$$

where $G_0$ and $G_\infty$ are the instantaneous and quasi-static shear moduli, respectively.

#### *5.2.2.3 Numerical Time-stepping Scheme*

A closed form for the convolution integral solution in Eq. (34) is often difficult to obtain, particularly when advanced strain energy functions with various strain histories are applied. Therefore, a method using finite time increments proposed by Taylor et al. [201] was implemented to solve the integral:

$$\sigma^{VH}(t_{n+1}) = \underbrace{\sigma_\infty^H(t_{n+1})}_{elastic\ comp.} + \underbrace{\sum_{i=1}^{n} \left( \exp\left(-\frac{\Delta t}{\tau_i}\right) h_i(t_n) + \frac{g_i \dfrac{1 - \exp\left(-\frac{\Delta t}{\tau_i}\right)}{\frac{\Delta t}{\tau_i}} [\sigma_\infty^H(t_{n+1}) - \sigma_\infty^H(t_n)]}{g_\infty} \right)}_{viscoelastic\ component}$$

$$\therefore \sigma^{VH}(t_{n+1}) = \sigma_\infty^H(t_{n+1}) + \sum_{i=1}^{n} h_i(t_{n+1}) \tag{36}$$

The first term relates to the hyperelastic (time-independent) stress ($\sigma_\infty^H$) obtained from the 3-term Ogden model parameters fit to the quasi-static tests (Eq. (32)). The second term describes the summation of the viscoelastic (time-dependent) stress contribution ($\sum_{i=1}^{n} h_i$). A detailed derivation can be found in [199,202]. Using this time-stepping scheme, the normalised viscoelastic moduli $g_i$ were determined from the experimental stress-strain responses obtained from monotonic tension-compression tests at low strain rates [20], and from the drop-tower impact tests described earlier for higher strain rates. The stress-strain curves from the drop-tower impacts were used up to a compressive strain of 0.3, prior to considerable barrelling of the bulk material specimen. The

determined constants were then validated using the FE model for the entire impact response at various impact speeds as presented in the next section.

### 5.2.3 Computational Methods

#### *5.2.3.1 New Cell Designs*

Our baseline design for the hexagonally packed arrays was a straight-wall cylindrical cell, a typical building block of regular circular cell honeycombs, which was assigned a 2 mm wall thickness ($t$) and a radius to height ($R/h$) ratio of 0.5 ($h$ = 25 mm, $R$ = 12.5 mm). Our new cell arrays, namely the concave and convex cell arrays, were generated by incorporating axisymmetric curvatures in the cell walls using equal arc angles ($\theta$ = 45$^o$) and radii ($r_1$ = 7.84 mm, $r_2$ = 9.84 mm) as annotated in Figure 23A. The curvatures are symmetric about the mid-plane between the top and bottom faces of the cell. It should be noted here that, unlike conventional sheet-metal hexagonal honeycombs with bonded walls, here we explore hexagonally packed circular cell arrays separated from one another with a spacing of 0.5 mm (Figure 23B). The potential effects of this are discussed.

For each curvature direction (concave and convex) we study four curvature amplitudes, referred to as shape amplitudes, leading to 9 shapes in total: Four concave (shape = -0.25, -0.50, -0.75 and -1.00), four convex (same magnitudes with the opposite sign) and a straight-wall cell (i.e. shape = 0). Each of the 9 cell shapes are tested under 0$^o$ (pure compressive) and 45$^o$ (shear-compressive) impacts at impact velocities of 2.5, 5.0 and 7.5 m/s. After each simulation, several postprocessing calculations are made, including the relative density of the cells ($\bar{\rho}$), average axial ($\sigma_{z(ave)}$) and shear stress ($\tau_{zy(ave)}$) during the post buckling region (region II), internal energy per unit volume ($\overline{U}$) and densification strain ($\varepsilon_D$) of the cells as annotated in Figure 23C. For further information, see Appendix 5.6.3.

#### *5.2.3.2 Geometrical Parametrisation and Mesh Morphing*

CAD models of a unit cell of the arrays were generated in SolidWorks (2020, Dassault Systèmes, France) and imported into HyperMesh (2019, Altair, US) for FE mesh generation, mesh morphing and specification of 'shape variables' via HyperMorph (2019, Altair, US). The mesh morphing ensured that mesh quality was maintained while changing the node locations of a mesh to that of a target geometry. Shape variables are essentially a set of nonlinear node paths, each defined by a polynomial, which provide a perturbation vector for each node to follow during shape morphing. Therefore, all intermediate mesh geometries between a straight cell arrays and the concave and convex cell arrays, and their corresponding thicknesses, were realised by ratio of the polynomial coefficients of the relevant shape variables. The resulting shapes can be seen in Figure 23E. This framework provides an efficient and robust method for parametrising FE designs without having to tediously revise and

remesh the CAD for each design, which enabled efficient utilisation of HyperStudy (2019, Altair, US) for directing the large number of simulations in this DoE. Further information and applications for mesh morphing can be found in human body [237,238] and automobile FE modelling [239,240].

#### 5.2.3.3 *Finite Element Modelling Validation of Cell Arrays*

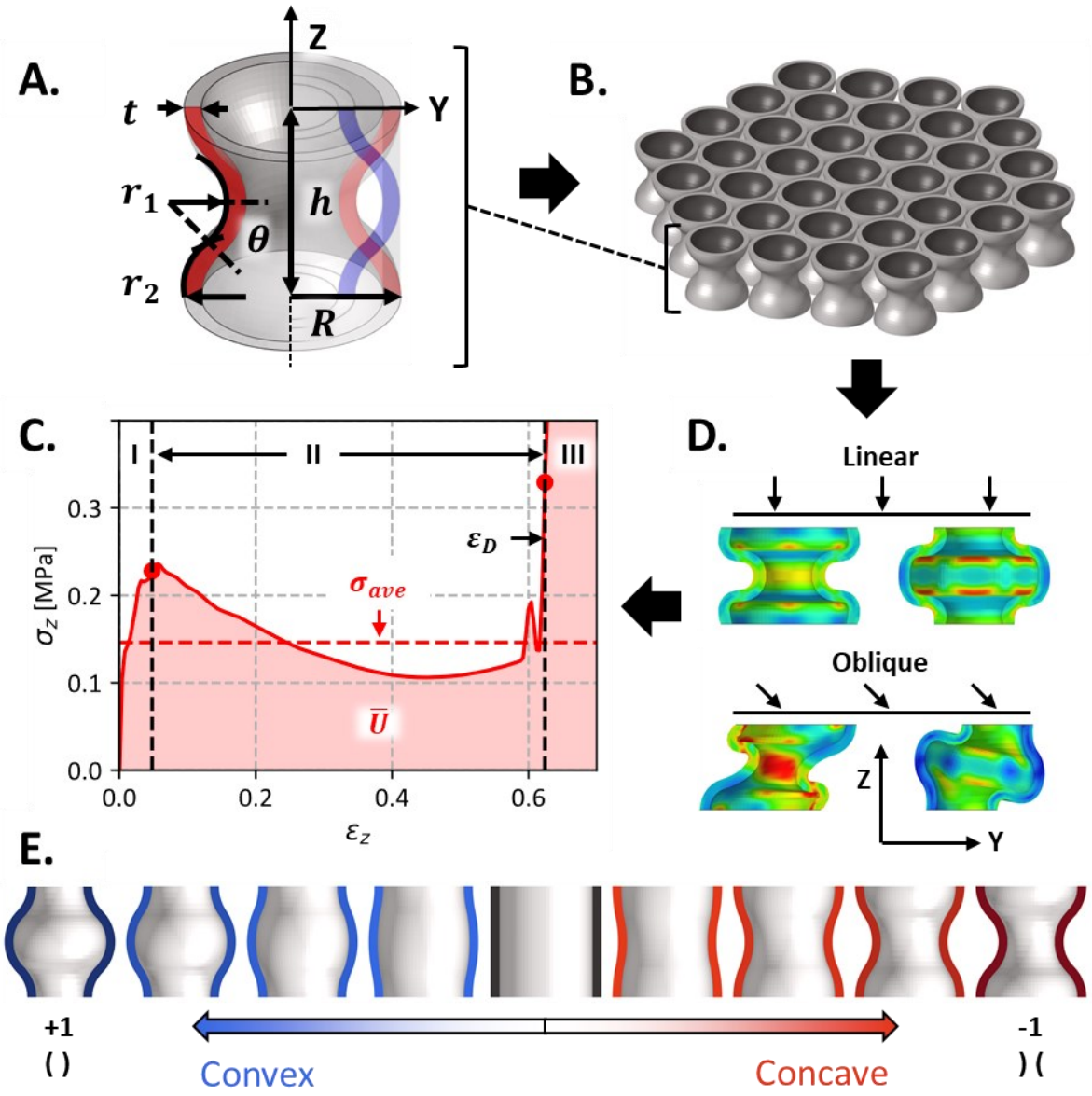


*Figure 42 – Computational pipeline.* ***A.*** *Parameterised unit cell with height $h$ and radius $R$, wall thickness $t$ and arc radii $r_1$ and $r_2$ and arc angle $\theta$.* ***B.*** *Hexagonal packing arrangement of unit cell to make the honeycomb.* ***C.*** *Axial and oblique load testing of cellular array.* ***D.*** *Postprocessing and pre-buckling (region I), post-buckling (region II) and densification (region III) parameter identification.* ***E.*** *The geometry of all shape amplitudes ranging from -1 (concave) to 1 (convex) with the intermediate shape amplitudes in increments of 0.25.*

For the purpose of validating the material model, the experimental drop-tower impacts on the cell arrays was simulated using the commercial finite element program LS-DYNA (R10.0, LSTC, US) via an

explicit time-stepping scheme for dynamic simulations [241]. The 5 kg impacting mass was assigned to a rigid-body and an initial velocity of 5.6 m/s to simulate the velocities of the impactor.

Likewise, the anvil was modelled with solid hexahedral elements assigned as a rigid body. A mesh sensitivity study was carried out on the cell arrays (see Appendix 5.6.2). The nominal outcome was reduced-integration solid hexahedral elements with two elements through thickness assigned MAT_77 with the parameters in Table 22.

The enclosed air was modelled using the control-volume method, a well-established method for modelling airbags and tyres, initiated with the *AIRBAG keyword for which the properties of ambient air were specified (Table 23).

#### *5.2.3.4 Design of Experiments on Cellular Arrays*

Modelling honeycombs with many unit cells, and hence elements, is computationally expensive. In order to explore whether an array can be represented with fewer cells, a code was developed to generate an FE mesh with a user-defined number of the hexagonally packed cells (Figure 23B). In order to assess the edge-effects on the stress-strain response during impact, the code was used to generate different packed areas obtained by changing the number of cell layers surrounding a central cell (see Appendix 5.6.4). Ultimately, for the full DoE, a customised periodic boundary condition was applied whereby an array of only one layer of cells was employed and modelled using null elements, which surrounded the central cell of the array modelled as before. Each node of the null-element cells in this layer were constrained to the corresponding node in the central cell. Therefore, this surrounding layer acted as a ghost-layer, offering only the geometry of a contact surface. Hence, the behaviour in this case resembles an infinite array of cells. To ensure compression occurred to densification at all relative densities, the *PRESCRIBED_MOTION keyword was used to impose the motion of the impactor to the desired strain-rates, resembling an ideal monotonic compression test. For more information, see Appendix 5.6.4.

*Table 22 – Visco-hyperelastic material model constants for Agilus30*

| **Quasi-static Ogden hyperelastic material model constants** | | | | | |
|---|---|---|---|---|---|
| $\mu_1$ **[MPa]** | $\alpha_1$ | $\mu_2$ **[MPa]** | $\alpha_2$ | $\mu_3$ **[MPa]** | $\alpha_3$ |
| 0.2127 | 1.3212 | 0.0375 | 4.318 | -0.001 | -1.0248 |
| **Viscoelastic Prony series material model constants** | | | | | |
| $G_i$ **[MPa]** | 1.10E+02 | 5.00E+01 | 1.60E+00 | 6.67E-02 | 9.33E-03 |
| $1/\tau_i$ **[ms$^{-1}$]** | 1.00E+01 | 5.00E+00 | 1.00E-02 | 1.00E-04 | 1.00E-05 |

*Table 23 – Thermodynamic properties of air*

| $c_v$ [J kg$^{-1}$ K$^{-1}$] | $c_p$ [J kg$^{-1}$ K$^{-1}$] | $T_0$ [K] | $P_{atm}$ [GPa] | $\rho_{atm}$ [kg/mm$^3$] |
|---|---|---|---|---|
| 0.718 | 1.01 | 295.15 | 1.013e-04 | 1.204e-09 |

## 5.3 Results

### 5.3.1 Finite Element Model Validation

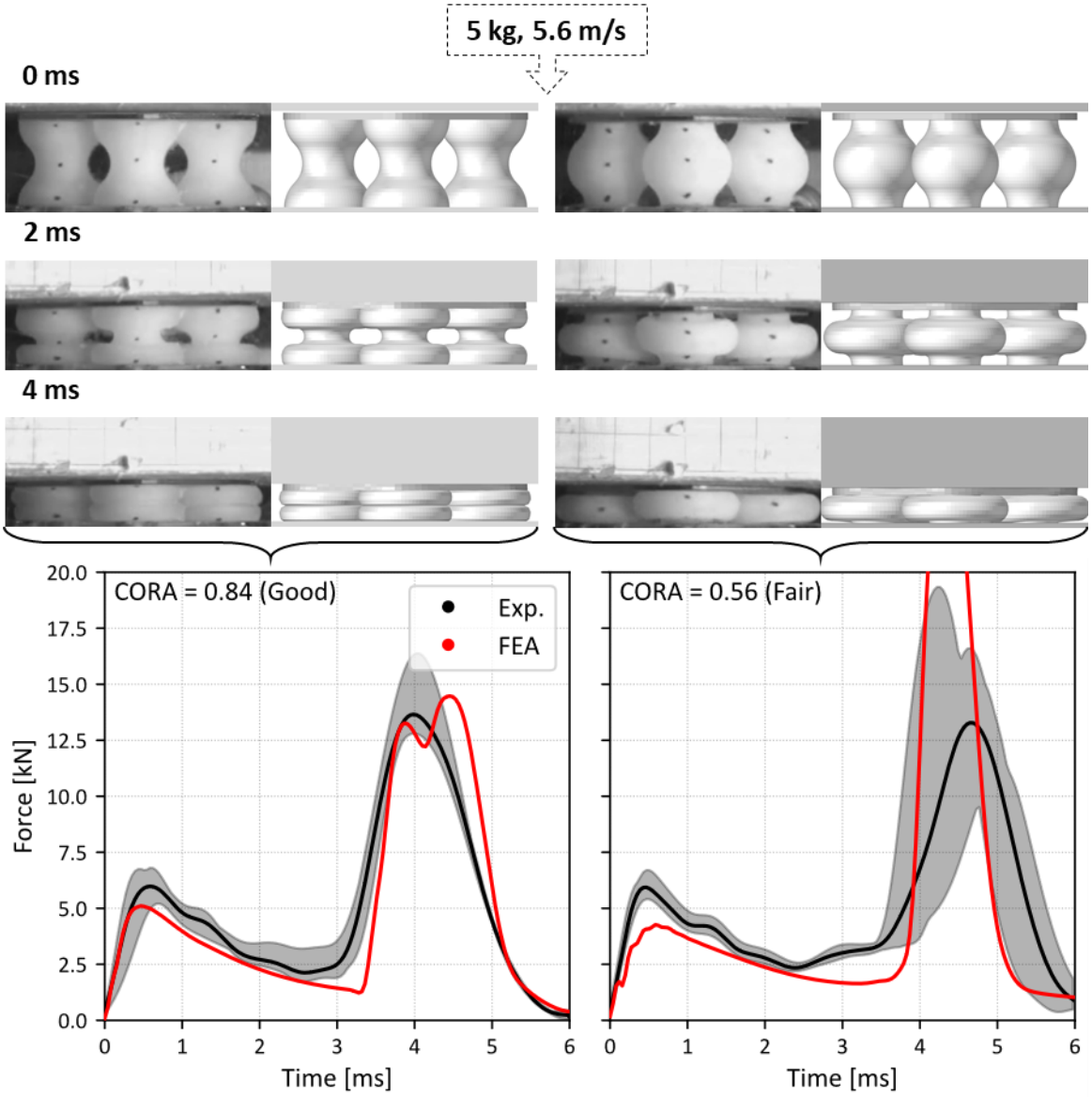


*Figure 43 – FE model validation of concave (left) and convex (right) cell arrays during axial impact via deformation and force-history responses. The test was set up such that a 5 kg aluminium impactor block was released from a height into guided free-fall such that the final velocity prior to impact was 5.6 m/s. CORA scores of the FEA axial force-history response (red) is 'Good' for concave cell arrays and 'Fair' for convex cell arrays in comparison to experimental (black). Shaded grey areas show the performance window of the combined experimental repeat impact tests.*

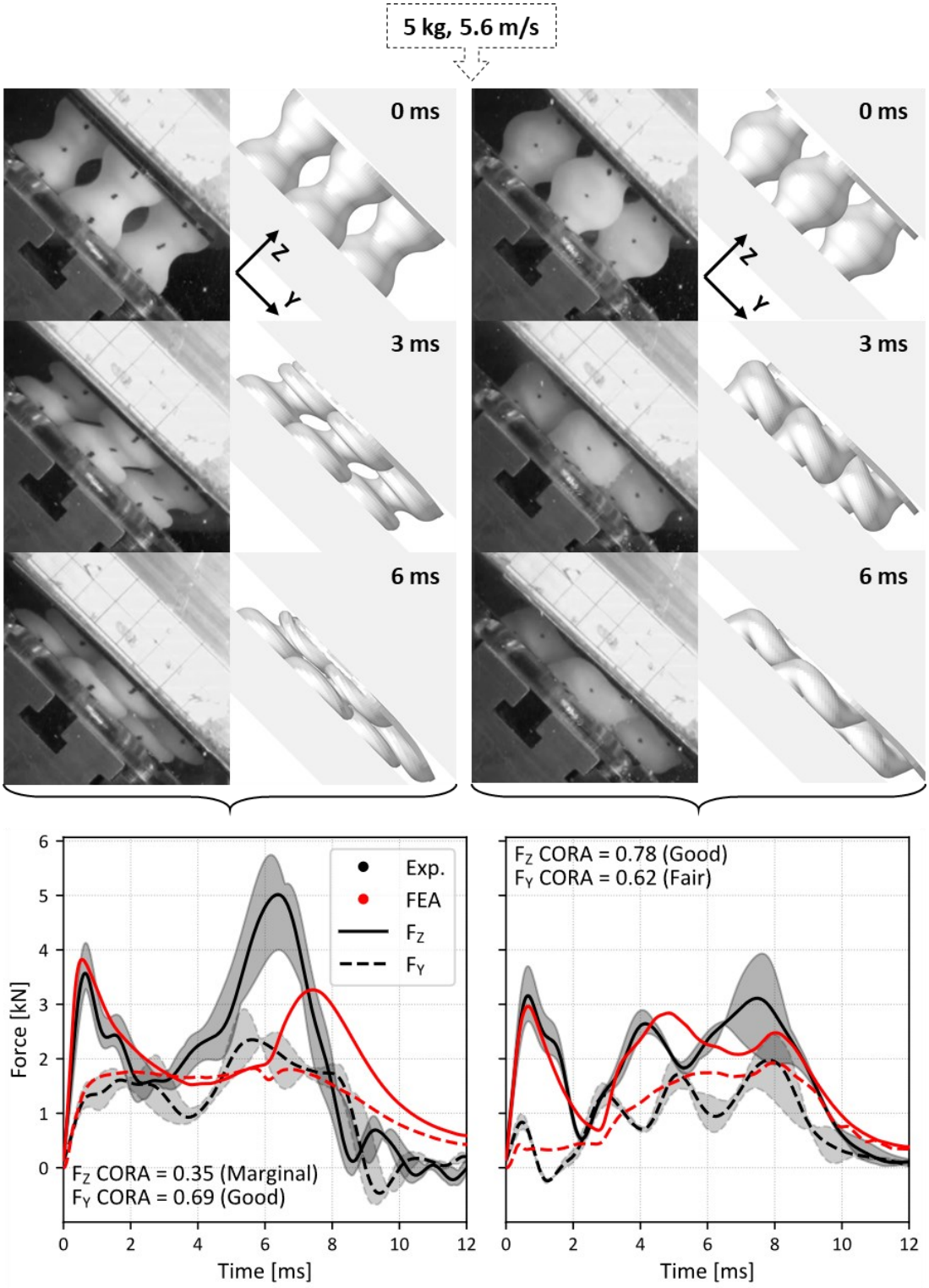


*Figure 44 – FE model validation of concave (left) and convex (right) cell arrays during oblique impact via deformation and force-history responses. The test was set up such that a 5 kg aluminium impactor block was released at 45$^o$ from a height into guided free-fall onto the specimens fixed to a swivel table inclined to 45$^o$ such that the final resultant velocity prior to impact was 5.6 m/s. CORA scores of the FEA axial (Z-axis) force-history response (solid red) is 'Marginal' for concave cell arrays and 'Good' for convex cell arrays in comparison to experimental (black). The scores were 'Good' and 'Fair' for the shear (Y-axis) forces (dashed), respectively. Shaded grey areas show the performance window of the combined experimental repeat impact tests.*

The validations for the axial impact condition of the cell arrays showed remarkable agreement between the experiment and FEA models (Figure 43). CORA scores of the force-history response

showed ‘Good’ fidelity for concave cell arrays and ‘Fair’ for convex arrays. The size rating was the main subtractor from the score of the convex cell validation owed to the large offshoot upon bottoming-out of the cell arrays starting at t = 4 ms owed to large finite element deformations in the model. The experimental impact results showed good repeatability particularly during the cell collapse region prior to bottoming-out.

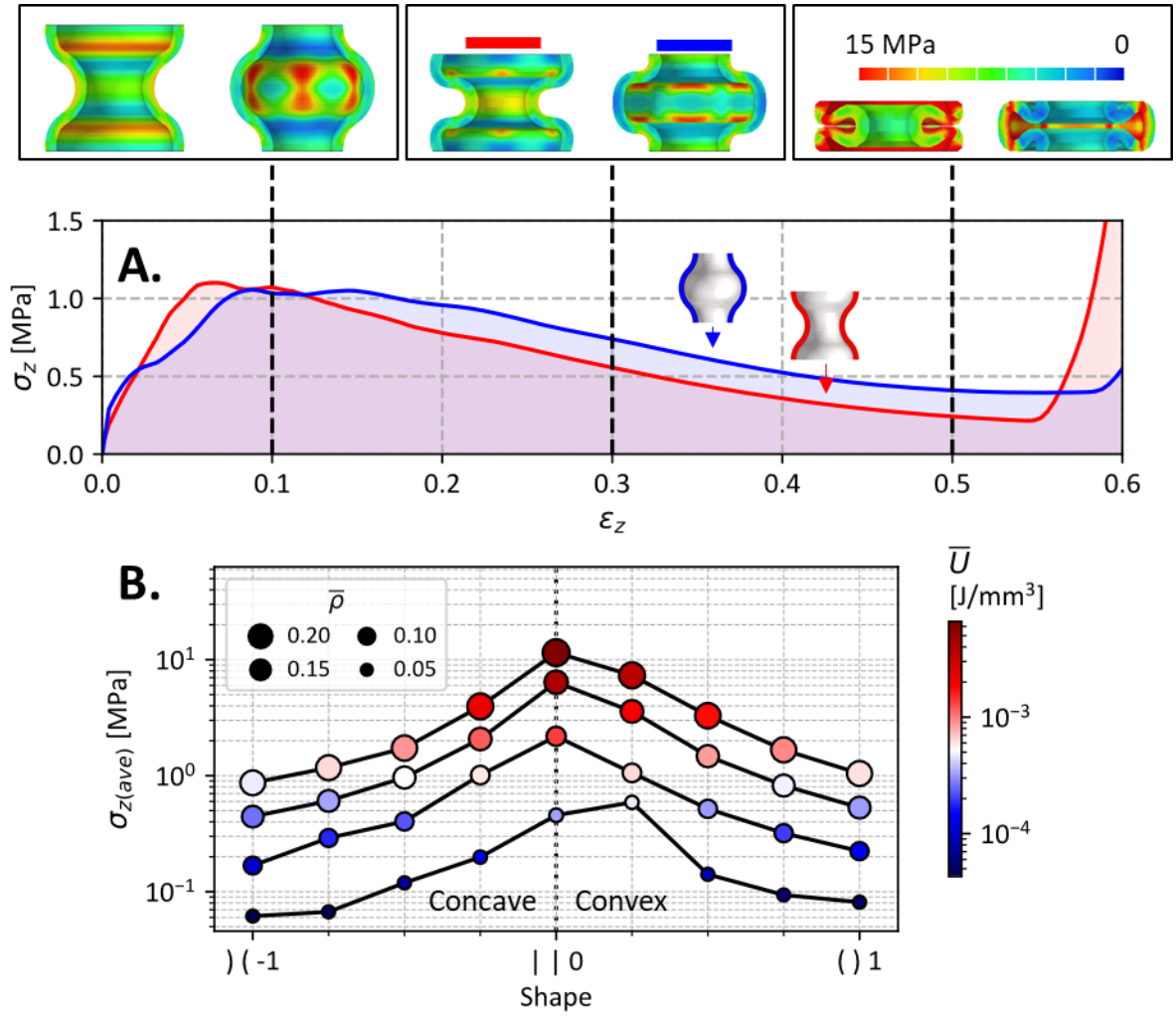


*Figure 45 – **A.** Axial stress-strain curves of 1.5 mm wall concave (red) and convex (blue) cell arrays at the extremities of the shape amplitudes investigated, i.e. -1 and 1 respectively, in axial compression at 7.5 m/s. The black vertical lines lead to FEA model deformation sequence at axial compressive strains of 0.1, 0.3 and 0.5 with contours of von-mises stress ($\sigma_{vm}$). **B.** The effect of different shape amplitudes, ranging from concave (-1) to convex (1), on $\sigma_{z(ave)}$ and $\bar{U}$ in axial loading at 5 m/s. Cell arrays with the same unit cell wall thickness are connected by non-orthogonal dotted lines, whose relative densities is represented by their marker size.*

Likewise, the oblique impact results showed promising correlation, ranging from ‘Good’ to ‘Marginal’ CORA scores for both axial and shear force-history impact responses (Figure 44). The main discrepancy was in the case of axial force-history in the concave oblique impacts which was again near the bottoming-out point at t = 6 ms. Nonetheless, the experimental results showed good repeatability and high-speed video analysis shows that the FEA captured the bi-axial deformation modes well.

Notably, the all the cell arrays tested fully recovered to their their undeformed shape within 2 minuites after impact, demonstrating their remarkable recoverability after large deformations at high strain rates.

### 5.3.2 Curvature Amplitude Effect in Axial Loading

We first focused on axial loading and explored the effects of amplitude and direction of cell curvature on the stress-strain response. To examine the effect of curvature direction, we used the stress-strain curves of two cell arrays with the same amplitude of curvature but in opposite directions (Figure 45A-B). We observe that the stress-strain profiles are very similar, with only a 2.8% difference in peak stresses.

We plotted the average axial stress vs. shape direction and amplitude (Figure 45B). The figure confirms that the average axial stress remains largely unaffected by the curvature direction across all shape amplitudes and relative densities, i.e., for the same amplitude, the curvature direction has a small effect on the axial stress. However, Figure 45C shows that the curvature amplitude has a large effect on the average stress. Increasing the amplitude reduces the average stresses and this reduction can be more than an order of magnitude at large amplitudes in comparison to straight wall cell arrays, regardless of curvature direction. We observe a symmetric inverted-V relationship between shape amplitude and the average axial stress in Figure 45C, with the peak lying at shape = 0 i.e. straight cell arrays. The sharp slope either side of the inverted-V highlight the substantial reduction of average with increasing curvature amplitude. On the other hand, the symmetry of the inverted-V indicates the modest influence of curvature direction on these measures. These observations remain consistent when examining the internal energy, which is the area under the stress-strain curves, shown with different colours in Figure 45C. This trend is consistent across all relative densities indicated with different marker sizes.

We also observe that increasing the relative density at any given shape amplitude increases the average axial stress and internal energy by a generally consistent amount along the log scale (Figure 45C).

### 5.3.3 Curvature Direction Effect in Oblique Impacts

Next, we explored the effects of the direction and amplitude of cell curvature on stress-strain response under oblique impacts of the cell arrays, where in contrast to axial impacts both axial and shear strains are present. To assess the effect of curvature direction, we used unit cells with the same curvature amplitude but opposite direction (Figure 46). For the axial components of stress-strain response, we again observed that the curvature direction has a marginal effect, with a less than 10% different in the peak axial stress (Figure 46A).

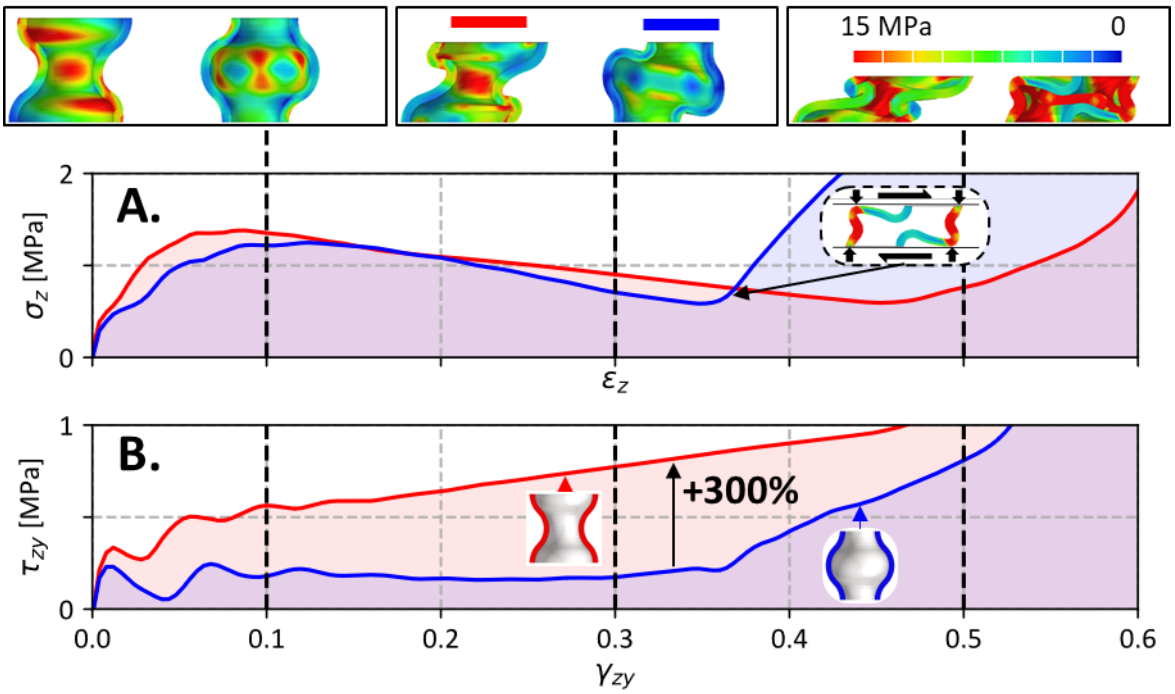


*Figure 46 - Axial (**A.**) and shear (**B.**) stress-strain curves of 2.0 mm wall concave (red) and convex (blue) cell arrays at the extremities of the shape amplitudes investigated, i.e. -1 and 1 respectively, in 45$^o$ compression at 7.5 m/s. The FEA model deformation sequence at axial compressive strains of 0.1, 0.3 and 0.6 are presented above the plot (connected with black dotted lines) with contours of von-mises stress ($\sigma_{vm}$).*

However, in sharp contrast, the curvature direction has a dramatic effect on the shear stress-strain response, with the concave shape offering much larger shear stresses at all strains than its convex counterpart up to densification, leading to a twofold increase in the average shear stress (Figure 46B and Table 24). The slope of the stress-strain curve in Figure 46B, i.e. the shear stiffness, is also larger for concave than convex, leading to more than 300% increase of the post-buckling shear stress.

To understand how these observations manifest in the rest of the shape amplitudes and relative densities, we plotted contours of stress vs. strain with shape on the x-axis (Figure 47A). Comparing the axial stress contours during axial and oblique loading in the figure, we observe the following similarities across all impacts: 1) the straight-wall cell arrays showed the largest axial stresses under both axial and oblique impacts, and 2) increasing the curvature amplitude in either direction leads to a gradual decline in axial stresses under both axial and oblique impacts regardless of curvature direction. These findings are consistent with earlier observations regarding the similarity of the axial stress-strain curves of concave and convex shapes of the same amplitude in both axial and oblique loading (Figure 46).

In contrast to the axial stress, distinctly asymmetric shear stress contours can be seen about the mid-lines for oblique loading (Figure 47A). Large shear stresses are clearly visible to the left of the mid-line (the region of concave shapes), in contrast to the right (the region of convex shapes). Such a distinct

asymmetric divide was not observed with the axial stress-strain components. This underscores the remarkable potential of decoupling the axial and shear responses of these cellular structures using curvature alone.

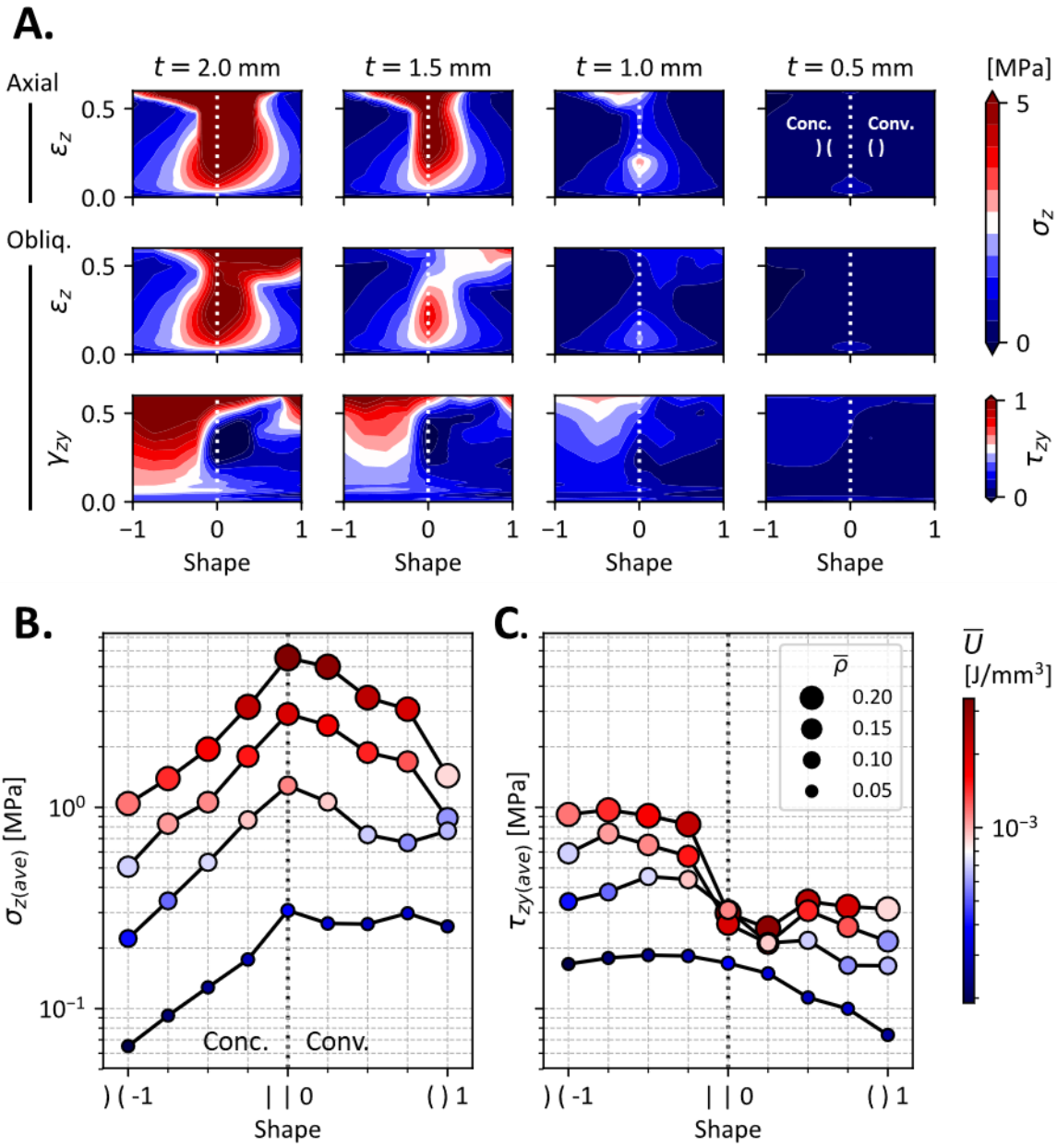


*Figure 47 - **A.** Axial stress contours of axial loading (top row) and oblique loading (middle row) as well as shear stress contours in oblique loading (bottom row) at an axial loading velocity of 5 m/s. The figure shows how the stress-strain relationship changes with shape. Each of the columns represents a different cell wall thickness. The effect of different shape amplitude on $\sigma_{z(ave)}$ (**B.**) and $\tau_{zy(ave)}$ (**C.**) in in 45° compression at 7.5 m/s. $\overline{U}$ of each data point is represented by the marker colour. Cell arrays with unit cells with the same wall thickness are connected by non-orthogonal dotted lines, whose relative densities is represented by their marker size.*

Notably, a steep rise in both axial and shear stress-strain curves for the convex shape are observed at strains ~0.4 during oblique loading. This is due to a secondary collapse of a shorter segment of the cell wall which, exclusively during oblique loading, becomes trapped between the anvil and impactor

leading to a sharp rise in the stress-curve as illustrated in Figure 46A. Hence, a patch of large axial and shear stresses can be seen on the upper right of the contours in Figure 47A relating to oblique loading as a consequence of this collapse mechanism. Interestingly, the onset of this patch seems to begin at strain of ~0.35 – 0.4 regardless of the convex shape amplitude and wall thickness.

*Table 24 - Buckling stress, average shear stress, and internal energy of concave and convex cell shapes with 2.0 mm wall thickness during 7.5 m/s oblique loading.*

| | $\sigma_{buckle}$ **[MPa]** | $\tau_{zy(ave)}$ [MPa] | $\bar{U}$ [J/mm$^3$ 10$^{-6}$] |
|---|---|---|---|
| **Convex ( ) 1** | 1.24 | 0.313 | 890 |
| **Concave ) ( -1** | 1.39 | 0.922 | 1185 |
| **% Difference** | +12.1 | **+194.6%** | **+33.1** |

To better understand the effects of the direction and amplitude of the cell curvature on the axial and shear responses, we plotted the average axial and shear stresses and internal energy during oblique loading vs. the shape (Figure 47B and C). Figure 47B shows an inverted-V trend peaking at shape = 0 as observed earlier during axial loading (Figure 45B). Nonetheless, the trend in Figure 47B is less symmetrical than in axial loading, revealing that the average axial stress and internal energy in oblique loading are marginally larger for convex shapes. This is likely a partial consequence of the unique secondary collapse of convex shapes reported earlier. On the other hand, the average shear stress is distinctly larger for concave shapes as illustrated in Figure 47C. This figure clearly reveals that the curvature direction has a largely asymmetric influence on the shear components in oblique impact. Quite surprisingly, we observe that for relative densities above 0.05, only marginal concavity is required to markedly increase the average shear stress compared to straight-wall and convex cell arrays (Figure 47C).

### 5.3.4 Shape Selection Strategy for Oblique Impact Performance

We then illustrated the effect of the shape on shear and axial stresses by plotting their ratio (Figure 48A). This figure clearly shows that convex shapes offer much wider shear to axial stress ratios and increasing the concave shape amplitude increases the ratio for all wall thicknesses. For convex shapes, the relationship is slightly more complicated and depends on the cell wall thickness. For 2mm cell wall thickness, the ratio decreases with increasing convex shape amplitude. The opposite appears to be true for thinner walls, where the ratio marginally increases with increasing shape amplitude. However, in all cases, straight wall and convex cell arrays offer a shear stress no more than approximately half the axial stress, and in some cases significantly less, making them ideal for situations where high axial stiffness with high shear compliance is required.

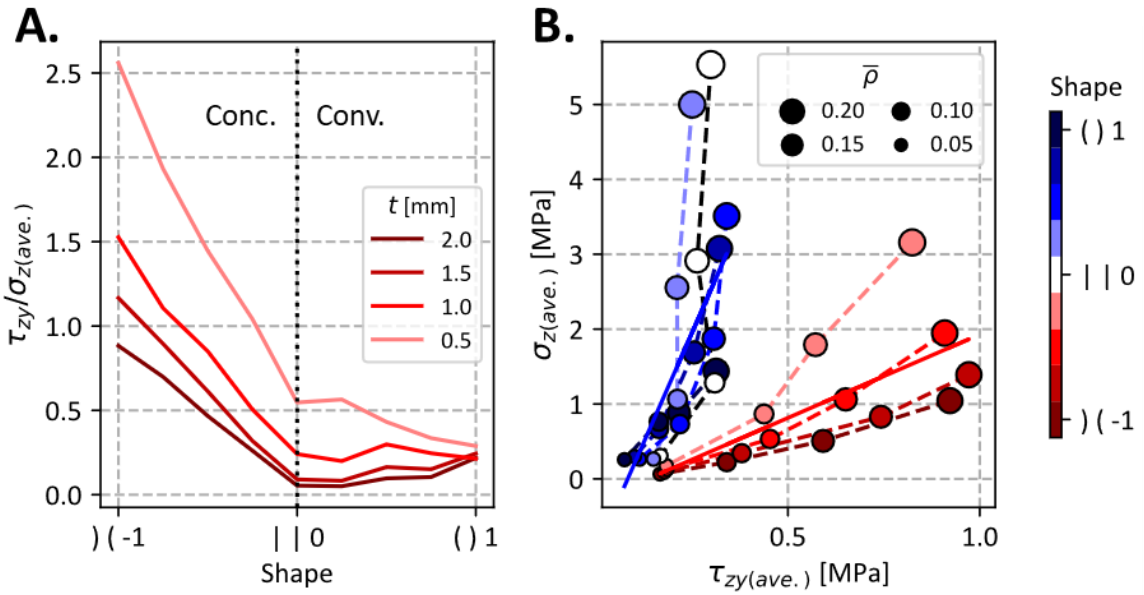


*Figure 48 - **A.** The influence of shape amplitude on the average shear to axial stress ratio during 7.5 m/s oblique loading with different wall thicknesses. Larger ratios are achieved with concave shapes in the region left of the dotted black vertical line which marks a straight-wall cell. **B.** Variation of the individual axial and shear stress components with different shapes, indicated by the maker colour. The relative densities are represented by the marker size. Solid lines represent lines of best fit. Dotted lines connect equivalent shapes of different relative densities.*

Given that the ratio is unitless, and the shape is entirely geometry dependent, Figure 48A can be used for a simple design selection with different materials where different axial and shear responses are desired.

Figure 48B, which shows the average axial vs. shear stresses of all shapes and relative densities, again shows the distinct effect of the curvature direction for oblique impacts. As we can see, the line of best fit to convex cell arrays (blue) lies distinctly more vertical than the line fitted to the concave cell arrays (red). This highlights the capacity for concave shapes to offer higher shear stiffness than convex shapes, and vice versa. Using this figure, one may find the appropriate shapes (marker colour) and relative densities (marker size) for a given design point which defines the required axial and shear stresses.

### 5.3.5 The Effect of Curvature with Strain Rate

We show the effect of increasing the oblique impact velocity on the compressive stress-strain response of a concave cell in Figure 49A, where $t$ = 2mm and shape = -1. We observe that increasing the impact velocity increases both the peak stress, average stress and hence the internal energy, represented by the shaded regions beneath each of the curves. Plotting the average axial and shear stress of all shapes shows that this effect is not exclusive to this cell shape, and in fact is manifested in all cell shapes (Figure 49B and C). These two figures also show that earlier observations relating to

the effect of cell shape on the axial and shear stress components in oblique impact remain consistent across the impact velocities explored here.

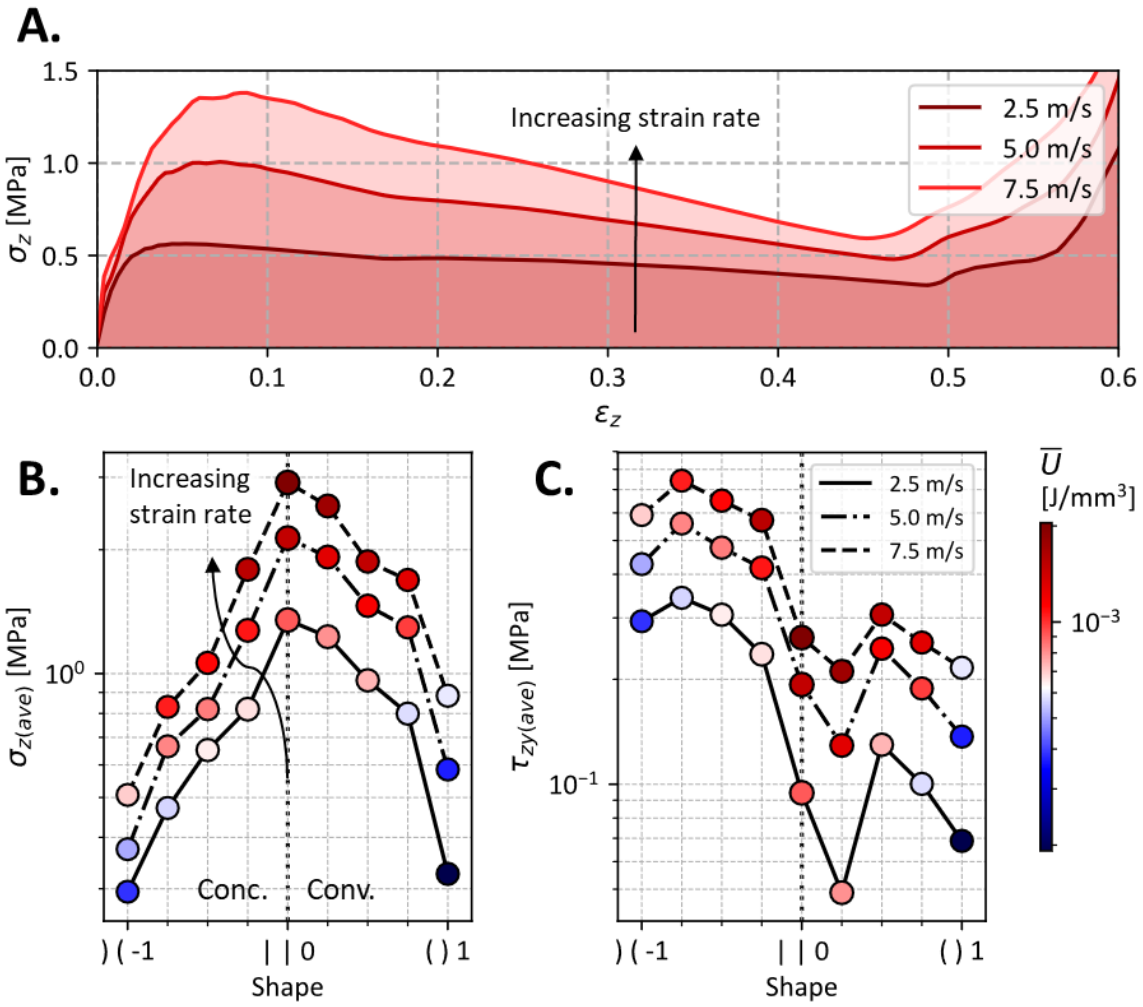


*Figure 49 - **A.** Stress-strain curves of 2.0 mm wall concave cell arrays (shape = -1) during 45$^o$ impact at 2.5, 5.0 and 7.5 m/s, with the shaded areas representing the internal energy at each impact velocity. The results show that increasing the impact speed increases the stresses at all strains until densification. **B.** and **C.** show the average axial and shear stresses respectively with overlaid internal energy results (marker colour) of all shape amplitudes with 1.5 mm cell walls during 45$^o$ impact at 2.5, 5.0 and 7.5 m/s. The results show that increasing the impact velocity increases both axial and shear stress components across all shapes whilst maintaining the underlying trend in the stresses observed due to shape changes.*

## 5.4 Discussion

In this study, we introduced a new class of cell array topologies with rate-sensitivity that allows us to tailor the oblique impact performance. We achieve this by applying simple shape changes to the cell walls, defined by arc curvatures, which produce concave and convex unit cell shapes. We show that concave and convex cell arrays enable remarkably different shear responses with a modest effect on the axial response during oblique loading. This highlights the capability to tailor shear and axial responses rather independently using curvature alone. This exciting potential has applications for

helmet liners, shoe soles and other applications where cellular materials are commonly deployed, yet tailorable compressive-shear responses are required.

The need for crashworthy structures capable of providing added or reduced shear resistance during compressive-shear loads has been highlighted previously [119,128,242,243]. However, limited solutions are offered due to the nonlinearity in geometry and large deformations cellular structures undergo during such load cases [244]. The capacity of lattices to offer solutions to this problem has been invesitgated [128,245]. Khosroshahi et al. [128] showed that adding diagonal struts to cubic lattices significantly increased the shear stiffnesss. However, such a change to topology cannot be easily achieved during use, and requires intricate manufacturing methods, limiting them to additive manufacturing technologies. Although we employed material jetting to prototype the cell arrays for experimental validation, the designs are simple enough to be manufactured using more affordable and conventional methods such as injection moulding. Moreover, the shape changes applied to the unit cell walls are also very simple, offering a capacity for real-time actuation and hence performance adjustment via thermomechanical programming [151,156] or otherwise. A recent study showed that viscoelastic bi-beams exhibit interesting effects under varying strain rates owed to their tendency to buckle in different directions at low and high strain rate [246]. Marrying such findings with what we have shown is achievable by these shape changes to viscoelastic cell arrays opens up new avenues to explore novel rate-sensitive cellular materials.

Our results showed that, unlike the shear stress, the axial stress during axial and oblique impacts of the present circular honeycombs was not largely influenced by cell wall curvature direction. However, the average axial stress considerably reduced with increasing curvature amplitude. This is consistent with previous research on the effect of sinusoidal imperfections on the buckling stress of axially loaded cylindrical shells [247,248]. Theoretical models were introduced to approximate ‘knock-down factors’ for the axial buckling stress of cylindrical shells which correlate with the amplitude of the imperfection [249]. Although the curvatures we implement are too large to be considered ‘imperfections’, a similar knock-down factor for the average axial stress which correlates with curvature amplitude may be introduced to this work. However, the aim of this study was to investigate the effect of such shape changes in both axial and oblique impacts well after the buckling phase, until densification. Hence, the derivation of emperical and theoretical models with such nonlinear materials and geometry is not trivial and is outside the scope of this paper. Regarding this, the use of FE models was extremely useful and indespensible for this study.

We offer a comparison between the performance of relevant and established cellular materials and the new cellular structures of this study under axial loading (Figure 50A). The comparison is in the

form of normalised peak stress vs. energy diagrams which isolate the effect of topology on these measures (methods in Appendix 5.6.6). Interestingly, the figure shows that almost any feasible performance range from out-of-plane honeycombs to foams is achievable simply by changing the cell wall curvature. Straight-wall cell arrays perform like conventional honeycombs in out-of-plane loading, whereas a large curvature leads to softer, bending-dominated deformations rivalling foams, irrelevant of the material used. Figure 50A reveals that concave and convex cell arrays offer a similar performance during axial loading, which is consistent with earlier observations drawn from Figure 45 – Figure 48. Therefore, it is reasonable to assume that the trends and conclusions drawn on the influence of shape on the compressive-shear performance of the cell arrays explored in this study will be applicable regardless of the material used. Notably, we observed that the densification strain was highly influenced by the impact condition (Figure 50B). This highlights the importance of considering the impact condition in empirical models that aim to predict or utilise densification strain of cellular materials, including honeycombs. In many applications, the average stress is simply multiplied by the densification strain to obtain the energy capable of being dissipated by cellular materials [250]. Figure 50B suggests that such methods may need to be revised when impact conditions are changed from axial to oblique.

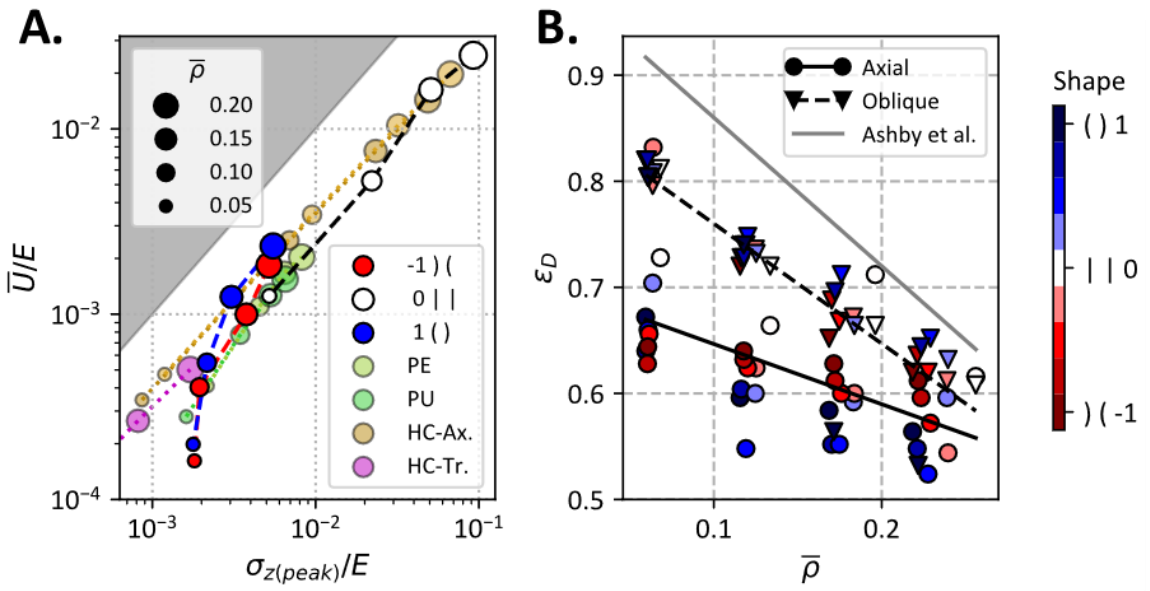


*Figure 50 - **A.** Normalised comparison of peak axial stress ($\sigma_z$) vs. internal energy ($\bar{U}$) between the concave, straight and convex cell arrays and other cellular materials, including Polyethylene (PE), Polyurethane (PU) foams and regular honeycombs (HC) in out-of-plane (Ax.) and in-plane (Tr.) loading, at different relative densities represented by their marker size. **B.** Relationship between densification strain ($\varepsilon_D$) and relative density ($\bar{\rho}$) of all shapes in axial and oblique impacts, with the lines of best fit marked with solid and dotted lines respectively for each impact condition. The grey line represents the relationship for foams and honeycombs following Ashby et al.* [80].

An outstanding agreement between the simulation and experiment is observed in both impacts, highlighting the high fidelity of the material model, not only at large strain but with varying strain-rate.

The experimental and simulation results both show the extremely high strain-rate dependency of Agilus30, as highlighted by the difference between the force-history response of the 2m/s and 4m/s impacts (Figure 55D). The deformation sequence of both simulation and experiment as captured by the high-speed camera also shows great agreement. The cylindrical specimens compressed to more than 70% of their original height in the 4m/s impacts leading to significant barreling in both the experiment and the finite element model. This gives confidence that the material model captures the large-strain behaviour under a complex stress-state very well. In partial concequence, good agreement was also observed between the experimental and simulated impact responses of the unit cell with air entrapped. This validation serves added confidence in the model for predicting the onset of buckling, the complex stress-state in the cell wall post-buckling and the model of the entrapped air within the cell. Although no experimental oblique impacts were carried out, the extensive validation of the bulk material and cellular material gives confidence in the finite element models in predicting all the explored loading conditions well.

All cell shapes showed considerable strain rate sensitivity in their mechanical responses inherent from the cell material, which increased the average axial stress by 211% and internal energy by 223% in some cases (Figure 49A). This unique rate-sensitivity, owed to the viscoelasticity of the cell wall material Agilus30, exemplifies why such structures are also promising candidates where different impact energies need to be managed. This is a typical case in American Football, where low and high severity impacts are endured by the helmets which both need to be managed by the same liner. In fact, helmets are typically optimised for one particular combination of impact speed and energy, dictated mainly by the liner thickness and material [116]. Such a limitation may be overcome when rate-sensitive cellular structures such as those we present here are employed [93].

This study reveals some physical limitations in tailoring the shear and axial responses using the changes to the cell wall shape. When inspecting the axial and shear components of all the shapes during oblique impact in Figure 48B, we observe a gap between the concave (red) and convex (blue) markers, indicating that a compromise is inevitable when tailoring the shear and axial stiffnesses of the cell arrays. Future work investigating additions to the cellular topology, such as connecting struts or plates may help overcome this limtation. We studied circular unit cells as they are axisymmetric, and hence provide a similar response regardless of the in-plane impact angle, which is advantageous in unforeseen crash circumstances. Nonetheless, different curvatures in each orthogonal direction which breaks this axisymmetry may lead to interesting and highly anisotropic behaviour for cases of more predictable loading directions. Along these lines of investigation, different arc radii ($r_1$ and $r_2$), aspect ratios ($R/h$) and the effect of bonding, hierarchical stacking, packing arrangements or packing cells of different shapes may be explored which will likely expand the performance range of the

structures. It is expected that the trends will remain consistent for unit cells with smaller $R/h$ ratios up to a limit, although higher-order buckling modes may be observed. Circular cells and tubes are known to buckle in either concertina or diamond collapse modes [251], both of which were observed in this study (see Appendix 5.6.5). Finally, future work may focus on actively morphing the unit cells to different shapes in order to alter the shear performance of the structure in operation.

## 5.5 Conclusion

In conclusion, we demonstrate the ability to tailor the shear and axial mechanical responses of a honeycomb arrangement of air-filled viscoelastic cell arrays in a relatively simple manner – by changing the axisymmetric curvature of the unit cell wall. Using a computational framework and a well-validated finite element model, different wall shapes and amplitudes were tested in axial and oblique impacts at speeds of 2.5 – 7.5 m/s in a full-factorial DoE. The results showed that concave cell arrays offer remarakbly larger shear stresses than their concave counterpart during oblique impacts (up to 300% increase), whilst minimally affecting the axial response. The average axial stress and internal energy increased with impact velocity by up to 200% due to the viscoelastic nature of the unit cells. This demonstrates the unique capacity of this new class of cellular topologies to significantly alter the shear response with simple shape changes that in future may be actively achieved during use, across a wide range of impact management applications.

## 5.6 Appendix

### 5.6.1 Bespoke Oblique Impact Drop Tower

A bespoke drop tower was built for the purpose of testing cellular structures in both axial and oblique impacts at speeds of up to 5.6 m/s with a mass of up to 5kg. The tower was constructed of four subassemblies: 1 – Main frame, 2 – Carriage, 3 – Magnet assembly, and 4 – Base. The main frame and much of the carriage and magnet assemblies consisted primarily of 45x45 mm extruded aluminium profiles (KJN Automation Ltd, UK) with 8mm T-slots (Figure 51).

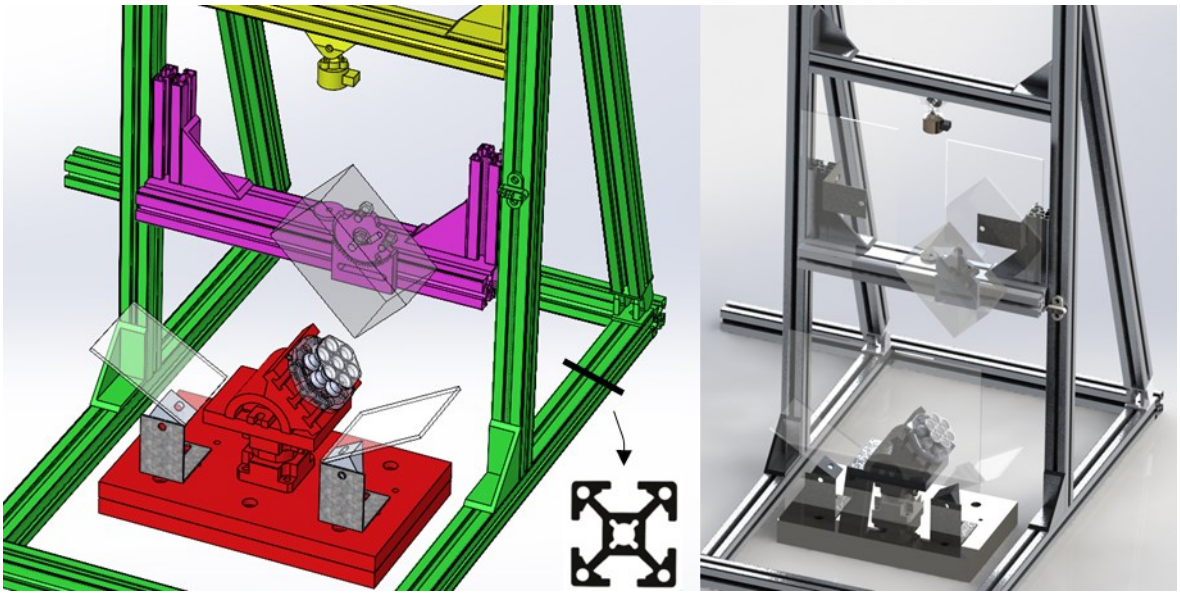

*Figure 51 – Left: Colour-coded drop tower subassemblies: Green: Main frame, Purple: Carriage, Yellow: Magnet assembly, Red: Base. The cross-sectional profile of the aluminium extrudes is outlined in black. A rendering of the drop tower is shown on the right.*

The base consisted of two large mild steel plates fixed to the floor using concrete anchor bolts. A 3-axis load cell (Kistler, UK) was bolted to the steel plates with 4xM8 bolts. An adjustable swivel table, capable of tilting 45 degrees each way, was mounted onto the load cell via an aluminium mating plate due to misalignment of the as-delivered holes in the load cell and the swivel table. The cell arrays to be tested would be bolted onto the swivel table via the T-slots on the swivel tabletop. This ensured that the bottom plate of the cell arrays would not slide off the table during an oblique impact. This bottom plate of the cell arrays, printed in VeroClear and fused to cell arrays by the nature of the material jetting process, was larger than the cell array to accommodate for holes designed to align with the T-slots on the swivel tabletop. This entire base subassembly was completely detached from the rest of the tower for noise isolation.

The purpose of the main frame is to support an upright twin-rail track to guide the carriage and magnet assembly. The carriage consisted of a horizontal aluminium extrude with two vertical stubby profiles at either end with four protruding M8 bolts to slot into the main frame tracks. These bolts were

jacketed with low-friction Nylon tubing and greased to ensure they slide smoothly along the vertical main frame T-slots.

A two-piece dial was designed and printed to carry a 5kg aluminium block, which acted as the impactor, at an adjustable angle between 0-45°. The dial consisted of two plates held together by a centre bolt and nut, one plate with open slots to hang the impactor, and another attached to the carriage via T-slots (Figure 52). The impacting block angle was simply adjusted by unscrewing the dial centre bolt which loosened the two plates from one another. The plate that carries the impactor would then be set to the desired angle. The dial centre bolt would then be tightened to fix the plates at that angle due to the friction between them. The dial angle would be set to match that of the swivel table at the base to ensure both the impactor and impacted surface were aligned, which are the top face of the cell array, and bottom face of the aluminium block respectively as seen in Figure 52.

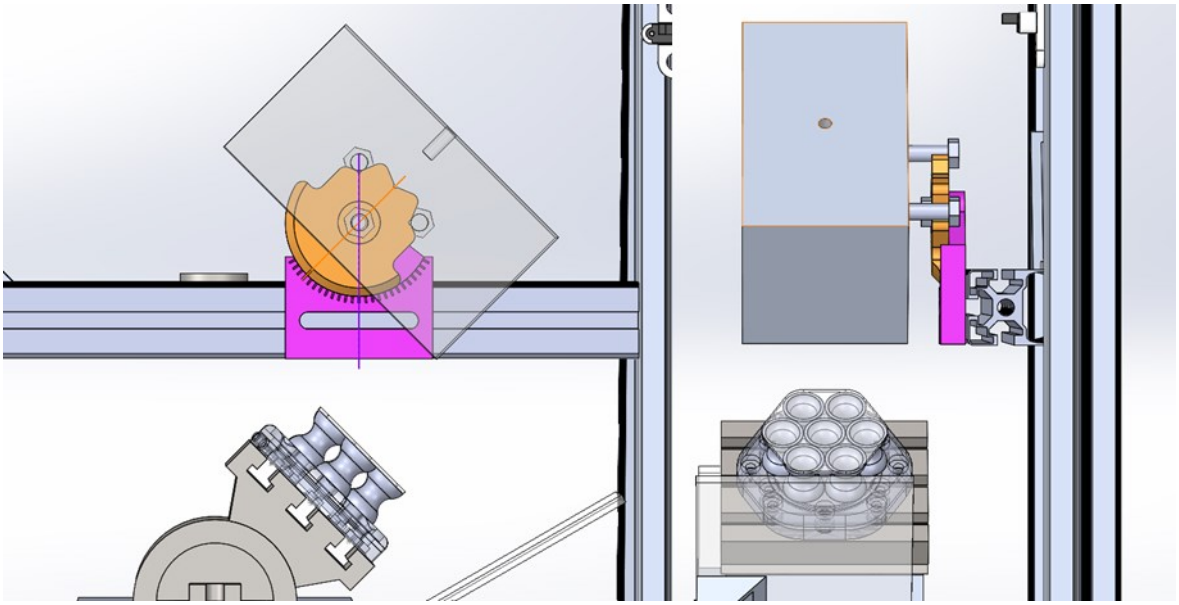

*Figure 52 – The dial mechanism: The plate bolted to the carriage (purple) is held to the slotted plate (orange) mounting the impacting block via a center bolt. This angle is adjusted by removing the impacting block, loosening the center bolt, pivoting the orange plate and retightening. The orange plate has open slots that allow the impacting block to detach and slide off during impact, whilst the carriage and dial continue to fall post impact till they are caught by a mat on the floor.*

A ferrous amateur plate was mounted to the top face of the carriage and aligned with the energise-to-hold 24DC 550N magnet hinged onto the magnet assembly. The magnet assembly was guided by the main frame in a similar method as the carriage. The magnet assembly is lowered and lifted via a hoist and pulley system, carrying the carriage with it when the magnet is energised. When the drop height is reached, the magnet is de-energised via an Arudino-controlled relay switch which would release the carriage and impactor. Transparent polycarbonate panels are mounted on the front and sides of the base and back of the carriage to protect the surrounds from the impact zone.

During this fall, the carriage would interrupt an optical switch which would trigger the data acquisition chassis (National Instruments, UK) and high-speed camera (Kron Technologies, Canada) synchronously via a 5V digital signal being sent from the Arduino. The high-speed camera and load cell connected to the charge amplifier (Kistler, UK) at this point are already recording data, however the trigger signal serves to provide a synchronised timestamp relative to the start of the impact. The data acquisition system and the routing of the signals is summarised in Figure 53.

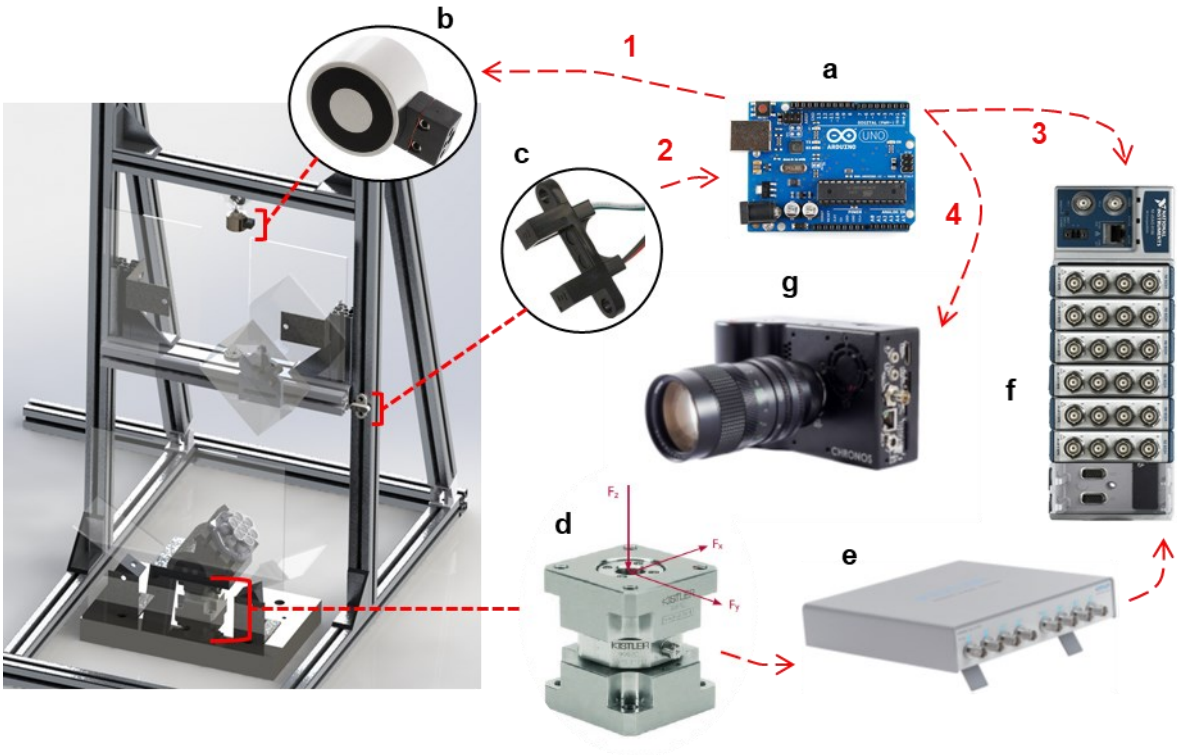


*Figure 53 – The trigger signal and data aquisition components and routes of the drop tower. 1 - An Aruindo (a) is used to energise the magnet (b) that lifts the carriage with the impactor. Once the hoist raises the carriage assembly to the desired drop height, the Arduino is once again triggered to de-energise the magnet and release the carraige. The carriage then falls with the impactor block it supports. As it falls, it interrupts an optical switch (c) placed on the main frame track. This sends a signal to the Arduino to send a trigger signal to the data aquisition module (National Istruments CDAQ) chassis (f) and the high-speed camera (g). The NI CDAQ is at this point already collecting data sent from the loadcell (d) through the Kistler LabAmp charge amplifier (e). The trigger signal only acts as a timestamp for time = 0ms.*

### 5.6.2 Bulk Material and Single Cell Validation

A separate drop tower was used to validate the bulk material given it exhibits increased stiffness in comparison to the cell arrays which required a larger mass to fully compress it. A batch of 6 solid Agilus30 cylindrical specimens (17.8 mm diameter; 25 mm height as per BS ISO 7743:2017 Type B [188]) were printed with the with the cylinder bases resting on the print bed. Similarly, hollow convex cells were printed for validation with through-holes at the base for removal of the support material. An adhesive (Permabond, UK) was then used to carefully glue the cells to a hard, plastic 'VeroClear' (Stratasys, USA) back plate, which forms a flat contact surface with the impactor and traps air inside the cell (Figure 54). For every impact test, the specimen was rested on a steel plate, which was

mounted on a 6-axis load cell (Sunrise Instruments, USA) (Figure 54). The central axis of the specimen was aligned with the axis of the impactor. The impactor had a mass of 16 kg with a flat face, 25mm in diameter. Impact force and speed-at-impact data were recorded at 25 kHz using a National Instruments PXIe data acquisition system (National Instruments, Newbury, Berkshire, UK). Data were filtered using a low-pass Butterworth filter with a cut-off frequency of 1 kHz. High speed video (PhantomV12.1, VisionResearch, Bedford, UK) was captured to determine the bulk material specimen deformation and impactor displacement at 11,000 frames per second.

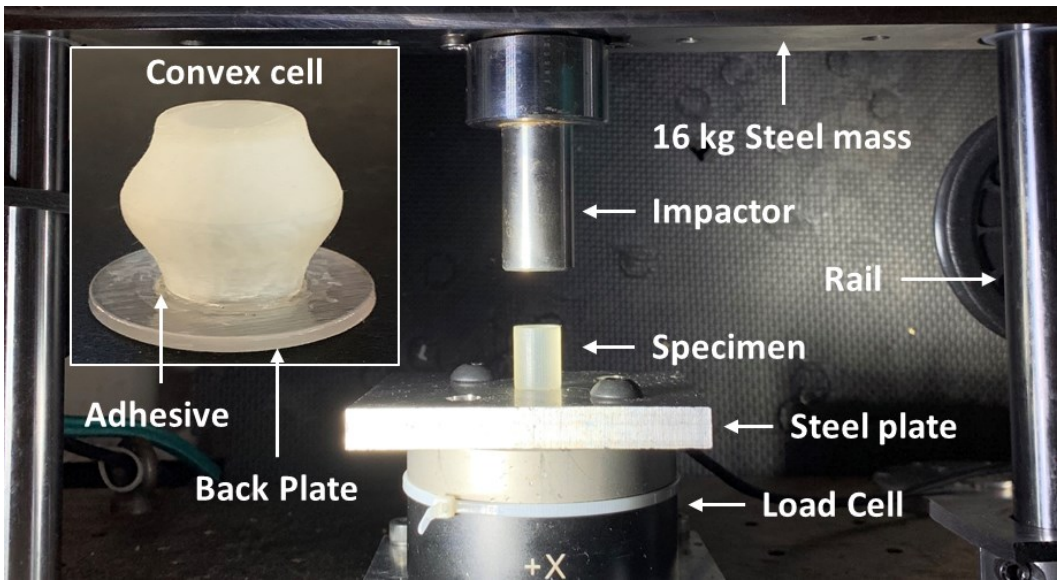


*Figure 54 – The experimental impact test setup showing a solid Agilus30 cylindrical specimen rested on the steel plate attached to the loadcell of which the impact response at different impact speeds is used for the subsequent finite element model validation. The upper left section of the figure shows the convex cell 3D printed in Agilus30 after the removal of the support material and adhesion to the hard plastic (VeroBlack) back plate.*

For the purpose of validating the material model, the experimental drop-tower impacts on the bulk material was simulated using the commercial finite element program LS-DYNA (R10.0, LSTC, US) via an explicit time-stepping scheme for dynamic simulations [241]. A 16kg mass was assigned to a rigid-

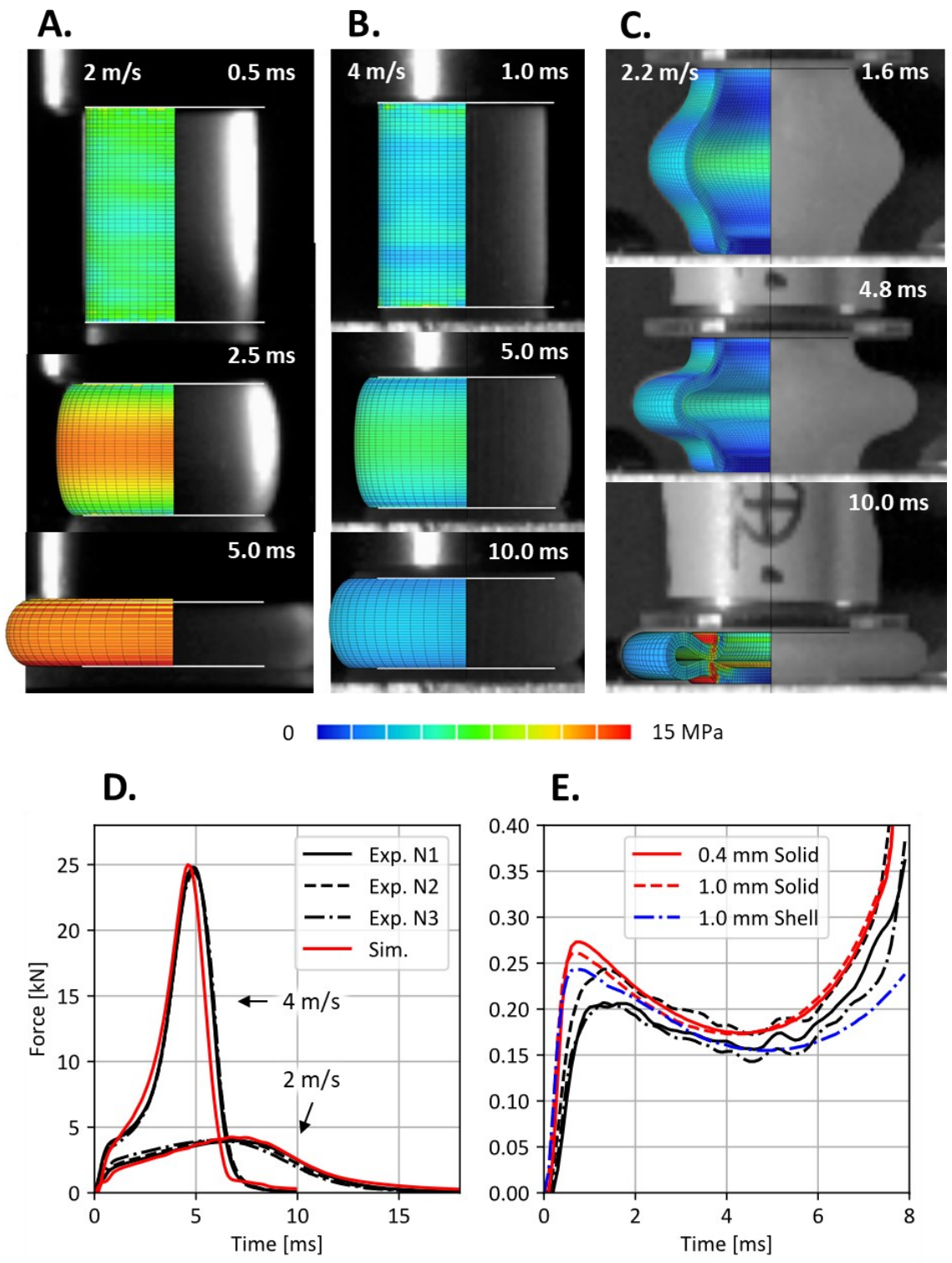


*Figure 55 – High-speed video of experimental test with the overlaid finite element model prediction of drop-tower impacts at 4 m/s (**A.**) and 2 m/s (**B.**) on bulk Agilus30 material samples and 2.2 m/s impact on convex cellular structure with entrapped air and 2mm wall thickness (**C.**). Experimental load-cell force-history of the repeat impacts on the bulk material sample (**D.**) and the cellular structure (**E.**) are compared to the finite element model prediction with different mesh densities and element formulations.*

body steel impactor and given an initial velocity of 2m/s and 4m/s to simulate the velocities of the impactor. Likewise, the anvil was modelled with solid hexahedral elements assigned as a rigid body. The bulk material specimen was modelled using reduced-integration solid hexahedral elements

assigned MAT_77 with the Ogden hyperelastic SEF coefficients and Prony relaxation coefficients (Table 22). A two-way contact algorithm (*AUTOMATIC_SURFACE_TO_SURFACE) was used between the impactor, specimen and anvil.

An identical setup was used to validate the cell FE models, replacing the bulk material specimen with an air-filled convex cell ($t$ = 2 mm). The mesh density and element type was varied to determine the most efficient method of modelling the cell wall. Five and two solid hexahedral elements through-thickness, as well as quadrilateral shell elements were tested and compared to the experimental data. The enclosed air was modelled using the control-volume method, a well-established method for modelling airbags and tyres, initiated with the *AIRBAG keyword for which the properties of ambient air were specified (Table 23).

We found remarkable agreement between the model predictions of large deformations during impacts and experimental results for both the solid specimen and air-filled convex specimen (Figure 55A-C). The predicted time history of the impact force was also in excellent agreement with the experimental results at both 2 and 4m/s impact velocities (Figure 55D). A comparison between the predicted and experimental results show that their difference for the peak force and its time was less than 7%. These results show the high fidelity of the finite element models in predicting the large deformation of the specimen during high-rate loading where extreme rate-sensitivity is observed (Figure 55D).

Our mesh sensitivity results showed that having five or two hexahedral elements through thickness had minimal effect on the simulation results, and two elements were sufficient to capture the bending response well (Figure 55E). This has also been observed in metal-sheet forming simulations [252]. Shell elements also showed good agreement with the exerpiments, however were avoided due to their inability to handle out-of-plane compression which occurs near densification. Hence, cells with 2 solid elements through the thickness were realised for the DoE.

*Table 25 - Experimental and simulated results of drop tower impacts on the bulk material specimens.*

| | **Vel.** | **Exp.** | **Sim.** | **% Diff.** |
|---|---|---|---|---|
| **Peak Force [kN]** | 2 m/s | 3.99 ± 0.05 | 4.24 | 6.27 |
| | 4 m/s | 24.63 ± 0.17 | 25.00 | 1.50 |
| @ Time [ms] | 2 m/s | 6.53 ± 0.38 | 6.73 | 3.06 |
| | 4 m/s | 4.93 ± 0.05 | 4.62 | -6.29 |

*Table 26 - Experimental and simulated results of drop tower impacts on convex cells.*

| | | Exp. | Sim. with mesh size: | | |
|---|---|---|---|---|---|
| | | | **0.4 mm solid** | **1 mm solid** | **1 mm shell** |
| **Force [kN] @** | **2 ms** | 0.21 ± 0.01 | 0.22 | 0.21 | 0.21 |
| | **4 ms** | 0.17 ± 0.01 | 0.18 | 0.17 | 0.16 |
| | **6 ms** | 0.19 ± 0.01 | 0.21 | 0.21 | 0.17 |

### 5.6.3 Parameter Calculation

Hexagonally packed circular cells occupy an effective volume ($V_{cell}$) calculated as:

$$V_{cell} = 6\left(\frac{R^2}{\sqrt{3}}\right)h$$

Where $R$ is the outermost radius of the cell, and $h$ is the height of the cell. Thereon, we may calculate the relative density of the cells:

$$\bar{\rho} = \frac{V_{wall}}{V_{cell}} = \frac{V_{wall}}{6\left(\frac{R^2}{\sqrt{3}}\right)h}$$

Where the volume of the cell wall ($V_{wall}$) was computationally calculated for each cell shape and wall thickness using the mesh geometry.

The effective nominal and axial ($\sigma_z$) and strain ($\varepsilon_z$) were calculated by dividing the axial impactor reaction force ($F_z$) and displacement ($d_z$) by the in-plane area of the cell ($A_{cell}$) and cell height ($h$) respecitvely:

$$\sigma_z = \frac{F_z}{A_{cell}} = \frac{F_z}{\pi R^2}$$

$$\varepsilon_z = d_z/h$$

Similarly, the shear components were calculated as:

$$\tau_{zy} = \frac{F_{zy}}{A_{cell}} = \frac{F_{zy}}{\pi R^2}$$

$$\gamma_{zy} = d_y/h$$

### 5.6.4 Edge Effects and Boundary Condition

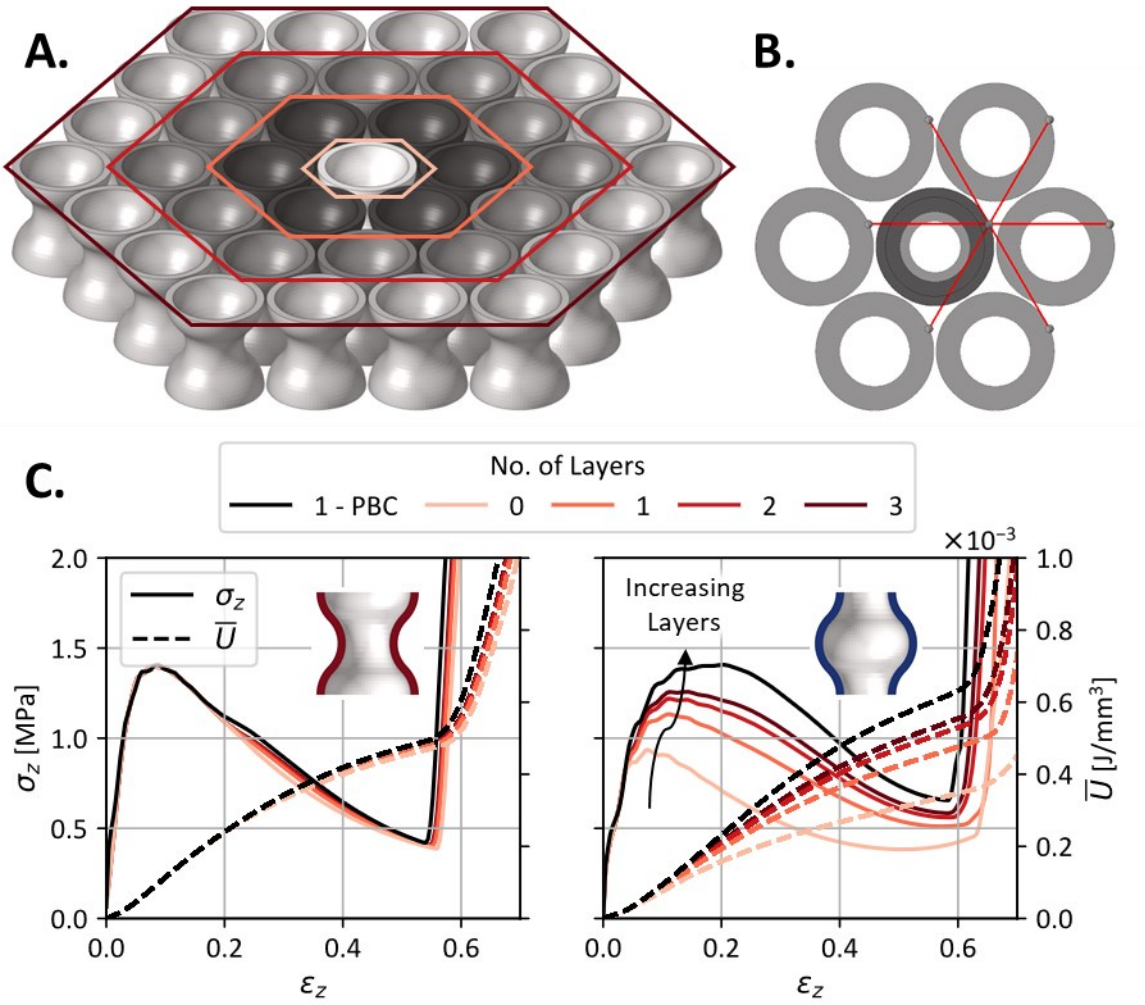


*Figure 56 – **A.** Finite element model of the honeycomb array with different centrally-packed layers with their regions marked by different colours. **B.** The finite element model with the periodic boundary condition which ties nodes of the outer null faces to the corresponding node of the central cell, with an exemplar constrained node set in red. **C.** The stress-strain and corresponding internal energy curves during axial loading of 2 mm concave and convex cells with different number of layers.*

The stiffness and internal energy per cell generally increased as the number of cells was increased, owing to the decreasing percentage of cells occupying the boundary of the total. However, the margin of increase was highly dependent on the direction of curvature. This observation is highlighted in Figure 56, where the stress-strain response of the convex array is considerably affected by the number of layers in contrast to the concave. This phenomenon sheds light on an interesting feature related to the Poisson's ratio of concave and convex cells discussed later.

### 5.6.5 Deformation Modes

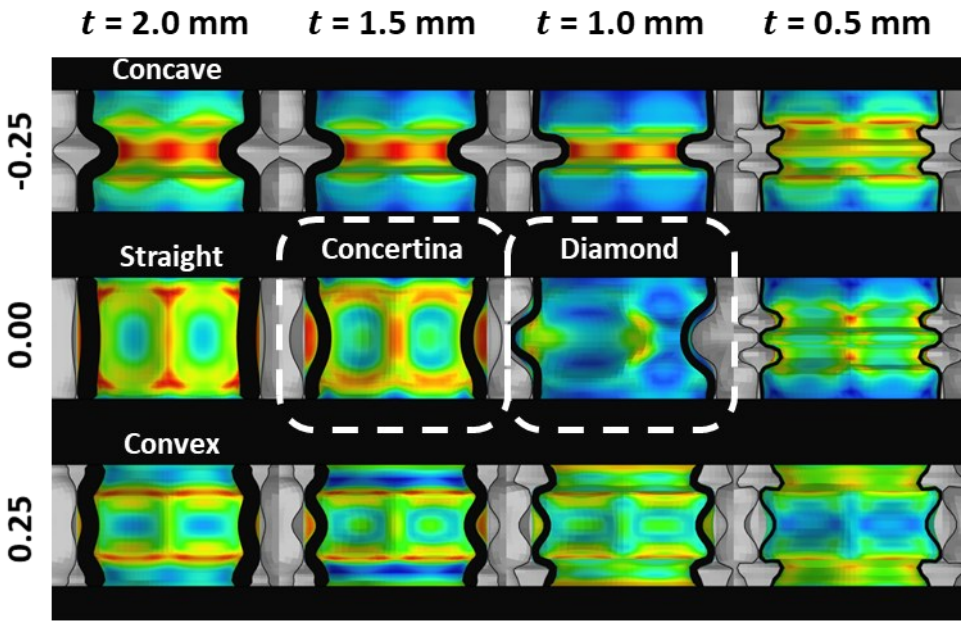


*Figure 57 – Deformation modes of concave (top) and convex (bottom) cells at small shape amplitudes. The figure shows that convex cell walls experience higher order buckling modes in comparison to concave cells of the same amplitude at all thicknesses above t = 0.5 mm.*

Convex cells bending outwards, which push out against one another during axial collapse, thus leading to a deformation constraint which, at small curvature amplitudes, promotes higher-order buckling modes. In contrast, this deformation constraint is non-existent in concave cells as they bend inwards and cause less interreference between one another, leading to lower-order buckling modes at all thicknesses below 0.5 mm (Figure 57). The consequence of this can be found in close observation of Figure 45B, which reveals marginally larger average stresses and thus larger internal energies with convex in comparison to concave cells of the same relative density. The post-buckling collapse stress and internal energy is larger by approximately 0.15 MPa and 22% respectively when comparing 1.5 mm concave and convex cells of amplitudes -1 and 1. Nonetheless, these values vary depending on shape amplitude and relative density (Figure 45B).

### 5.6.6 Derivation of Axial Performance of Benchmark Materials

#### *5.6.6.1 Elastomeric foam buckling stress*

Relationship between stress at elastic limit of the elastomeric foam ($\sigma_{el}^{*}$) and elastic modulus of parent material ($E_s$) can be approximated with relative density ($\bar{\rho}$) (Eq. 5.18 - 5.19 [219]):

$$\frac{\sigma_{el}^{*}}{E_s} \approx 0.03\bar{\rho}^{2}(1+\bar{\rho}^{0.5})^{2}$$

Which, for $\bar{\rho} < 0.3$, the relationship is approximately:

$$\frac{\sigma_{el}^*}{E_s} \approx 0.05\bar{\rho}^2$$

Relationship between post buckling stress ($\sigma^*$) and stress at elastic limit ($\sigma_{el}^*$) can be approximated as (Eq. 5.55 [219]):

$$\frac{\sigma^*}{\sigma_{el}^*} = \frac{1}{D}\left(\frac{\varepsilon_D}{\varepsilon_D - \varepsilon}\right)^m$$

Where $m$ = 1, $D$ = 1.55 for polyurethane, $m$ = 1, $D$ = 1 for polyethylene. The densification strain $\varepsilon_D$ for both elastomeric and plastic foams can be estimated as (Eq. 5.30 [219]):

$$\varepsilon_D = 1 - 1.4\bar{\rho}$$

Therefore,

$$\boxed{\frac{\sigma^*}{E_s} = \frac{\sigma^*}{\sigma_{el}^*}\frac{\sigma_{el}^*}{E_s} \approx 0.05\bar{\rho}^2\frac{1}{D}\left(\frac{\varepsilon_D}{\varepsilon_D - \varepsilon}\right)^m}$$

#### *5.6.6.2 Elastomeric honeycomb in-plane axial buckling stress*

The in-plane buckling stress of elastomeric honeycombs ($\sigma_2^*$) can be approximated from the critical buckling load of the columns like before (Eq. 4.20 [219]):

$$\frac{\sigma_2^*}{E_s} = \frac{n^2\pi^2 t^3}{24lh^2\cos\theta}$$

Where $n$ = 0.5 if the walls are free from rotational constraints, and 2 if they are fully constrained. For regular hexagons, $n$ = 0.69. Therefore (Eq. 4.21 [219]):

$$\boxed{\frac{\sigma_2^*}{E_s} \approx 0.22\left(\frac{t}{l}\right)^3 \approx 0.22\left(\frac{\sqrt{3}}{2}\bar{\rho}\right)^3 \approx 0.14\bar{\rho}^3}$$

Densification strain of honeycombs can be approximated in terms of relative density as:

$$\varepsilon_D \approx 1 - 1.4\left(\frac{2 + \frac{h}{l}}{2\cos\theta\left(\frac{h}{l} + \sin\theta\right)}\right)\left(\frac{t}{l}\right) \approx 1 - 1.4\bar{\rho}$$

#### *5.6.6.3 Elastomeric honeycomb out-of-plane axial buckling stress*

##### 5.6.6.3.1 Single-walled

The critical buckling load $P_{crit}$ for a honeycomb loaded in the axial (out-of-plane) direction is given by (Eq. 4.107 [219]):

$$P_{crit} = \frac{KE_s}{(1 - v_s^2)}\frac{t^3}{l}$$

$K$ is an end constraint factor for the vertical edges along the axial direction. $K$ = 2 if these edges are free to rotate, and 6.2 if they are clamped. Taking an intermediate for clamped edge conditions, $K$ = 4, and therefore (Eq. 4.108 [219]):

$$\frac{\sigma_3^*}{E_s} \approx \frac{2}{1-v_s^2}\left(\frac{\left(\frac{l}{h}+2\right)}{\left(\frac{h}{l}+\sin\theta\right)\cos\theta}\left(\frac{t}{l}\right)^3\right)$$

For regular hexagons, $l/h$ = 1 and the cell wall angle $\theta$ = 30°. Therefore:

$$\frac{\sigma_3^*}{E_s} \approx \frac{2}{1-v_s^2}\left(\frac{4\sqrt{3}}{3}\right)\left(\frac{t}{l}\right)^3 = \frac{8\sqrt{3}}{3(1-v_s^2)}\left(\frac{t}{l}\right)^3$$

For relative densities below 0.3, the relationship is approximated as:

$$\frac{t}{l} \approx \frac{\sqrt{3}}{2}\bar{\rho}$$

$$\therefore \frac{\sigma_3^*}{E_s} \approx \frac{8\sqrt{3}}{3(1-v_s^2)}\left(\frac{\sqrt{3}}{2}\bar{\rho}\right)^3 \approx 4\bar{\rho}^3$$

#### 5.6.6.3.2 Double-walled

Regular hexagons with a pair of double thickness vertical walls, the relative density is related to elastic moduli and the wall cross section aspect ratio by [253]:

$$\frac{E_3}{E^*} = \frac{2}{\cos\theta\,(1+\sin\theta)}\left(\frac{t}{l}\right) = \bar{\rho}$$

Therefore, for regular double-walled hexagonal honeycombs:

$$\frac{E_3}{E^*} = \frac{8\sqrt{3}}{9}\left(\frac{t}{l}\right) = \bar{\rho}$$

Like the analysis with single-walled honeycombs, the critical buckling stress in the axial direction can be expressed as:

$$\frac{\sigma_3^*}{E_s} \approx \frac{5K}{(1-v_s^2)\cos\theta\,(1+\sin\theta)}\left(\frac{t}{l}\right)^3 \approx 5.5\bar{\rho}^3$$

# 6 Chapter Six: Influence of Compressive-Shear Properties of Novel Helmet Liners on Brain Injury Metrics During Oblique Impacts

It is well known that rotational head motion is one of the major contributors to brain tissue strain during head impacts, which correlates with traumatic brain injury. In attempts to address this, several new helmet technologies have come to market promising enhanced protection against such head motion by leveraging enhanced compressive-shear properties in comparison to their conventional foam counterparts. However, the compressive-shear impact properties of these technologies at a coupon level has seldom been scientifically documented prior to their integration and performance assessment in a full helmet. In this study, we build upon previous work which has introduced novel air-filled viscoelastic cell arrays where several design parameters such as cell wall curvature and thickness were varied to analyse their influence on average crushing stress and absorbed energy in both compressive and compressive-shear loadings. Here, we take a step further by analysing how these different cell parameters affect the oblique impact performance of a validated bicycle helmet, and how they compare to a conventional helmet using validated computational models.

*Keywords*: Helmets; oblique impact; energy absorption; viscoelastic; brain injury

## 6.1 Introduction

As established in earlier chapters, cycling is one of the most popular modes of active mobility [6]. Cycling also brings about a myriad of health benefits, from reduced cardiovascular health risks and improved mental health [1–3]. However, cyclists are among the most vulnerable road users. Their severe injury and fatality rate per passenger miles are several folds larger than car occupants and bus passengers, with the head being the most common body part subject to severe injury [7,8]. Such injuries to head often lead to concussion or traumatic brain injury (TBI) with life-long consequences and impairment [9]. The associated direct medical treatment costs for cyclist head injuries exceeded $2 billion annually in the US alone [254].

Currently, and for the foreseeable future, helmets are the most effective method of protecting a cyclist from head injuries such as TBI [255]. A study by Dodds et al. showed that 19% of helmeted cyclists suffered severe TBI compared to 48% of non-helmeted cyclists [12]. Hence, cyclists are often advised to wear helmets as helmets can play a key role in protecting their head and brain against impacts [10–12].

Today, bicycle helmets must pass tests set by helmet testing standards such as EN1078. The majority of such standards stipulate that a helmet must not exceed a translational acceleration threshold in a vertical impact where only linear motion is assessed [13]. In contrast, a significant amount of research

has concluded that rotational head motion, not translational, is the major contributor to straining of brain tissue which is a key contributor to TBI [14–17]. Analyses of accident data show that rotational head motion occurs in vast majority of real-world head collisions as the head typically impacts other surfaces at an angle, a type of impact named oblique impact. These findings led to new proposals from Fédération Internationale de Motocyclisme (FIM) and European Committee for Standardization Working Group 11 (CEN/TC158/WG11) for helmet testing under oblique impacts and using injury criteria based on head rotation [58–61]. Several elements of the CEN/TC158/WG11 proposal are implemented in this study.

However, as of today, most helmets have been designed to reduce linear accelerations as stipulated in the current requirements, with minor or no consideration of rotational acceleration. Most helmets utilise EPS foam which dissipates energy through plastic collapse of cell walls. This is effective in reducing the peak translational deceleration loads applied to the head and skull and hence reduced the risk of skull fracture. However, EPS foam lacks the ability to decouple axial and shear stiffness i.e., EPS foam with increased axial stiffness also exhibits increased shear stiffness. It is hypothesised that reducing shear stiffness is necessary to reduce rotational head motion which is relevant to brain injury. Hence, this hypothesis was tested by comparing the performance of two helmets with cell arrays of similar axial stiffness, yet different shear stiffness. This would not be possible with conventional EPS foam as studies have shown the foam's shear stiffness increases with axial stiffness [XX].

The new helmet standard testing proposals have prompted several helmet liner technologies to come to market with the aim of replacing EPS given the limitations it has in addressing head rotation resulting from oblique head-to-surface impacts albeit its widespread use. Such technologies typically introduce a regular cellular structure such as WaveCel, Koroyd and HEXR, or they add a slip layer such as MIPS and SPIN which were investigated in detail in Chapter 3. As explained in that chapter, WaveCel is a cellular structure formed of interconnected 'wavy' walls that crumple upon impact whilst allowing shearing to reduce rotational stiffness. This technology does not entirely replace EPS foam, rather is typically inserted as the inner layer of a bi-layered helmet liner to allow shear deformation between the helmet and headform, hence reducing rotational acceleration. In a previous study, we tested these technologies in oblique impacts and showed that they may offer potential improvements to rotational acceleration and strain in certain brain regions. However, the results were highly subject to impact condition and location [19]. We believe this bottleneck is likely because none of these technologies entirely replace the EPS foam as we aim to in this study.

Moreover, little is understood about the compressive-shear behaviour of these helmet liners at coupon level isolated from the entire helmet system in oblique impacts prior to their integration into

a full helmet liner. Hence, how differences in the unit cell design influence the compressive-shear behaviour of the larger helmet system itself has not been reported. As a result, improved helmet designs have been limited due to the lack of information on how the cell shape, which influences mechanical behaviour, influences a larger helmet system particularly in oblique impacts.

In this study, we continue bridging this gap by building on from our previous findings from studying how different cell shapes influence compressive-shear response. We previously found that we were able to tailor their axial and shear stress-strain responses in oblique impacts by introducing axisymmetric concave and convex curvatures to hexagonally packed circular cell walls. The oblique impacts induced different compressive-shear deformations and reaction forces which differed depending on the direction of curvature (concave or convex). Here, we take unit cells at the extreme of each of the curvatures, concave and convex, to form an array that entirely replaces the EPS liner of a bicycle helmet.

Furthermore, we assess how these different helmet liner cell designs, as well as the conventional EPS helmet, compared in three oblique impact conditions using both pure kinematic and brain injury metrics. We do this by means of a detailed and validated brain injury model which allows us to assess metrics such as brain strain in various locations such as sulci and corpus callosum which are known to be linked with traumatic brain injuries such as diffuse axonal injury when strained.

## 6.2 Materials and Methods

### 6.2.1 Experimental Methods

A medium-sized urban cycling helmet was used as a benchmark for the performance assessment of the proposed viscoelastic cellular arrays. The helmet was tested under axial and oblique impacts in

various impact conditions as part of a larger group of helmets tested in our previous study employing a new testing method proposed by CEN WG11 [19]. The conditions of the test are such that a guided helmeted-headform is dropped onto a 45$^{o}$ anvil coated with 80-grit sandpaper, resulting in an oblique impact where both translational and rotational headform accelerations are recorded. The test is carried out for three different impact locations on the helmet which lead to predominant rotational accelerations about each of the anatomical axes of the head.

Impact 1, with the initial position of the headform X-, Y- and Z-axis 0°, produces predominant rotation about the X-axis. For impact 2, the initial position of the headform was X-, Y-axis 0° and Z-axis -90°, which produces predominant rotation about the Y axis. For impact 3, the Initial position of the headform was X- and Z-axis 0° and 65° around Y-axis. This impact produces large rotation about the Z-axis compared to the other impacts.

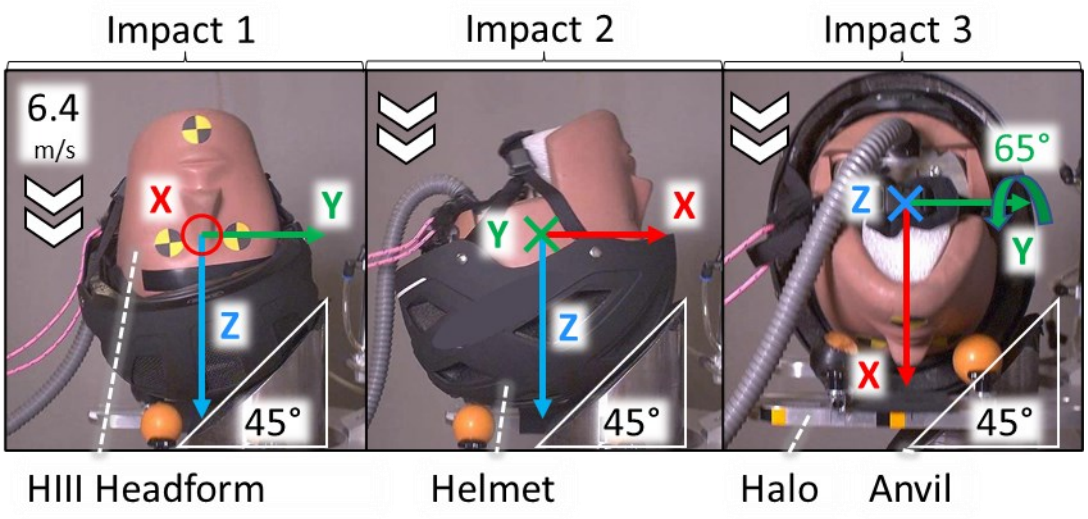


*Figure 58 – Experimental impact setup for all three oblique impact tests carried out for following validations and comparison. Prior to each impact, a halo ring attached to a monorail simply supports the helmeted headform during free fall. During the impact, the halo ring drops past the anvil leaving the helmeted headform free during impact during which headform translational and rotational accelerations are recorded for further analyses.*

### 6.2.2 Helmet Modelling

#### *6.2.2.1 3D Scanning*

The helmet has an in-mould polycarbonate shell with EPS liner. Hence, no rivets or embedded parts are holding the shell to the foam liner which enabled accurate modelling using 3D surface scanning. For an accurate representation of the complicated geometry, a FARO Design ScanArm laser line probe scanner was used to obtain a 3D scan of the helmet. The straps, comfort foam and other accessories were removed to facilitate the scanning of the components critical to the crash performance of the helmet.

An overview of the process of reverse-engineering the helmet can be seen in Figure 59. The first step was scanning the helmet using the FARO Design ScanArm laser line probe scanner (A). This leads to a surface mesh saved as an STL file that can be viewed using a desktop computer (B). This raw STL is then postprocessed to remove any miniscule gaps and holes left in the surface in areas that are difficult to reach for the scanner. This results in a watertight mesh which is further postprocessed to remove any unnecessary details that do not directly contribute to the crash performance such as Velcro patches. This is done by a combination of mesh smoothing and resampling using advanced tools such as MeshLab. The resampled mesh (C) is then imported into HyperMesh (Altair, 2021) for the generation of a finite element model that may be used for crashworthiness and impact assessment.

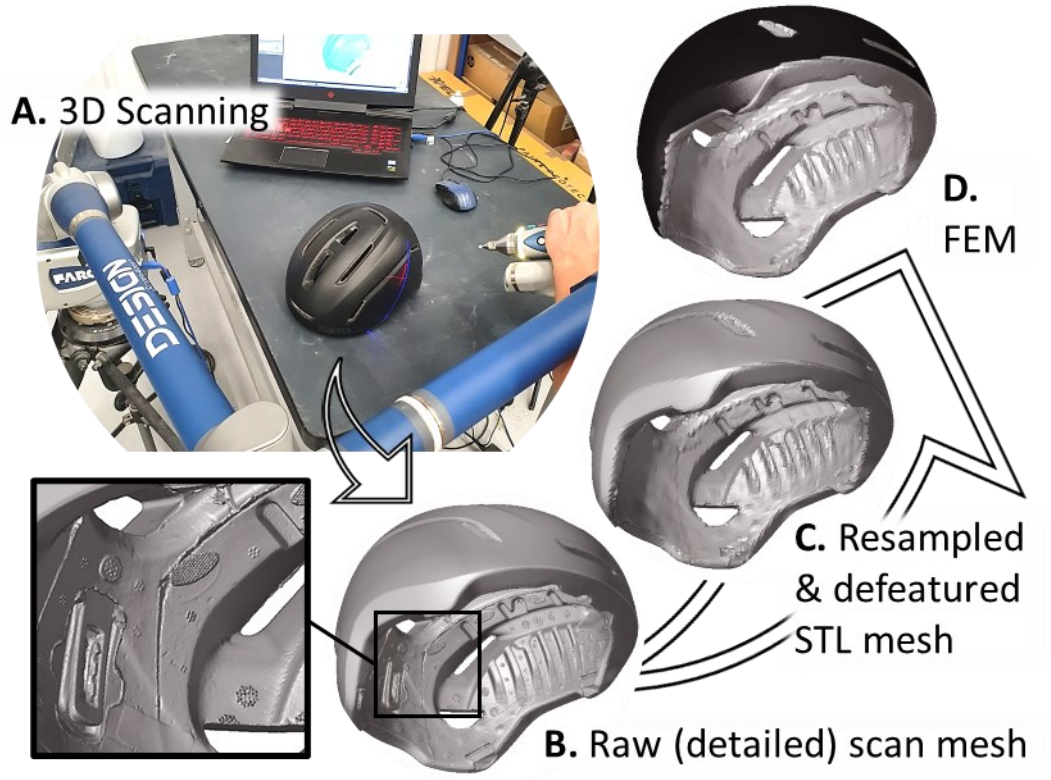


*Figure 59 – The process of reverse engineering the bicycle helmet.*

This stage involved generating the EPS foam representation using a tetrahedral mesh which fills the volume encompassed by the watertight surface mesh. This process was followed by shell finite element mesh generation using tetrahedral faces in areas representing the polycarbonate helmet outer shell (D).

The FARO laser line probe precision is 100 $\mu m^2$. For the purposes of FEA, the mesh resolution was reduced in MeshLab using mesh resampling techniques which ensured minimum surface accuracy loss. The resampled mesh was then imported into HyperMesh (Altair, 2021) for finite element modelling of the foam and shell. The foam was modelled using 4-node tetrahedral elements with an average element size of 4mm. This ensured at least 5 elements through the helmet thickness at any given cross-section. The helmet shell was modelled using 3-node triangular elements with nodes shared with the foam tetrahedral elements.

#### *6.2.2.2 Material Properties*

The helmet liner foam is EPS of density 120 g/l. Hence, the compressive stress-strain material properties of the EPS liner could be inferred using well established empirical equations from Gibson

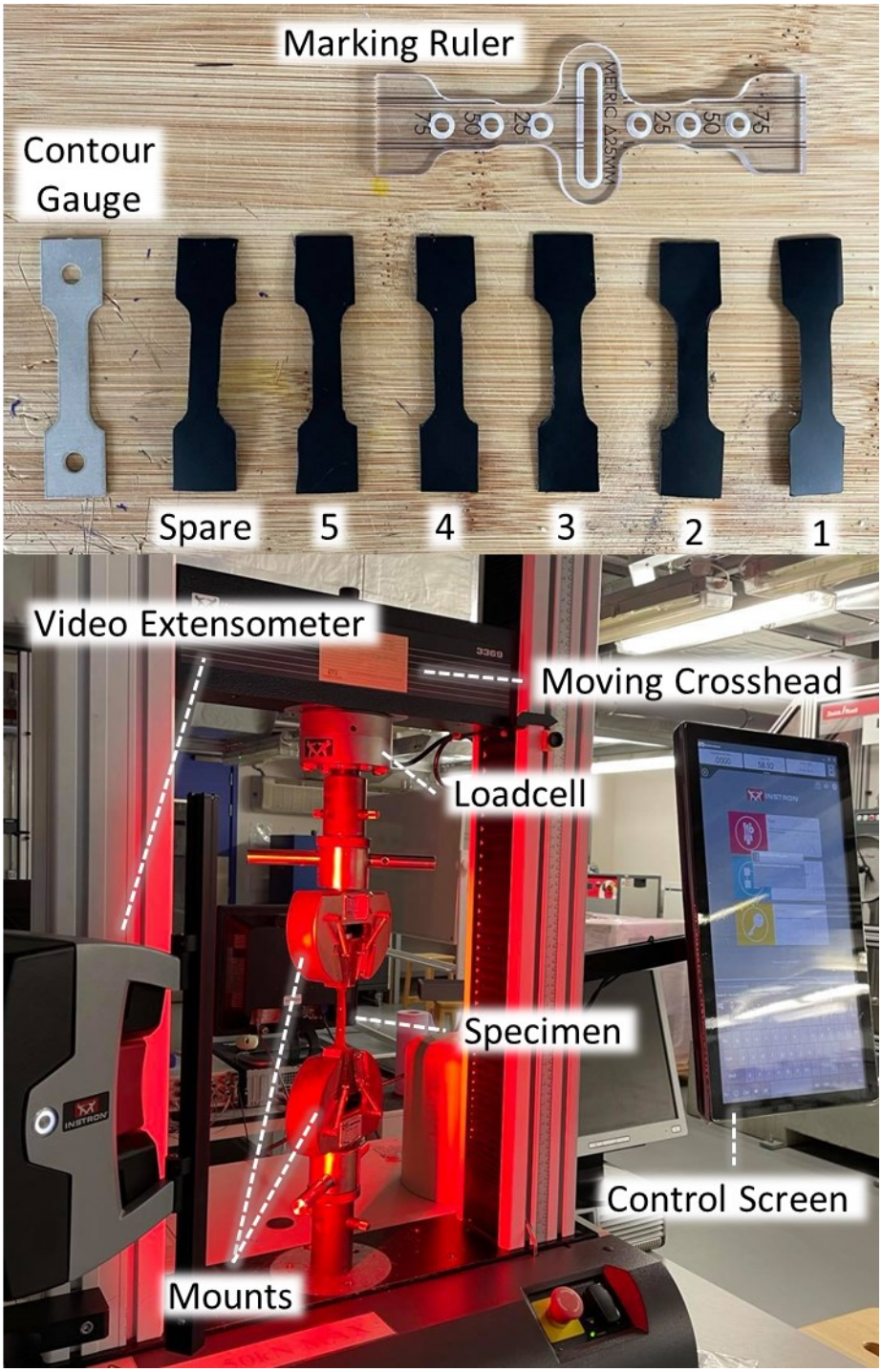


*Figure 60 – Experimental setup for obtaining the material properties of the polycarbonate that forms the helmet shell in study.*

and Ashby's book titled Cellular Solids: Structure and Properties, which have previously been successfully used to model helmeted impacts [256]. The equations predict the behaviour at three distinct phases of compression – namely phase I, II and III. Phase I is the elastic compression whereby the foam elastically deforms through bending and buckling of the cell walls. This stage usually exists at very low strain which relates to the stress as follows:

$$\sigma = E\varepsilon + \frac{p_0 \varepsilon}{1 - \varepsilon - R} \tag{37}$$

Where $E$ is the elastic modulus of foam which itself can be approximated through the relationship $E = AR^2 + BR$ where $A$ and $B$ are material constants determined and validated for EPS helmet impacts by Cernicchi et al. [256], being $6.64 \cdot 10^9$ Pa and $2.58 \cdot 10^7$ Pa for EPS respectively. $R$ is the relative density of the foam i.e. $\rho_f / \rho_b$ - the density of the foam divided by the density of the bulk parent material (polystyrene in the case of EPS). The second term of Equation (37) accounts for the stiffness contribution of the air trapped within the cells. Hence, $p_0$ is initial cell internal air pressure assumed to be equal to the atmospheric pressure (101.3 kPa).

Phase II is where the predominant amount of impact energy is dissipated through plastic crushing and collapse of the cell walls. The compressive stress-strain relationship in this phase can be approximated as follows, where it is assumed that the cells collapse at a near-constant stress, rising gently as the air pressure increases:

$$\sigma = \sigma_Y + \frac{p_0 \varepsilon}{1 - \varepsilon - R} \tag{38}$$

The yield stress ($\sigma_Y$) in Equation (38) is related to the relative density as $\sigma_Y = CR^{1.5}$ where the constant $C$ = $3.77 \cdot 10^7$ Pa for EPS [256].

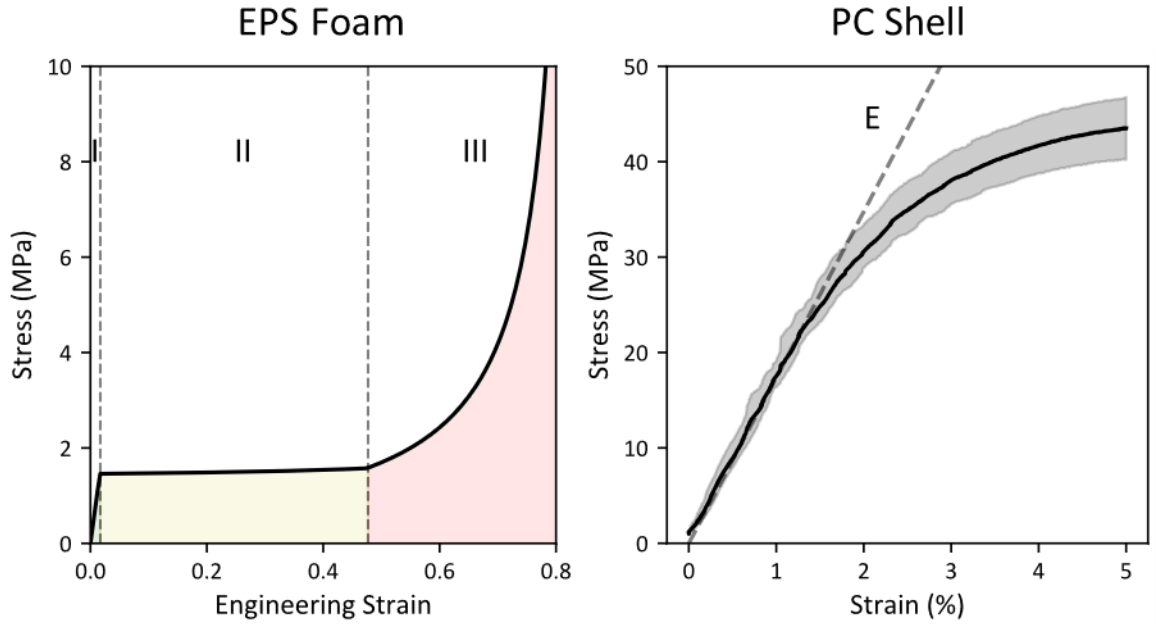


*Figure 61 – Left: compressive stress-strain curve of EPS foam with a density of 120 g/l as used in the finite element model of the conventional helmet. Right: Tensile stress-strain curves of the PC helmet shell material.*

Finally, after most of the cells have entirely collapsed, the stress sharply rises with any further compressive strain as cell walls begin self-contact, forming more of a bulk. This is phase III, which is known as densification and is described as:

$$\sigma = \frac{\sigma_Y}{D}\left(\frac{\varepsilon_D}{\varepsilon_D - \varepsilon}\right)^m + \frac{p_0 \varepsilon}{1 - \varepsilon - R} \quad (39)$$

The material constants $D$ and $m$ are 2.3 and 1 respectively for EPS [256]. The resulting stress-strain curve derived using these equations can be found in Figure 61.

The outer shell is 0.75mm thick polycarbonate (PC) which is moulded onto the EPS foam during manufacturing. Preliminary results showed that the shell dissipated only 8% of the energy during impact. Hence, a linear elastic model was used (MAT_01, LSTC) to model the stress-strain behaviour of the polycarbonate. The tensile modulus of the PC was determined from dog-bone tensile specimen cut out directly from the shell and tested using an Instron mounted with a video extensometer (Figure 60). The results of these tests indicated that the mean elastic modulus $E$ of the polycarbonate used in the shell is 1740 ± 110 MPa.

#### *6.2.2.3 Cell Arrays*

The cell arrays are constructed using a unit cell which comprises of a circular wall with axisymmetric curvature as annotated in Figure 62. In a previous study, these cellular arrays were morphed to different curvatures to assess the influence of this on their axial and shear response under compressive-shear impact loading resulting from oblique impacts. These same cell arrays are now adapted to the helmet as outlined in the next section.

The cell arrays were additively manufactured using a PolyJet multi-material 3D-printer (Connex3, Objet500, Stratasys, USA) which utilises multi-material jetting technology. The cell arrays were then cleaned and tested using a bespoke impact rig in both axial and oblique impacts. This allowed for the development and thorough validation of a finite element model which captures the large-strain visco-hyperelastic response of both the constituent material, Agilus30, and the cell arrays themselves in their array configuration. The validation of both the Agilus30 bulk material model and the finite element model of the manufactured cell arrays during both axial and oblique impacts are detailed in separate publications [20].

#### *6.2.2.4 Retrofitting*

To assess the performance of the new cell arrays presented here in comparison to the conventional EPS liner, it was important to keep all other aspects of the assessment unchanged. This included the helmet shell, headform, impact velocities, angles, and locations.

Hence, a Python code was developed to replace the EPS foam with the new cells using the original helmet shell. This was achieved using a series of transformations applied to the nodes of the finite element mesh of each individual cell using the *INCLUDE_TRANSFORM keyword in LS-DYNA (R10.0, LSTC, US). The transformations were informed by the shell element normal at each of the chosen

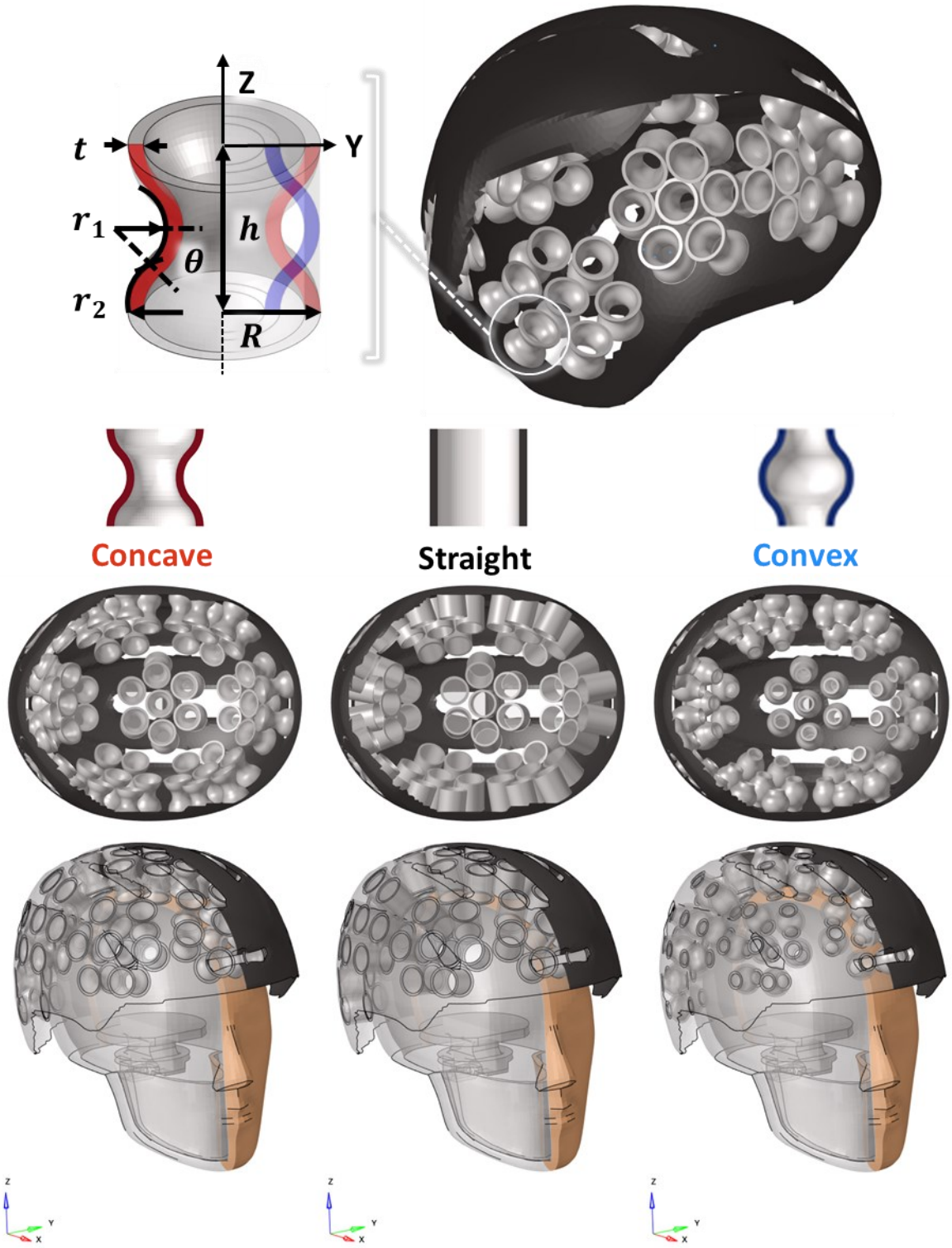


*Figure 62 – Top left shows a unit cell of the retrofitted helmet liner with a section cut showing the height $h$ and radius $R$, wall thickness $t$ and arc radii $r_1$ and $r_2$ and arc angle $\theta$. In this study, three variations were chosen, where the following base values were used: $h$ = 25mm, $R$ = 12.5mm and $t$ = 2mm. The arc radii $r_1$ and $r_2$ and arc angle $\theta$ were reversed to obtain the concave and convex cell variants assessed in this study. The helmeted head models fitted with concave, straight and convex cells are shown in the bottom left, middle, and right respectively.*

locations, forming an inward normal-facing array of 7 cells at these locations. In total, each helmet had 9 arrays resulting in 63 cells. The cell arrays were adhered to the helmet shell by means of a tied

contact model at the shell-facing side of the array. The head-facing side of each of the 7 cells within an array were connected using a nodal rigid body to model a plate they would adhere to which is free to displace relative to the head.

#### *6.2.2.5 Injury Metrics*

The kinematics data of the tests were processed to obtain four brain injury metrics: peak translational acceleration (PTA), peak rotational acceleration (PRA), peak rotational velocity (PRV) and brain injury criterion (BrIC) [16] (See Section 3.2.3, Eq. (13)-(16)). As discussed previously, PTA is used as an injury criteria in most bicycle and motorcycle helmet impact test standards as it is associated with risk of skull fractures and focal injuries [257,258]. PRA has been suggested as a metric for predicting SDH [259,260]. PRV and BrIC have been shown to predict risk of diffuse axonal injuries [16,261]. There has been debate on whether peak rotational acceleration or velocity are better metrics for predicting brain injury. Takhounts et al. developed BrIC based on injury risk curves and evaluates rotational velocity, not rotational acceleration, as a determinant of brain injury risk [16]. On the other hand, several studies have shown that peak rotational acceleration is a key metric to monitor for predicting the onset of subdural hematoma and brain tissue strain [260,262]. Hence, both metrics have been included in the analyses.

### 6.2.3 Brain Injury Modelling

In addition to the kinematic injury metrics described above, the Imperial College Traumatic Brain Injury FE model has been used to determine the strain experienced by the brain globally, in the corpus callosum and the sulci. As detailed in Section 2.1.2, these known to be linked with traumatic brain injuries such as diffuse axonal injury when strained.

A method like that described in Chapter 3 (Figure 18) was employed. However, in this case, the procedure started with the accelerations from the CoG of the finite element Hybrid III headform, rather than a physical one. This meant that an initial oblique impact simulation with the helmet and Hybrid III headform was carried out, from which the acceleration components of each helmet (conventional and retrofitted) resulting from the impacts were extracted and then applied to the skull at the CoG of the ICL TBI model in a separate simulation. Simulations were carried out using the non-linear explicit dynamics solver LS-DYNA (R10.0, LSTC, US). Each simulation spanned 30 ms. These durations ensured full capture of the peak brain deformation and strains resulting from the impact. The simulation outputs were postprocessed to determine the maximum value of the 1$^{st}$ principal Green-Lagrange strain at each element of the brain (called strain hereafter) and results were written into a NIFTI (Neuroimaging Informatics Technology Initiative) file for further analysis.

For more details on this process, see Section 3.2.4 and 3.2.5.

## 6.3 Results

### 6.3.1 Validation

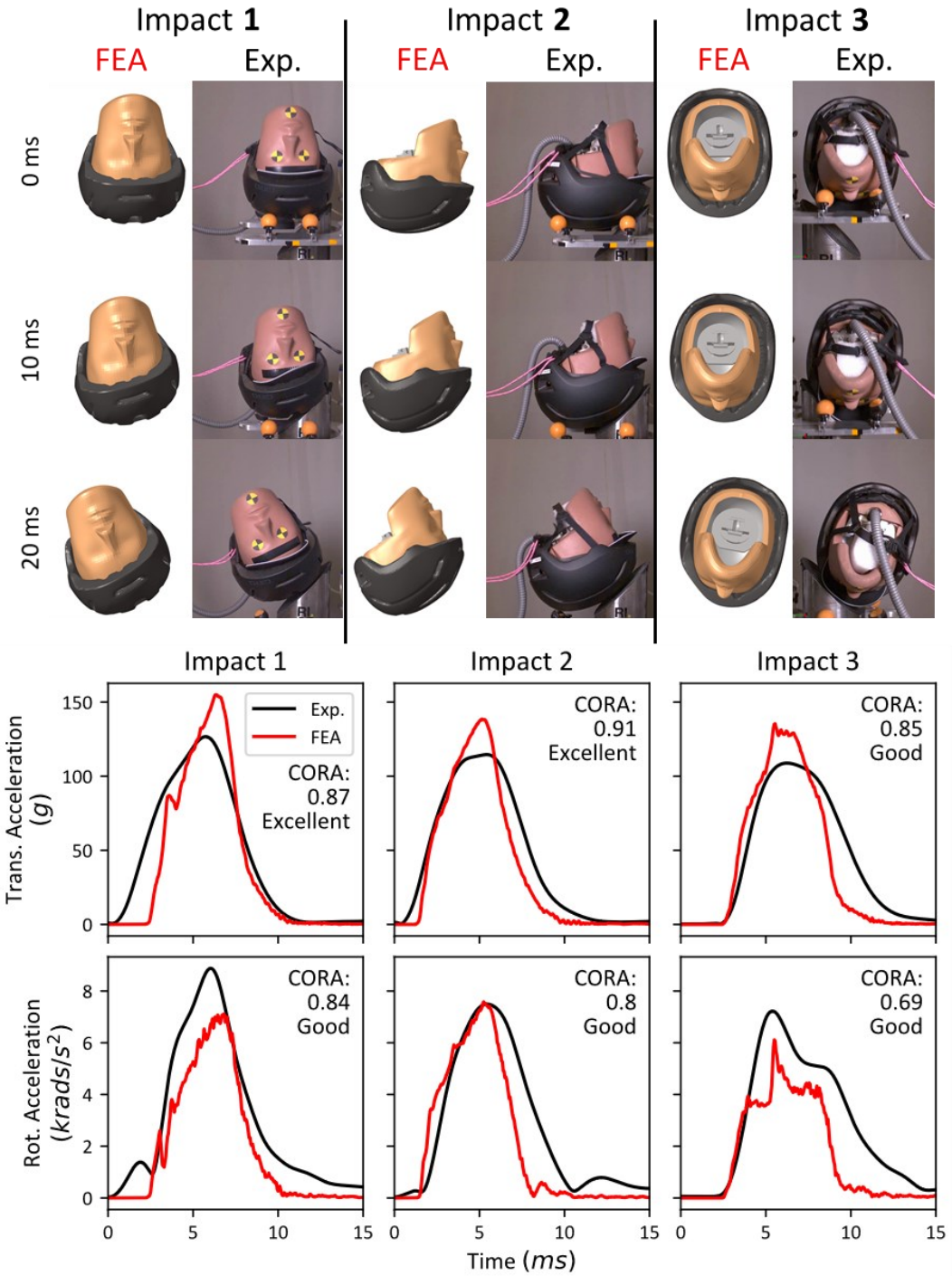


*Figure 63 – Validation of the helmet finite element model in three oblique impact conditions. The top half of the figure shows the figure shows animation frames at 0 ms, 10 ms and 20 ms of the FEA and experimental predictions. The bottom half shows the resultant translational and rotational time-histories of each impact showing the correlation between the experimental results and finite element model predictions.*

The test and validation results of the FE model of the helmeted impacts showed 'Excellent' to 'Good' correlation as per the CORA score banding. CORA scores ranged from 0.85 – 0.91 and 0.69 – 0.84 for resultant translational and rotational accelerations of the headform respectively (Figure 63).

The overall average CORA score for all impacts and readings is 0.83 which lies in the top quartile of the 'Good' CORA band. This gave confidence in the fidelity of the FE model of the helmet head impacts allowing us to carry it forward for further analysis comparing performance of different cell structures.

### 6.3.2 Performance Comparison

The comparison of kinematics and brain injury metrics between the helmets fitted with cell arrays and the conventional helmet foam showed remarkable improvements in most cases.

#### *6.3.2.1 Kinematic Metrics*

Helmets fitted with cell array liners reduced all the assessed kinematic injury metrics in comparison to the conventional helmet in all impacts except for PTA in impact 3 with convex cell liners which, upon assessment of the acceleration pulses in that impact, was due to a late, sharp, and short peak in translational acceleration indicating the liner bottomed out (Figure 66).

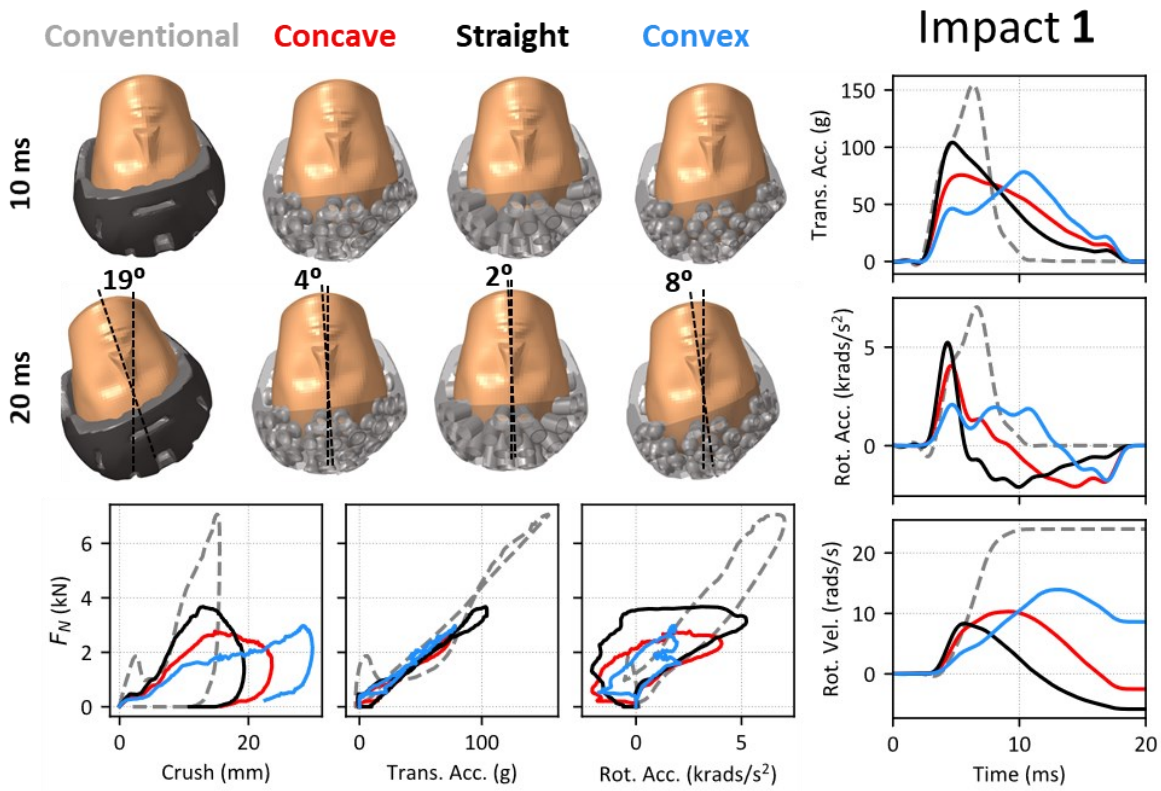


*Figure 64 – Animation frames at 10 and 20 ms after impact, and translational and rotational time-histories of each helmet in impact 1.*

#### 6.3.2.1.1 PTA

Concave cells reduced the PTA across all impacts, particularly in impact 1 which showed a 50% reduction. Impact 2 and 3 resulted in reductions of 34% and 32% respectively, resulting in PTA less than 100 g in all impacts. Comparing the PTA of concave cell impacts to one another, PTA was lowest in impact 1 (78 g), followed by impact 3 (90 g) and impact 2 (91 g).

Similar improvements were observed with impact 1 using convex cells, which reduced the PTA by 49%. However, the PTA reductions were less pronounced with convex cells in impact 2, reducing PTA by only 1%, and increased PTA in impact 3 by 80%, reaching 238 g due to bottoming-out. Hence, when observing PTA for the convex cell impacts, impact 3 was worst performing (238 g), followed by impact 2 (137 g) and impact 1 (79 g).

Straight cells reduced the PTA across all impacts in comparison to conventional helmets, albeit increasing PTA in comparison to cell-fitted helmets in impact 1. Comparing the PTA of straight cell impacts to one another, PTA was lowest in impact 3 (87 g), followed by impact 1 (104 g) and impact 1 (114 g).

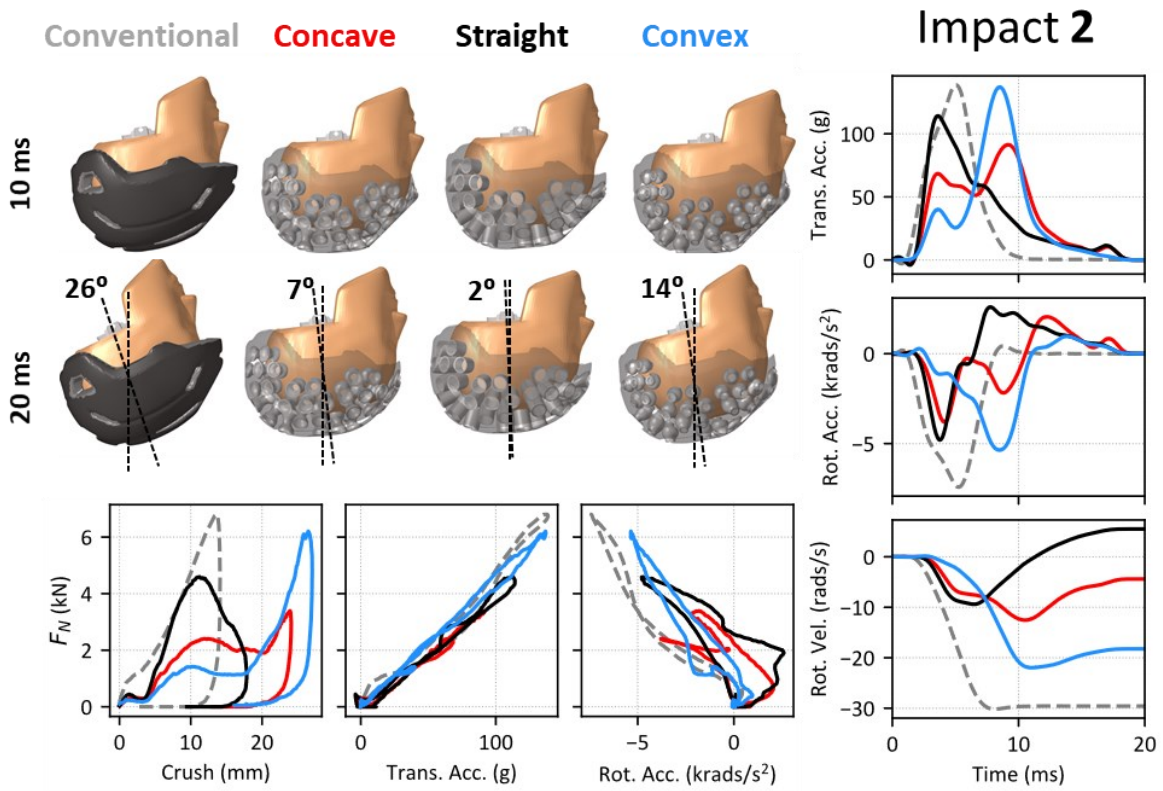


*Figure 65 – Animation frames at 10 and 20 ms after impact, and translational and rotational time-histories of each helmet in impact 2.*

#### 6.3.2.1.2 PRA

Observing the rotational kinematics, concave cells once more reduced the PRA and PRV across all impacts. The largest reduction in PRA was observed in impact 3 (42%), closely followed by impact 2 (41%) and impact 1 (22%). The same order followed when comparing absolute PRA across concave cell impacts, where impact 3 led to the lowest PRA, followed by impact 2 and impact 1 (3.1, 4.4 and 5.4 krads/s$^2$ respectively).

Likewise, convex cells showed reductions to PRA across all impacts, with impact 1 showing the largest reduction (64%) followed by impact 2 (30%) and impact 3 (13%). However, comparing across the convex cell impacts, PRA was lowest in impact 1 followed by impact 3 and 2 (2.5, 4.6 and 5.3 krads/s$^2$ respectively).

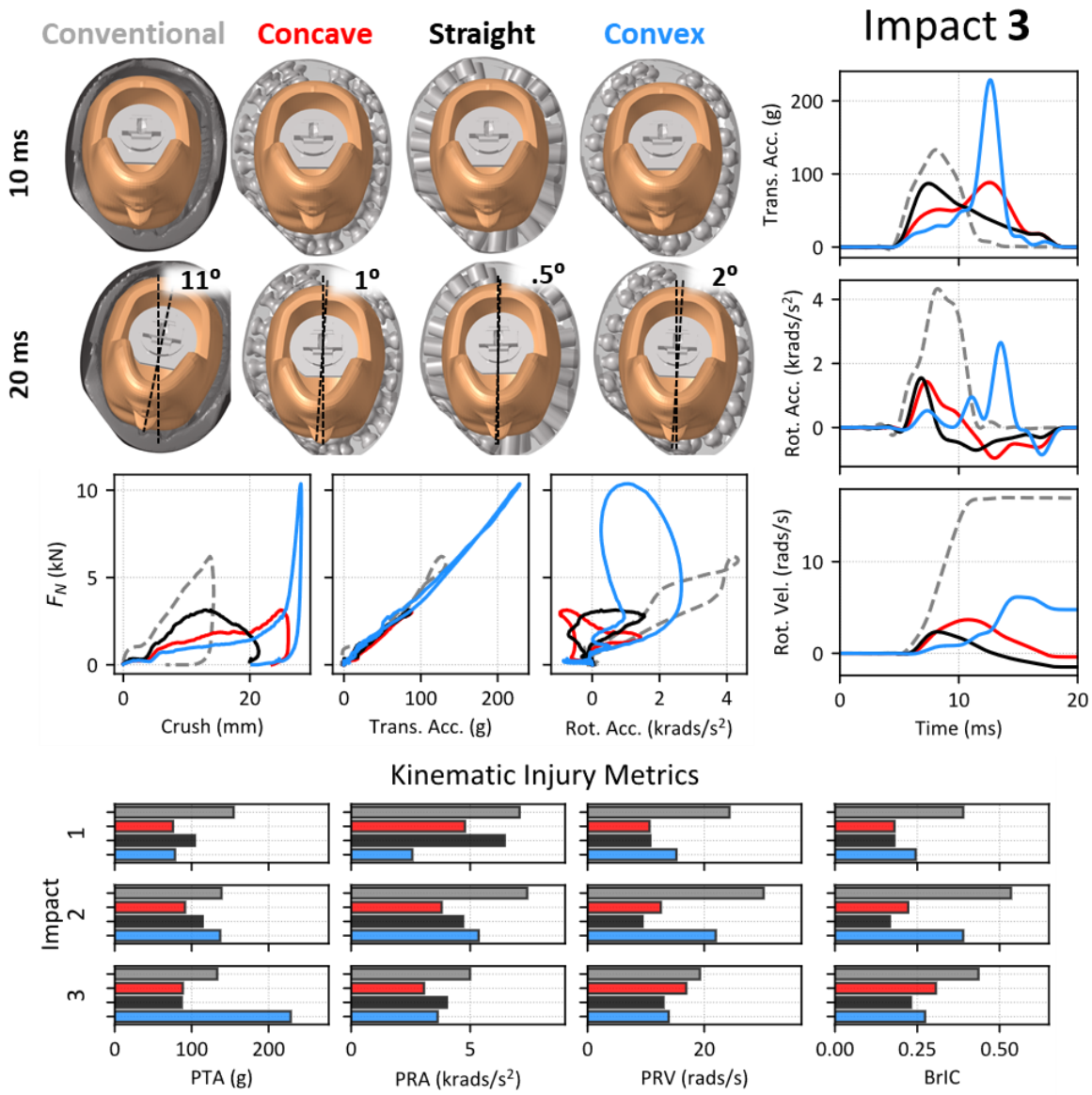


*Figure 66 – Animation frames at 10 and 20 ms after impact, and translational and rotational time-histories of each helmet in impact 3. The bar chart shows a summary of the kinematic injury metrics (PTA, PRA, PRV and BrIC) of each of the helmets in each of the impact conditions.*

PRA was reduced with straight cells in comparison to conventional helmets, however resulted in the highest PRA in comparison to the cell-fitted helmets. The exception to this is in impact 2 where the PRA with straight cells was exceeded with convex cells due to the bottoming-out of convex cells in this impact. Comparing across impacts, PRA was lowest in impact 3 followed by impact 2 then impact 1. (4.0, 4.7 and 6.4 krads/s$^2$ respectively).

#### 6.3.2.1.3 PRV

The PRV improvements observed with concave cells were largest in impact 2 (58%) followed by impact 1 (56%) and impact 3 (9%). However, comparing across the concave cell impacts, PRV was lowest in impact 1 followed by impact 2 and 3 (11, 13 and 18 rads/s respectively).

Convex cells showed the largest reduction in PRV in impact 1 (37%) followed by impact 3 (28%) and impact 1 (28%). However, comparing across the convex cell impacts, PRV was lowest in impact 3 followed by impact 1 and 2 (14, 15 and 22 rads/s respectively).

Straight cells generally had the lowest PRV across all helmets, both conventional and cell-fitted across all impacts. Comparing across the straight cell impacts, PRV was lowest in impact 2 followed by impact 1 and 3 (9.4, 10.7 and 13.0 rads/s respectively).

#### 6.3.2.1.4 BrIC

The results and comparison of BrIC align with those from PRV due to the nature of the derivation of BrIC from PRV. Concave cells showed the largest reduction in BrIC in impact 2 (58%) followed closely by impact 1 (54%) and impact 3 (27%). However, comparing the BrIC across the concave cell impacts, BrIC was lowest in impact 1, followed by impact 2 and 3 (0.18, 0.22 and 0.32 respectively).

Convex cells showed the largest reduction in BrIC in impact 1 (37%) followed closely by impact 3 (36%) and impact 2 (27%). Comparing the BrIC across the convex cell impacts, BrIC was lowest in impact 1, followed by impact 3 and 2 (0.25, 0.28 and 0.39 respectively).

Straight cells generally had the lowest BrIC across all helmets, both conventional and cell-fitted across all impacts. Comparing across the straight cell impacts, BrIC was lowest in impact 2 followed by impact 1 and 3 (0.17, 0.18 and 0.23 rads/s respectively).

### *6.3.2.2 Brain Injury Metrics*

All helmets with cell array liners reduced the brain strain both globally and in both regions of interest, CC and Sulci, in comparison to the conventional helmet (Figure 67). Generally, the improvements were more pronounced with concave cells than convex in impact 2 and 3, whereas the opposite was true for impact 1. Straight cells often resulted in 90$^{th}$ percentile strains between that of concave and convex cells.

#### 6.3.2.2.1 Global

Assessing the 90$^{th}$ percentile strain across the entire brain, we observe that concave cells led to the largest reductions in impact 2 (66%) followed by impact 3 (55%) and 1 (52%). Nonetheless, comparing across the concave impacts, the lowest global 90$^{th}$ percentile strain was recorded in impact 3 followed by 2 and 1 (0.033, 0.037 and 0.044 respectively).

On the other hand, convex cells showed the largest reductions in global 90$^{th}$ percentile strain in impact 1 (69%) followed by impact 2 (42%) and 3 (35%). Comparing across the concave impacts, the lowest global 90$^{th}$ percentile strain was recorded in impact 1 followed by 3 and 2 (0.029, 0.048 and 0.063 respectively).

For straight cells, impact 3 resulted in the lowest global 90$^{th}$ percentile strain followed by impact 2 and finally impact 1 (0.040, 0.048 and 0.060 respectively). The same trend was observed with convex cells which exhibit similar shear stiffness, however convex cells consistently led to higher strain across all three impacts than straight cells.

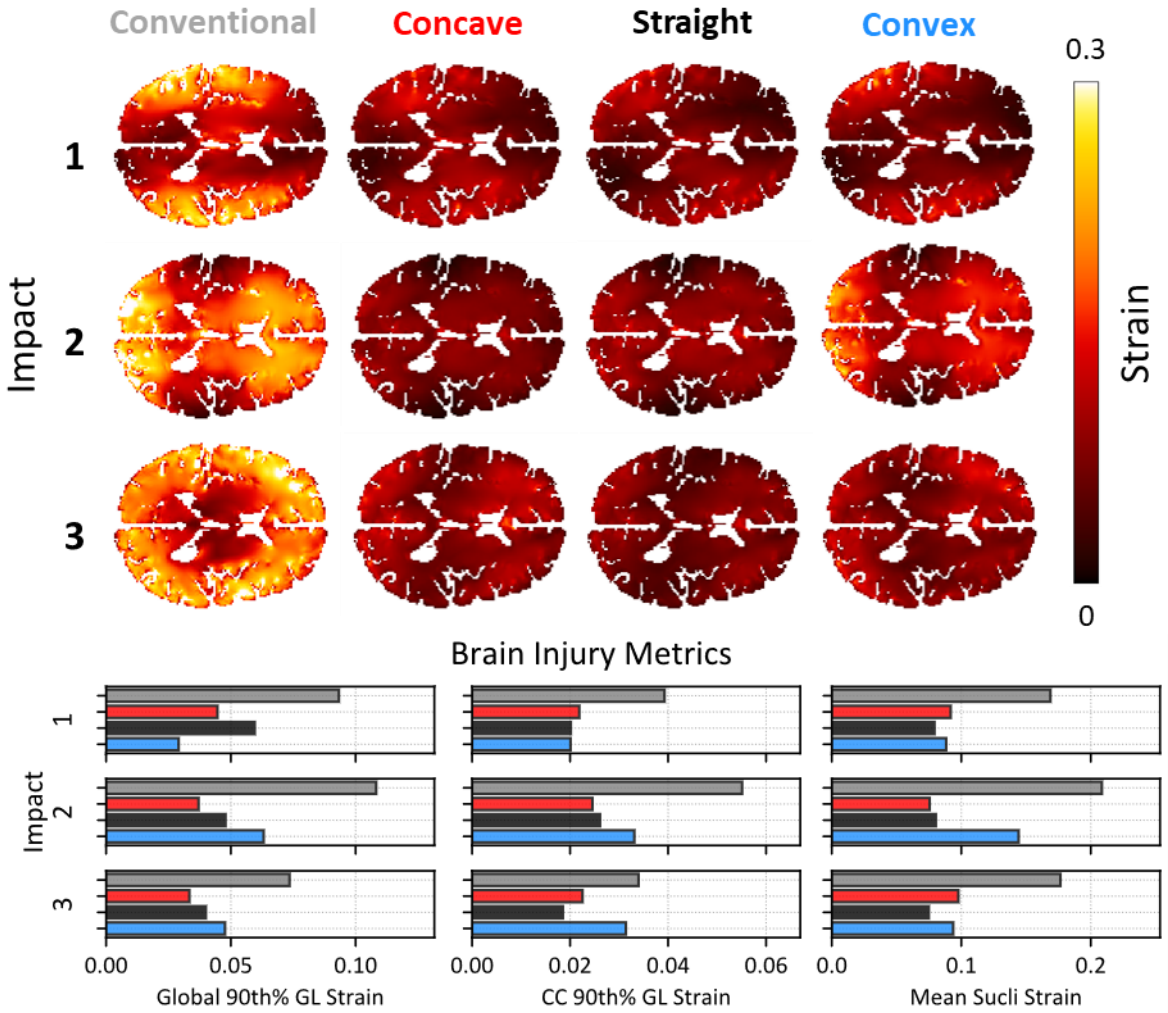


*Figure 67 – Horizonal (z-normal) plane sections of the brain showing strain contour predictions for each helmet in all impact conditions. The bar chart below summarises the 90$^{th}$ percentile GL strain and the mean strain across the sulci for each helmet in each impact condition.*

#### 6.3.2.2.2 Corpus Callosum

Assessing the 90$^{th}$ percentile strain across the CC, we observe that concave cells led to the largest reductions in impact 2 (55%) followed by impact 1 (44%) and 3 (34%). Nonetheless, comparing across

the concave impacts, the lowest 90$^{th}$ percentile CC strain was recorded in impact 1 followed by 3 and 2, albeit being only marginally different from one another (0.022, 0.023 and 0.025 respectively).

On the other hand, convex cells showed the largest reductions in 90$^{th}$ percentile CC strain in impact 1 (49%) followed by impact 2 (40%) and 3 (8%). Comparing across the concave impacts, the lowest 90$^{th}$ percentile CC strain was recorded in impact 1 followed by 3 and 2 (0.020, 0.031 and 0.033 respectively).

For straight cells, impact 3 resulted in the lowest 90$^{th}$ percentile strain in the CC, followed by impact 1 and finally impact 2 (0.019, 0.020 and 0.026 respectively). The same trend was observed with convex cells which exhibit similar shear stiffness, however convex cells consistently led to lower strain in the CC than straight cells in impact 3 albeit bottoming out.

#### 6.3.2.2.3 Sulci

Assessing the mean strain across all the sulci regions, we observe that concave cells led to the largest reductions in impact 2 (64%) followed by impact 1 (46%) and 3 (45%). Nonetheless, comparing across the concave impacts, the lowest mean sulci strain was recorded in impact 2 followed by 1 and 3 (0.076, 0.092 and 0.098 respectively).

On the other hand, convex cells showed the largest reductions in mean sulci strain in impact 1 (48%) closely followed by impact 3 (47%) and 2 (31%). Comparing across the concave impacts, the lowest mean sulci strain was recorded in impact 1 followed by 3 and 2 (0.088, 0.094 and 0.144 respectively).

For straight cells, impact 3 resulted in the lowest mean sulci strain, followed by impact 1 and finally impact 2 (0.074, 0.079 and 0.080 rads/s respectively). In comparison to convex cells which exhibit similar shear stiffness, straight cells resulted in higher mean strain in the sulci in impact 1 and 3 albeit bottoming out in the latter.

## 6.4 Discussion

We have presented the outcome of an investigation on the influence of novel cellular arrays decoupling axial and shear stiffness on the crash performance of a conventional bicycle helmet with particular interest in the oblique impact performance. Oblique impacts currently lead to rotational head motion which is known to be a key contributor to brain tissue strain and subsequent brain damage [14–17]. The results were promising and showed the potential improvements that are possible if we strive towards novel helmet technologies that leverage engineered cellular structures with controlled compressive-shear stiffnesses and entirely replace conventional cellular structures such as EPS foam.

### 6.4.1 Influence of Shear Stiffness

Our results show that convex (shear-compliant) cell arrays initially led to lower rotational acceleration and velocity in comparison to their concave (shear-stiffened) counterpart in all three impact conditions investigated. However, this effect was short lived, lasting only for the first ~5ms before the shear-complaint cells bottomed-out in two of the three impacts. This led to a sharp rise in both translational and rotational accelerations which in turn increased the rotational velocity. This is indicative that a substantial amount of the impact energy is dissipated via shearing of the cells around the impact zone as seen in Figure 68, which in turn means that shear-compliant cells may bottom out earlier than shear-stiffened counterparts with the same axial stiffness. Rarely do any of the cells deform purely axially i.e. with no shear deformation. Even the cells directly below the impact zone undergo complex deformation that includes a mixture of axial compression, shear and even bending as seen in Figure 68. Hence, introducing shear-compliance in helmets should be carried out with cautious consideration for how other stiffness components influence the considered set of impacts.

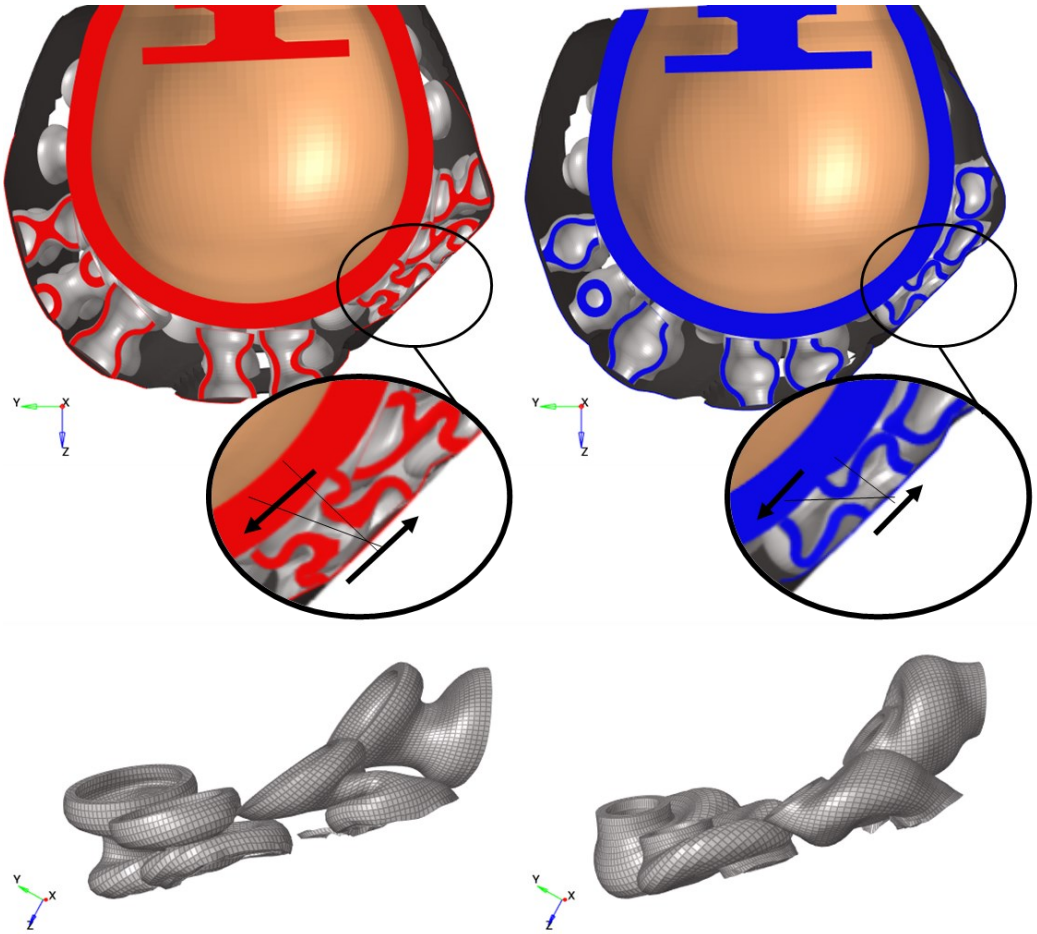

*Figure 68 – Section cut view of the helmeted head with concave (left) and convex (right) cell liners with close-up views showing the shearing of the cells at and around the impact zone. As concave cells have a higher shear stiffness than convex cells, helmets with concave cells had a lower shear strain as seen in the close-ups. Helmets with the shear-stiffened cells had a larger accelerations and energy dissipation at the start which meant the crush distance was reduced.*

The bottoming-out of the shear-compliant cells was most severe in impact 3 where the impact location was near the temple and closest to the edge of the helmet shell. This part of the helmet is known to have reduced stiffness compared to the crown area usually tested by helmet standards which has added shell stiffness owed to the double-convex curvature [115]. Indeed, the shear-compliant cells outperformed the shear-stiffened cells in impact 1 as this was nearest to the crown and hence neither helmet bottomed-out. This reveals that, if tuned well, shear-compliant cells can reduce rotational head motion, brain tissue strain and hence injury likelihood. Hence, it may be useful to place cells with varying amounts of shear stiffness in a single helmet, with the most shear-compliant cells near the crown and the least near the temples.

### 6.4.2 Influence of Axial Stiffness

The second comparison is looking at how axial stiffness plays a role when both cells have low shear stiffness. Cell arrays with straight walls had a high axial stiffness in contrast to those with convex cell walls which were axially compliant. This, as expected, resulted in higher PTA in impact 1. The axially compliant cells resulted in higher PTA in impact 2 and 3 due to bottoming out. This does not come as a surprise given that reduced axial stiffness and similar shear stiffness of convex cells in comparison to straight cells means that convex cells are able to dissipate less energy in deformation overall.

Interestingly, the axial stiffness resulted in higher PRA as seen in impact 1. This is likely due to the force vector not passing through the head centre of gravity and hence the larger normal force that results from the axially stiff cells contributes to an increased moment about the head and hence a higher PRA. However, the peak rotational velocity, and hence BrIC, were either the same or lower in axially stiff cells in comparison to axially compliant cells. Observing the rotational acceleration and velocity curves about each axis of predominant rotation (X-axis) of impact 1 sheds some light into why this is the case. With axially stiff cells, the headform rotational acceleration and deceleration is more rapid than with axially compliant cells, hence giving the headform less time to reach a higher PRV. Moreover, as seen in Figure 64, the rotational acceleration with straight cells remains in the negative quadrant (deceleration) for longer than with convex cells, leading to the overall PRV with straight cells being lower.

In any case, this comparison highlights that axial stiffness plays a significant role in the resulting rotational head kinematics, both rotational acceleration and velocity. Although this is the first study confirming this for such cellular arrays, it remains in agreement with conclusions of previous studies which found that the normal force vector component, which is a factor of the foam stiffness, may not pass through the head centre of gravity, and hence generates to a moment about the head leading to rotational acceleration whereby the direction of rotational acceleration reversed ~5ms after impact

as observed here [72]. Interestingly, the authors observed this with direct impacts where the head impacted a stationary anvil perpendicularly i.e. with no initial velocity tangential to the impact surface.

### 6.4.3 Comparison to the Conventional Helmet

Almost all metrics indicated that cell-fitted helmets outperformed the conventional foam-fitted counterpart in all the assessed metrics in all impacts with one exception: PTA when the cells bottomed-out in impact 3. Observing the force-displacement plots, we can see that this is likely due to the high foam stiffness in comparison to the cells which meant that much of the available crushing distance remained unutilised with conventional EPS foam.

The reason helmets today employ such stiff foams that do not utilise the entire crushing distance for impacts with flat surfaces is because they must also pass impact tests against kerbstone and hemispherical anvils [60]. Such anvils distribute the impact force over a much smaller area leading to a large pressure and complex stress state in the impact zone. To pass these tests successfully, a higher foam stiffness is often required to ensure it does not bottom-out. This makes kerbstone and hemispherical anvils the constraining requirement for the choice of helmet foam stiffness and hence density which is suboptimal for impacts against flat surfaces [60]. In turn, as observed here, this also leads to larger rotational accelerations, velocities, and brain strain in oblique impacts. A limitation of helmets employing cell liners as those explored here is that they reduce the overall bending stiffness of the helmet, i.e. the bending stiffness of the shell and foam combined, and hence may bottom-out and underperform in impacts against the more severe tests mentioned earlier i.e. against hemispherical and kerbstone anvils. A potential way to overcome this is to increase the shell stiffness such that the shell engages more of the cells in the helmet rather only those beneath the small impact zone resulting from kerbstone impacts.

### 6.4.4 Reversal of Rotational Acceleration Direction in Retrofitted Helmets

As observed, the helmets retrofitted with cell arrays experienced an interesting reversal of rotational acceleration and velocity in all three impacts in contrast to the conventional helmet which did not experience this in any of the impacts. This was initially hypothesised to be caused by a change in the ratio of the normal and tangential forces at the impact site which reversed the side the resultant force vector passed through relative to the headform centre of gravity. Observing the plots showing the normal force against the rotational acceleration in Figure 64 - Figure 66 revealed that the direction of rotational acceleration often reversed at a constant normal force and without a change in the direction of tangential force. This indicated that the hypothesis is true, and that a shift in the centre of pressure on the headform and the resultant force vector relative to the head centre of gravity during impact

resulted in the reversal of the rotational acceleration. Similar observations have been made by Mills et al. in previous studies looking at oblique impact testing of bicycle helmets [263].

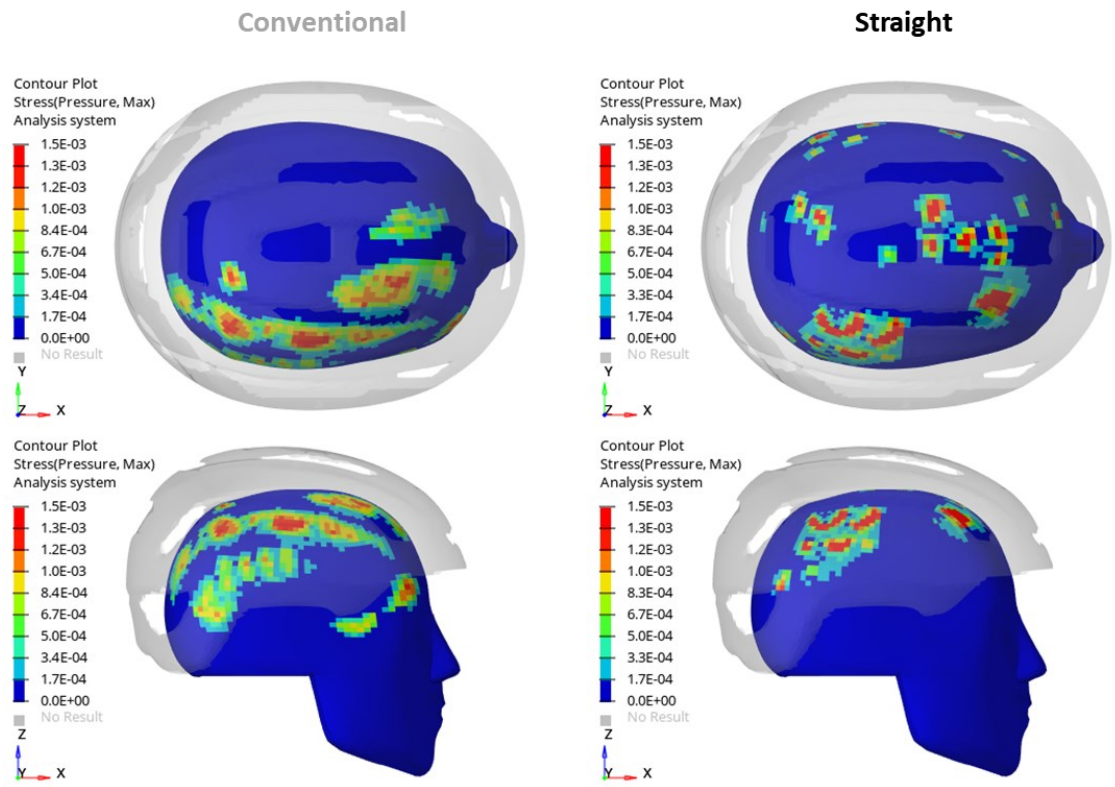


*Figure 69 – Enveloped pressure distribution on the head across time in impact 1 resulting from contact with the conventional (left) and straight cell-fitted (right) helmet liners. The conventional helmet displays a much more asymmetric pressure distribution leading to a large bending moment about the head, whereas the straight cells resulted in a more symmetric distribution later in the impact due to the flexibility of the shell, resulting in an eventual reversal of the rotational acceleration.*

Hence, the pressure distribution on the headform was investigated to determine whether the centre of pressure played a role. Indeed, as shown in Figure 69, the pressure distribution of the helmets with cell arrays differed from that of the conventional helmet, being more asymmetric with conventional helmets than any of the cell-fitted helmets in all impacts. In all impacts, the rotational acceleration of all helmets, both conventional and cell-fitted, increased in the same direction due to the shear force at the zone where the head initially begins to crush the liner. However, the bending stiffness of the foam is added to that of the shell through the adhesion in the conventional helmet which serves to increase the bending stiffness in comparison to the cell-fitted helmets. As the helmet and head are not perfectly round i.e. of dissimilar curvatures, the conventional helmet begins to contact the head further from the contact site and hence introduces a large torque and rotational acceleration. However, in the cell-fitted helmets, the shell stiffness is much lower due to the absence of the foam and hence contact is more even across the head as it begins to pocket the liner. This results in a

reduction and reversal of the rotational acceleration as the centre of pressure shifts during the impact, resulting in much more favourable peak rotational velocity and brain strain.

### 6.4.5 Limitations and Future Work

There are several limitations that come as part of this study. Although the cells showed some serious improvements in comparison to conventional helmets, it would be ideal to assess the performance of the conventional helmets against the cell-fitted helmets in a manner that allows for a fairer comparison. In an ideal situation, the foam thickness would be the same as the cell heights at all locations across the helmet to match the utilised crushing distances. Moreover, it would also be fairer for the helmet foam to have a compressive stiffness that matches that of the cells used. However, given that the compressive stiffness of the cells was one of the variables of the study through variation of the cell shape, satisfying this criterion would mean assessing against helmets with different foam densities that match each of the cell axial stiffnesses. Nonetheless, this would be pointless without first ensuring the available crushing distance of the cells and the foam are identical around the helmet which would be difficult to achieve due to the channels and grooves introduced in modern helmet foams for aerodynamic reasons. This gives them a complex interior surface which would be difficult to conform the cell arrays to both computationally and physically for such a comparison.

If the above limitations are addressed in future work, another challenge would remain which would be matching the helmet masses. The cell-fitted helmets were heavier than conventional helmets which is not favourable given that helmets should be as light as possible to reduce strain on the neck and kinetic energy during impact. As the shell was identical for all assessments (77.5 ± 2.5 g), the differences in mass are solely attributed to the liner. The original foam liner weighed 217.5 ± 2.5 g, whereas the concave, straight and convex cell array liners weighed 234.3 g, 272.8 g and 234.3 g respectively. The added mass stems from the fact that polystyrene, the parent material of EPS, is plastic and is stiffer than the Agilus30, the parent elastomer of the cells. However, Agilus30 has the added benefit of being recoverable, enabling it to sustain repeat impacts, as well as flexible enough to fold in case of collapsible helmets, or inflate and deflate to sustain impacts of different severities. This is a paradigm shift from the long-standing conventional EPS foam helmets.

We used a Hybrid III headform in this study, which is one of the most biofidelic headforms with regards to the head shape and size, mass and moments of inertia [136]. However, it has a vinyl rubber skin which has a larger coefficient of friction in contact with fabric than the human scalp [137]. The coefficient of friction of the surrogate skin should be improved in future to produce more biofidelic test conditions. Similar to previous studies [138], we used an isolated headform, thus ignored the potential effects of the neck during impacts. Several studies have shown that primary peak loads from

head-first impacts are less affected by the presence of a neck [114,139]. Some studies on helmets have used a HIII neck, but this neck has limitations, such as stiffness in axial loading [75], which can have adverse effects on the results [110,113]. Future work should address the development of a surrogate neck that is biofidelic in head-first impacts.

In addition to the potential future work outlined above, one may assess different combination of cells to optimise the performance in different locations. I.e., in locations of double-convex curvature such as the crown, one may adopt convex cells for their reduced stiffness and shear compliance and adopt straight cells near the edge of the helmet shell such as the temples for their added compressive stiffness. However, it may not be possible to have a configuration optimal for all possible impact conditions, or even the three assessed in this study. It was apparent from the results that no impact was the worst for all helmets. Some of the worst for convex were the best for concave and vice versa. This emphasises the need to assess several impact conditions in future standards adopting an oblique impact condition as highlighted in Chapter 2 and previous studies [19].

It is noteworthy to mention that attempts have been made to conduct experimental impact tests, replicating the simulations presented, on physical prototypes of the cell-fitted helmets. However, several issues prevented this from happening, including difficulties removing the foam from the original helmet without damaging the shell, securing the cell arrays onto the shell, as well as cleaning the cell arrays. Cleaning the cell arrays was a time consuming and labour-intensive process and often resulted in damage of the cells, requiring reprinting of the entire array once more. In future, a better method of manufacturing the cell arrays may be developed.

## 6.5 Conclusion

We have assessed the influence of shear and axial stiffness of novel cell arrays on the oblique impact response of a retrofitted bicycle helmet, and how this compares to the conventional helmet. The hypothesis was that lower shear stiffness would lead to lower rotational acceleration and brain strain, and that higher axial stiffness would lead to larger translational acceleration with marginal effect on rotational acceleration and brain strain. The study was enabled by the unique difference in shear stiffness of concave and convex cells, whereby the axial stiffness was unchanged, and straight and convex cells whereby the axial stiffness differed, and shear stiffness was unchanged. The study revealed that:

- Shear-compliant cell arrays do not necessitate lower rotational acceleration as the resultant force vector leading to rotational motion (by not passing through the headform centre of gravity) is influenced by both shear and axial liner stiffness. Optimising this resultant force vector to pass through the centre of gravity and hereby eliminating rotational head motion is

complicated and may require shear-stiffness or shear-compliance depending on the impact scenario and parameters such as coefficient of friction, etc.

- Cell arrays with similar axial stiffness yet lower shear stiffness often bottomed out. Hence, a considerable amount of energy is dissipated via cell shearing around the impact zone.
- In all cases, the kinematic and brain injury metrics indicated improvements with the novel cell arrays over conventional EPS foam. This is likely due to a combination of the high EPS foam stiffness, as well as the relatively higher bending stiffness of conventional helmets by nature of the design and manufacture of the conventional helmets whereby the helmet and foam are bonded.

This study provides an early glimpse on the influence of the compressive-shear properties of cell arrays on the global response of oblique helmeted-head impacts. It reveals that there is rarely a 'one size fits all' approach to the problem and that several impact conditions and scenarios must be assessed to determine the optimal compressive-shear properties for a helmet liner with the aim of minimising rotational head motion and consequential brain injury likelihood.

# 7 Conclusions and Future Work

In this thesis, we started by reviewing the literature around rotational head motion and its relevance to brain injury. We then reviewed how conventional helmets and testing standards are lagging in addressing oblique impacts that lead to brain injury, and how the industry is responding to improving helmets – the primary protective mechanism for cyclists and many other vulnerable road users.

We then tackled the first hypothesis in Chapter 3; *Helmet technologies that include shear-management layers will reduce the rotational head motion and hence reduce brain tissue strain*, by assessing how current helmet technologies with shear-management and rotational damping systems such as MIPS, WaveCel and SPIN, compare with conventional helmets in different oblique impact conditions. The comparison showed that, although improvements offered by these technologies were observed, the extent of the improvement was highly dependent on the impact location and angle, injury metric used, and the helmet to which the technology was added. There were instances where helmets with one of the technologies were worse, or significantly worse, than conventional helmets, and vice versa. Hence, incorporating different impact locations in future oblique impact test methods and designing helmet technologies for the mitigation of head rotation in different planes are key to reducing brain injuries in bicycle accidents, where helmets are worn. However, the chapter was limited in the number of cyclist helmets that were tested. Less than 10 conventional helmets were tested which is arguably a small control group to derive the statistics presented in the chapter. A similar limitation exists when looking at the helmets with novel technologies; only one WaveCel and two SPIN helmets were assessed – however this is more difficult to address given that these are the only models that exist. A better assessment may try to match the conventional helmets in terms of mass, dimensions and liner thickness with those helmets employing the new technologies to provide a fairer comparison, as well as assess the helmets in both flat and oblique anvils with both female and male headforms to ensure robustness and consistency in any measured improvements. Female headforms are lighter and may not benefit from slip layers as much as they would from a softer foam.

In Chapter 4 we characterise the latest and most widely employed PolyJet elastomers, A30 and T+, under a range of loading conditions and strain rates for different print orientations. Moreover, we present a visco-hyperelastic model that accurately captures the time-dependent response of the PolyJet materials using stress relaxation and DMA tests. The results showed that the tensile stress at 50% strain of A30 was larger than T+ and increased by 67% across two orders of magnitude of strain rate for X- and Y- samples, and by more than 127% for Z- samples. Hence, A30 was carried forward as the parent material for the design of the cell arrays presented in Chapter 5 where the visco-hyperelastic material model accurately predicted the relaxation and monotonic tension-compression

responses of the elastomer and further validated for higher strain rates more relevant to the impact conditions typically experienced in a helmet crash. This enabled computational methods such as FEA to be utilised to explore the compressive-shear impact performance of several designs that could potentially replace foam liners via a design of experiments. In this chapter, we demonstrated the ability to tailor the shear and axial mechanical responses of a honeycomb arrangement of air-filled viscoelastic cell arrays in a relatively simple manner – by changing the axisymmetric curvature of the unit cell wall. Using a computational framework and a well-validated finite element model, different wall shapes and amplitudes were tested in axial and oblique impacts at speeds of 2.5 – 7.5 m/s in a full-factorial DoE. The results showed that concave cell arrays offer remarakbly larger shear stresses than their concave counterpart during oblique impacts (up to 300% increase), whilst minimally affecting the axial response. The average axial stress and internal energy increased with impact velocity by up to 200% due to the viscoelastic nature of the unit cells. This demonstrates the unique capacity of this new class of cellular topologies to significantly alter the shear response with simple shape changes that in future may be actively achieved during use, across a wide range of impact management applications.

Finally, these designs with their unique anisotropy were carried over for a specific use case in chapter 6 where the influence of axial and shear stiffness of helmet liners on the kinematic and brain injury response during oblique impacts was investigated. The hypothesis was that cell arrays with engineered shear-compliance which would lead to lower kinematic and brain injury metrics than those engineered to shear-stiffness. However, the results showed that reducing the shear stiffness of helmet liners does not necessitate lower rotational acceleration and velocity of the head due to complications of the impact physics around and further away from the impact site. A large portion of the impact energy is dissipated via shearing at the sides of the anvil contact area as helmets fitted with cells of the same axial stiffness, yet lower shear stiffness bottomed out in two of the three impacts. This also highlights the potential benefits of auxetic materials which involve more material in the compressed regions, hence stiffening gradually rather than stiffening sharply after bottoming out. Nonetheless, in all cases, the results were better than conventional helmets due to high foam stiffness which was likely driven by kerbstone and hemispherical impact test requirements.

One major limitation this project has faced is the constraints of today's multi-material jetting printers. Cleaning the cell arrays has proven to be very time consuming and potentially damaging to the cells. This limits the potential of these cells being employed at scale. Moreover, the results of Chapter 4 have proved that the employed materials are very sensitive to temperature and are likely to enter the glassy regime at temperatures typically experienced by a ski helmet (<0°C). This seems to be attributed with their favourable rate-sensitivity. Future work should focus on developing new materials that can

be 1) easily manufactured and not constrained to one manufacturing method, and 2) have low glass transition temperatures, below that which may be experienced by anyone wearing personal protective equipment such as a helmet. This would mean a glass transition temperature below -30°C or less. Further to that, one should explore how the rate-sensitivity of the parent material itself influences the impact dissipation capacity of the cellular structures at different impact speeds.

If time had permitted, the impacts presented in Chapter 6 would have been carried out on different impact speeds to assess this, as well as experimentally to validate the system, and on a set of different helmet shapes and types, rather than one cycling helmet as that presented here. This would show whether the shear stiffness of cellular structures has an effect even in motorcycle and ski helmets, which are often larger and full-faced and have different impact dynamics and coupling to the head than bicycle helmets.

In future, this work may be carried further by assessing how methods of active safety, such as inflation, alongside novel shell designs to accommodate for the increased liner space during inflation, can better protect the brain against oblique impacts of different severities. One may imagine adjusting the axial and shear stiffness through geometric tuning enabled by pneumatic actuation using the knowledge acquired from the influence of the cell geometry on the axial and shear responses. Although the compressive-shear properties of the presented cell arrays were applied to a bicycle helmet, the lightweight and impact-attenuating nature of cellular materials makes them useful for a myriad of applications such as in shoes, vests, and car interiors with which these designs, variations of them and other ideas are yet to be explored.

# 8 References


[1] L. Ming Wen, C. Rissel, Inverse associations between cycling to work, public transport, and overweight and obesity: Findings from a population based study in Australia, Prev. Med. (Baltim). 46 (2008) 29–32. https://doi.org/10.1016/j.ypmed.2007.08.009.

[2] M. Hamer, Y. Chida, Active commuting and cardiovascular risk: A meta-analytic review, Prev. Med. (Baltim). 46 (2008) 9–13. https://doi.org/10.1016/j.ypmed.2007.03.006.

[3] N.C. Møller, L. Østergaard, J.R. Gade, J.L. Nielsen, L.B. Andersen, The effect on cardiorespiratory fitness after an 8-week period of commuter cycling - A randomized controlled study in adults, Prev. Med. (Baltim). 53 (2011) 172–177. https://doi.org/10.1016/j.ypmed.2011.06.007.

[4] U.S. Department of Transportation National Highway Traffic Safety Administration (NHTSA), Traffic Safety Facts 2009 Data: Bicyclists and Other Cyclists, 2011. papers2://publication/uuid/C071D6BC-D260-4EDE-B3AC-7FA105A7C8F3.

[5] H. Coleman, K. Mizenko, Traffic Safety Facts Research Note: Pedestrian and Bicyclist Data Analysis, 2018. https://www.nhtsa.gov/sites/nhtsa.dot.gov/files/documents/812502_pedestrian-and-bicyclist-data-analysis-tsf-research-note.pdf.

[6] Transport Secretary's statement on coronavirus (COVID-19): 4 June 2020 - GOV.UK, (n.d.). https://www.gov.uk/government/speeches/transport-secretarys-statement-on-coronavirus-covid-19-4-june-2020 (accessed November 13, 2020).

[7] P. Nilsson, H. Stigson, M. Ohlin, J. Strandroth, Modelling the effect on injuries and fatalities when changing mode of transport from car to bicycle, Accid. Anal. Prev. 100 (2017) 30–36. https://doi.org/10.1016/j.aap.2016.12.020.

[8] M. Rizzi, H. Stigson, M. Krafft, Cyclist injuries leading to permanent medical impairment in sweden and the effect of bicycle helmets, 2013 IRCOBI Conf. Proc. - Int. Res. Counc. Biomech. Inj. (2013) 412–423.

[9] B. Te Ao, P. Brown, M. Tobias, S. Ameratunga, S. Barker-Collo, A. Theadom, K. McPherson, N. Starkey, A. Dowell, K. Jones, V.L. Feigin, Cost of traumatic brain injury in New Zealand: Evidence from a population-based study, Neurology. 83 (2014) 1645–1652. https://doi.org/10.1212/WNL.0000000000000933.

[10] M. Fahlstedt, P. Halldin, S. Kleiven, The protective effect of a helmet in three bicycle accidents

- A finite element study, Accid. Anal. Prev. 91 (2016) 135–143. https://doi.org/10.1016/j.aap.2016.02.025.

[11] P.A. Cripton, D.M. Dressler, C.A. Stuart, C.R. Dennison, D. Richards, Bicycle helmets are highly effective at preventing head injury during head impact: Head-form accelerations and injury criteria for helmeted and unhelmeted impacts, Accid. Anal. Prev. 70 (2014) 1–7. https://doi.org/10.1016/j.aap.2014.02.016.

[12] N. Dodds, R. Johnson, B. Walton, O. Bouamra, D. Yates, F.E. Lecky, J. Thompson, Evaluating the impact of cycle helmet use on severe traumatic brain injury and death in a national cohort of over 11000 pedal cyclists: A retrospective study from the NHS England Trauma Audit and Research Network dataset, BMJ Open. 9 (2019) 1–8. https://doi.org/10.1136/bmjopen-2018-027845.

[13] European Committe for Standardization, EN1078: Helmets for pedal cyclists and for users of skateboards and roller skates, (1997) 1–13.

[14] A.K. Ommaya, P. Yarnell, A.E. Hirsch, E.H. Harris, Scaling of experimental data on cerebral concussion in sub-human primates to concussion threshold for man, SAE Tech. Pap. (1967). https://doi.org/10.4271/670906.

[15] S. Kleiven, Predictors for traumatic brain injuries evaluated through accident reconstructions., Stapp Car Crash J. 51 (2007) 81–114. https://doi.org/2007-22-0003 [pii].

[16] E.G. Takhounts, M.J. Craig, K. Moorhouse, J. McFadden, V. Hasija, Development of Brain Injury Criteria (BrIC), SAE Tech. Pap. 2013-Novem (2013) 243–266. https://doi.org/10.4271/2013-22-0010.

[17] A.H.S. Holbourn, M.A. Edin, P. Oxfd, Mechanics of Head Injuries, Lancet. 242 (1943) 438–441.

[18] A. Alshareef, J.S. Giudice, J. Forman, R.S. Salzar, M.B. Panzer, A Novel Method for Quantifying Human In Situ Whole Brain Deformation under Rotational Loading Using Sonomicrometry , J. Neurotrauma. 35 (2017) 780–789. https://doi.org/10.1089/neu.2017.5362.

[19] F. Abayazid, K. Ding, K. Zimmerman, H. Stigson, M. Ghajari, A New Assessment of Bicycle Helmets: The Brain Injury Mitigation Effects of New Technologies in Oblique Impacts, Ann. Biomed. Eng. (2021). https://doi.org/10.1007/s10439-021-02785-0.

[20] F.F. Abayazid, M. Ghajari, Material characterisation of additively manufactured elastomers at different strain rates and build orientations, Addit. Manuf. 33 (2020) 101160. https://doi.org/10.1016/j.addma.2020.101160.

[21] O. E.E., C. M.C., M. W.C., U. E.O., I. I., O. E., D. G., Outcome of management of elevated skull fractures in Enugu, South-East Nigeria, Niger. J. Clin. Pract. 21 (2018) 859–864. https://doi.org/10.4103/njcp.njcp_347_17.

[22] J.S. Ruan, T. Khalil, A.I. King, Dynamic Response of the Human Head to Impact by Three-Dimensional Finite Element Analysis, J. Biomech. Eng. 116 (2008) 44. https://doi.org/10.1115/1.2895703.

[23] N. Garg, B.I. Devi, P. Maste, Elevated Skull Fracture, Indian J. Neurotrauma. 04 (2007) 133–133. https://doi.org/10.1016/s0973-0508(07)80031-1.

[24] D.F. Meaney, D.H. Smith, D.I. Shreiber, A. C, R.T. Miller, D.T. Ross, T.A. Gennarelli, Experimental Injury, J. Comput. Assist. Tomogr. 12 (1995).

[25] M. Aare, S. Kleiven, P. Halldin, Injury tolerances for oblique impact helmet testing, Int. J. Crashworthiness. 9 (2004) 15–23. https://doi.org/10.1533/ijcr.2004.0268.

[26] R.J. Fijalkowski, B.D. Stemper, B.M. Ellingson, N. Yoganandan, F.A. Pintar, T.A. Gennarelli, Inducing mild traumatic brain injury in the rodent through coronal plane angular acceleration, Int. Res. Counc. Biomech. Impact - 2006 Int. IRCOBI Conf. Biomech. Impact, Proc. (2006) 115–125.

[27] S. Pomeranz, U. Wald, D. Zagzag, M. Gomori, M. Shalit, Chronic epidural hematoma of the vertex: Problems in detection with computed tomography, Surg. Neurol. 22 (1984) 409–411. https://doi.org/10.1016/0090-3019(84)90148-4.

[28] S.T. Casper, How the 1950s changed our understanding of traumatic encephalopathy and its sequelae, Cmaj. 190 (2018) E140–E142. https://doi.org/10.1503/cmaj.171204.

[29] M. Langlois, Jean A. Scd, M. Wesley Rytland-Brown, M. Marlena M Wald, MLS, The Epidemiology and Impact of Traumatic Brain Injury, J. Head Trauma Rehabil. 21 (2006) 375–378.

[30] What is traumatic brain injury? - Queensland Brain Institute - University of Queensland, (n.d.). https://qbi.uq.edu.au/concussion/what-traumatic-brain-injury (accessed February 26, 2022).

[31] D. Riascos, E. Buriticá, E. Jiménez, O. Castro, F. Guzmán, M. Palacios, N. Garcia-Cairasco, C. Geula, M. Escobar, H. Pimienta, Neurodegenerative Diversity in human cortical contusion: Histological analysis of tissue derived from decompressive craniectomy, Brain Res. 1537 (2013) 86–99. https://doi.org/10.1016/j.brainres.2013.09.016.

[32] L.K. Gilmer, K.N. Roberts, P.G. Sullivan, K. Miller, S. Scheff, Early mitochondrial dysfunction following cortical contusion injury, J. Neurotrauma. 1280 (2009) 110306202455053. https://doi.org/10.1089/neu.2008-0857.

[33] C.A. Tagge, A.M. Fisher, O. V. Minaeva, A. Gaudreau-Balderrama, J.A. Moncaster, X.L. Zhang, M.W. Wojnarowicz, N. Casey, H. Lu, O.N. Kokiko-Cochran, S. Saman, M. Ericsson, K.D. Onos, R. Veksler, V. V. Senatorov, A. Kondo, X.Z. Zhou, O. Miry, L.R. Vose, K.R. Gopaul, C. Upreti, C.J. Nowinski, R.C. Cantu, V.E. Alvarez, A.M. Hildebrandt, E.S. Franz, J. Konrad, J.A. Hamilton, N. Hua, Y. Tripodis, A.T. Anderson, G.R. Howell, D. Kaufer, G.F. Hall, K.P. Lu, R.M. Ransohoff, R.O. Cleveland, N.W. Kowall, T.D. Stein, B.T. Lamb, B.R. Huber, W.C. Moss, A. Friedman, P.K. Stanton, A.C. McKee, L.E. Goldstein, Concussion, microvascular injury, and early tauopathy in young athletes after impact head injury and an impact concussion mouse model, Brain. 141 (2018) 422–458. https://doi.org/10.1093/brain/awx350.

[34] D.C. Viano, I.R. Casson, E.J. Pellman, L. Zhang, A.I. King, K.H. Yang, Concussion in professional football: Brain responses by finite element analysis: Part 9, Neurosurgery. 57 (2005) 891–915. https://doi.org/10.1227/01.NEU.0000186950.54075.3B.

[35] D. V. Agoston, A. Kamnaksh, Protein biomarkers of epileptogenicity after traumatic brain injury, Neurobiol. Dis. 123 (2019) 59–68. https://doi.org/10.1016/j.nbd.2018.07.017.

[36] A. Mohammadipour, A. Alemi, Micromechanical analysis of brain's diffuse axonal injury, J. Biomech. 65 (2017) 61–74. https://doi.org/10.1016/j.jbiomech.2017.09.029.

[37] A.S. Jagoda, Mild traumatic brain injury: Key decisions in acute management, Psychiatr. Clin. North Am. 33 (2010) 797–806. https://doi.org/10.1016/j.psc.2010.09.004.

[38] N. YOGANANDAN, F.A. PINTAR, A. Sances, P.R. Walsh, C.L. Ewing, D.J. Thomas, R.G. SNYDER, Biomechanics of skull fracture., J. Neurotrauma. 12 (1995) 659–668. https://doi.org/10.1089/neu.1995.12.659.

[39] M. Ghajari, P.J. Hellyer, D.J. Sharp, Computational modelling of traumatic brain injury predicts the location of chronic traumatic encephalopathy pathology, Brain. 140 (2017) 333–343. https://doi.org/10.1093/brain/aww317.

[40] F.C.M. Reith, R. Van den Brande, A. Synnot, R. Gruen, A.I.R. Maas, The reliability of the Glasgow Coma Scale: a systematic review, Intensive Care Med. 42 (2016) 3–15. https://doi.org/10.1007/s00134-015-4124-3.

[41] N.C. Chou R, Totten AM, Pappas M, Carney N, Dandy S, Grusing S, Fu R, Wasson N, Glasgow

Coma Scale for Field Triage of Trauma: A Systematic Review, 2017. www.effectivehealthcare.ahrq.gov/reports/final.cfm.

[42] J.H. Mena, A.I. Sanchez, A.M. Rubiano, A.B. Peitzman, J.L. Sperry, M.I. Gutierrez, J.C. Puyana, Effect of the modified glasgow coma scale score criteria for mild traumatic brain injury on mortality prediction: Comparing classic and modified glasgow coma scale score model scores of 13, J. Trauma - Inj. Infect. Crit. Care. 71 (2011) 1185–1193. https://doi.org/10.1097/TA.0b013e31823321f8.

[43] M. Faul, L. Xu, M.M. Wald, V.G. Coronado, Traumatic Brain Injury in the United States, U.S. Dep. Heal. Hum. Serv. Centres Dis. Control Prevenetion. (2006). https://doi.org/10.1016/B978-0-444-52910-7.00011-8.

[44] D.B. Douglas, M. Iv, P.K. Douglas, A. Anderson, S.B. Vos, R. Bammer, M. Zeineh, M. Wintermark, Diffusion tensor imaging of TBI: Potentials and challenges, Top. Magn. Reson. Imaging. 24 (2015) 241–251. https://doi.org/10.1097/RMR.0000000000000062.

[45] V.A. Cubon, M. Murugavel, K.W. Holmes, A. Dettwiler, Preliminary evidence from a prospective DTI study suggests a posterior-to-anterior pattern of recovery in college athletes with sports-related concussion, Brain Behav. 8 (2018) 1–13. https://doi.org/10.1002/brb3.1165.

[46] K.L. O'Connor, S. Rowson, S.M. Duma, S.P. Broglio, Head-Impact–Measurement Devices: A Systematic Review, J. Athl. Train. 52 (2017) 206–227. https://doi.org/10.4085/1062-6050.52.2.05.

[47] Folksam, Bicycle Helmets 2017 tested by Folksam, (2017). http://conehead.squareeyes.com.au/conehead-technology/bicycle-helmets/.

[48] K.M. Breedlove, E.L. Breedlove, T.G. Bowman, E.A. Nauman, Impact attenuation capabilities of football and lacrosse helmets, J. Biomech. 49 (2016) 2838–2844. https://doi.org/10.1016/j.jbiomech.2016.06.030.

[49] M. Kurt, K. Laksari, C. Kuo, G.A. Grant, D.B. Camarillo, Modeling and Optimization of Airbag Helmets for Preventing Head Injuries in Bicycling, Ann. Biomed. Eng. 45 (2017) 1148–1160. https://doi.org/10.1007/s10439-016-1732-1.

[50] I. Levadnyi, J. Awrejcewicz, Y. Zhang, M.F. Goethel, Y. Gu, Finite Element Analysis of Impact for Helmeted and Non-helmeted Head, J. Med. Biol. Eng. 38 (2018) 587–595. https://doi.org/10.1007/s40846-017-0324-3.

[51] J.F. Kraus, C. Peek, The Impact of Two Related Prevention Strategies on Head Injury Reduction

among Nonfatally Injured Motorcycle Riders, California, 1991–1993, J. Neurotrauma. 12 (1995) 873–881. https://doi.org/10.1089/neu.1995.12.873.

[52] W.Y. Yu, C.Y. Chen, W.T. Chiu, M.R. Lin, Effectiveness of different types of motorcycle helmets and effects of their improper use on head injuries, Int. J. Epidemiol. 40 (2011) 794–803. https://doi.org/10.1093/ije/dyr040.

[53] G. Gopalakrishna, C. Peek-Asa, J.F. Kraus, Epidemiologic features of facial injuries among motorcyclists, Ann. Emerg. Med. 32 (1998) 425–430. https://doi.org/10.1016/S0196-0644(98)70170-2.

[54] M. Fahlstedt, F. Abayazid, M.B. Panzer, A. Trotta, W. Zhao, M. Ghajari, M.D. Gilchrist, S. Ji, S. Kleiven, X. Li, A.N. Annaidh, Ranking and Rating Bicycle Helmet Safety Performance in Oblique Impacts Using Eight Different Brain Injury Models, Ann. Biomed. Eng. (2020). https://doi.org/10.1007/s10439-020-02703-w.

[55] J. Ho, S. Kleiven, Can sulci protect the brain from traumatic injury?, J. Biomech. 42 (2009) 2074–2080. https://doi.org/10.1016/j.jbiomech.2009.06.051.

[56] D.J. Sharp, G. Scott, R. Leech, Network dysfunction after traumatic brain injury, Nat. Rev. Neurol. 10 (2014) 156–166. https://doi.org/10.1038/nrneurol.2014.15.

[57] A.C. McKee, T.D. Stein, C.J. Nowinski, R.A. Stern, D.H. Daneshvar, V.E. Alvarez, H.S. Lee, G. Hall, S.M. Wojtowicz, C.M. Baugh, D.O. Riley, C.A. Kubilus, K.A. Cormier, M.A. Jacobs, B.R. Martin, C.R. Abraham, T. Ikezu, R.R. Reichard, B.L. Wolozin, A.E. Budson, L.E. Goldstein, N.W. Kowall, R.C. Cantu, The spectrum of disease in chronic traumatic encephalopathy, Brain. 136 (2013) 43–64. https://doi.org/10.1093/brain/aws307.

[58] S. Meng, M. Fahlstedt, P. Halldin, The effect of impact velocity angle on helmeted head impact severity: A rationale for motorcycle helmet impact test design, Conf. Proc. Int. Res. Counc. Biomech. Inj. IRCOBI. 2018-Septe (2018) 454–469.

[59] P. Halldin, A. Gilchrist, N.J. Mills, A new oblique impact test for motorcycle helmets, Int. J. Crashworthiness. 6 (2001) 53–64. https://doi.org/10.1533/cras.2001.0162.

[60] N.J. Mills, S. Wilkes, S. Derler, A. Flisch, FEA of oblique impact tests on a motorcycle helmet, Int. J. Impact Eng. 36 (2009) 913–925. https://doi.org/10.1016/j.ijimpeng.2008.12.011.

[61] H. Stigson, M. Rizzi, A. Ydenius, E. Engström, A. Kullgren, Consumer Testing of Bicycle Helmets, Conf. Proc. Int. Res. Counc. Biomech. Inj. IRCOBI. 2017-Septe (2017) 173–181.

[62] M. Tsai, D. Hemenway, M. Tsai, D. Hemenway, Effect of the mandatory helmet law in Taiwan BRIEF REPORTS E V ect of the mandatory helmet law in Taiwan, (1999) 290–292.

[63] D. Lloyd, A. Murphy, Reported road casualties in Great Britain: 2019 annual report, 2019. https://www.gov.uk/government/ (accessed November 13, 2020).

[64] How to choose the best motorcycle helmet, (n.d.). https://www.bennetts.co.uk/bikesocial/reviews/products/helmets/how-to-choose-the-best-motorcycle-helmet (accessed February 26, 2022).

[65] F.A.O. Fernandes, R.J. Alves De Sousa, Motorcycle helmets - A state of the art review, Accid. Anal. Prev. 56 (2013) 1–21. https://doi.org/10.1016/j.aap.2013.03.011.

[66] V. Kostopoulos, Y.P. Markopoulos, G. Giannopoulos, D.E. Vlachos, Finite element analysis of impact damage response of composite motorcycle safety helmets, Compos. Part BEngineering. 33 (2002) 99–107. https://doi.org/10.1016/S1359-8368(01)00066-X.

[67] A. CERNICCHI, U. GALVANETTO, R. OLSSON, Virtual Testing of Composite Motorcycle Helmets, Int. J. Mod. Phys. B. 22 (2008) 1705–1711. https://doi.org/10.1142/s0217979208047298.

[68] M. Ghajari, U. Galvanetto, L. Iannucci, R. Willinger, Influence of the body on the response of the helmeted head during impact, Int. J. Crashworthiness. 16 (2011) 285–295. https://doi.org/10.1080/13588265.2011.559798.

[69] D.H. Blanco, A. Cernicchi, U. Galvanetto, Design of an innovative optimized motorcycle helmet, Proc. Inst. Mech. Eng. Part P J. Sport. Eng. Technol. 228 (2014) 95–110. https://doi.org/10.1177/1754337113518748.

[70] M.J. Kendall, C.R. Siviour, Experimentally simulating high-rate behaviour: Rate and temperature effects in polycarbonate and PMMA, Philos. Trans. R. Soc. A Math. Phys. Eng. Sci. 372 (2014). https://doi.org/10.1098/rsta.2013.0202.

[71] CAMPUSplastics, (n.d.). https://www.campusplastics.com/ (accessed February 26, 2022).

[72] N.J. Mills, A. Gilchrist, Finite-element analysis of bicycle helmet oblique impacts, Int. J. Impact Eng. 35 (2008) 1087–1101. https://doi.org/10.1016/j.ijimpeng.2007.05.006.

[73] G. Milne, C. Deck, N. Bourdet, R.P. Carreira, Q. Allinne, A. Gallego, R. Willinger, Bicycle helmet modelling and validation under linear and tangential impacts, Int. J. Crashworthiness. 19 (2014) 323–333. https://doi.org/10.1080/13588265.2013.859470.

[74] L.J. Gibson, M.F. Ashby, The structure of cellular solids, 2014.

https://doi.org/10.1017/cbo9781139878326.004.

[75] E. Bliven, A. Rouhier, S. Tsai, R. Willinger, N. Bourdet, C. Deck, S.M. Madey, M. Bottlang, Evaluation of a novel bicycle helmet concept in oblique impact testing, Accid. Anal. Prev. 124 (2019) 58–65. https://doi.org/10.1016/j.aap.2018.12.017.

[76] B.J. Ramirez, O.T. Kingstedt, R. Crum, C. Gamez, V. Gupta, Tailoring the rate-sensitivity of low density polyurea foams through cell wall aperture size, J. Appl. Phys. 121 (2017). https://doi.org/10.1063/1.4985280.

[77] A. Karimi, M. Navidbakhsh, R. Razaghi, An experimental-finite element analysis on the kinetic energy absorption capacity of polyvinyl alcohol sponge, Mater. Sci. Eng. C. 39 (2014) 253–258. https://doi.org/10.1016/j.msec.2014.03.009.

[78] S. Farajzadeh Khosroshahi, R. Olsson, M. Wysocki, M. Zaccariotto, U. Galvanetto, Response of a helmet liner under biaxial loading, Polym. Test. 72 (2018) 110–114. https://doi.org/10.1016/j.polymertesting.2018.10.012.

[79] L. Di Landro, G. Sala, D. Olivieri, Deformation mechanisms and energy absorption of polystyrene foams for protective helmets, Polym. Test. 21 (2002) 217–228. https://doi.org/10.1016/S0142-9418(01)00073-3.

[80] L.J. Gibson, M.F. Ashby, The mechanics of foams: basic results, 2014. https://doi.org/10.1017/cbo9781139878326.007.

[81] C. Ling, J. Ivens, P. Cardiff, M.D. Gilchrist, Deformation response of EPS foam under combined compression-shear loading. Part II: High strain rate dynamic tests, Int. J. Mech. Sci. 145 (2018) 9–23. https://doi.org/10.1016/j.ijmecsci.2018.06.015.

[82] A. Gilchrist, N.J. Mills, Deformation Analysis for Motorcycle Helmets, Ircobi. (1993) 268–280.

[83] M. Richter, D. Otte, U. Lehmann, B. Chinn, E. Schuller, D. Doyle, K. Sturrock, C. Krettek, Head injury mechanisms in helmet-protected motorcyclists: prospective multicenter study, J. Trauma. 51 (2001) 949–958. https://doi.org/10.1097/00005373-200111000-00021.

[84] NFL Play Smart Play Safe, NFL Engineering Roadmap Factsheet, NFL Eng. Roadmap Factsheet. (2019).

[85] J.S. Giudice, G. Park, K. Kong, A. Bailey, R. Kent, M.B. Panzer, Development of Open-Source Dummy and Impactor Models for the Assessment of American Football Helmet Finite Element Models, Ann. Biomed. Eng. 47 (2019) 464–474. https://doi.org/10.1007/s10439-018-02155-3.

[86] L. Lamb, T.B. Hoshizaki, Deformation mechanisms and impact attenuation characteristics of thin-walled collapsible air chambers used in head protection, Proc. Inst. Mech. Eng. Part H J. Eng. Med. 223 (2009) 1021–1031. https://doi.org/10.1243/09544119JEIM573.

[87] B.J. Ramirez, V. Gupta, Evaluation of novel temperature-stable viscoelastic polyurea foams as helmet liner materials, Mater. Des. 137 (2018) 298–304. https://doi.org/10.1016/j.matdes.2017.10.037.

[88] D.C. Viano, C. Withnall, M. Wonnacott, Football helmet drop tests on different fields using an instrumented hybrid III head, Ann. Biomed. Eng. 40 (2012) 97–105. https://doi.org/10.1007/s10439-011-0377-3.

[89] Västra Hamnen Corporate Finance, Hövding : Safely ahead, (2019) 1–24.

[90] P. Halldin, M. Aare, S. Kleiven, H. von Holst, Improved helmet design and test methods to reduce rotational induced brain injuries, (2003) 1–8. http://www.diva-portal.org/smash/get/diva2:502481/FULLTEXT01.pdf.

[91] What is MIPS? - Whitelines Snowboarding, (n.d.). https://whitelines.com/snowboard-gear/reviews/helmets-protection/what-is-mips.html (accessed February 26, 2022).

[92] B.J. Ramirez, U. Misra, V. Gupta, Viscoelastic foam-filled lattice for high energy absorption, Mech. Mater. 127 (2018) 39–47. https://doi.org/10.1016/j.mechmat.2018.08.011.

[93] P. Siegkas, D.J. Sharp, M. Ghajari, The traumatic brain injury mitigation effects of a new viscoelastic add-on liner, Sci. Rep. 9 (2019) 1–10. https://doi.org/10.1038/s41598-019-39953-1.

[94] Conehead Helmets, (n.d.). http://coneheadhelmets.com.au/ (accessed February 27, 2022).

[95] S.F. Khosroshahi, S.A. Tsampas, U. Galvanetto, Feasibility study on the use of a hierarchical lattice architecture for helmet liners, Mater. Today Commun. 14 (2018) 312–323. https://doi.org/10.1016/j.mtcomm.2018.02.002.

[96] T.L. Teng, C.C. Liang, V.H. Nguyen, Innovative design of bicycle helmet liners, Proc. Inst. Mech. Eng. Part L J. Mater. Des. Appl. 228 (2014) 341–351. https://doi.org/10.1177/1464420713493590.

[97] M. Nicotra, M. Moncalero, M. Messori, E. Fabbri, M. Fiorini, M. Colonna, Thermo-mechanical and impact properties of polymeric foams used for snow sports protective equipment, Procedia Eng. 72 (2014) 678–683. https://doi.org/10.1016/j.proeng.2014.06.115.

[98] S. Signetti, M. Nicotra, M. Colonna, N.M. Pugno, Modeling and simulation of the impact behavior of soft polymeric-foam-based back protectors for winter sports, J. Sci. Med. Sport. (2018) 1–9. https://doi.org/10.1016/j.jsams.2018.10.007.

[99] C.R. Siviour, J.L. Jordan, High Strain Rate Mechanics of Polymers: A Review, J. Dyn. Behav. Mater. 2 (2016) 15–32. https://doi.org/10.1007/s40870-016-0052-8.

[100] C.M. Roland, Viscoelastic Behavior of Rubbery Materials, Viscoelastic Behav. Rubbery Mater. 9780199571 (2011) 1–344. https://doi.org/10.1093/acprof:oso/9780199571574.001.0001.

[101] J.M. Johnston, H. Ning, J.E. Kim, Y.H. Kim, B. Soni, R. Reynolds, L. Cooper, J.B. Andrews, U. Vaidya, Simulation, fabrication and impact testing of a novel football helmet padding system that decreases rotational acceleration, Sport. Eng. 18 (2015) 11–20. https://doi.org/10.1007/s12283-014-0160-4.

[102] M. Ghajari, S. Peldschus, U. Galvanetto, L. Iannucci, Effects of the presence of the body in helmet oblique impacts, Accid. Anal. Prev. 50 (2013) 263–271. https://doi.org/10.1016/j.aap.2012.04.016.

[103] S. Farajzadeh Khosroshahi, U. Galvanetto, M. Ghajari, Optimization of the Chin Bar of a Composite-Shell Helmet to Mitigate the Upper Neck Force, Appl. Compos. Mater. 24 (2017) 931–944. https://doi.org/10.1007/s10443-016-9566-4.

[104] I. Snell Memorial Foundation, 1995 Standard for Protective Headgear, (1995) 1–36.

[105] ASTM International, ASTM F1952-15, Standard Specification for Helmets Used for Downhill Mountain Bicycle Racing, (2015). https://doi.org/10.1520/F1952-15.

[106] B. Pipkorn, V. Alvarez, M. Fahlstedt, L. Lundin, Head Injury Risks and Countermeasures for a Bicyclist Impacted by a Passenger Vehicle, in: Int. Res. Counc. Biomech. Inj., 2020: pp. 289–306.

[107] L. Zhang, K.H. Yang, A.I. King, A proposed injury threshold for mild traumatic brain injury., J. Biomech. Eng. 126 (2004) 226–36. https://doi.org/10.1115/1.1691446.

[108] E.G. Takhounts, S. a Ridella, S. Rowson, S.M. Duma, Kinematic Rotational Brain Injury Criterion (BRIC), 22nd Enhanc. Saf. Veh. Conf. Proc. (2011) Paper No. 11-0263.

[109] R.W. Nightingale, J.H. McElhaney, D.L. Camacho, M. Kleinberger, B.A. Winkelstein, B.S. Myers, The Dynamic Responses of the Cervical Spine: Buckling, End Conditions, and Tolerance in Compressive Impacts, SAE Tech. Pap. Ser. 1 (1997) 451–471. https://doi.org/10.4271/973344.

[110] N. Yoganandan, A. Sances, F. Pintar, Biomechanical Evaluation of the Axial Compressive

Responses of the Human Cadaveric and Manikin Necks, J. Biomech. Eng. 111 (2009) 250. https://doi.org/10.1115/1.3168374.

[111] J. Foster, J. Kortge, M. Wolanin, Hybrid III - A biomechanically based crash test dummy, Stapp Car Crash J. 21 (1977) 975–1014. https://doi.org/SAE 770938.

[112] J.G. Paver, J. Caplinger, G. Mattos, D. Friedman, An improved dummy neck assembly for dynamic rollover testing, ASME 2010 Summer Bioeng. Conf. SBC 2010. (2010) 811–812. https://doi.org/10.1115/SBC2010-19656.

[113] F.A. Pintar, A. Sances Jr., N. Yoganandan, J. Reinartz, D.J. Maiman, J.K. Suh, G. Unger, J.F. Cusick, S.J. Larson, Biodynamics of the total human cadaveric cervical spine, Soc. Automot. Eng. Pap. No. 902309. (1990) 55–72. https://doi.org/10.4271/902309.

[114] R.W. Nightingale, J.H. McElhaney, W.J. Richardson, B.S. Myers, Dynamic responses of the head and cervical spine to axial impact loading, J. Biomech. 29 (1996) 307–318. https://doi.org/10.1016/0021-9290(95)00056-9.

[115] N.J. mills, A. Gilchrist, The effectiveness of foams in bicycle and motorcycle helmets, Accid. Anal. Prev. 23 (1991) 153–163. https://doi.org/10.1016/0001-4575(91)90045-7.

[116] A. Gilchrist, N.J. Mills, Modelling of the impact response of motorcycle helmets, Int. J. Impact Eng. 15 (1994) 201–218. https://doi.org/10.1016/S0734-743X(05)80013-2.

[117] A. Castiglioni, L. Castellani, G. Cuder, S. Comba, Relevant materials parameters in cushioning for EPS foams, Colloids Surfaces A Physicochem. Eng. Asp. 534 (2017) 71–77. https://doi.org/10.1016/j.colsurfa.2017.03.049.

[118] N.J. Mills, C. Fitzgerald, A. Gilchrist, R. Verdejo, Polymer foams for personal protection: Cushions, shoes and helmets, Compos. Sci. Technol. 63 (2003) 2389–2400. https://doi.org/10.1016/S0266-3538(03)00272-0.

[119] N.J. Mills, A. Gilchrist, Response of helmets in direct and oblique impacts, Int. J. Crashworthiness. 2 (1996) 7–24. https://doi.org/10.1533/cras.1997.0032.

[120] M. Bottlang, A. Rouhier, S. Tsai, J. Gregoire, S.M. Madey, Impact Performance Comparison of Advanced Bicycle Helmets with Dedicated Rotation-Damping Systems, Ann. Biomed. Eng. 48 (2020) 68–78. https://doi.org/10.1007/s10439-019-02328-8.

[121] S. Kleiven, Influence of direction and duration of impacts to the human head evaluated using the finite element method, Int. Res. Counc. Biomech. Impact - 2005 Int. IRCOBI Conf. Biomech.

Impact, Proc. (2005) 41–57.

[122] M.L. Bland, C. McNally, J.B. Cicchino, D.S. Zuby, B.C. Mueller, M.L. McCarthy, C.D. Newgard, P.E. Kulie, B.N. Arnold, S. Rowson, Laboratory Reconstructions of Bicycle Helmet Damage: Investigation of Cyclist Head Impacts Using Oblique Impacts and Computed Tomography, Ann. Biomed. Eng. (2020). https://doi.org/10.1007/s10439-020-02620-y.

[123] A.L. DeMarco, D.D. Chimich, S.J. Bonin, G.P. Siegmund, Impact Performance of Certified Bicycle Helmets Below, On and Above the Test Line, Ann. Biomed. Eng. 48 (2020) 58–67. https://doi.org/10.1007/s10439-019-02422-x.

[124] R. Willinger, C. Deck, P. Halldin, D. Otte, Towards advanced bicycle helmet test methods, Int. Cycl. Saf. Conf. (2014) 1–11. http://www.icsc2014.eu/program/program-proceedings.

[125] N. Bourdet, C. Deck, R.P. Carreira, R. Willinger, Head impact conditions in the case of cyclist falls, Proc. Inst. Mech. Eng. Part P J. Sport. Eng. Technol. 226 (2012) 282–289. https://doi.org/10.1177/1754337112442326.

[126] A.J. Padgaonkar, K.W. Krieger, A.I. King, Measurement of Angular Acceleration of a Rigid Body Using Linear Accelerometers., Am. Soc. Mech. Eng. (1975) 552–556.

[127] M. Aare, P. Halldin, A new laboratory rig for evaluating helmets subject to oblique impacts, Traffic Inj. Prev. 4 (2003) 240–248. https://doi.org/10.1080/15389580309879.

[128] S.F. Khosroshahi, H. Duckworth, U. Galvanetto, M. Ghajari, The effects of topology and relative density of lattice liners on traumatic brain injury mitigation, J. Biomech. 97 (2019) 109376. https://doi.org/10.1016/j.jbiomech.2019.109376.

[129] G.R. DeVore, Computing the Z score and centiles for cross-sectional analysis a practical approach, J. Ultrasound Med. 36 (2017) 459–473. https://doi.org/10.7863/ultra.16.03025.

[130] K. Bian, H. Mao, Mechanisms and variances of rotation-induced brain injury: a parametric investigation between head kinematics and brain strain, Biomech. Model. Mechanobiol. (2020). https://doi.org/10.1007/s10237-020-01341-4.

[131] A.A. Weaver, K.A. Danelson, J.D. Stitzel, Modeling brain injury response for rotational velocities of varying directions and magnitudes, Ann. Biomed. Eng. 40 (2012) 2005–2018. https://doi.org/10.1007/s10439-012-0553-0.

[132] M.L. Bland, C. McNally, D.S. Zuby, B.C. Mueller, S. Rowson, Development of the STAR Evaluation System for Assessing Bicycle Helmet Protective Performance, Ann. Biomed. Eng. 48 (2020) 47–

57. https://doi.org/10.1007/s10439-019-02330-0.

[133] A.C. Bain, D.F. Meaney, Tissue-level thresholds for axonal damage in an experimental model of central nervous system white matter injury, J. Biomech. Eng. 122 (2000) 615–622. https://doi.org/10.1115/1.1324667.

[134] C. Donat, M. Yanez-Lopez, M. Sastre, M. Baxan, M. Goldfinger, Seeamber, M. R. Reneira., D. F., H. P., S. P.J., G. P., D.J. Sharp, M. Ghajari, From biomechanics to pathology: predicting axonal injury from patterns of strain after traumatic brain injury, Brain. (2020).

[135] J.D. Cherry, Y. Tripodis, V.E. Alvarez, B. Huber, P.T. Kiernan, D.H. Daneshvar, J. Mez, P.H. Montenigro, T.M. Solomon, M.L. Alosco, R.A. Stern, A.C. McKee, T.D. Stein, Microglial neuroinflammation contributes to tau accumulation in chronic traumatic encephalopathy, Acta Neuropathol. Commun. 4 (2016) 112. https://doi.org/10.1186/s40478-016-0382-8.

[136] R.P. Hubbard, D.G. Mcleod, Definition and Development of A Crash Dummy Head, SAE Tech. Pap. Ser. 1 (2010) 3836–3851. https://doi.org/10.4271/741193.

[137] A. Trotta, A. Ní Annaidh, R.O. Burek, B. Pelgrims, J. Ivens, Evaluation of the head-helmet sliding properties in an impact test, J. Biomech. 75 (2018) 28–34. https://doi.org/10.1016/j.jbiomech.2018.05.003.

[138] C. Deck, N. Bourdet, F. Meyer, R. Willinger, Protection performance of bicycle helmets, J. Safety Res. 71 (2019) 67–77. https://doi.org/10.1016/j.jsr.2019.09.003.

[139] F.A. Pintar, A. Sances, N. Yoganandan, J. Reinartz, D.J. Maiman, J.K. Suh, G. Unger, J.F. Cusick, S.J. Larson, Biodynamics of the total human cadaveric cervical spine, SAE Tech. Pap. (1990). https://doi.org/10.4271/902309.

[140] Bugatti - World premiere: brake caliper from 3-D printer, (n.d.). https://www.bugatti.com/media/news/2018/world-premiere-brake-caliper-from-3-d-printer/ (accessed August 7, 2019).

[141] Y.C. Wang, T. Chen, Y.L. Yeh, Advanced 3D printing technologies for the aircraft industry: a fuzzy systematic approach for assessing the critical factors, Int. J. Adv. Manuf. Technol. (2018) 1–11. https://doi.org/10.1007/s00170-018-1927-8.

[142] A.D. Knight, P.P. Anderson, M.D. Beachler, C.L. Dearth, L.M. Hassinger, B.D. Hendershot, T.J. Sleeman, P.C. Liacouras, Customized 3D-Printed Prosthetic Devices for Wounded Warriors, Am. J. Phys. Med. Rehabil. 98 (2018) 1. https://doi.org/10.1097/phm.0000000000001047.

[143] D. Ackland, D. Robinson, P.V.S. Lee, G. Dimitroulis, Design and clinical outcome of a novel 3D-printed prosthetic joint replacement for the human temporomandibular joint, Clin. Biomech. 56 (2018) 52–60. https://doi.org/10.1016/j.clinbiomech.2018.05.006.

[144] B. Rochlitz, D. Pammer, R. Kiss, Functionality and load-bearing analysis of 3D-printed prosthetic feet, Mater. Today Proc. 5 (2018) 26566–26571. https://doi.org/10.1016/j.matpr.2018.08.117.

[145] X. Li, Y. Wang, Y. Zhao, J. Liu, S. Xiao, K. Mao, Multilevel 3D Printing Implant for Reconstructing Cervical Spine with Metastatic Papillary Thyroid Carcinoma, Spine (Phila. Pa. 1976). 42 (2017) E1326–E1330. https://doi.org/10.1097/BRS.0000000000002229.

[146] A.J. Jacobsen, W. Barvosa-Carter, S. Nutt, Micro-scale truss structures formed from self-propagating photopolymer waveguides, Adv. Mater. 19 (2007) 3892–3896. https://doi.org/10.1002/adma.200700797.

[147] C. Qiu, S. Yue, N.J.E. Adkins, M. Ward, H. Hassanin, P.D. Lee, P.J. Withers, M.M. Attallah, Influence of processing conditions on strut structure and compressive properties of cellular lattice structures fabricated by selective laser melting, Mater. Sci. Eng. A. 628 (2015) 188–197. https://doi.org/10.1016/j.msea.2015.01.031.

[148] Z. Ozdemir, A. Tyas, R. Goodall, H. Askes, Energy absorption in lattice structures in dynamics: Nonlinear FE simulations, Int. J. Impact Eng. 102 (2017) 1–15. https://doi.org/10.1016/j.ijimpeng.2016.11.016.

[149] N.A. Meisel, D.A. Dillard, C.B. Williams, Impact of material concentration and distribution on composite parts manufactured via multi-material jetting, Rapid Prototyp. J. 24 (2018) 872–879. https://doi.org/10.1108/RPJ-01-2017-0005.

[150] J. Herzberger, J.M. Sirrine, C.B. Williams, T.E. Long, Polymer Design for 3D Printing Elastomers: Recent Advances in Structure, Properties, and Printing, Prog. Polym. Sci. 97 (2019) 101144. https://doi.org/10.1016/j.progpolymsci.2019.101144.

[151] S. Akbari, A.H. Sakhaei, K. Kowsari, B. Yang, A. Serjouei, Z. Yuanfang, Q. Ge, Enhanced multimaterial 4D printing with active hinges, Smart Mater. Struct. 27 (2018). https://doi.org/10.1088/1361-665X/aabe63.

[152] K. Che, C. Yuan, H.J. Qi, J. Meaud, Viscoelastic multistable architected materials with temperature-dependent snapping sequence, Soft Matter. 14 (2018) 2492–2499. https://doi.org/10.1039/c8sm00217g.

[153] Q. Ge, G. Gu, D. Wang, B. Zhang, N. Zhang, C. Yuan, H. Hingorani, N. Ding, Y.-F. Zhang, Fast-

Response, Stiffness-Tunable Soft Actuator by Hybrid Multimaterial 3D Printing, Adv. Funct. Mater. (2019) 1806698. https://doi.org/10.1002/adfm.201806698.

[154] G. Dammer, S. Gablenz, A. Hildebrandt, Z. Major, Design and shape optimization of PolyJet bellows actuators, 2018 IEEE Int. Conf. Soft Robot. RoboSoft 2018. (2018) 282–287. https://doi.org/10.1109/ROBOSOFT.2018.8404933.

[155] A. Kakogawa, S. Ma, A Differential Elastic Joint for Multi-linked Pipeline Inspection Robots, IEEE Int. Conf. Intell. Robot. Syst. (2018) 949–954. https://doi.org/10.1109/IROS.2018.8593872.

[156] Z. Ding, C. Yuan, X. Peng, T. Wang, H.J. Qi, M.L. Dunn, Direct 4D printing via active composite materials, Sci. Adv. 3 (2017). https://doi.org/10.1126/sciadv.1602890.

[157] T. Chen, O.R. Bilal, K. Shea, C. Daraio, Harnessing bistability for directional propulsion of untethered, soft robots, (2017). https://doi.org/10.1073/pnas.1800386115.

[158] Y. Mao, Z. Ding, C. Yuan, S. Ai, M. Isakov, J. Wu, T. Wang, M.L. Dunn, H.J. Qi, 3D Printed Reversible Shape Changing Components with Stimuli Responsive Materials., Sci. Rep. 6 (2016) 24761. https://doi.org/10.1038/srep24761.

[159] S.N.R. Kantareddy, T.W. Simpson, Z. Ounaies, M. Frecker, 3D Printing of Shape Changing Polymer Structures: Design and Characterization of Materials, Solid Free. Fabr. Symp. (2016) 2224–2235. http://sffsymposium.engr.utexas.edu/sites/default/files/2016/178-Kantareddy.pdf.

[160] J. Wu, C. Yuan, Z. Ding, M. Isakov, Y. Mao, T. Wang, M.L. Dunn, H.J. Qi, Multi-shape active composites by 3D printing of digital shape memory polymers, Sci. Rep. 6 (2016) 1–11. https://doi.org/10.1038/srep24224.

[161] L.S. Dimas, G.H. Bratzel, I. Eylon, M.J. Buehler, Tough composites inspired by mineralized natural materials: Computation, 3D printing, and testing, Adv. Funct. Mater. 23 (2013) 4629–4638. https://doi.org/10.1002/adfm.201300215.

[162] Y. Han, W.F. Lu, Structural design of wearable electronics suitable for highly-stretched joint areas, Smart Mater. Struct. 27 (2018). https://doi.org/10.1088/1361-665X/aadf05.

[163] D.M.J. Dykstra, J. Busink, B. Ennis, C. Coulais, Viscoelastic Metamaterials, (2019). http://arxiv.org/abs/1904.11888.

[164] V. Slesarenko, S. Rudykh, Towards mechanical characterization of soft digital materials for multimaterial 3D-printing, Int. J. Eng. Sci. 123 (2018) 62–72.

https://doi.org/10.1016/j.ijengsci.2017.11.011.

[165] V. Slesarenko, S. Rudykh, Harnessing viscoelasticity and instabilities for tuning wavy patterns in soft layered composites, Soft Matter. 12 (2016) 3677–3682. https://doi.org/10.1039/c5sm02949j.

[166] S. Rudykh, C. Ortiz, M.C. Boyce, Flexibility and protection by design: Imbricated hybrid microstructures of bio-inspired armor, Soft Matter. 11 (2015) 2547–2554. https://doi.org/10.1039/c4sm02907k.

[167] H. Cho, J.C. Weaver, E. Pöselt, P.J. in't Veld, M.C. Boyce, G.C. Rutledge, Engineering the Mechanics of Heterogeneous Soft Crystals, Adv. Funct. Mater. 26 (2016) 6938–6949. https://doi.org/10.1002/adfm.201601719.

[168] A.S. Dalaq, D.W. Abueidda, R.K. Abu Al-Rub, I.M. Jasiuk, Finite element prediction of effective elastic properties of interpenetrating phase composites with architectured 3D sheet reinforcements, Int. J. Solids Struct. 83 (2016) 169–182. https://doi.org/10.1016/j.ijsolstr.2016.01.011.

[169] V. Slesarenko, N. Kazarinov, S. Rudykh, Distinct failure modes in bio-inspired 3D-printed staggered composites under non-aligned loadings, Smart Mater. Struct. 26 (2017). https://doi.org/10.1088/1361-665X/aa59eb.

[170] J. Shen, S. Zhou, X. Huang, Y.M. Xie, Simple cubic three-dimensional auxetic metamaterials, Phys. Status Solidi Basic Res. 251 (2014) 1515–1522. https://doi.org/10.1002/pssb.201451304.

[171] A.S. Dalaq, D.W. Abueidda, R.K. Abu Al-Rub, Mechanical properties of 3D printed interpenetrating phase composites with novel architectured 3D solid-sheet reinforcements, Compos. Part A Appl. Sci. Manuf. 84 (2016) 266–280. https://doi.org/10.1016/j.compositesa.2016.02.009.

[172] L. Wang, J. Lau, E.L. Thomas, M.C. Boyce, Co-continuous composite materials for stiffness, strength, and energy dissipation, Adv. Mater. 23 (2011) 1524–1529. https://doi.org/10.1002/adma.201003956.

[173] L. Bass, N.A. Meisel, C.B. Williams, Exploring variability of orientation and aging effects in material properties of multi-material jetting parts, Rapid Prototyp. J. 22 (2016) 826–834. https://doi.org/10.1108/RPJ-11-2015-0169.

[174] J.E. Ryu, E. Salcedo, H.J. Lee, S.J. Jang, E.Y. Jang, H. Al Yassi, D. Baek, D. Choi, E. Lee, Material models and finite analysis of additively printed polymer composites, (2019).

https://doi.org/10.1177/0021998318785672.

[175] E. Salcedo, D. Baek, A. Berndt, J.E. Ryu, Simulation and validation of three dimension functionally graded materials by material jetting, Addit. Manuf. 22 (2018) 351–359. https://doi.org/10.1016/j.addma.2018.05.027.

[176] G. Dämmer, S. Gablenz, A. Hildebrandt, Z. Major, PolyJet-printed bellows actuators: Design, structural optimization, and experimental investigation, Front. Robot. AI. 6 (2019) 1–10. https://doi.org/10.3389/frobt.2019.00034.

[177] A. KĘSY, J. KOTLIŃSKI, Mechanical properties of parts produced by using polymer jetting technology, Arch. Civ. Mech. Eng. 10 (2012) 37–50. https://doi.org/10.1016/s1644-9665(12)60135-6.

[178] T. Stanković, J. Mueller, K. Shea, The effect of anisotropy on the optimization of additively manufactured lattice structures, Addit. Manuf. 17 (2017) 67–76. https://doi.org/10.1016/j.addma.2017.07.004.

[179] J. Mueller, K. Shea, C. Daraio, Mechanical properties of parts fabricated with inkjet 3D printing through efficient experimental design, Mater. Des. 86 (2015) 902–912. https://doi.org/10.1016/j.matdes.2015.07.129.

[180] A. Cazón, P. Morer, L. Matey, PolyJet technology for product prototyping: Tensile strength and surface roughness properties, Proc. Inst. Mech. Eng. Part B J. Eng. Manuf. 228 (2014) 1664–1675. https://doi.org/10.1177/0954405413518515.

[181] D. Blanco, P. Fernandez, A. Noriega, Nonisotropic experimental characterization of the relaxation modulus for PolyJet manufactured parts, J. Mater. Res. 29 (2014) 1876–1882. https://doi.org/10.1557/jmr.2014.200.

[182] H. Miyanaji, N. Momenzadeh, L. Yang, Effect of printing speed on quality of printed parts in Binder Jetting Process, Addit. Manuf. 20 (2018) 1–10. https://doi.org/10.1016/j.addma.2017.12.008.

[183] G. Yerbolat, A. Shynggys, M.H. Ali, Mechanical property prediction method based on multi-material 3D printer, 2018 Jt. 7th Int. Conf. Informatics, Electron. Vis. 2nd Int. Conf. Imaging, Vis. Pattern Recognition, ICIEV-IVPR 2018. (2019) 498–502. https://doi.org/10.1109/ICIEV.2018.8641073.

[184] V.S. Joshi, C. Qualters, E. Chen, J.R. Santiago, K. O'Neill, Dynamic characterization of anisotropy effects in 3-D printed materials for high-G survivability, AIP Conf. Proc. 1979 (2018).

https://doi.org/10.1063/1.5044924.

[185] R. Adams, S.P. Soe, R. Santiago, M. Robinson, B. Hanna, G. McShane, M. Alves, R. Burek, P. Theobald, A novel pathway for efficient characterisation of additively manufactured thermoplastic elastomers, Mater. Des. 180 (2019) 107917. https://doi.org/10.1016/j.matdes.2019.107917.

[186] I.Q. Vu, L.B. Bass, C.B. Williams, D.A. Dillard, Characterizing the effect of print orientation on interface integrity of multi-material jetting additive manufacturing, Addit. Manuf. 22 (2018) 447–461. https://doi.org/10.1016/j.addma.2018.05.036.

[187] B. Standards, BS ISO 37 : 2017 BSI Standards Publication Rubber , vulcanized or thermoplastic — Determination of tensile stress-strain properties, (2017).

[188] B. Standards, BS ISO 7743 : 2017 BSI Standards Publication Rubber , vulcanized or thermoplastic — Determination of compression stress-strain properties, (2017).

[189] TA Instruments, TA Instruments DMA Q800 Specifications, (2010) 1–14.

[190] D. Gutierrez-Lemini, Engineering viscoelasticity, Eng. Viscoelasticity. (2014) 1–353. https://doi.org/10.1007/978-1-4614-8139-3.

[191] G.W. Ehrenstein, G. Riedel, P. Trawiel, Chapter 6 Dynamic Mechanical Analysis, Therm. Anal. Plast. Theory Pract. (2004) 236–299.

[192] S.H. Chae, J.H. Zhao, D.R. Edwards, P.S. Ho, Characterization of the Viscoelasticity of Molding Compounds in the Time Domain, J. Electron. Mater. 39 (2010) 419–425. https://doi.org/10.1007/s11664-010-1078-7.

[193] R.W. Ogden, G. Saccomandi, I. Sgura, Fitting hyperelastic models to experimental data, Comput. Mech. 34 (2004) 484–502. https://doi.org/10.1007/s00466-004-0593-y.

[194] Dassault Systèmes Simulia, Analysis User's Manual Volume 3: Materials, Abaqus 6.12. III (2012).

[195] T. Frank, A. Kurz, M. Pitzer, M. Söllner, Development and validation of numerical pedestrian impactor models, 4th Eur. LS-DYNA Users Conf. (2003) 1–18.

[196] G.A. Holzapfel, Nonlinear Solid Mechanics : a Continuum Approach for Engineering, Work. First Edit (2000) 205. https://doi.org/10.1023/A:1020843529530.

[197] H. Cho, S. Mayer, E. Pöselt, M. Susoff, P.J. Veld, G.C. Rutledge, M.C. Boyce, Deformation mechanisms of thermoplastic elastomers: Stress-strain behavior and constitutive modeling,

Polymer (Guildf). 128 (2017) 87–99. https://doi.org/10.1016/j.polymer.2017.08.065.

[198] C. Tzikang, Determining a Prony Series for a Viscoelastic Material From Time Varying Strain Data, Nasa. (2000).

[199] S.M. Goh, M.N. Charalambides, J.G. Williams, Determination of the constitutive constants of non-linear viscoelastic materials, Mech. Time-Dependent Mater. 8 (2004) 255–268. https://doi.org/10.1023/B:MTDM.0000046750.65395.fe.

[200] A. Takeh, S. Shanbhag, A computer program to extract the continuous and discrete relaxation spectra from dynamic viscoelastic measurements, Appl. Rheol. 23 (2013) 1–10. https://doi.org/10.3933/ApplRheol-23-24628.

[201] R.L. Taylor, K.S. Pister, G.L. Goudreau, Thermomechanical analysis of viscoelastic solids, Int. J. Numer. Methods Eng. 2 (1970) 45–59.

[202] M. Kaliske, H. Rothert, Formulation and implementation of three-dimensional viscoelasticity at small and finite strains, Comput. Mech. 19 (1997) 228–239. https://doi.org/10.1007/s004660050171.

[203] H. Cho, R.G. Rinaldi, M.C. Boyce, Constitutive modeling of the rate-dependent resilient and dissipative large deformation behavior of a segmented copolymer polyurea, Soft Matter. 9 (2013) 6319–6330. https://doi.org/10.1039/c3sm27125k.

[204] R.G. Rinaldi, M.C. Boyce, S.J. Weigand, D.J. Londono, M.W. Guise, Microstructure evolution during tensile loading histories of a polyurea, J. Polym. Sci. Part B Polym. Phys. 49 (2011) 1660–1671. https://doi.org/10.1002/polb.22352.

[205] Stratasys, Digital Materials Data Sheet, (2022). https://www.stratasys.com/-/media/files/material-spec-sheets/mss_pj_digitalmaterialsdatasheet_0617a.pdf.

[206] D. Mohotti, T. Ngo, S.N. Raman, M. Ali, P. Mendis, Plastic deformation of polyurea coated composite aluminium plates subjected to low velocity impact, Mater. Des. 56 (2014) 696–713. https://doi.org/10.1016/j.matdes.2013.11.063.

[207] D. Mohotti, T. Ngo, P. Mendis, S.N. Raman, Polyurea coated composite aluminium plates subjected to high velocity projectile impact, Mater. Des. 52 (2013) 1–16. https://doi.org/10.1016/j.matdes.2013.05.060.

[208] R.D. Hussein, D. Ruan, G. Lu, S. Guillow, J.W. Yoon, Crushing response of square aluminium tubes filled with polyurethane foam and aluminium honeycomb, Thin-Walled Struct. 110

(2017) 140–154. https://doi.org/10.1016/j.tws.2016.10.023.

[209] S.S. Sarva, S. Deschanel, M.C. Boyce, W. Chen, Stress-strain behavior of a polyurea and a polyurethane from low to high strain rates, Polymer (Guildf). 48 (2007) 2208–2213. https://doi.org/10.1016/j.polymer.2007.02.058.

[210] M.H.R. Ghoreishy, Determination of the parameters of the Prony series in hyper-viscoelastic material models using the finite element method, Mater. Des. 35 (2012) 791–797. https://doi.org/10.1016/j.matdes.2011.05.057.

[211] M.A.P. Mohammed, E. Tarleton, M.N. Charalambides, J.G. Williams, Mechanical characterization and micromechanical modeling of bread dough, J. Rheol. (N. Y. N. Y). 57 (2012) 249–272. https://doi.org/10.1122/1.4768463.

[212] I. Emri, B.S. von Bernstorff, R. Cvelbar, A. Nikonov, Re-examination of the approximate methods for interconversion between frequency- and time-dependent material functions, J. Nonnewton. Fluid Mech. 129 (2005) 75–84. https://doi.org/10.1016/j.jnnfm.2005.05.008.

[213] D.E. Abram, A. Wikarna, F. Golnaraghi, G.G. Wang, A modular impact diverting mechanism for football helmets, J. Biomech. 99 (2020) 109502. https://doi.org/10.1016/j.jbiomech.2019.109502.

[214] B.A. Fulcher, D.W. Shahan, M.R. Haberman, C.C. Seepersad, P.S. Wilson, Analytical and experimental investigation of buckled beams as negative stiffness elements for passive vibration and shock isolation systems, J. Vib. Acoust. Trans. ASME. 136 (2014) 1–12. https://doi.org/10.1115/1.4026888.

[215] M.R. Shariatmadari, R. English, G. Rothwell, Effects of temperature on the material characteristics of midsole and insole footwear foams subject to quasi-static compressive and shear force loading, Mater. Des. 37 (2012) 543–559. https://doi.org/10.1016/j.matdes.2011.10.045.

[216] Y. Shimazaki, S. Nozu, T. Inoue, Shock-absorption properties of functionally graded EVA laminates for footwear design, Polym. Test. 54 (2016) 98–103. https://doi.org/10.1016/j.polymertesting.2016.04.024.

[217] F. Nazzi, The hexagonal shape of the honeycomb cells depends on the construction behavior of bees, Sci. Rep. 6 (2016) 1–6. https://doi.org/10.1038/srep28341.

[218] Z.L. Yu, N. Yang, L.C. Zhou, Z.Y. Ma, Y.B. Zhu, Y.Y. Lu, B. Qin, W.Y. Xing, T. Ma, S.C. Li, H.L. Gao, H.A. Wu, S.H. Yu, Bioinspired polymeric woods, Sci. Adv. 4 (2018).

https://doi.org/10.1126/sciadv.aat7223.

[219] L.J. Gibson, M.F. Ashby, The mechanics of honeycombs, 2014. https://doi.org/10.1017/cbo9781139878326.006.

[220] T. Shepherd, K. Winwood, P. Venkatraman, A. Alderson, T. Allen, Validation of a Finite Element Modeling Process for Auxetic Structures under Impact, Phys. Status Solidi Basic Res. 1900197 (2020) 1–14. https://doi.org/10.1002/pssb.201900197.

[221] X. Tan, B. Wang, S. Chen, S. Zhu, Y. Sun, A novel cylindrical negative stiffness structure for shock isolation, Compos. Struct. 214 (2019) 397–405. https://doi.org/10.1016/j.compstruct.2019.02.030.

[222] M. J. Mirzaali, H. Pahlavani, E. Yarali, A.A. Zadpoor, Non-affinity in multi-material mechanical metamaterials, (2020). https://www.nature.com/articles/s41598-020-67984-6.

[223] D. Zhang, Q. Fei, D. Jiang, Y. Li, Numerical and analytical investigation on crushing of fractal-like honeycombs with self-similar hierarchy, Compos. Struct. 192 (2018) 289–299. https://doi.org/10.1016/j.compstruct.2018.02.082.

[224] J. Zhai, Y. Liu, X. Geng, W. Zheng, Z. Zhao, C. Cui, M. Li, Energy absorption of pre-folded honeycomb under in-plane dynamic loading, Thin-Walled Struct. 145 (2019) 106356. https://doi.org/10.1016/j.tws.2019.106356.

[225] J.A. Harris, Additively Manufactured Metallic Cellular Materials for Blast and Impact Mitigation, (2017).

[226] C. Ling, J. Ivens, P. Cardiff, M.D. Gilchrist, Deformation response of EPS foam under combined compression-shear loading. Part I: Experimental design and quasi-static tests, Int. J. Mech. Sci. 144 (2018) 480–489. https://doi.org/10.1016/j.ijmecsci.2018.06.014.

[227] C. Ling, P. Cardiff, M.D. Gilchrist, Mechanical behaviour of EPS foam under combined compression-shear loading, Mater. Today Commun. 16 (2018) 339–352. https://doi.org/10.1016/j.mtcomm.2018.07.001.

[228] D. Mohr, M. Doyoyo, Experimental investigation on the plasticity of hexagonal aluminum honeycomb under multiaxial loading, J. Appl. Mech. Trans. ASME. 71 (2004) 375–385. https://doi.org/10.1115/1.1683715.

[229] A.S.M. Ashab, D. Ruan, G. Lu, Y.C. Wong, Quasi-static and dynamic experiments of aluminum honeycombs under combined compression-shear loading, Mater. Des. 97 (2016) 183–194.

https://doi.org/10.1016/j.matdes.2016.02.074.

[230] F. López Jiménez, N. Triantafyllidis, Buckling of rectangular and hexagonal honeycomb under combined axial compression and transverse shear Dedicated to Prof. S. Kyriakides on the occasion of his 60th birthday., Int. J. Solids Struct. 50 (2013) 3934–3946. https://doi.org/10.1016/j.ijsolstr.2013.08.001.

[231] D. Zhang, G. Lu, D. Ruan, Q. Fei, W. Duan, Quasi-static combined compression-shear crushing of honeycombs: An experimental study, Mater. Des. 167 (2019) 107632. https://doi.org/10.1016/j.matdes.2019.107632.

[232] B. Hou, A. Ono, S. Abdennadher, S. Pattofatto, Y.L. Li, H. Zhao, Impact behavior of honeycombs under combined shear-compression. Part I: Experiments, Int. J. Solids Struct. 48 (2011) 698–705. https://doi.org/10.1016/j.ijsolstr.2010.11.004.

[233] B. Hou, S. Pattofatto, Y.L. Li, H. Zhao, Impact behavior of honeycombs under combined shear-compression. Part II: Analysis, Int. J. Solids Struct. 48 (2011) 687–697. https://doi.org/10.1016/j.ijsolstr.2010.11.005.

[234] J. Fang, Y. Gao, G. Sun, N. Qiu, Q. Li, On design of multi-cell tubes under axial and oblique impact loads, Thin-Walled Struct. 95 (2015) 115–126. https://doi.org/10.1016/j.tws.2015.07.002.

[235] C. GEHRE, H. GADES, P. WERNICKE, Objective Rating of Signals Using Test and Simulation Responses, Proc. 21ST Int. Tech. Conf. Enhanc. Saf. Veh. HELD JUNE 2009, STUTTGART, Ger. (2009).

[236] C. Giordano, S. Kleiven, Development of an Unbiased Validation Protocol to Assess the Biofidelity of Finite Element Head Models used in Prediction of Traumatic Brain Injury, SAE Tech. Pap. 60 (2016). https://doi.org/10.4271/2016-22-0013.

[237] K.M. Yates, C.D. Untaroiu, Finite element modeling of the human kidney for probabilistic occupant models: Statistical shape analysis and mesh morphing, J. Biomech. 74 (2018) 50–56. https://doi.org/10.1016/j.jbiomech.2018.04.016.

[238] L. Grassi, N. Hraiech, E. Schileo, M. Ansaloni, M. Rochette, M. Viceconti, Evaluation of the generality and accuracy of a new mesh morphing procedure for the human femur, Med. Eng. Phys. 33 (2011) 112–120. https://doi.org/10.1016/j.medengphy.2010.09.014.

[239] M. Danti, M. Meneguzzo, R. Saponaro, I. Kowarska, Multi-objective optimization in vehicle concept modeling, Proc. ISMA 2010 - Int. Conf. Noise Vib. Eng. Incl. USD 2010. (2010) 4095–4108.

[240] O. Wagersten, B. Lindau, L. Lindkvist, R. Šoderberg, Using morphing techniques in early variation analysis, J. Comput. Inf. Sci. Eng. 14 (2014) 1–9. https://doi.org/10.1115/1.4025719.

[241] L. Dev, L.I.S. Oftware, T.E.C. Orporation, LSTC. LS-DYNA Theory Manual Version 970. r:6030, n.d.

[242] S.P. Soe, P. Martin, M. Jones, M. Robinson, P. Theobald, Feasibility of optimising bicycle helmet design safety through the use of additive manufactured TPE cellular structures, Int. J. Adv. Manuf. Technol. 79 (2015) 1975–1982. https://doi.org/10.1007/s00170-015-6972-y.

[243] G. Li, Z. Zhang, G. Sun, X. Huang, Q. Li, Comparison of functionally-graded structures under multiple loading angles, Thin-Walled Struct. 94 (2015) 334–347. https://doi.org/10.1016/j.tws.2015.04.030.

[244] A. Asadpoure, L. Valdevit, Topology optimization of lightweight periodic lattices under simultaneous compressive and shear stiffness constraints, Int. J. Solids Struct. 60 (2015) 1–16. https://doi.org/10.1016/j.ijsolstr.2015.01.016.

[245] F. Côté, V.S. Deshpande, N.A. Fleck, A.G. Evans, The compressive and shear responses of corrugated and diamond lattice materials, Int. J. Solids Struct. 43 (2006) 6220–6242. https://doi.org/10.1016/j.ijsolstr.2005.07.045.

[246] S. Janbaz, K. Narooei, T. Van Manen, A.A. Zadpoor, Strain rate – dependent mechanical metamaterials, (2020).

[247] J.W. Hutchinson, R.C. Tennyson, D.B. Muggeridge, Effect of a local axisymmetric imperfection on the buckling behaviorof a circular cylindrical shell under axial compression, AIAA J. 9 (1971) 48–52. https://doi.org/10.2514/3.6123.

[248] R.C. Tennyson, D.B. Muggeridge, Buckling of axisymmetric imperfect circular cylindrical shells underaxial compression, AIAA J. 7 (1969) 2127–2131. https://doi.org/10.2514/3.5568.

[249] C.D. Babcock, Shell stability, J. Appl. Mech. Trans. ASME. 50 (1983) 935–940. https://doi.org/10.1115/1.3167206.

[250] A.G. Evans, M.Y. He, V.S. Deshpande, J.W. Hutchinson, A.J. Jacobsen, W.B. Carter, Concepts for enhanced energy absorption using hollow micro-lattices, Int. J. Impact Eng. 37 (2010) 947–959. https://doi.org/10.1016/j.ijimpeng.2010.03.007.

[251] W. Abramowicz, N. Jones, Dynamic axial crushing of circular tubes, Int. J. Impact Eng. 2 (1984) 263–281. https://doi.org/10.1016/0734-743X(84)90010-1.

[252] T. Borrvall, A heuristic attempt to reduce transverse shear locking in fully integrated hexahedra with poor aspect ratio, Dynamore.De. (2009). https://www.dynamore.de/en/downloads/papers/09-conference/papers/G-I-02.pdf.

[253] J. Zhang, M.F. Ashby, The out-of-plane properties of honeycombs, Int. J. Mech. Sci. 34 (1992) 475–489. https://doi.org/10.1016/0020-7403(92)90013-7.

[254] T.W. Gaither, T.A. Sanford, M.A. Awad, E.C. Osterberg, G.P. Murphy, B.A. Lawrence, T.R. Miller, B.N. Breyer, Estimated total costs from non-fatal and fatal bicycle crashes in the USA: 1997-2013, Inj. Prev. 24 (2018) 135–141. https://doi.org/10.1136/injuryprev-2016-042281.

[255] A. Høye, Bicycle helmets – To wear or not to wear? A meta-analyses of the effects of bicycle helmets on injuries, Accid. Anal. Prev. 117 (2018) 85–97. https://doi.org/10.1016/j.aap.2018.03.026.

[256] A. Cernicchi, U. Galvanetto, L. Iannucci, Virtual modelling of safety helmets: Practical problems, Int. J. Crashworthiness. 13 (2008) 451–467. https://doi.org/10.1080/13588260802055460.

[257] D.L. Allsop, C.Y. Warner, M.G. Wille, D.C. Schneider, A.M. Nahum, Facial impact response a comparison of the hybrid III dummy and human cadaver, SAE Tech. Pap. (1988). https://doi.org/10.4271/881719.

[258] E.S. Gurdjian, V.L. Roberts, L.M. Thomas, Tolerance curves of acceleration and intracranial pressure and protective index in experimental head injury, J. Trauma - Inj. Infect. Crit. Care. 6 (1966) 600–604. https://doi.org/10.1097/00005373-196609000-00005.

[259] B. Depreitere, C. Van Lierde, J. Vander Sloten, R. Van Audekercke, G. Van Der Perre, C. Plets, J. Goffin, Mechanics of acute subdural hematomas resulting from bridging vein rupture, J. Neurosurg. 104 (2006) 950–956. https://doi.org/10.3171/jns.2006.104.6.950.

[260] T.A. Gennarelli, L.E. Thibault, Biomechanics of acute subdural hematoma, J. Trauma - Inj. Infect. Crit. Care. 22 (1982) 680–686. https://doi.org/10.1097/00005373-198208000-00005.

[261] S.S. Margulies, L.E. Thibault, A proposed tolerance criterion for diffuse axonal injury in man, J. Biomech. 25 (1992) 917–923. https://doi.org/10.1016/0021-9290(92)90231-O.

[262] N. Yoganandan, J. Li, J. Zhang, F.A. Pintar, T.A. Gennarelli, Influence of angular acceleration-deceleration pulse shapes on regional brain strains, J. Biomech. 41 (2008) 2253–2262. https://doi.org/10.1016/j.jbiomech.2008.04.019.

[263] N.J. Mills, A. Gilchrist, Oblique impact testing of bicycle helmets, Int. J. Impact Eng. 35 (2008)

1075–1086. https://doi.org/10.1016/j.ijimpeng.2007.05.005.